EFFECTS OF EARTHQUAKE RECORD SCALING
ON NONLINEAR STRUCTURAL RESPONSE

Report on PEER-LL Program Task 1G00 Addendum (Sub-Task 1 of 3)

Nicolas Luco & Paolo Bazzurro
AIR Worldwide Corporation (San Francisco, CA)

Abstract

Limitations in the existing ground motion database force the scaling of real records to obtain accelerograms that are consistent with the ground motion target for structural design and evaluation. In the seismology and engineering communities the acceptance of the limits for "legitimacy" of scaling varies from one (no scaling allowed) to ten. The concerns expressed by detractors are mostly based on the knowledge of systematic and unquestionable differences in ground motion characteristics for different magnitude-distance (M_w-R_close) scenarios and much less on their effects on structures. At the other end of the spectrum Cornell and his co-workers at Stanford University have claimed that scaling is not only legitimate but also useful for assessing post-elastic response statistics of structures. Such studies, however, did not draw conclusions valid over the entire spectrum of structural vibration periods and did not state the conditions under which scaling may fail.

This study investigates whether scaling of a record randomly selected from a M_w-R_close bin introduces bias in nonlinear structural response. Can one scale up a M_w=6.5, R_close=20km record to obtain a ground motion level expected for a M_w=7.25 event at 5km from the fault? Is scaling legitimate for assessing the response of structures of all periods? Are the effects of scaling constant for all periods and for different levels of nonlinear response? We consider the legitimacy of scaling within a M_w-R_close bin and across M_w-R_close bins. In both cases, the records are scaled up and down by large factors to determine whether the response to scaled records departs from the response of un-scaled ones that are "naturally" at that level. The answers to these questions are sought by investigating the nonlinear response of a suite of single-degree-of-freedom (SDOF) systems with multiple "strengths" to achieve increasing levels of nonlinear responses. Also considered are elastic and ductile models of a multi-degree-of-freedom (MDOF) building.

The results of this study demonstrate that scaling earthquake records can, in fact, introduce a bias in the nonlinear structural drift response to such records. The extent of bias depends on the period of vibration and overall strength of the structure of interest, and whether its drift response is dominated by excitation input at a single or multiple periods (i.e., SDOF versus MDOF structures). The severity of the bias also depends on the characteristics (e.g., M_w-R_close) of the records that are scaled, as well as those of the target ground motion scenario. For the most part, the bias can be explained by systematic differences between the elastic response spectra for records that are scaled up (or down) and those that are naturally (without scaling) at a target spectral acceleration level.

1 Motivation

With the advent of Performance-Based Earthquake Engineering, and the availability of sophisticated structural analysis software and faster computers, nonlinear dynamic time-history analysis (NDTHA) has recently become more widely used for both design and evaluation of structures. Perhaps one of the biggest obstacles preventing more widespread use of NDTHA is the selection of appropriate ground motion records. Engineers often seek to obtain from seismologists real ground motion records that closely match the spectral acceleration at a specified hazard level (e.g., 10% in 50 years) as well as the magnitude-distance (M_w-R_{close}) pair(s) of the events controlling the seismic hazard at the building site. The spectral acceleration of interest at many sites in seismically active regions of the world such as California is often relatively large, and the earthquake scenarios that control the hazard are often large magnitude events generated by nearby faults. Despite the recent increase in the number of records provided by large earthquakes occurred recently around the world (e.g., the 1999 M_w=7.6 Chi-Chi Earthquake, the 1999 M_w=7.5 Kocaeli Earthquake, the 2002 M_w=7.9 Denali Earthquake, and the 2003 M_w=8.0 Hokkaido Earthquake), the existing database for such spectral acceleration and M_w-R_{close} conditions is still very limited. Furthermore, the hazard at a site may be characterized by specific rupture-directivity conditions and site classifications (e.g., NEHRP D), further limiting the number of earthquake records available. Given the preference of the vast majority of engineers to use synthetic ground motions, scaling real records to obtain accelerograms that are consistent with a design target ground motion level is often the only remaining option.

In the seismology and engineering communities, the acceptance of ground motion scaling limits varies wildly from one (no scaling allowed) to ten or more (e.g., the earthquake records used for the PEER Testbeds were scaled by factors as large as 11). These limits are based more on a "comfort feeling" than on a sound technical basis. This study attempts to provide the quantitative technical basis for threshold limits beyond which scaling of a record randomly selected from a pool of accelerograms belonging to a magnitude-distance (M_w-R_{close}) scenario introduces bias in the nonlinear response of structures. The bias is computed with respect to an estimate of the "true" structural response that, for these purposes, is taken to be the estimate of the median response to records that are, by nature, already at a particular intensity level without any need for scaling. To avoid any misunderstanding, by "ground motion scaling" here we simply mean multiplying a record by a constant scalar factor in order to reach a target spectral acceleration level. The time scale (and therefore, the frequency content) of the record is left untouched by the scaling operation.

This study was intended to support another PEER Lifelines project (1F01), namely the Design Ground Motion Library (DGML), which will develop a library of recorded ground motions suitable for use by engineers for dynamic analysis of various structures. In addition to the library of earthquake records, the DGML will likely provide guidance for scaling the recommended records, if necessary. The extent to which earthquake records can be scaled before introducing excessive bias in nonlinear structural response, as investigated in this study, is also important for deciding on the recommended records themselves.

2 Background

The issue of whether ground motion scaling produces different structural response statistics has been debated in the engineering community for at least a decade. The concerns expressed by many individuals are mostly based on the knowledge of systematic and unquestionable differences in ground motion characteristics (e.g., spectral shape, duration, etc.) for different M_w-R_{close} scenarios and much less on their effects on structures. The claim that such systematic differences in the input caused systematic differences in the response is often based only on engineering intuition or, at best, on experience gained in evaluating linear elastic rather than nonlinear post-elastic structural responses. Testing the legitimacy of ground motion scaling for assessing nonlinear responses of structures was almost uncharted territory until the studies by Cornell and his students at Stanford University (e.g., Sewell 1989; Inoue and Cornell 1991; Bazzurro and Cornell 1994; Shome *et al.* 1998; Luco 2002). All such studies found that judicious scaling was not only legitimate but, under certain conditions, also useful for the purpose of efficiently assessing post-elastic response statistics of structures.

Perhaps with the exception of the work by Shome *et al.*, however, all the other cited studies have not had a large impact on engineering practice mainly because the main conclusions were obscured by arguments heavily based on statistical concepts and findings. The work by Shome *et al.*, although confined in scope (i.e., only one structures was analyzed, only 20 records for each of four M_w-R_{close} bins were used, and no near-source records were considered) reached out to the practicing engineers by addressing their concerns about ground motion scaling more directly. The study, however, did not reach conclusions over the entire spectrum of structural periods, and did not state the conditions under which scaling may fail. Some of the conclusions that led to the purported legitimacy of scaling were also made somewhat less conclusive by the limited sample size of records adopted. In the study reported on here, in an attempt to avoid obscuring the results we will seek to answer the questions above by keeping statistical arguments to a minimum.

Furthermore, Shome *et al.* addressed the ground motion scaling issue from a slightly different perspective than the one used here. The focus there was on the legitimacy of scaling a pool of records from a source M_w-R_{close} bin to match the median "intensity" level of records belonging to the same bin or a different target M_w-R_{close} bin. The legitimacy was assessed in terms of bias of the median response generated by scaling the entire suite of source records that were scaled, on average, by a certain quantity. Some of the source records were scaled by a large amount and some by a small amount. Here we also tackle a different but very much related issue. Does a record selected at random from a M_w-R_{close} bin and scaled (in practice, almost always up but, perhaps more academically, also down) to a target intensity level produce a nonlinear structural response that is, on average, materially "different" than that generated, on average, by records that are already naturally at the target intensity level? If there is bias, how large is it? Is the bias constant or does it vary with structural period and level of nonlinear response? Does the bias change if the source record scaled to match the target ground motion is characterized by values of M_w and R_{close} that are different from those that control the site hazard? Or, in other words, given the same level of scaling, do the magnitude and distance of the source and target records affect the bias in the nonlinear structural response?

3 Objective

Shortly put, the objective of this study is to investigate whether amplitude scaling of input earthquake records to a target pseudo spectral acceleration (S_a) level introduces a bias in the resulting nonlinear structural drift response. As alluded to above, the bias is defined as

$$\text{Bias} = \frac{\text{median response to scaled records}}{\text{median response to unscaled records (that are naturally at target } S_a\text{)}}$$

This definition is used in this study to quantify the bias (if any) and thereby provide a technical basis for limits on scaling.

Also investigated in this study is whether the bias depends on (i) the general characteristics of the target ground motion scenario (e.g., M_w and R_close), (ii) the general characteristics of the records that are scaled, (iii) the vibration period(s) of the structure of interest, (iv) the overall strength of the structure, and (v) the contribution of higher (than the first) modes of vibration to the structural response.

4 Organization of Report

In total, 469 earthquake ground motion records grouped into 7 different bins are used in this study, as described in Section 5. As described in Section 6, the nonlinear dynamic response of 48 single-degree-of-freedom (SDOF) and 2 multi-degree-of-freedom (MDOF) structures is analyzed. The procedure developed to quantify the bias induced by scaling is outlined in Section 7, and the results are presented in Section 8. In Section 9 an overall summary of the results is provided, some general conclusions are drawn in Section ?, and Section 11 describes a few potential topics for future work.

5 Description of Earthquake Records

5.1 Bins I to VI

As explained in the introduction, both intra- and inter-bin scaling are investigated in this study. Six different bins based on earthquake magnitude (M_w) and closest source-to-site distance (R_close) are defined here, as listed in Table 1.

Besides the M_w and R_close differences, the other general characteristics of the six bins are identical. More specifically, they each contain 73 earthquake records that are

- from the PEER Strong Ground Motion Database (processed by Dr. Walt Silva)
- from shallow crustal events,
- from stations that are situated on stiff-soil sites (USGS B-C or Geomatrix B-D classification),

Table 1. Earthquake moment magnitude, M_w, and closest source-to-site distance, R_{close}, ranges for six of the bins of earthquake records considered in this report.

Bin Label	M_w	R_{close}
I	6.4-6.8	0-15km
II	6.4-6.8	15-30km
III	6.4-6.8	30-50km
IV	6.9-7.6	0-15km
V	6.9-7.6	15-30km
VI	6.9-7.6	30-50km

- not from instruments on dams or above the lowest level of buildings, and
- filtered with high- and low-pass corner-frequencies greater than 0.2 hertz and less than 18 hertz, respectively.

The last constraint above is used because, according to Silva, the widest usable bandwidth of such records is 1.25/18=0.07 to 1/(0.2*1.25)=4 seconds. As described in a subsequent section, this covers the range of fundamental vibration periods considered in this study.

A complete list of the earthquake records in each bin is provided in the appendix. Note that only a randomly selected subset of the Chi-Chi records that satisfy constraints described above were included in order to minimize the number of records from any one single event.

The "median" (computed as the geometric mean in this paper, unless noted otherwise) of the elastic response spectra for each bin of earthquake records (including the "Near-Source Bin" described in the next subsection) is shown in Figure 1.

5.2 Near-Source Bin

In addition to the six M_w-R_{close} bins of earthquake records described above, a seventh bin of 31 "near-source" earthquake records is also considered. This near-source bin very similar to Bin I (e.g., M_w=6.5-6.9 and R_{close}=0-16km), except that all of its earthquake records are (i) from stations in the forward rupture-directivity region, and (ii) strike-normal components of the ground motion. The forward rupture-directivity region is defined using Somerville *et al.*'s (1997) rupture directivity modification factor, by assuming that values greater than unity signify forward directivity. For a detailed description of these near-source earthquake records, the reader is referred to (Luco 2002).

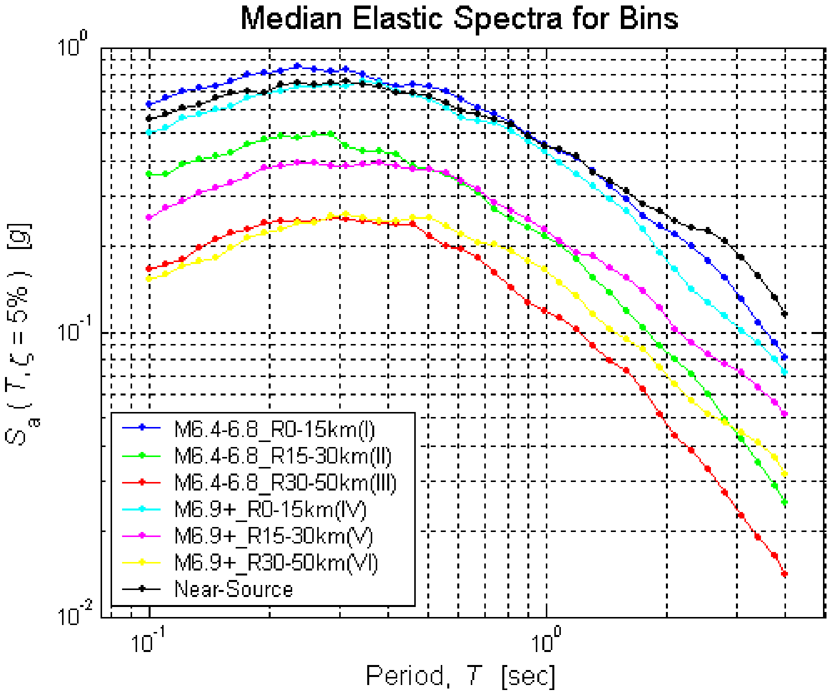

Figure 1. Median (computed as geometric mean) elastic response spectra for the seven bins of earthquake records considered in this report.

6 Description of Structures

As mentioned above, both single-degree-of-freedom (SDOF) and multi-degree-of-freedom (MDOF) structures are considered in this study. In all, 48 SDOF structures of different periods and strength and 2 MDOF structures are considered. The SDOF structures are representative of, for example, first-mode-dominated buildings or bridge bents. Multiple modes contribute significantly to the response of the two MDOF structures, which are elastic and ductile models of a realistic 9-story steel moment-resisting frame (SMRF) building. All of these structures are described in more detail below.

Note that dynamic time-history analysis of the SDOF structures is performed using a MATLAB implementation of Newmark's linear acceleration method (as described in Chopra 1995). For the MDOF structures, DRAIN-2DX (Prakash 1993) is employed, with P-Delta effects included.

6.1 Single-Degree-of-Freedom (SDOF) Oscillators

The SDOF (a.k.a., "lollipop") structures considered have vibration periods of T = 0.1, 0.2, 0.3, 0.5, 1, 2, 3, and 4 seconds. The first six periods are the same as those for which the U.S. Geological Survey has provided seismic hazard curves (Frankel & Leyendecker 2001), whereas the last (and largest) period is based on the filter corners for the earthquake records used (as explained above in Section 5.1). Also like the USGS hazard maps (and typical attenuation relations), the damping ratio for each of the SDOF structures is set to ζ=5%.

For each vibration period, six different yield forces (F_y's) of the SDOF structures are considered, each based on the particular target spectral acceleration (S_a) of interest. (Note that, in this paper, S_a always refers to the spectral acceleration at the fundamental period of the structure under consideration). The largest F_y considered is equal to the target S_a multiplied by the mass (m) of the structure (here we use "mass normalized" structures, such that m=1), which corresponds to a strength reduction factor of R=1 and therefore elastic response. The other five yield forces are fractions of this largest strength, namely (target S_a)*m/R where R = 2, 4, 6, 8, and 10. In what follows, these strengths of the SDOF structures will be referred to by the corresponding value of R only. Note that R=10 corresponds to a highly inelastic structure.

As depicted in Figure 2, the force-displacement hysteretic behavior of the SDOF structures considered is bilinear inelastic with a strain hardening ratio of α=2%.

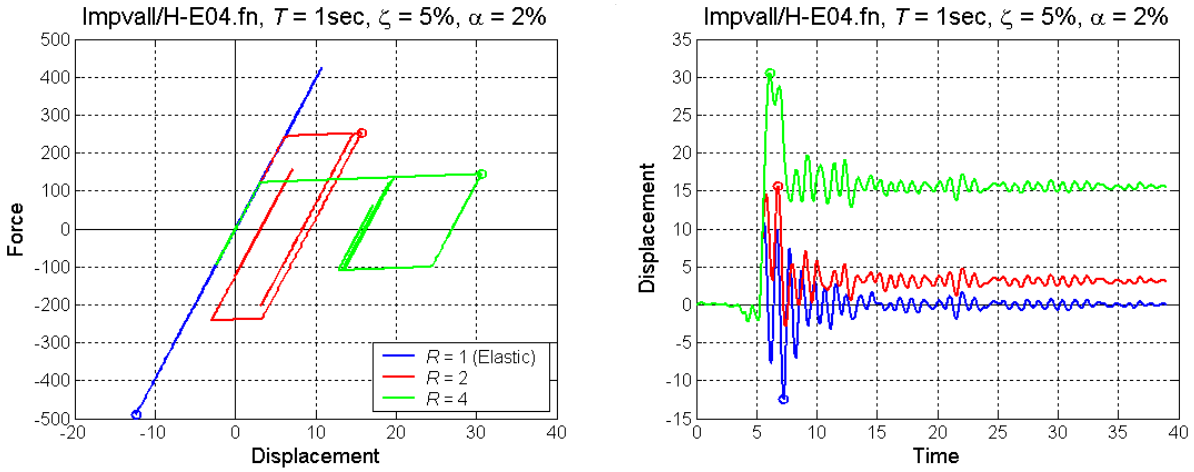

Figure 2. Examples of the force-displacement hysteresis and displacement time histories for the SDOF structures considered in this paper.

6.2 Multi-Degree-of-Freedom (MDOF) Buildings

The two MDOF structures considered are (1) an elastic model and (2) a ductile model of a 9-story (plus basement), 5-bay steel moment-resisting frame (SMRF) building that was designed by consulting engineers for Los Angeles conditions as part of the SAC Steel Project. As illustrated in Figure 3, a two-dimensional model of one of the exterior moment-resisting frames of the building is analyzed. For the ductile model, the beam ends (immediately to the right and left of each column) and column ends (immediately above and below each floor, and at the column splices) are modeled as plastic hinges with 3% strain hardening relative to the elastic stiffness of the beam and column, respectively. The fundamental period of the building model is T=2.3sec, and the first-mode damping ratio is 2%. For additional details, the reader is referred to FEMA 355C (2000) and (Luco 2002).

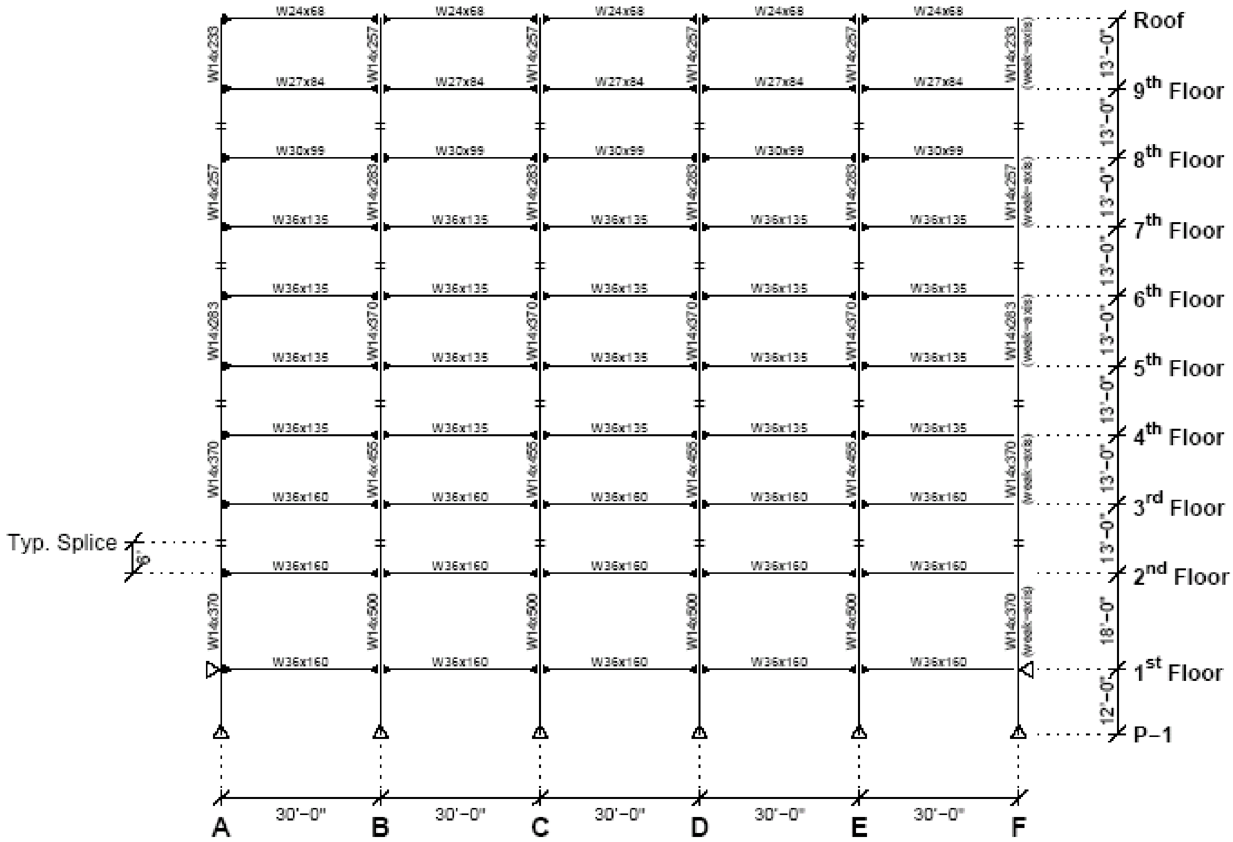

Figure 3. Elevation of a 9-story steel moment-resisting frame designed by practicing engineers for Los Angeles conditions as part of the SAC Steel Project (Phase II). An elastic and a ductile MDOF model of this frame are considered in this report.

Note that the two MDOF building models as considered in order to compare the SDOF results with those for a more realistic structure, as well as to assess how the contribution of higher modes may alter the effects of scaling.

7 Outline of Procedure

The procedure developed for quantifying the bias in nonlinear structural response induced by scaling of the input earthquake record(s) is relatively simple, and the same procedure is applied for both intra- and inter-bin scaling. For a given structure, the following steps are taken:

(1) Decide on a target spectral acceleration (at the fundamental period of the structure of interest and a damping ratio of 5%) that is associated with an earthquake record in the "target" bin.
(2) For this earthquake record, un-scaled, compute the nonlinear inelastic structural response (e.g., inelastic spectral displacement for the SDOF structures). This is considered to be the "true" nonlinear structural response that serves as the basis of comparison.

(3) Scale all of the earthquake records in the "source" bin (same as the target bin for intra-bin scaling, different for inter-bin scaling) to the target spectral acceleration, and record the scale factors.
(4) Compute the nonlinear inelastic structural response for the scaled earthquake records.
(5) Plot the ratio of the nonlinear inelastic structure responses for the scaled over un-scaled earthquake records versus the scale factors.
(6) Repeat Steps 1-5 for another target spectral acceleration associated with another earthquake record in the target bin, until all of them have been considered.

8 Results

The results of the procedure for quantifying the bias induced by intra- and inter-bin scaling are first presented for the suite of simple SDOF oscillators (of a range of different periods and strengths) and then for the two MDOF buildings (one elastic, the other ductile). For one of the SDOF oscillators, namely that of "moderate" period (T=1sec) and strength (R=4), the procedure is demonstrated in a step-by-step fashion. For the other structures, only a summary of the final results presented.

Note that in investigating intra-bin scaling for each of the 48 SDOF structures (8 periods and 6 strengths), 73^2 dynamic analyses are carried out for each of Bins I-VI, plus 31^2 for the Near-Source Bin, for a total of 1,580,880 dynamic analyses. Similarly, for 10 different intra-bin scaling combinations considered (as described below), a total of 2,263,584 SDOF dynamic analyses are performed. For each of the 2 MDOF structures, however, just 31^2 and 31x73 dynamic analyses for intra- and inter-bin scaling, respectively, are carried out, for a total of 6448 MDOF dynamic analyses.

8.1 SDOF Structures

For each SDOF oscillator of a given period (T), damping ratio (ζ=5%), strength reduction factor (R), and strain-hardening ratio (α=2%), note that the nonlinear structural response measure considered is the peak relative (to the ground) displacement, a.k.a., the inelastic spectral displacement S_d^I.

8.1.1 Intra-Bin Scaling

To reiterate, intra-bin scaling refers to scaling of an earthquake record from a given M_w-R_{close} "source" bin to a target S_a associated with the same M_w-R_{close} bin. The purpose of intra-bin scaling is to obtain a record in the M_w-R_{close} bin that is at the S_a level of interest.

The procedure outlined in Section 7 for quantifying the effects of intra-bin scaling on nonlinear structural response is demonstrated here in a step-by-step fashion for the Near-Source Bin and a moderate period (T=1sec) and strength (R=4) oscillator. Subsequently, a summary of the results is provided (i) for Bins I-VI and the same "moderate" oscillator, and (ii) for all 48 oscillators considered and the Near-Source Bin.

8.1.1.1 Near-Source Bin, Moderate Period and Strength Structure

Step 1:

As illustrated in Figure 4a on a plot of the elastic response spectra for all 31 of the earthquake records in the Near-Source Bin, the first target spectral acceleration considered is S_a=2.0g. This spectral acceleration value is the largest (at T=1s) in the bin, and is associated with the 1994 Northridge Rinaldi Receiving Station (RRS) earthquake record.

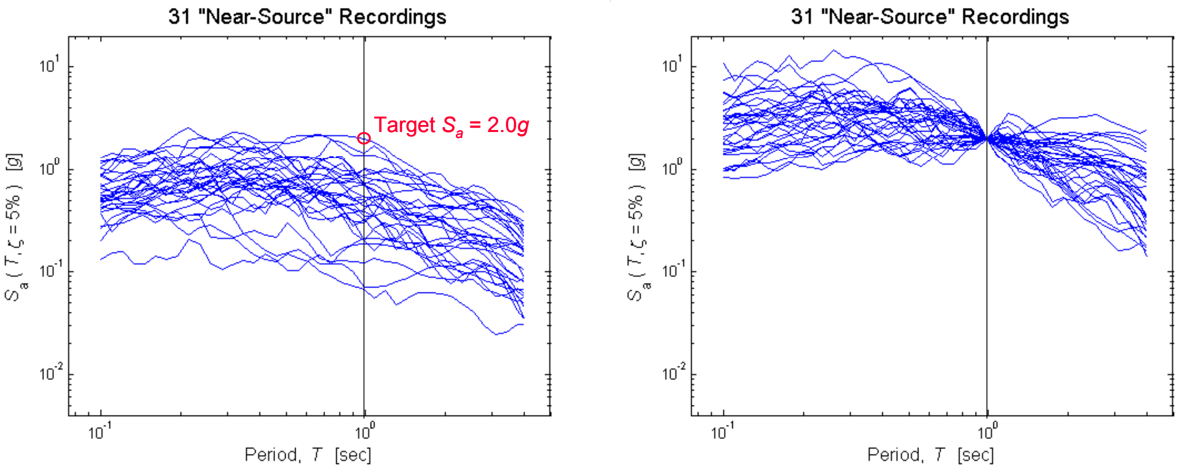

Figure 4. Elastic response spectra **(a)** before and **(b)** after scaling (intra-bin) the earthquake records in the Near-Source Bin to a target spectral acceleration of 2.0g (at a period of 1sec).

Step 2:

The inelastic spectral displacement for the un-scaled "target record" specified in Step 1 is shown in Figure 5a. Recall that this value, S_d^I=49.4cm, is taken to be the "true" inelastic spectral displacement for this target S_a level. Also shown in the figure, as a basis of comparison, are the S_d^I values for the other records in the bin, before they are scaled in the next step.

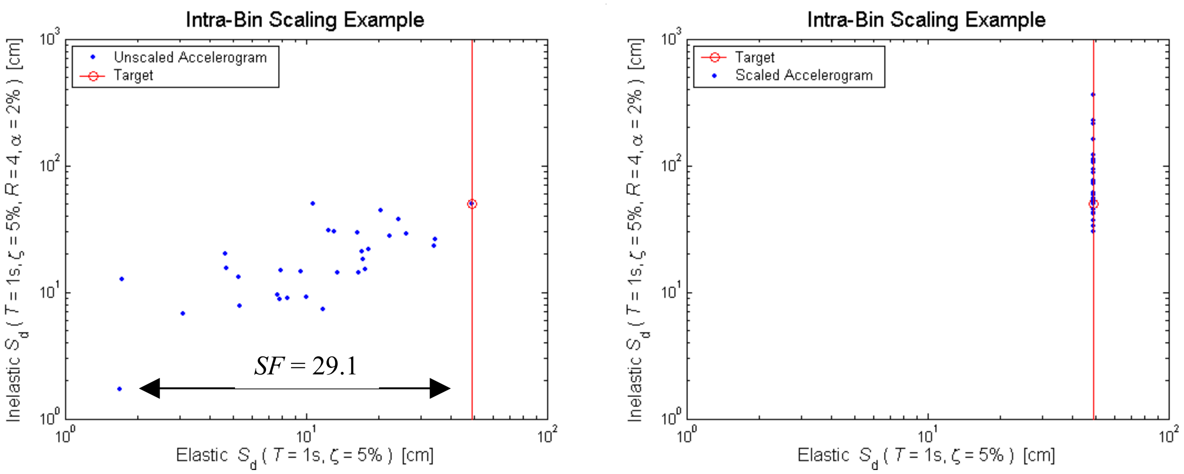

Figure 5. Inelastic spectral displacement responses (versus elastic spectral displacement, which is proportional to spectral acceleration) **(a)** before and **(b)** after scaling (intra-bin) the earthquake records in the Near-Source Bin to a target spectral acceleration of 2.0*g* (or, equivalently, a target elastic spectral displacement of approximately 50cm). Note that the period of the oscillator is *T*=1sec, and the strength reduction factor is *R*=4.

Step 3:

The elastic response spectra after scaling all of the earthquake records in the Near-Source Bin to the target S_a=2*g* (specified in Step 1) are shown in Figure 4b. Note how the response spectra (and the underlying records) are scaled in amplitude only, not in shape. As depicted in Figure 5a, the scale factors in this case range from 1 (for the target record) to 29.1, indicative of the substantial intra-bin variability in S_a.

Step 4:

The inelastic spectral displacement responses (S_d^{I}) to the 30 scaled records from Step 3 are shown in Figure 5b. Note that most of the S_d^{I} values are larger than the "true" S_d^{I} from the un-scaled target record.

Step 5:

The ratios of the S_d^{I} values for the scaled earthquake records (from Step 4) to that for the un-scaled "target" record (from Step 2) are plotted against the corresponding scale factors in Figure 6. Note that there appears to be a trend, albeit noisy, that suggests that the larger the scale factor, the larger the median ratio of the scaled to un-scaled S_d^{I} (the bias). However, the record-to-record variability of S_d^{I} for un-scaled records with the same (or similar) values of S_a, as evident in Figure 5a, prevents us from drawing general conclusions before Steps 1-5 are repeated for the other 30 target records and S_a levels in the Near-Source Bin. This is done in Step 6.

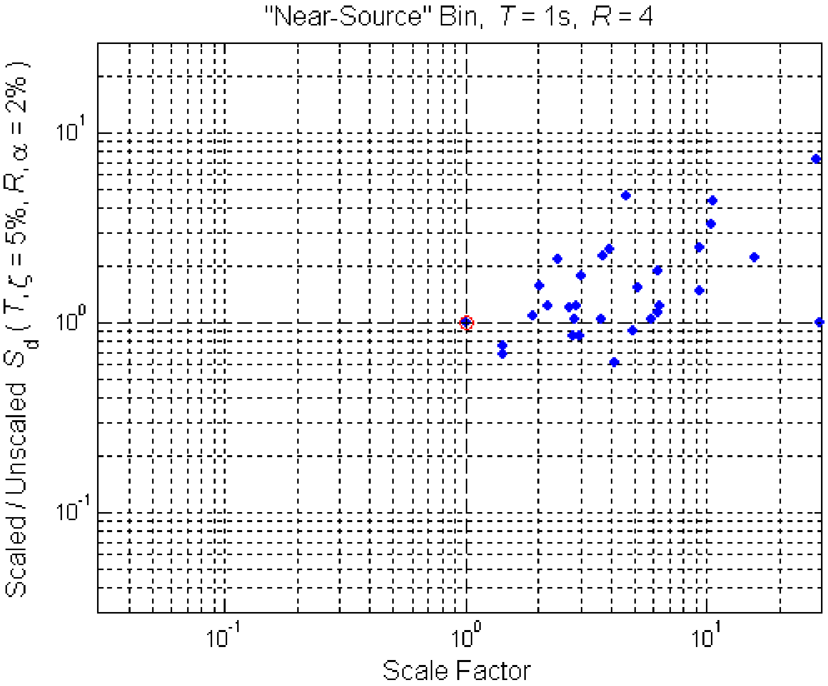

Figure 6. Ratios of the inelastic (R=4) spectral displacement responses to (i) the Near-Source records scaled to a target S_a (at T=1sec) of 2.0g versus (ii) the un-scaled Near-Source record that is naturally at the target S_a=2.0g (circled in red), all plotted against the corresponding scale factors.

Step 6:

For the second "loop" of the procedure, the next-to-lowest S_a in the Near-Source Bin, namely 0.07g, is considered as the target. The elastic response spectra before and after scaling are illustrated in Figure 7, and the corresponding ratios of scaled to un-scaled S_d^I are plotted in Figure 8. Included in this figure are the results that were obtained by scaling to the largest S_a in the Near-Source Bin, i.e., 2.0g (first shown in Figure 6). For those results the scale factors were all larger than unity, whereas now the scale factors range from 0.04 to 1.02.

Like in Figure 6, a trend is apparent in Figure 7 that suggests that the median ratio of the S_d^I response to scaled versus un-scaled records, i.e., the bias, increases with increasing scale factor (nearly linearly in log-log scale). In one case, however, a small ratio of scaled to un-scaled S_d^I (in the 0.1-0.2 range) is observed at a scale factor near one; as mentioned above in Step 5, this is due to the record-to-record variability in S_d^I, even for records with similar S_a, and emphasizes the need to consider multiple target records.

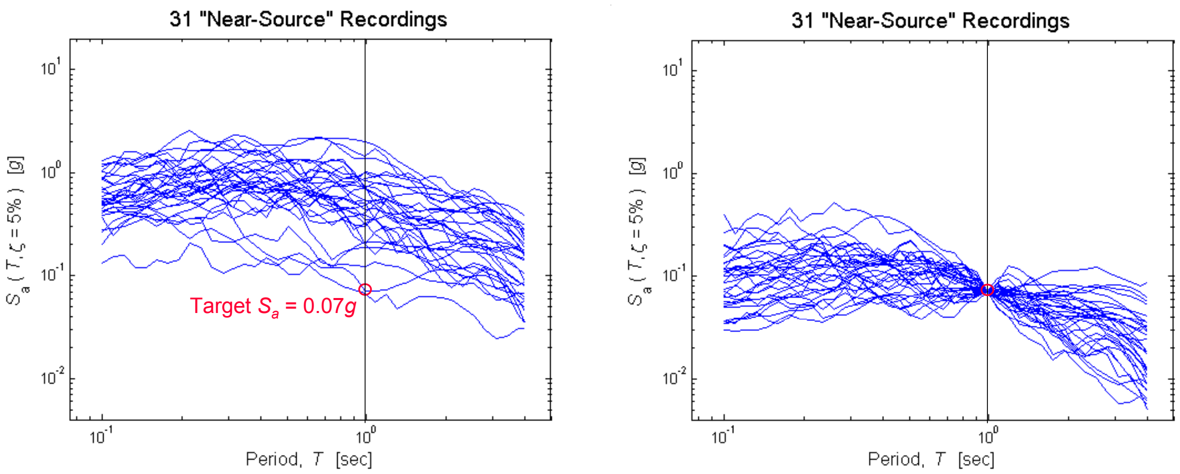

Figure 7. Elastic response spectra **(a)** before and **(b)** after scaling (intra-bin) the earthquake records in the Near-Source Bin to a target spectral acceleration of 0.07*g*.

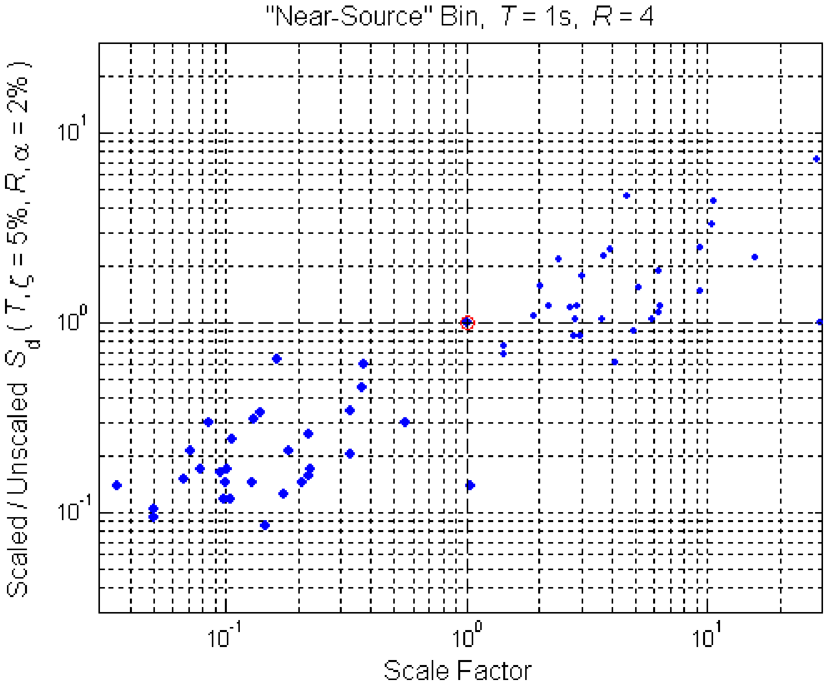

Figure 8. Ratios of the inelastic (R=4) spectral displacement responses to (i) the Near-Source records scaled to a target S_a (at T=1sec) of 0.07*g* versus (ii) the un-scaled Near-Source record that is naturally at the target S_a=0.07*g* (circled in red), all plotted against the corresponding scale factors. The smaller blue data points with scale factors larger than unity are the same as those plotted in Figure 6 above.

As another example, the target S_a level that corresponds to the median (found conventionally in this case, not computed as the geometric mean) of the Near-Source Bin, namely 0.50*g*, is considered for the third "loop" of the procedure. The S_d^{I} responses before and after scaling the earthquake records are shown in Figure 9, and, as obtained from Figure 9b, the ratios of the S_d^{I} responses for the scaled records to that for the un-scaled target record are plotted in Figure 10. Consistent with the results obtained by scaling to a higher (2.0g) and lower (0.07g) target S_a (shown in Figure 8), the results in Figure 10 show a positive trend, albeit mild, with scale factor in the scaled to un-scaled S_d^{I} ratios, abbreviated here as $r(S_d^{\mathrm{I}})$. Unlike the previous results, however, note that most of the $r(S_d^{\mathrm{I}})$ values are less than unity, both for scale factors larger and less than unity; again, this is more likely an indication that the S_d^{I} response to the particular un-scaled target record used in this case is relatively large, not that the S_d^{I} response to the scaled records is in general biased low. Again, this is why we consider multiple target S_a levels and records.

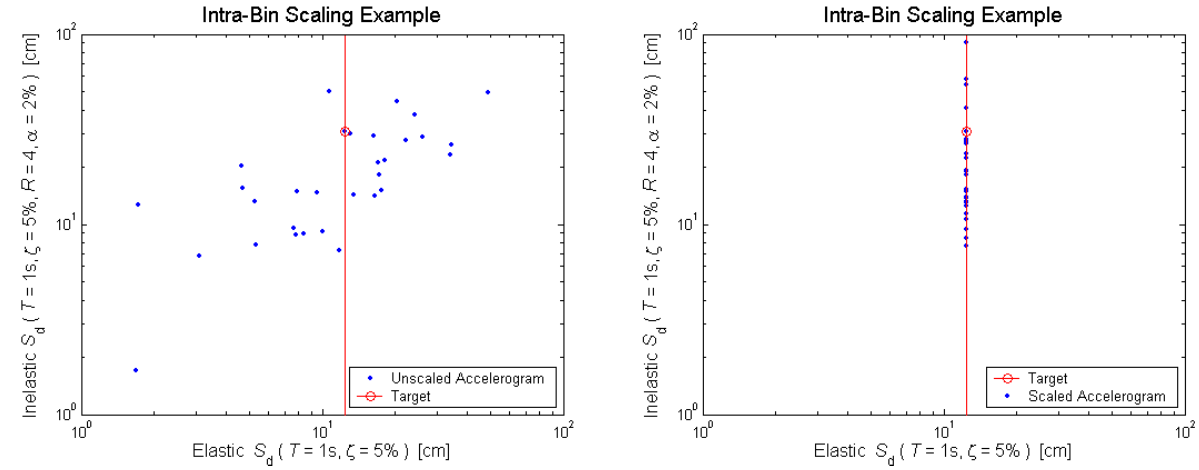

Figure 9. **.** Inelastic spectral displacement responses (versus elastic spectral displacement, which is proportional to spectral acceleration) **(a)** before and **(b)** after scaling (intra-bin) the earthquake records in the Near-Source Bin to a target spectral acceleration of 0.5*g* (or, equivalently, a target elastic spectral displacement of approximately 12cm).

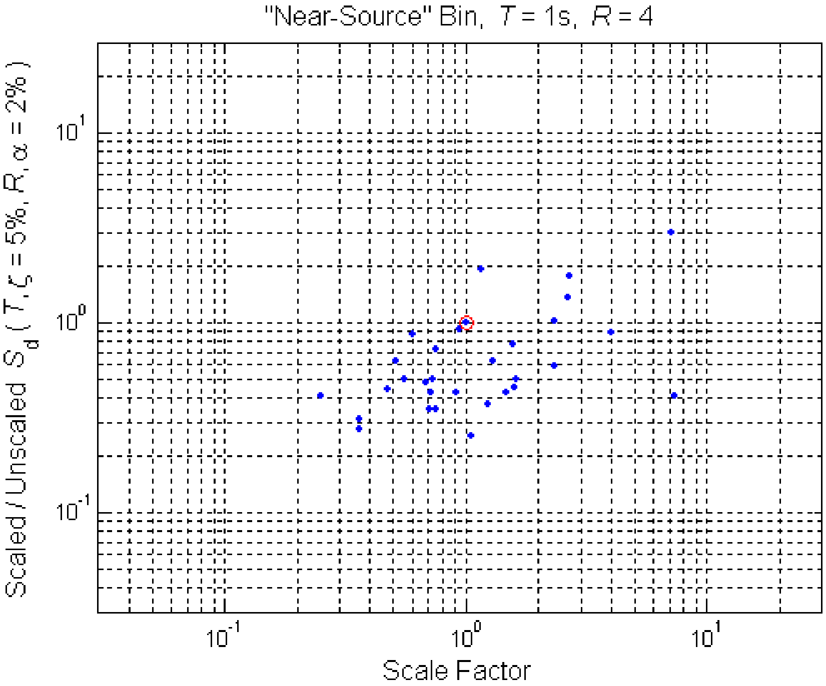

Figure 10. Ratios of the inelastic (R=4) spectral displacement responses to (i) the Near-Source records scaled to a target S_a (at T=1sec) of 0.5g versus (ii) the un-scaled Near-Source record that is naturally at the target S_a=0.5g (circled in red), all plotted against the corresponding scale factors.

Finally, for all 31 of the target S_a values in the Near-Source Bin (including the highest, next-to-lowest, and median values detailed above), the $r(S_d^I)$ versus scale factor results (analogous to those in Figure 6, Figure 8, and Figure 10) are shown in Figure 11. Recall that each of the 31 records in the bin is scaled to each of the 31 target S_a levels, for a total of 961 data points. Also shown in Figure 11 is a linear (in log-log space) regression fit based on all of the data points. By definition, the regression fit provides the average (expected value) of $\ln[r(S_d^I)]$ for a given value of the scale factor, and therefore the "bias" defined above in Section 3. The parameters of the regression fit, as listed in the figure, indicate that (i) there is no bias when the scale factor is equal to unity (i.e., a=1), as expected (but not pre-specified), and (ii) the bias is proportional (in log-log space) to the scale factor, with a slope of b=0.38. As examples, at a scale factor of 0.1 and 2 the scaled records result in S_d^I responses that are, on average, 0.4 and 1.3 times higher than un-scaled records, respectively.

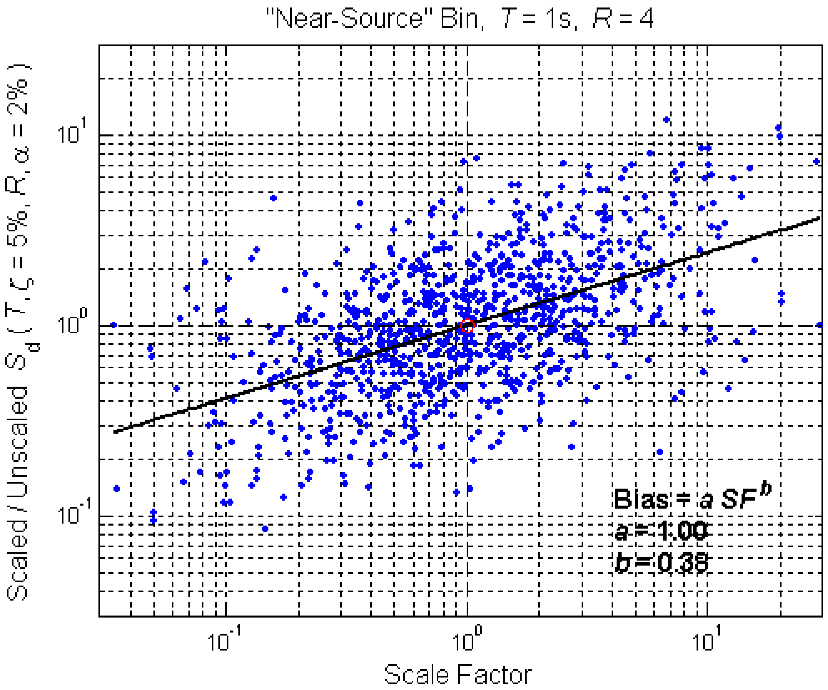

Figure 11. Intra-bin scaling results for the Near-Source earthquake record and the SDOF structure with *T*=1sec and *R*=4. Note that the blue data points include those shown in Figure 8 and Figure 10 above.

Explanation of Results:

The positive and negative biases observed for scale factors larger and less than one, respectively, can be explained by looking at the shapes of the elastic response spectra for records that are scaled up versus down. In Figure 12a, for example, the response spectra for three of the earthquake records in the Near-Source Bin are highlighted: the "target record" that is naturally (i.e., without scaling) at the target S_a level (in this case 0.5g), and two records that must be scaled by factors of 6.8 and 0.35 to reach the target S_a. As shown in Figure 12b, after scaling it is apparent that the record scaled by a factor of 6.8 has larger spectral ordinates at periods longer than *T*=1sec (the period of the oscillator under consideration) than does the target record. As the period of the oscillator, in effect, elongates due to inelasticity, it is therefore expected that the S_d^I response for the scaled record will be larger than that of the un-scaled target record. This is precisely what is observed, on average, in Figure 11 (i.e., positive bias for scale factors greater than one). Conversely, the record scaled by a factor of 0.35 has smaller spectral ordinates than the target record at periods to the right of *T*=1sec (again, see Figure 12b). It is expected, therefore, to result in smaller S_d^I response than the un-scaled target record, again consistent (on average) with Figure 11.

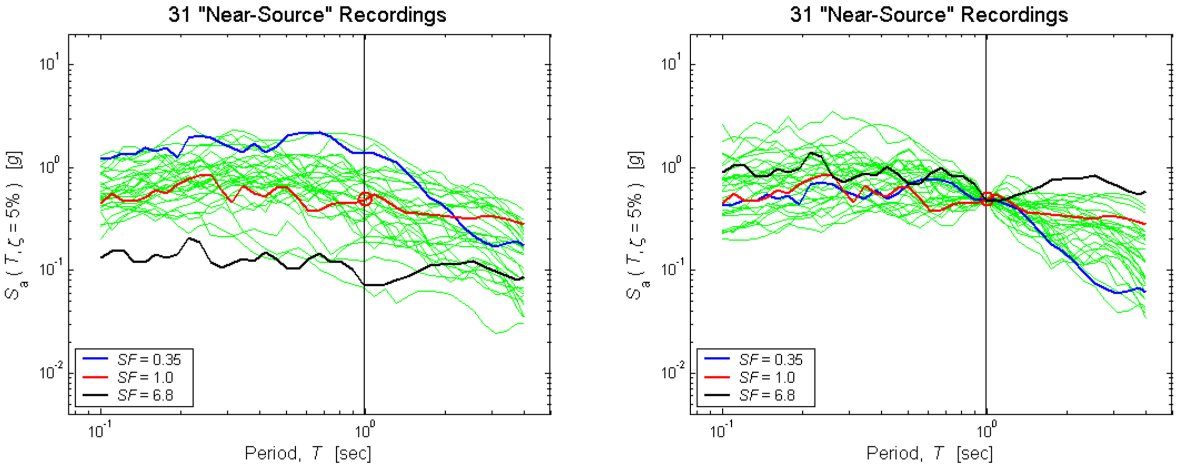

Figure 12. Elastic response spectra for three of the earthquake records in the Near-Source bin **(a)** before and **(b)** after scaling to a target spectral acceleration (0.5*g* in this case). Note how the spectral ordinates at periods longer than the elastic period of the structure (i.e., T=1sec) are larger for the record that is scaled up, and smaller for the one that is scaled down, relative to the un-scaled response spectrum.

Similar to Figure 12a, Figure 13a shows the median of the elastic response spectra associated with (i) the 10 earthquake records in the Near-Source Bin that have the largest S_a values (at T=1sec), (ii) the 10 that have the smallest, and (iii) the remaining 11 records that have S_a values in between. As noted in the figure, the median of the scale factors needed to reach the target S_a level (0.45*g* in this case) for each of these three subsets of records is (i) 0.5, (ii) 2.9, and (iii) 1.0. In a more average sense than Figure 12b, Figure 13b also suggests that the spectral shape for records that are scaled up vs. down to the target S_a will result in, respectively, larger vs. smaller S_d^I responses than records that are naturally at (or near) the target S_a.

Generally speaking, earthquake records that are scaled up to a target S_a are likely scaled up because they exhibit a "pit," or relatively low point in their elastic response spectrum, at the period under consideration. Conversely, records that are scaled down to the target S_a likely exhibit a "peak" in their response spectrum at the period of interest. As demonstrated in Figure 12 and Figure 13, a pit will generally result in biased high S_d^I response, and a peak in biased low S_d^I, both relative to un-scaled records.

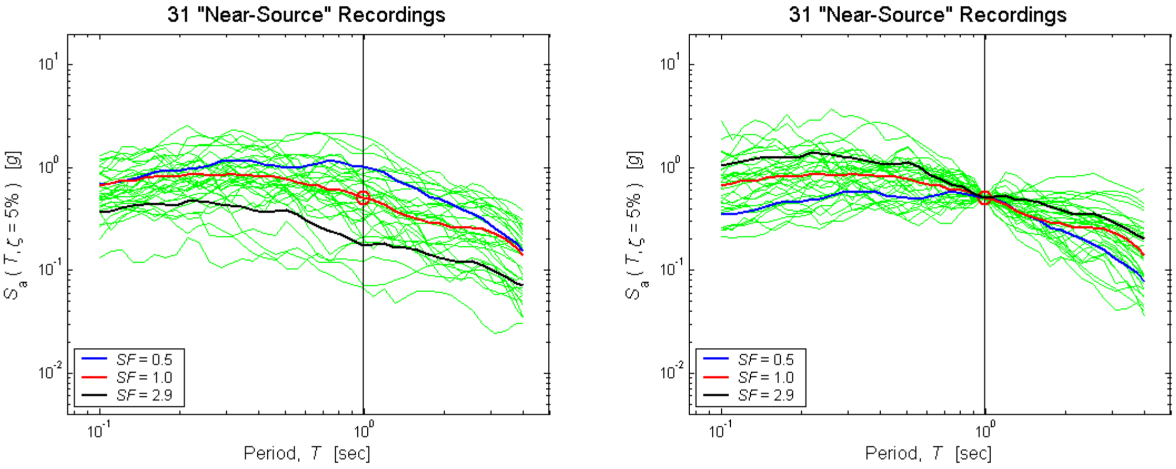

Figure 13. Medians of the elastic response spectra for the 10 largest, the 10 smallest, and the 11 Near-Source earthquake records in between (in terms of their spectral accelerations at T=1sec) **(a)** before and **(b)** after scaling to a target S_a (0.45g in this case). Note how the spectral ordinates at periods longer than the elastic period of the structure are larger for the records that are, on average, scaled up (by a median scale factor of 2.9), and smaller for the ones that are scaled down, both relative to the median response spectrum of the records that are, on average, un-scaled.

Aside:

In Figure 11 above, each data point represents the ratio of (i) the S_d^{I} response to a record scaled by the given factor, to (ii) the S_d^{I} response to an un-scaled record that is naturally at the target S_a level. Above, this type of data is used to quantify the bias (i.e., average of this ratio) induced by scaling a record by a *single* given factor. Alternatively, one may be interested in quantifying the bias induced by scaling a suite of records, all to a target S_a and hence each by a *different* factor, as a function of the median scale factor. (Again the bias is relative to records that are naturally at the target S_a level.) The same underlying data can be used to investigate this issue, but in a slightly different format, as illustrated in Figure 14 and Figure 15.

The data points shown in Figure 14 are the same ones shown above in Figure 10, namely the $r(S_d^{\mathrm{I}})$ ratios versus scale factors for the "loop" of the procedure in which the 31 records in the Near-Source Bin are scaled to its median S_a (conventional median, not geometric mean). Also depicted in the figure is the point defined by (i) the median (geometric mean) of the 31 scale factors, and (ii) the median of the 31 $r(S_d^{\mathrm{I}})$ values.

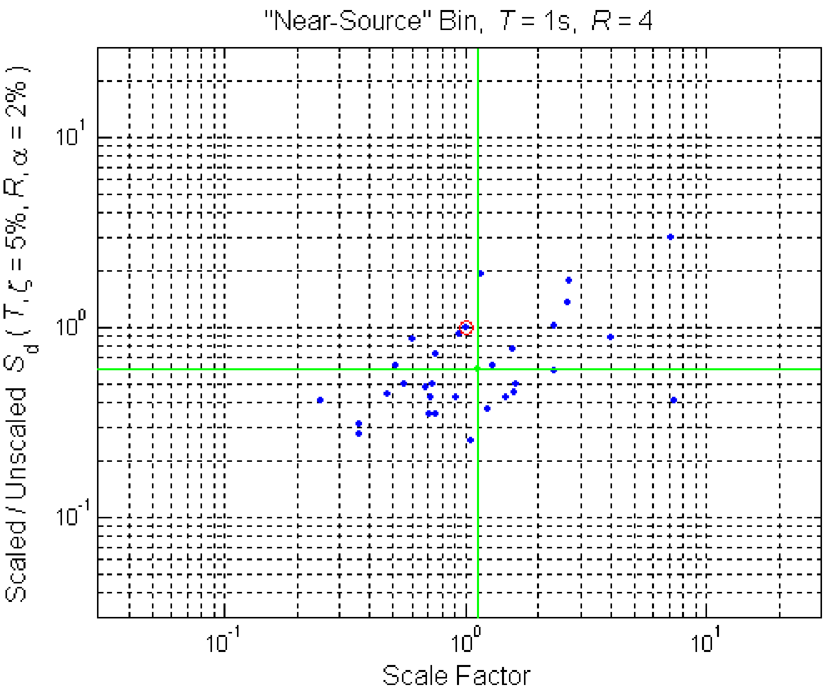

Figure 14. Medians (in green) of the scaled/un-scaled S_d^{I} ratios and the corresponding scale factors from Figure 10 above, which illustrated the results of scaling the Near-Source earthquake records to a target spectral acceleration of 0.5*g*.

Shown in Figure 15 are the median $r(S_d^{\mathrm{I}})$ versus median scale factor data points, like the one in Figure 14, obtained after scaling the records in the Near-Source Bin to all 31 of the target S_a levels considered. Also shown in the figure is a log-log linear regression fit to these 31 data points, with its parameters noted. This line gives the bias of the median S_d^{I} response for a suite of records that have been scaled, on average, by a given median scale factor. Note from the parameters that this line is precisely the same as that found in Figure 11 using all 31x31 of the underlying data points, as can be expected based upon the nature of (log-log) linear regression. Hence, in summary, the bias of a record scaled by a factor of *SF* is equivalent in value to bias of the median a suite of records scaled, on average, by a *median* factor of *SF*.

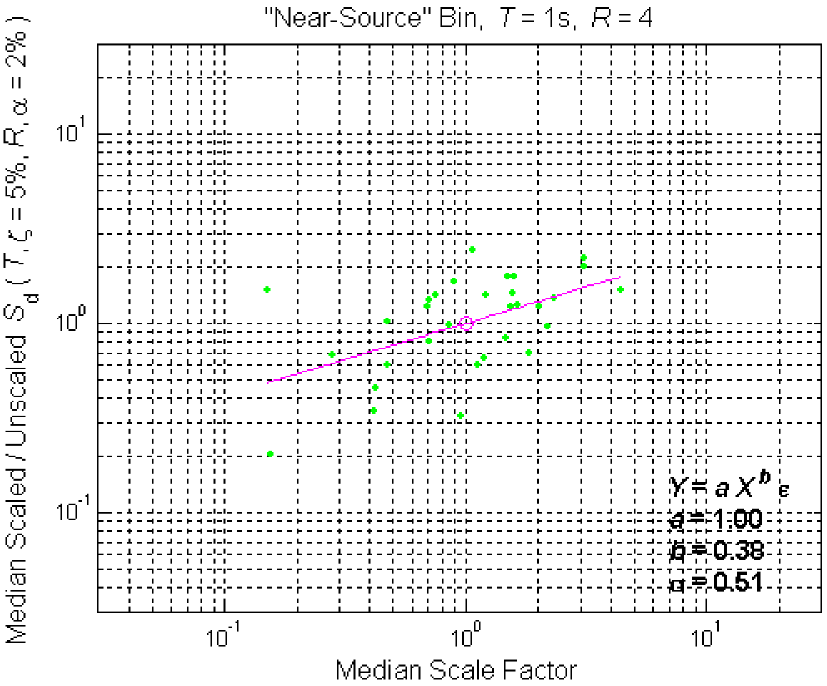

Figure 15. Bias (shown with magenta line) of the median inelastic spectral displacement (at T=1sec and R=4) from the suite of 31 Near-Source earthquake records scaled by the median factor on the abscissa. Note that this is equivalent to the bias for a single Near-Source record scaled by a given factor, which was presented above in Figure 11. One of the green data points shown in the figure is from Figure 14.

8.1.1.2 Bins I-VI, Moderate Period and Strength Structure

Besides the Near-Source Bin, recall that 6 other bins of earthquake records are considered in this study (as described in Section 5). Still for the same T=1sec and R=4 "moderate" oscillator considered in the preceding subsection, the bias versus scale factor regression fits (but not the underlying data) obtained via the same intra-bin scaling procedure demonstrated above are illustrated in Figure 16 for all 7 of the bins. Plots of the data upon which these regression fits are based, as well as the resulting regression parameters (*a* and *b*) are provided in the Appendix.

Note from Figure 16 that intra-bin scaling within the Near-Source Bin results in, for this SDOF structure, the largest bias in S_d^I response for a given scale factor; at the other end of the spectrum, Bin III (M_w=6.4-6.8, R_{close}=30-50km) results in the smallest bias. It is somewhat appropriate that these two bins bracket the results, because one might expect the Near-Source Bin and Bin III to be, respectively, the most aggressive and most benign of those considered in terms of S_d^I response. The trend over the other 5 bins of records, unfortunately, is not as clear, even in light of the median response spectra for all the bins (shown in Figure 2).

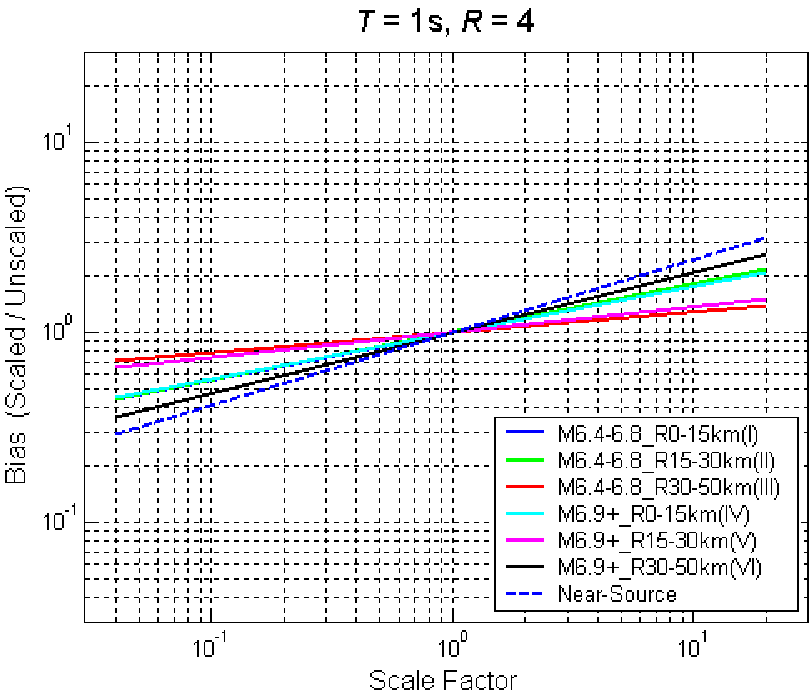

Figure 16. Bias in inelastic spectral displacement (for an SDOF structure with *T*=1sec, *R*=4) induced by intra-bin scaling within each of the seven different bins of the earthquake records. Note that the lines for Bins I, II, and IV are nearly coincident. The line for the Near-Source Bin is the same as the regression fit in Figure 11.

8.1.1.3 Near-Source Bin, All Structures

To this point, the results presented are for the *T*=1sec and *R*=4 oscillator only, but as described above in Section 6.1, SDOF structures of several other periods and strengths are considered in this study. In Figure 17, the log-log linear regression fits based on data like those in Figure 11 (above) are provided for oscillators with (a) a period of *T*=1sec but strengths ranging from *R*=1 to 10, and (b) a strength of *R*=4 but periods ranging from *T*=0.1 to 4seconds. Plots of the data upon which these regression fits are based, as well as the resulting regression parameters (*a* and *b*) are provided in the Appendix.

From Figure 17a it is apparent that the stronger the oscillator (i.e., the lower the *R*), the smaller the bias in S_d^I induced by a given scale factor, at least if *T*=1sec. In the limit (*R*=1), there is no bias induced for any scale factor because the oscillator is elastic and hence its response is simply equal to the target spectral displacement, which is proportional to the target S_a.

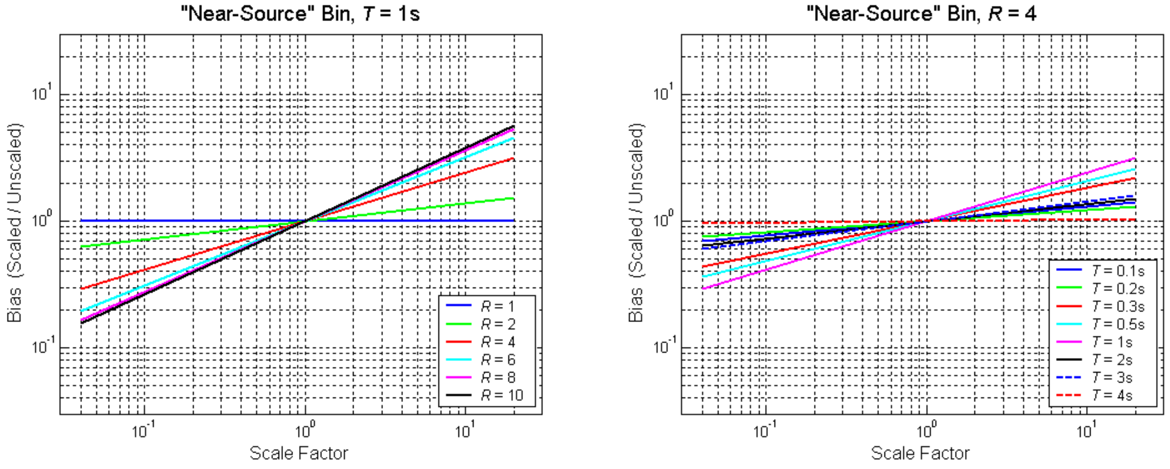

Figure 17. Bias in inelastic spectral displacement induced by intra-bin scaling withing the Near-Source Bin for SDOF structures with **(a)** a period of *T*=1sec but *R* ranging from 1 to 10, and **(b)** *T* ranging from 0.1 to 4sec but a strength reduction factor of *R*=4.

From Figure 17b we see that, at the *R*=4 strength level, the bias for the *T*=1sec oscillator considered in preceding subsections is the larger (for a given scale factor) than that for any of the other periods considered. This may be linked to the predominant period of the pulse-like records in the Near-Source Bin. At the other end of the spectrum, note that for the *T*=4sec oscillator there is nearly no bias in S_d^I induced at any scale factor. It can be reasoned that at *T*=4sec the "equal-displacements rule" applies (more so than at the other periods), such that the S_d^I response is roughly proportional to the target S_a, and hence the results are similar to those for an elastic (*R*=1) oscillator (i.e., no bias, as seen in Figure 17a).

To summarize the results for all 48 combinations of period (*T*) and strength (*R*) considered, the slope (in log-log scale) of each bias versus scale factor regression fit, denoted *b*, is plotted as a function of *T* and *R* in Figure 18. (The regression parameter *a*, which gives the bias for a scale factor of one, is not plotted because it is always equal to unity.) As already observed in Figure 17, the value of *b*, and thereby the bias at a given scale factor (since *a*=1), is relatively small for the stronger (approaching *R*=1) and longer period (approaching *T*=4sec) oscillators.

8.1.1.4 Summary

Depending, of course, on the vibration period (*T*) and strength (*R*) of the SDOF structure, the results presented above demonstrate that scaling earthquake records up can result in nonlinear structural responses (in this case inelastic spectral displacements) that are biased high, whereas the converse is true for scaling down (i.e., scale factor less than unity). The magnitude of the bias for a given scale factor is smaller for longer period structures and for stronger (closer to elastic) structures; it also depends on the characteristics (e.g., M_w and R_{close}) of the earthquake records that are scaled. More specific comments regarding the magnitude of the bias can be found in Section 9, the overall summary of results.

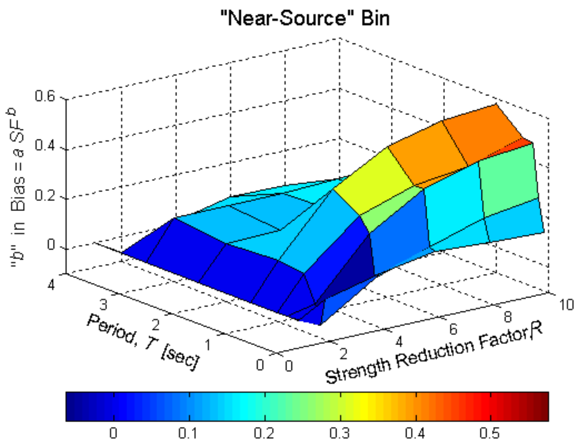

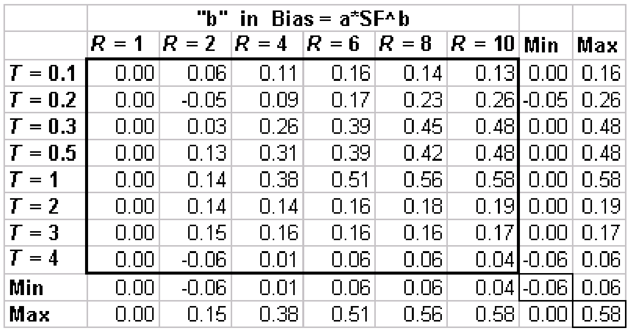

	"b" in Bias = a*SF^b							
	R = 1	*R* = 2	*R* = 4	*R* = 6	*R* = 8	*R* = 10	Min	Max
T = 0.1	0.00	0.06	0.11	0.16	0.14	0.13	0.00	0.16
T = 0.2	0.00	-0.05	0.09	0.17	0.23	0.26	-0.05	0.26
T = 0.3	0.00	0.03	0.26	0.39	0.45	0.48	0.00	0.48
T = 0.5	0.00	0.13	0.31	0.39	0.42	0.48	0.00	0.48
T = 1	0.00	0.14	0.38	0.51	0.56	0.58	0.00	0.58
T = 2	0.00	0.14	0.14	0.16	0.18	0.19	0.00	0.19
T = 3	0.00	0.15	0.16	0.16	0.16	0.17	0.00	0.17
T = 4	0.00	-0.06	0.01	0.06	0.06	0.04	-0.06	0.06
Min	0.00	-0.06	0.01	0.06	0.06	0.04	-0.06	0.06
Max	0.00	0.15	0.38	0.51	0.56	0.58	0.00	0.58

Figure 18. Slope with respect to scale factor (in log-log space) of the bias in inelastic spectral displacement induced by intra-bin scaling within the Near-Source Bin for SDOF structures of a range of periods and strength reduction factors. Note that larger values of the slope *b* translate into larger biases for a given scale factor (since *a*=1 for intra-bin scaling).

8.1.2 Inter-Bin Scaling

To reiterate, inter-bin scaling involves the scaling of an earthquake record from a "source" M_w-R_{close} bin to a S_a level associated with a different M_w-R_{close} "target" bin. The purpose of inter-bin scaling is to obtain a record for an empty (or sparsely populated) M_w-R_{close} target bin, although here the target bins considered must be adequately populated in order to maintain a basis of comparison. It is assumed that the results presented here can be extrapolated to inter-bin scaling cases for which the number of records in the target bin is minimal (e.g., M_w>7.6).

Detailed results for two different inter-bin scaling scenarios, namely (i) Bin III to Bin I and (ii) Bin I to the Near-Source Bin, are provided here, followed by a summary of results for 8 other inter-bin combinations. The detailed results are for the same moderate period (T=1sec) and strength (R=4) oscillator considered above in the detailed intra-bin scaling results (i.e., in Sections 8.1.1.1 and 8.1.1.2), but all of the periods and strengths considered are included in the summary of results.

8.1.2.1 Bin III to Bin I, Moderate Period and Strength Structure

Recall from Section 5 that the "target bin" for this inter-bin scenario, namely Bin I, includes earthquake records with M_w=6.4-6.8 and R_{close}=0-15km. The "source bin," Bin III, on the other hand, is also made up of records with M_w=6.4-6.8, but with R_{close}=30-50km. Bin I is used as the target bin (and Bin III as the source bin) here because, in general, earthquake records at shorter distances are in shorter supply and hence are more likely to be the target for inter-bin scaling.

Step 1:

As illustrated in Figure 19a, the first target S_a (at T=1sec) considered is 0.4g. This target S_a is associated with the 1979 Imperial Valley Brawley Airport (H-BCR140) record in Bin I (the target bin), whose elastic response spectrum is highlighted in the figure to distinguish it from the response spectra for the 73 records in Bin III (the source bin).

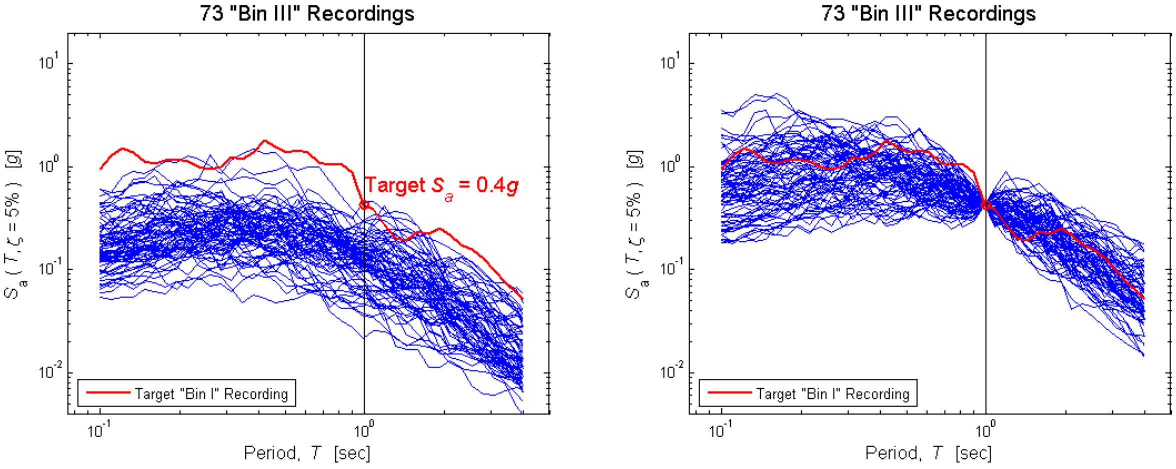

Figure 19. Elastic response spectra **(a)** before and **(b)** after scaling (inter-bin) the earthquake records in Bin III (M_w=6.4-6.8, R_{close}=30-50km) to a target spectral acceleration associated with Bin I (M_w=6.4-6.8, R_{close}=0-15km). The response spectrum in red is for the earthquake record in Bin I (the target bin) that is naturally at the target S_a=0.4g.

Step 2:

Recall that the S_d^I response to the un-scaled target record specified in Step 1 serves as a "true" S_d^I for this target S_a level; its value (9.2cm) is shown in Figure 20a, along with the S_d^I values for (i) the other un-scaled records in the target bin (Bin I), and (ii) the source bin (Bin III) records before they are scaled.

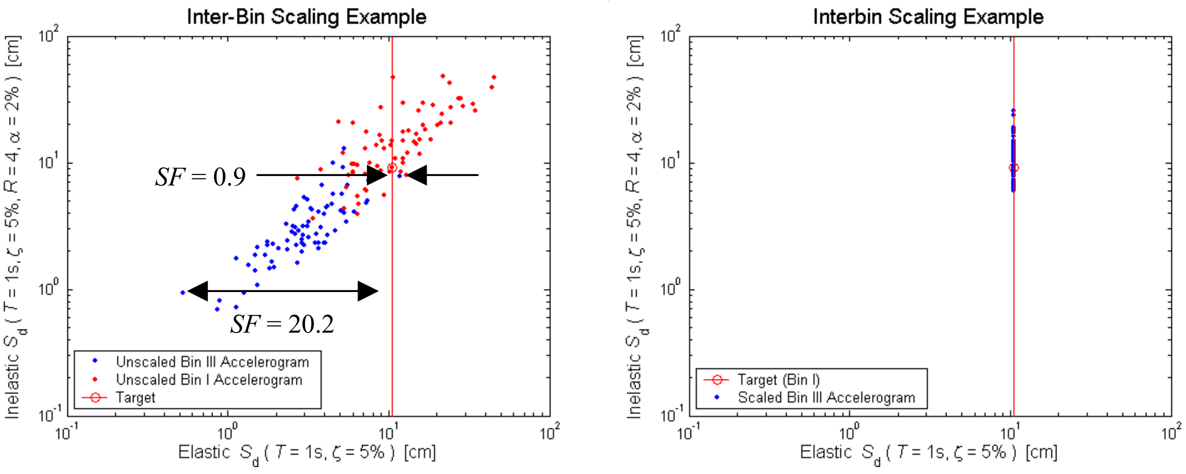

Figure 20. Inelastic spectral displacement responses **(a)** before and **(b)** after scaling (inter-bin) the earthquake records in Bin III to a target spectral acceleration associated with Bin I (namely S_a=0.4g or, equivalently, S_d=10cm). For comparison, the S_d^I responses to the un-scaled earthquake records in Bin I (the target bin) are also shown. The S_d^I response to the un-scaled target bin record (circled in red) serves as the "true" response for this iteration of the procedure.

Step 3:

The elastic response spectra after scaling all of the records in the source bin (Bin III) to the target S_a (0.4g) are shown in Figure 19b, still with the response spectrum for the target record highlighted. As depicted in Figure 20a, the scale factors in this case range from 0.9 to 20.2.

Step 4:

For all 73 of the source-bin records scaled in Step 3, the S_d^I values are shown in Figure 20b. Note that most of the S_d^I values are larger than the "true" S_d^I of the un-scaled target record.

Step 5:

The ratios of the S_d^I values for the scaled source-bin records (from Step 4) to that for the un-scaled target record (Step 2), which are denoted in the text as $r(S_d^I)$, are plotted against the corresponding scale factors in Figure 21. No trend with the scale factor is apparent, but the average ratio appears to be slightly greater than unity, suggesting that the inter-bin scaled records are biased high, albeit mildly. This, perhaps, can be expected given the shape of the response spectrum for the target record (shown in Figure 19), but recall (e.g., from the intra-bin scaling results that the record-to-record variability of S_d^I for un-scaled records with the same (or similar) values of S_a prevents us from drawing general conclusions before Steps 1-5 are repeated (in Step 6) for the other 72 target records and S_a levels in Bin I.

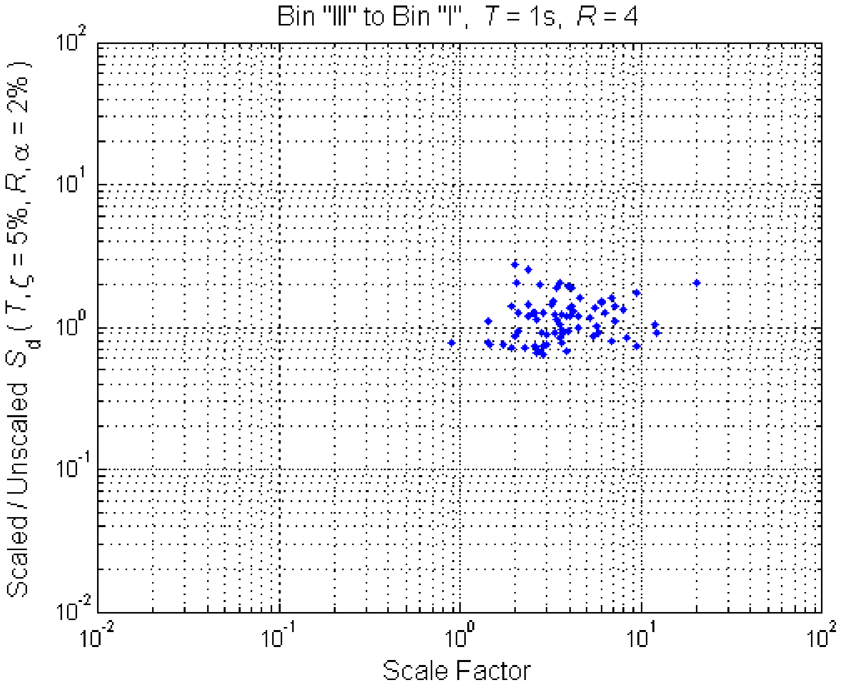

Figure 21. Ratios of the inelastic spectral displacement responses to (i) the Bin III (source bin) records scaled to the target S_a=2.0g versus (ii) the un-scaled Bin I (target bin) record that is naturally at S_a=2.0g, both from Figure 20b..

Step 6:

For all 73 of the target S_a values associated with the earthquake records in Bin I, the $r(S_d^I)$ versus scale factor results (including those shown in Figure 21 for the first target S_a) are plotted in Figure 22. Recall that each of the 73 records in the source bin (Bin III) is scaled to each of the 73 target S_a levels associated with the target bin (Bin I), for a total of 5329 data points. Also shown in Figure 22 is the log-log linear regression fit based on all of the data points, and its parameters, a and b. Recall that the regression fit, by definition, provides the average (expected value) of $\ln[r(S_d^I)]$ for a given value of the scale factor, and hence quantifies the "bias" induced by, in this case, inter-bin scaling. The parameters of the regression fit indicate that (i) when the scale factor is equal to unity, the S_d^I response to the scaled records is biased low (i.e., a=0.61), and (ii) the bias increases linearly (in log-log scale) with scale factor (i.e., b=0.19), as found for intra-bin scaling.

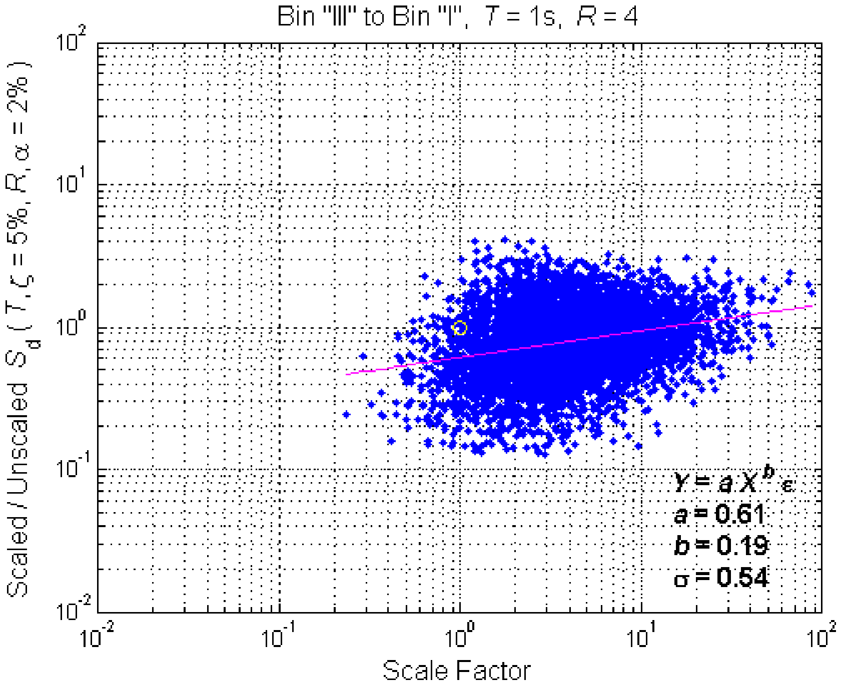

Figure 22. Inter-bin scaling results for the Bin III to Bin I case and the SDOF structure with T=1sec and R=4. The blue data points include those shown in Figure 21 above. The magenta line gives the bias in inelastic spectral displacement response induced by a given inter-bin scale factor.

Explanation of Results:

The same "peak versus pit" concept used to explain the intra-bin scaling results can be used to explain the $r(S_d^{\mathrm{I}})$ versus scale factor results observed in Figure 22 for inter-bin scaling. As evident from Figure 20a above, scale factors near unity are usually obtained when a source-bin record with a relatively large S_a value for it M_{w} and R_{close} (likely because there is a peak in its elastic response spectrum at the period under consideration) is scaled to the target S_a level associated with a target-bin record that is naturally at a relatively low S_a value for its M_{w} and R_{close} (likely because it is in a pit of its response spectrum). Since the "peaked" source-bin record is expected to produce relatively small S_d^{I} response, especially as compared to a "pitted" target-bin record, it is expected that the bias in S_d^{I} response at a scale factor of unity will be less than one (i.e., biased low S_d^{I}), as was observed in Figure 22.

Given the explanation above, one might expect to find that the S_d^{I} response to inter-bin scaled records is unbiased at a scale factor equal to the average separation (in terms of S_a) between the target and source bins. It is around this scale factor that one would expect to find $r(S_d^{\mathrm{I}})$ results for "peaked" source-bin records scaled to "peaked" target-bin records, for example. After scaling the source-bin (Bin III) records by the ratio of the median S_a for the target (Bin I) and source bins (before scaling), the S_a (actually, S_d=S_a*$(T/2\pi)^2$) and S_d^{I} values for the two bins are illustrated in

Figure 23. In this case, the ratio of the median S_a values, denoted here as r(m[S_a]), is equal to 3.8.

To check whether the S_d^I response to inter-bin scaled source-bin records is unbiased at a scale factor equal to r(m[S_a]), the scale factor axis in Figure 22 is divided by r(m[S_a])=3.8 and re-plotted in Figure 24. From the figure we see that there is still a bias at an "adjusted" scale factor of one, although it is smaller than before (i.e., a=0.79 versus 0.61 in Figure 22). As will be demonstrated in the subsequent section (for the second inter-bin scaling scenario), the remaining bias can be explained by considering the differences in the shapes of the elastic response spectra for the source and target bins.

Note that in all of the inter-bin scaling results to follow, the scale factors reported have already been divided by the ratio of the median S_a values for the target and source bins, r(m[S_a]). In other words, what is reported hereafter is the scale factor *after* the source-bin has been pre-scaled by the average S_a separation between the source and target bins, or r(m[S_a]). This factor for pre-scaling can be quantified using an attenuation relation, but here it is calculated based upon the specific records in each bin.

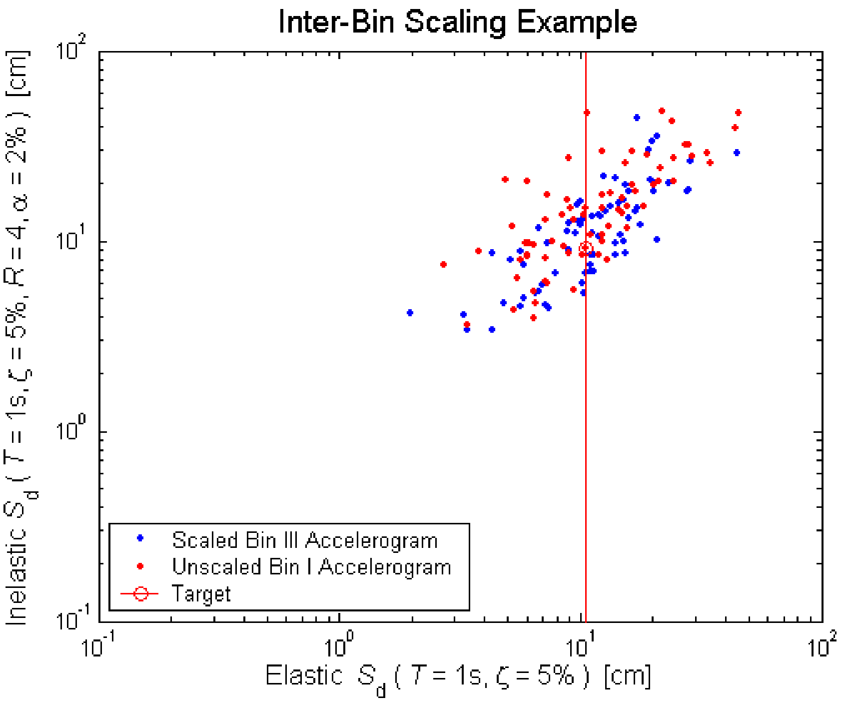

Figure 23. Illustration of "pre-scaling" the earthquake records in the source bin (Bin III) by a common factor such that their median spectral acceleration (or spectral displacement) matches that of the target bin (Bin I). This pre-scaling factor is removed (by division) from the scale factors in Figure 22 to obtain Figure 24.

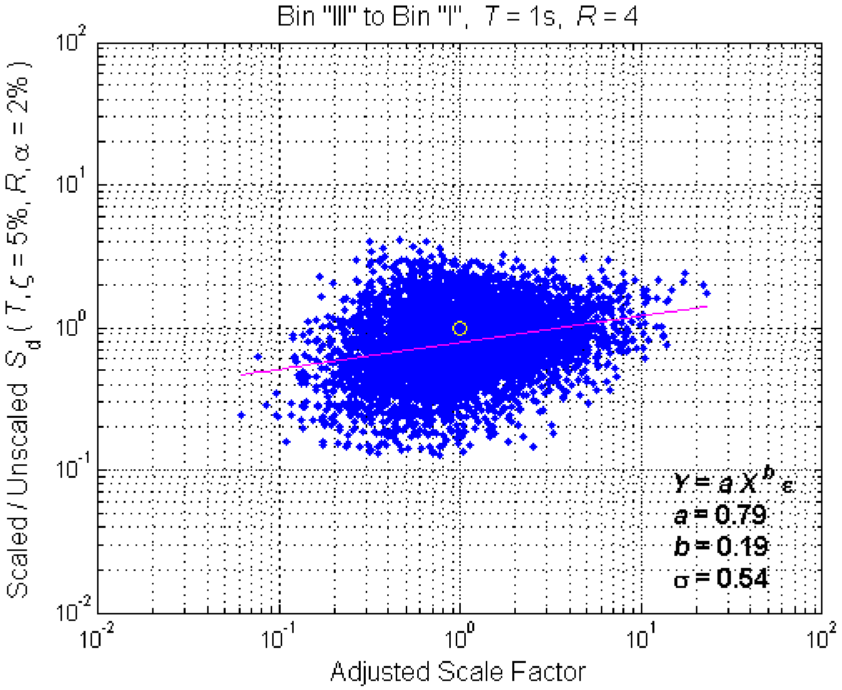

Figure 24. Inter-bin scaling results *after* removing the "pre-scaling" factor illustrated in Figure 23 from the un-adjusted results shown in Figure 22. The ratio of the median spectral accelerations for the target and source bins is *not* included in the adjusted scale factor.

8.1.2.2 Bin I to Near-Source Bin, Moderate Period and Strength Structure

The results detailed here consider the same target ground motion scenario ("Near-Source") and SDOF structure (T=1s, R=4) that was considered in Section 8.1.1.1 on intra-bin scaling. In order to consider inter-bin scaling, here earthquake records from a different "source" bin are scaled, namely those from "Bin I". Recall from the descriptions in Section 5 that Bin I is similar in M_w and R_{close} to the Near-Source bin, but Bin I includes records from backward as well as forward directivity conditions, and is comprised of random horizontal components rather than strictly strike-normal components. As a result, Bin I includes fewer pulse-like records as compared to the Near-Source bin.

The ratios of the S_d^I responses to scaled source-bin records versus un-scaled target bin records (i.e., $r(S_d^I)$ values) are plotted in Figure 25 as a function of the scale factor. Recall that each of the 73 records in Bin I, the source bin, is scaled to each of the 31 target S_a levels associated with the target Near-Source Bin, for a total of 2263 data points. The log-log linear regression fit to all of these data points and its parameters, a and b, are also shown in Figure 25.

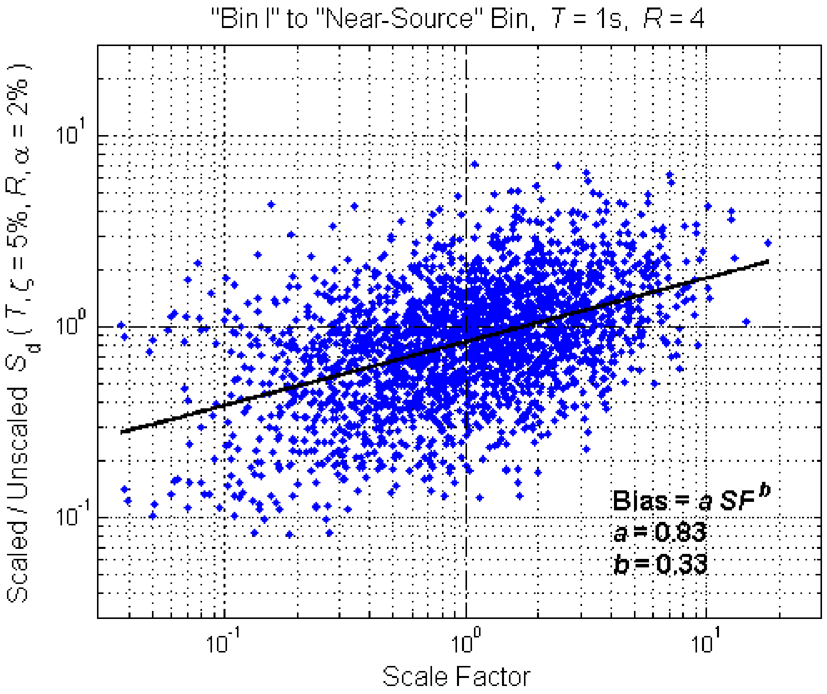

Figure 25. Inter-bin scaling results for the Bin I to Near-Source Bin case, still for the SDOF structure with T=1.0sec and R=4. The scale factor presented here (and hereafter) has already been divided by the pre-scaling factor that brings the median S_a of the source bin (Bin I) to that of the target bin (Near-Source).

Similar to the results for the Bin III to Bin I scenario considered in the preceding subsection, note from Figure 25 that there is a bias at a scale factor of unity (i.e., a=0.83). Recall that here the source-bin records have been pre-scaled, all by a single factor, such that the median of their S_a values is equal to that of the target bin. The median elastic response spectrum for (i) Bin I (the source bin), after the pre-scaling, and (ii) the Near-Source Bin (the target bin), is illustrated in Figure 26. Note that at periods longer than that of the structure under consideration here (i.e., T=1sec), the median response spectrum for Bin I drops off more quickly than that for the Near-Source Bin. As a result, it is expected that the S_d^I response to the Bin I records will, on average, be smaller than that to the records in the Near-Source Bin. This is precisely what was observed in Figure 25, which indicated that after the pre-scaling alone (i.e., at a scale factor of unity in the figure), the S_d^I response of the source-bin (Bin I) records is biased low relative to the target Near-Source Bin. If one looks back at the median response spectra (before any scaling) for Bin III and Bin I shown in Figure 4, the same explanation can also be made for the inter-bin scaling results reported in the preceding section.

Another observation to note from Figure 25 above is that the log-log slope of the bias versus scale factor, b=0.33, is rather similar to that observed from the intra-bin scaling results for the same target bin and structure, namely b=0.39 from Figure 11. This similarity will be commented on further in the subsequent subsection.

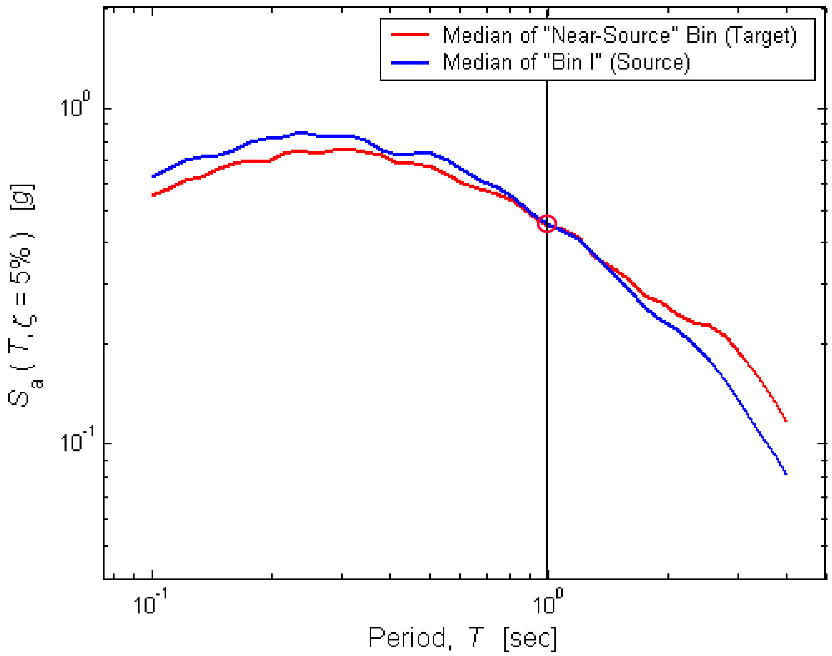

Figure 26. Median elastic response spectra for the earthquake records in Bin I (the source bin) and the Near-Source Bin (the target). Note that the median spectra happen to match at T=1.0sec (the period of the structure under consideration), so no "pre-scaling" is necessary. The higher spectral amplitudes at periods above 1.0sec suggest that the inelastic response to the near-source records will be larger than that to the records in Bin I.

8.1.2.3 Bin I to Near-Source Bin, All Structures

For all of the SDOF structures considered in this study, but still for the Bin I to Near-Source Bin inter-bin scaling scenario considered in the preceding subsection, a graphical summary of the regression parameters a and b is provided in Figure 27 (for a) and Figure 28 (for b). Recall that the parameter a quantifies the bias in S_d^I induced by merely pre-scaling the source-bin records by a single factor such that their median S_a (at the particular T) is equal to that of the records in the target bin (i.e., "adjusted" scale factor SF=1). The parameter b, on the other hand, quantifies how quickly the bias increases (or decreases) with increasing (or decreasing) scale factor (not including, or after, the pre-scaling).

Similar to what was observed for the b values in the intra-bin scaling results, the values of a for inter-bin scaling (shown in Figure 27) approach unity (no bias) for longer period and stronger structures (e.g., T=4sec and R=1). For shorter period and weaker structures, the bias quantified by a appears to increase. The smallest value of a (and most bias) observed is 0.68, for T=0.2sec and R=6.

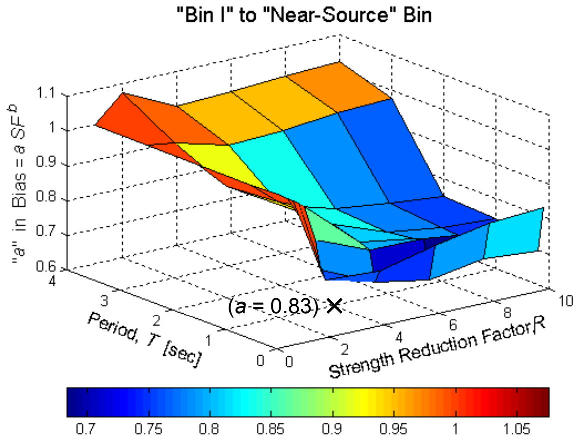

	"a" in Bias = a*SF^b							
	R = 1	R = 2	R = 4	R = 6	R = 8	R = 10	Min	Max
T = 0.1	1.00	0.76	0.75	0.79	0.82	0.83	0.75	1.00
T = 0.2	1.00	0.78	0.71	0.68	0.71	0.70	0.68	1.00
T = 0.3	1.00	0.86	0.80	0.80	0.78	0.76	0.76	1.00
T = 0.5	1.00	0.95	0.81	0.79	0.75	0.73	0.73	1.00
T = 1	1.00	0.93	0.83	0.78	0.75	0.74	0.74	1.00
T = 2	1.00	0.92	0.83	0.79	0.77	0.75	0.75	1.00
T = 3	1.00	0.99	0.95	0.95	0.97	0.98	0.95	1.00
T = 4	1.00	1.08	1.00	1.01	1.02	1.02	1.00	1.08
Min	1.00	0.76	0.71	0.68	0.71	0.70	0.68	1.00
Max	1.00	1.08	1.00	1.01	1.02	1.02	1.00	1.08

Figure 27. Bias at a scale factor of unity (after pre-scaling), given by *a*, for the Bin I to Near-Source Bin case and SDOF structures of a range of periods and strengths. For the most part, this bias can be explained by the differences between the median elastic response spectra of the source and target bins.

The values of *b* shown in Figure 28a are very similar to those observed in the intra-bin scaling results for the same target bin (the Near-Source Bin). The difference between the two sets of *b* values is plotted in Figure 28b, which shows that the two are nearly the same at all but very short periods.

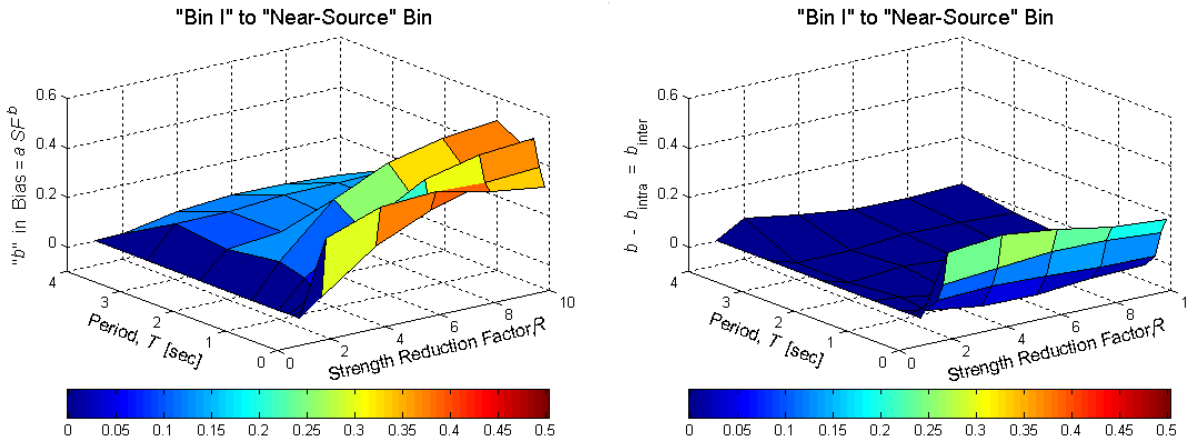

Figure 28. Slope with respect to scale factor (in log-log space) of the bias in inelastic spectral displacement induced by inter-bin scaling from Bin I to the Near-Source Bin for SDOF structures of a range of periods and strength reduction factors. The figure on the right shows that the difference in minimal between the slope *b* for this inter-bin scaling case and that for intra-bin scaling within the target (Near-Source) bin, except perhaps at short periods.

8.1.2.4 Other Inter-Bin Combinations, All Structures

Including the combinations described above (i.e., Bin III to Bin I, and Bin I to Near-Source Bin), a total of 10 different inter-bin scaling scenarios are considered, as listed in Table 2. Plots like Figure 27 of the regression fit parameter *a* for these scenarios are left to the appendix. The associated regression parameters, *b*, for the most part, are similar to those found for intra-bin scaling within the target bin; the latter results are also provided in the appendix.

Table 2. Inter-bin scaling scenarios considered in this study. Detailed results for these scenarios can be found in the appendix.

Scenario #	**Source Bin**	**Target Bin**
1	"I" (M_w=6.4-6.8, R_{close}=0-15km)	"Near-Source"
2	"Near-Source"	"I" (M_w=6.4-6.8, R_{close}=0-15km)
3	"I" (M_w=6.4-6.8, R_{close}=0-15km)	"IV" (M_w=6.9-7.6, R_{close}=0-15km)
4	"II" (M_w=6.4-6.8, R_{close}=15-30km)	"IV" (M_w=6.9-7.6, R_{close}=0-15km)
5	"V" (M_w=6.9-7.6, R_{close}=15-30km)	"IV" (M_w=6.9-7.6, R_{close}=0-15km)
6	"II" (M_w=6.4-6.8, R_{close}=15-30km)	"V" (M_w=6.9-7.6, R_{close}=15-30km)
7	"III" (M_w=6.4-6.8, R_{close}=30-50km)	"V" (M_w=6.9-7.6, R_{close}=15-30km)
8	"VI" (M_w=6.9-7.6, R_{close}=30-50km)	"V" (M_w=6.9-7.6, R_{close}=15-30km)
9	"III" (M_w=6.4-6.8, R_{close}=30-50km)	"VI" (M_w=6.9-7.6, R_{close}=30-50km)
10	"III" (M_w=6.4-6.8, R_{close}=30-50km)	"I" (M_w=6.4-6.8, R_{close}=0-15km)

Note that the majority of the scenarios, i.e., #3-9, considered use one of the three larger magnitude bins (IV-VI) as a target and scale records from bins with smaller magnitudes and similar or larger distances. These scenarios are motivated by the fact that the existing database contains fewer records from larger earthquake magnitudes and closer source-to-site distances. In practice, therefore, it is more likely that records from smaller M_w and larger R_{close} bins are scaled to represent larger M_w and smaller R_{close} bins, not vice-versa. (The primary goal of inter-bin scaling, recall, is extrapolation to larger M_w and shorter R_{close} bins.)

It is also assumed here that scaling from "adjacent" bins is more likely than scaling across bins that are more different in magnitude and/or distance (e.g., R_{close}=30-50km to R_{close}=0-15km). In any case, in this respect only two scenarios are left out: Bin III and VI to Bin IV. Recall that the inter-bin scenario detailed above Section 8.1.2.1 (i.e., #10), however, does consider scaling across two bins in distance (i.e., from Bin III to I), because it is intended to check the most extreme inter-bin scaling within the lower magnitude bins.

Finally, note that scenario #2 (Near-Source Bin to Bin I) is merely included to check that its results are equal and opposite those from the first scenario (which they are).

8.1.2.5 Summary

Inter-bin scaling appears to introduce a bias in inelastic spectral displacement that varies with scale factor in a manner similar to that induced by intra-bin scaling within the target bin. For a given scale factor, this bias is smaller for longer period and stronger (i.e., closer to elastic) oscillators. Unlike intra-bin scaling, however, an additional bias that is roughly independent of scale factor is also introduced. The degree of this bias can be related to the difference between the shapes of the median elastic response spectra for the source and target bins. More specific comments regarding the magnitude of the bias are left to the overall summary in Section 9.

8.2 MDOF Structures

The same procedure for quantifying the effects of intra- and inter-bin scaling that is applied for the SDOF structure in Section 8.1 (as outlined in Section 7) is followed here for the MDOF structures considered in this study, namely the elastic and the ductile 2-D models of a 9-story steel moment-resisting frame building.

Analogous the peak relative displacement response considered for the SDOF structures (i.e., inelastic spectral displacement, S_d^I), the following three drift response measures are considered for the MDOF structures:

θ_{roof} = the peak roof drift ratio (i.e., peak roof displacement relative to the ground, normalized by the height of the roof),

$\theta_{\max}$ = the maximum, over all stories, peak (over time) inter-story drift ratio, and

θ_{i} = the peak inter-story drift ratio for story i (= 1 to 9).

Like in Sections 8.1.1.1 and 8.1.2.2 for intra- and inter-bin scaling, respectively, the Near-Source Bin is used here as the target (for both intra- and inter-bin scaling), and Bin I is used as the source of earthquake records to scale (for inter-bin scaling). Due to the computational intensity of analyzing the MDOF structures, these are the only intra- and inter-bin scaling cases considered in this study. However, the analogy between the SDOF and MDOF results described below can, perhaps, be used to extrapolate the effects of scaling for the MDOF structures to other intra- and inter-bin cases.

One conceptual difference between the SDOF and MDOF results to note is that the strength of the ductile MDOF structure is *not* modified relative to each target S_a value (which, for the SDOF structure, created "constant R" results). Instead, here the strength of the ductile MDOF structure remains fixed, and hence "constant strength" results are produced. This is done because modifying the strength of an MDOF structure in a realistic fashion is not a straightforward and unique process like it is for SDOF structures. The implications of this difference are described in what follows.

8.2.1 Intra-Bin Scaling

As mentioned above, intra-bin scaling with the Near-Source Bin of earthquake records is considered here, for both the elastic and ductile models of the 9-story SMRF building.

8.2.1.1 Elastic Model

Analogous to Figure 11 above for an SDOF structure with vibration period T=1sec and strength reduction factor R=4, the intra-bin scaling results in terms of θ_{roof} and θ_{max} are shown in Figure 29 for the elastic model of the 9-story SMRF building. Since θ_{roof} is dominated by the first mode of response and hence is nearly proportional to first-mode spectral acceleration, it is expected, and observed (in Figure 29a), that intra-bin scaling does not induce a bias in elastic θ_{roof} response (i.e., a=1 and b=0). In contrast, a bias (albeit relatively minor) in θ_{max} is observed that is proportional in log-log space to the earthquake record scale factor (e.g., a bias of 9% and 32% for scale factors of 2 and 10, respectively). Recall that the bias increases with scale factor for the SDOF structures as well, but for differing reasons, since here the MDOF response is elastic. As one might expect (and as detailed below), the bias in the θ_{max} response is a result of the fact that more than just the first mode contributes significantly to it.

For the second, fifth, and eighth stories of the elastic building model, the intra-bin scaling results for θ_{i} (i.e., the ratio of the scaled versus un-scaled θ_{i} results as a function of the scale factor) are shown in Figure 30, alongside those for the ductile building model results to be discussed in the next subsection. The θ_{i} results for the other six stories, which follow the same trends observed here, are included in the appendix.

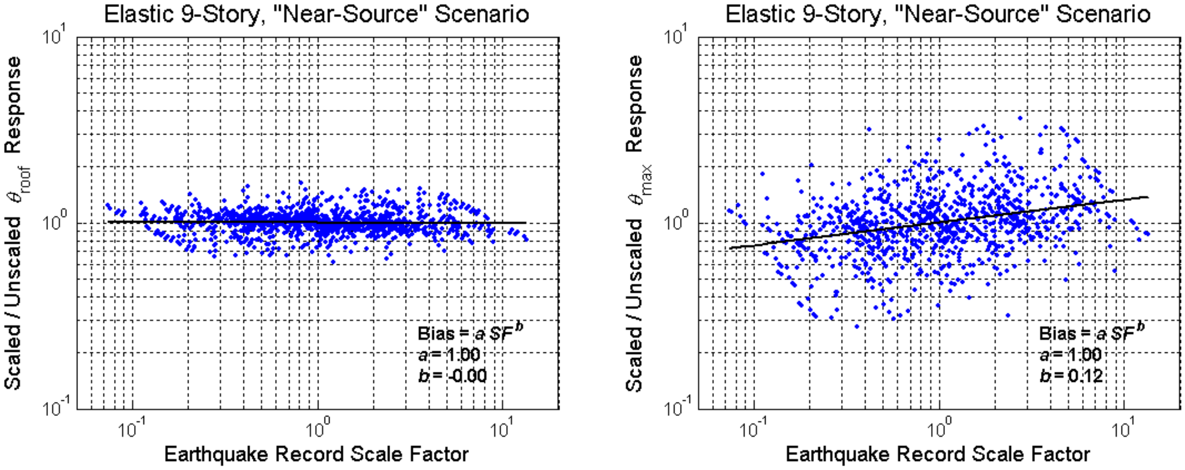

Figure 29. Intra-bin scaling results in terms of **(a)** peak roof drift ratio (θ_{roof}), and **(b)** maximum (over all stories) peak inter-story drift ratio (θ_{max}) for the elastic model of the 9-story building considered and the Near-Source Bin of earthquake records.

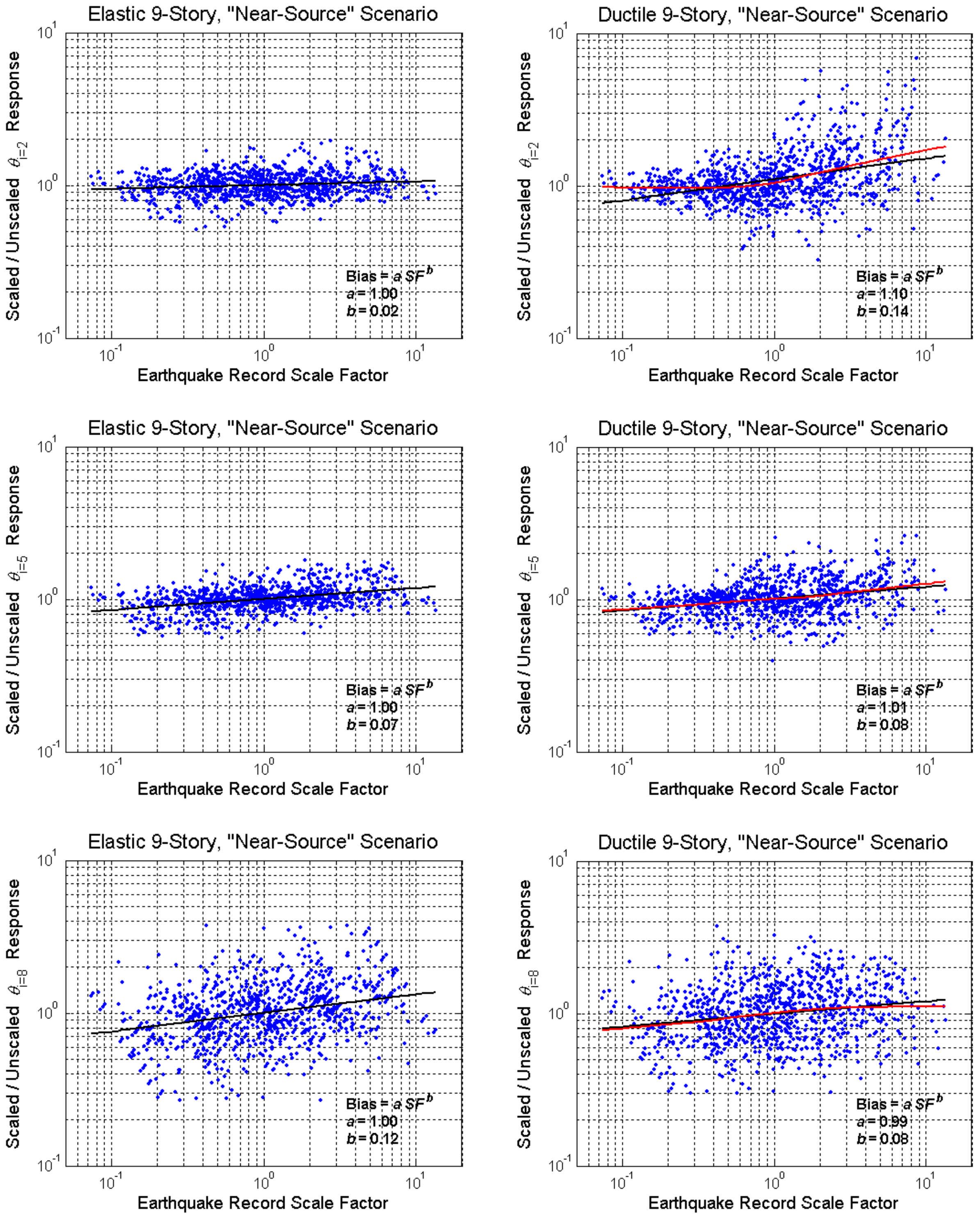

Figure 30. Intra-bin scaling results in terms of the peak inter-story drift ratios (θ_i) at the 2nd story (top row), 5th story (middle row), and 8th story (bottom row), for the elastic (left column) and ductile (right column) models of the 9-story building considered. The curve fit shown in red on the ductile results is obtained via a non-parametric local regression (LOESS). The analogous results for the other 6 of the 9 stories are provided in the appendix.

At the 2nd story, practically no scaling-induced bias in θ_2 is observed in Figure 30 (top left panel, a=1 and b=0.02) because, like for θ_{roof}, the contribution of higher modes to θ_2 is relatively minor. In contrast, higher modes contribute significantly to the response at the 8th story, θ_8, and a bias is observed (albeit relatively minor). Note that the extent of the bias in θ_8 is identical to that in $\theta_{\max}$ (i.e., b=0.12) because the maximum inter-story drift ratio typically occurs in the upper stories. The bias in θ_5 is intermediate to those at θ_2 and θ_8.

The scaling-induced bias observed for the $\theta_{\max}$ and θ_8 response (in Figure 29a and Figure 30) can be explained by looking at the shapes of the elastic response spectra for records that are scaled up versus down. The same approach was taken to explain the observed bias in inelastic spectral displacement for the SDOF structures, with one fundamental difference: instead of looking at the spectral amplitudes at periods longer than the fundamental period of the structure (to reflect inelasticity), here we look at shorter periods, specifically the second-mode period, since response spectrum analysis concepts apply.

In Figure 31a the median of the elastic response spectra associated with (i) the 10 earthquake records in the Near-Source Bin that have the largest S_a values (at T=2.3sec), (ii) the 10 that have the smallest, and (iii) the remaining 11 records that have S_a values in between. As noted in the figure, the median of the scale factors needed to reach the target S_a level (0.23g in this case) for each of these three subsets of records is (i) 0.5, (ii) 2.6, and (iii) 1.0. After scaling all of the earthquake records to the target S_a, the median response spectra for the same three subsets of records are plotted in Figure 31b. Note how, on average, the records that are scaled up have larger spectral amplitudes at the second-mode period (0.9sec), and those that are scaled down have smaller, relative to the un-scaled records. It is therefore expected, as observed, that the second mode contribution to $\theta_{\max}$ and θ_8 (and hence the overall response, since the first-mode component is normalized) will be biased high/low for scale factors larger/less than unity.

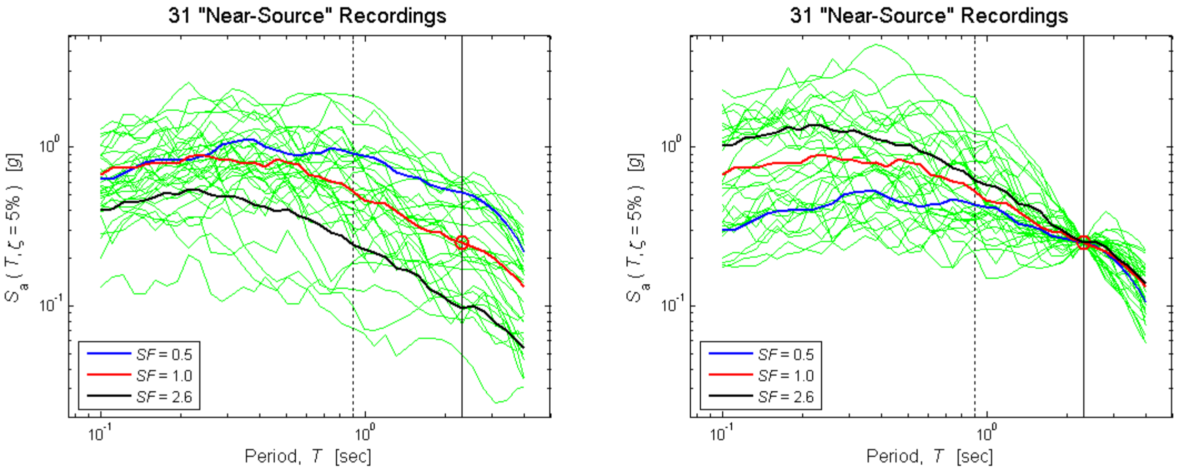

Figure 31. Medians of the elastic response spectra for the 10 largest, the 10 smallest, and the 11 Near-Source earthquake records in between (in terms of their spectral accelerations at T=2.3sec, the fundamental period of the 9-story building) **(a)** before and **(b)** after scaling to a target S_a (0.23g in this case). Note how the spectral ordinate at the second-mode period, T=0.9sec, is larger for the records that are, on average, scaled up (by a median scale factor of 2.6), and smaller for the ones that are scaled down, both relative to the median response spectrum of the records that are, on average, un-scaled.

8.2.1.2 Ductile Model

The analogous results presented in the preceding subsection for the elastic building model are presented here for the ductile model of the building. In Figure 32, the intra-bin scaling results in terms of θ_{roof} and θ_{max} are presented. For θ_{roof}, the data shown in the figure appear to be very similar to that for the elastic building model (shown in Figure 29), up to a scale factor near unity. At higher scale factors, there is a slight "upward swing" in the data, suggesting that the θ_{roof} response to the scaled records is biased high. The change near a scale factor of unity can be explained as a gradual shift from linear elastic to nonlinear inelastic results. It happens to be the case that the overall strength of the ductile building model, in terms of the spectral acceleration that induces notable nonlinearity, is roughly near the median S_a (at T=2.3sec) of the target Near-Source Bin, namely 0.23g. So, when the target S_a is near 0.23g, and the hence the median scale factor is near unity (not including, recall, the "pre-scaling" factor), the θ_{roof} (or θ_{max}, θ_{i}) response is in the transition between elastic and nonlinear behavior. At lower scale factors the response is essentially elastic, whereas at higher scale factors it is progressively more nonlinear.

As is clear in Figure 32, the "upward swing" in the data described above cannot be captured by a log-log linear regression fit. Hence, a non-parametric LOESS (Cleveland 1979) local regression fit is also plotted in the figure, using a "windowing fraction" of 0.75. The LOESS fit indicates that the scaled records provide an unbiased θ_{roof} response at scale factors lower than unity (roughly), as was observed for the elastic building model in the preceding section. At higher scale factors, however, the θ_{roof} response to the scaled records is somewhat biased high (e.g., by 30% at a scale factor). This bias can be explained via (again) the illustration in Figure 31 (above) of the median response spectra for records that are scaled up versus down. Although difficult to discern, there the median response spectrum of the records scale by a median factor of *SF*=2.6 is shown to be higher at periods longer than the fundamental period of the MDOF structures (*T*=2.3sec), as compared to the median spectrum of the un-scaled records (*SF*=1). Hence, as the fundamental period effectively elongates due to nonlinearity, it is expected (as observed) that the θ_{roof} response to the records that are scaled up will be biased high.

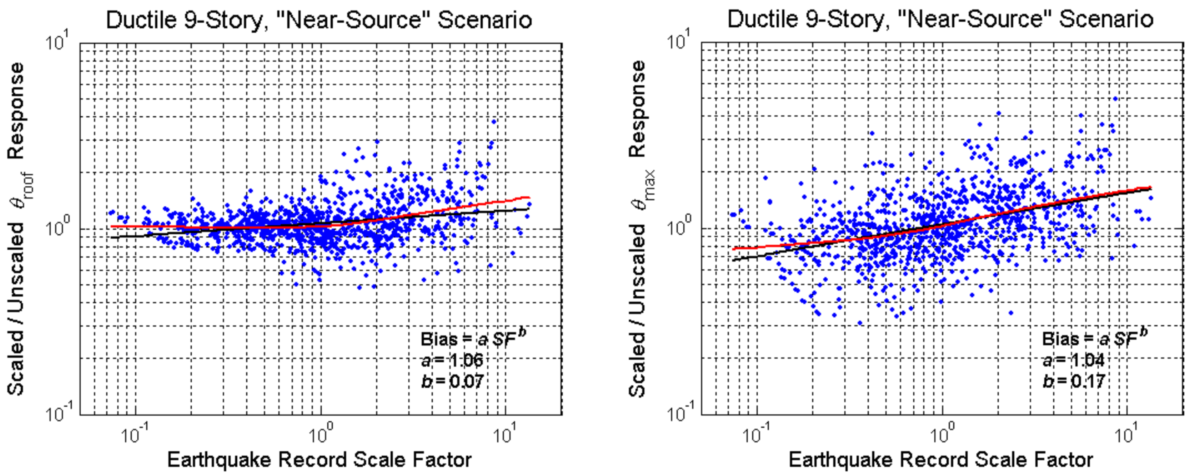

Figure 32. Intra-bin scaling results in terms of **(a)** peak roof drift ratio (θ_{roof}), and **(b)** maximum (over all stories) peak inter-story drift ratio (θ_{max}) for the *ductile* model of the 9-story building considered and the Near-Source Bin of earthquake records. The curve fits shown in red are obtained via a non-parametric local regression (LOESS).

Unlike the θ_{roof} results, the θ_{max} results shown in Figure 32b are very much similar to those for the elastic building model, even at large scale factors (and hence, most likely, large target S_a values) for which the structural response in notably nonlinear. At the large scale factors is not readily apparent whether the θ_{max} response to the scaled records is biased high because of (i) the same higher mode contributions to θ_{max} the resulted in a bias for the elastic building model (in Figure 29b), or (ii) the same effect of nonlinearity observed for the θ_{roof} response (in Figure 32a). As a final remark on the θ_{max} results, it is noted that the linear and LOESS fits (in log-log space) are almost identical, except at the very low end of the data (i.e., lowest scale factors).

For the 2nd, 5th, and 8th stories, the θ_{i} results for the ductile building model are presented alongside the corresponding results for the elastic building model in Figure 30 (above). Comments similar to those made for the elastic results, as well as those for the θ_{roof} and θ_{max} response of the ductile model, apply.

8.2.1.3 Summary

Intra-bin scaling of the elastic MDOF building model introduces a bias in the drift response measures that are sensitive to multiple modes (e.g., $\theta_{\max}$), but not those that are first-mode-dominated (e.g., θ_{roof}). For both of these response measures, intra-bin scaling introduces a bias for the ductile building model, except for the responses that are first-mode-dominated and essentially elastic due to the small target S_a level (typically corresponding to small scale factors).

At lower (than unity) scale factors, the response of even the ductile building model considered is more-or-less elastic, and hence no bias is observed in drift responses that are dominated by the first mode of vibration (e.g., θ_{roof}), whereas the response of multi-mode-sensitive drift responses (e.g., $\theta_{\max}$) is biased low. The latter can be explained by the shape of the response spectra for records with relatively low scale factors.

At higher scale factors, the multi-mode-sensitive (but not the first-mode-dominated) drift responses of the elastic building model are biased high, consistent with the response spectral shape for records with relatively large scale factors. For the ductile building model, on the other hand, both the first-mode-dominated and multi-mode-sensitive responses are biased high are larger scale factors, to varying degrees. Again, both can be explained by the shape of the response spectra for records with relatively high scale factors, at periods either smaller (for higher modes) or larger (for the effects of nonlinearity).

For more specific comments regarding the extent of the biases observed for the MDOF structures and intra-bin scaling, as well as a comparison with the SDOF results presented above, the reader is referred to the overall summary in Section 9.

8.2.2 Inter-Bin Scaling

The inter-bin scaling results presented here are for the same "target bin" considered in the preceding intra-bin scaling section, namely the Near-Source Bin, but a different "source bin," i.e., Bin I.

8.2.2.1 Elastic Model

For the elastic model of the 9-story SMRF building considered, the inter-bin scaling results in terms of θ_{roof} and $\theta_{\max}$ are plotted in Figure 33. As expected, practically no bias in θ_{roof} is observed (a=1.03, b=0.02) because the first-mode-dominated θ_{roof} is effectively proportional to the target S_a values to which all the source bin records are scaled. For the multi-mode-sensitive $\theta_{\max}$ response, however, a bias proportional (in log-log space) to scale factor is observed (b=0.17), similar to the intra-bin scaling results (b=0.12). The pre-scaling of the source bin (Bin I) records such that their median S_a is equal to that of the target (Near-Source) bin does not appear to introduce a significant bias (i.e., a=1.03). Given the differences between the median response spectra for the pre-scaled Bin I and the Near-Source Bin records, shown in Figure 34, this lack of bias is somewhat unexpected. Perhaps other differences between the target and source bins not reflected in the response spectra (e.g. time-domain features of the records) compensate for the disparity in spectral shape.

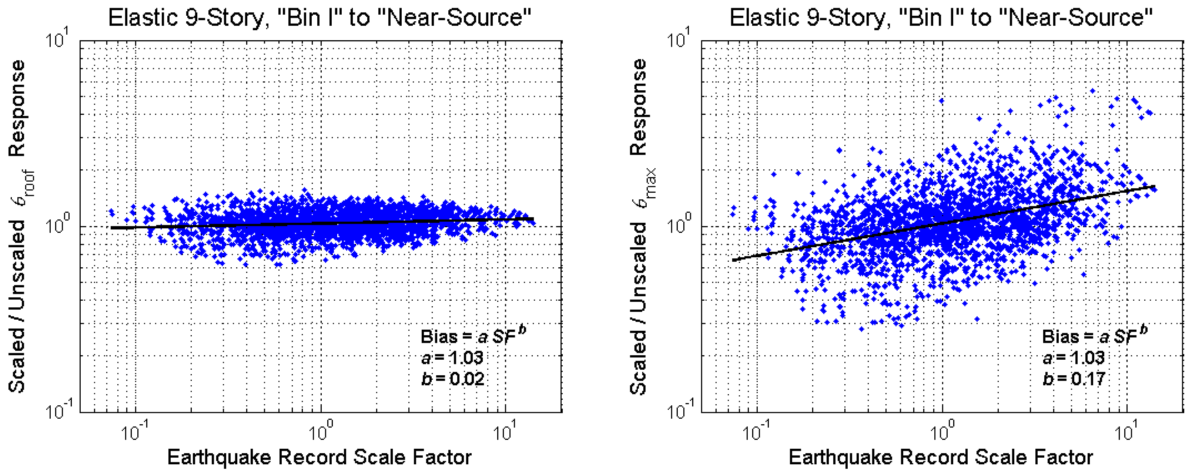

Figure 33. *Inter*-bin scaling results in terms of **(a)** peak roof drift ratio (θ_{roof}), and **(b)** maximum (over all stories) peak inter-story drift ratio (θ_{max}) for the elastic model of the 9-story building considered and the Bin I to Near-Source Bin scenario.

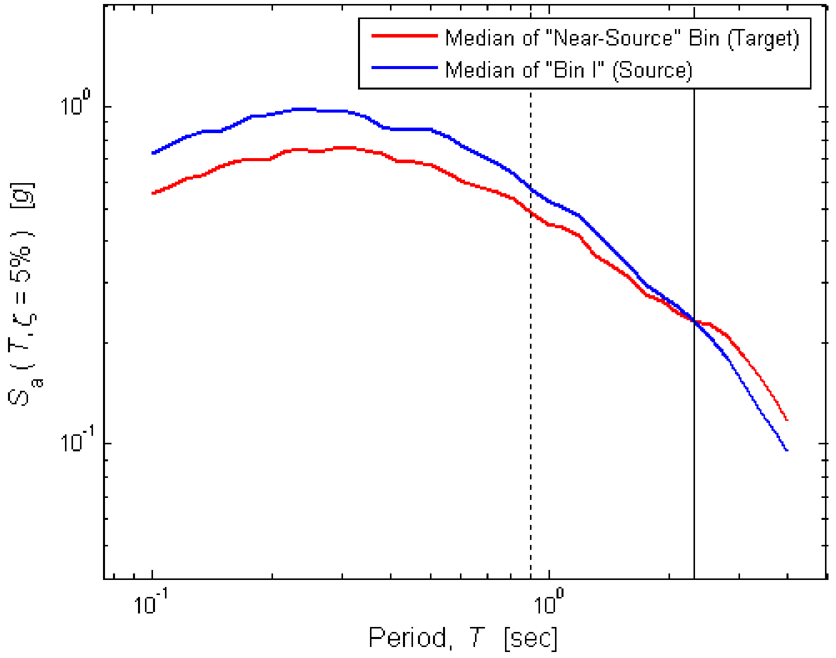

Figure 34. Median elastic response spectra for the Near-Source Bin and the earthquake records in Bin I scaled by a common factor such that their median S_a matches that of the Near-Source Bin at a period of T=2.3sec (the fundamental period of the 9-story building considered). Note that while the spectral ordinates at periods longer that 2.3sec are larger for the Near-Source Bin, the opposite is true at the second-mode period 0.9sec.

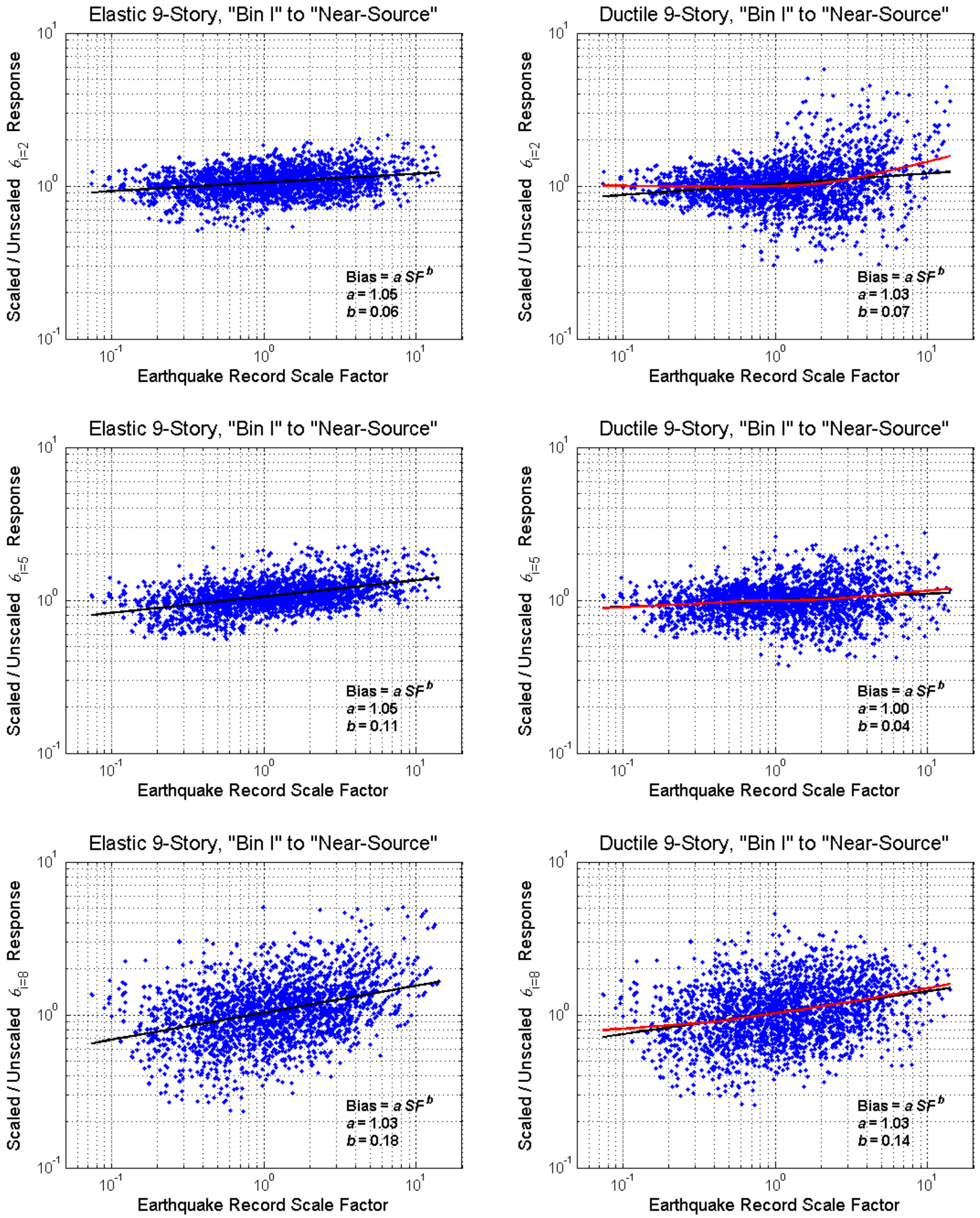

Figure 35. *Inter*-bin scaling results in terms of the peak inter-story drift ratios (θ_i) at the 2nd story (top row), 5th story (middle row), and 8th story (bottom row), for the elastic (left column) and ductile (right column) models of the 9-story building considered. The curve fit shown in red on the ductile results is obtained via a non-parametric local regression (LOESS). The analogous results for the other 6 of the 9 stories are provided in the appendix.

Like the intra-bin results shown in Figure 30, the inter-bin scaling results for the elastic building model are plotted in terms of θ_2, θ_5, and θ_8 in Figure 35, alongside the analogous results for the ductile building model. Comments similar to those already stated for the intra-bin results and the inter-bin results for θ_{roof} and θ_{max} apply to this figure as well.

8.2.2.2 Ductile Model

Lastly, for the ductile model of the 9-story SMRF building, the inter-bin scaling results for θ_{roof} and θ_{max} are plotted in Figure 36. For θ_{roof}, the log-log linear regression fit to the data suggests that practically no bias is introduced by scaling (a=1.02, b=0.03), which is confirmed by the LOEES fit at the smaller scale factors. At larger scale factors the LOEES fit (and the data itself) indicates that the scaled θ_{roof} response is biased high (e.g., by about 20% at a scale factor of 10), as was observed (and explained) for the intra-bin scaling results presented above.

For θ_{max}, the ductile results shown in Figure 36b are very similar to those for the elastic building model (shown in Figure 33b), and in turn the intra-bin scaling results for both the elastic and ductile building models. Also note that the differences between the linear and LOESS regression fits to the θ_{max} results are relatively minor, even at the extreme scale factors.

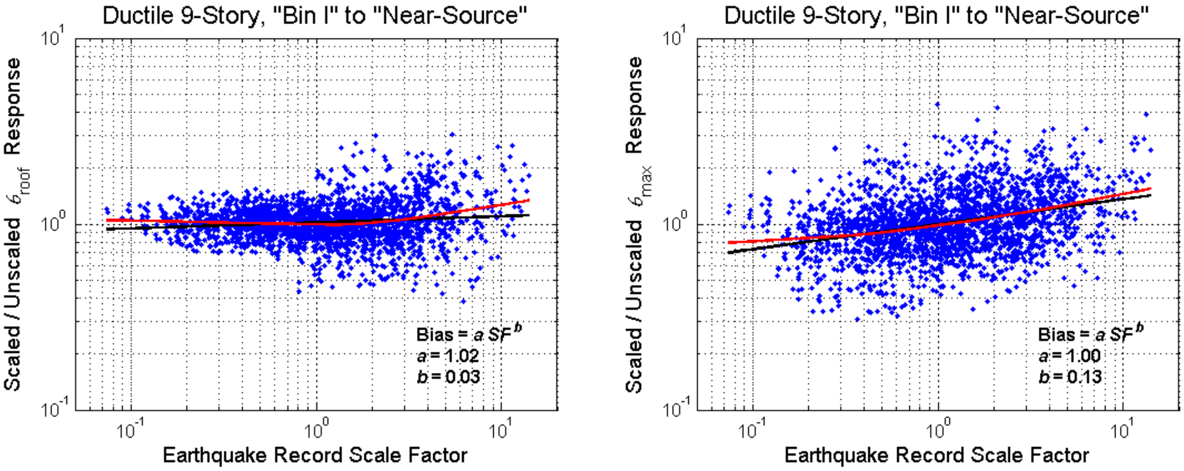

Figure 36. Inter-bin scaling results in terms of **(a)** peak roof drift ratio (θ_{roof}), and **(b)** maximum (over all stories) peak inter-story drift ratio (θ_{max}) for the *ductile* model of the 9-story building and the Bin I to Near-Source Bin scenario. The curve fits shown in red are obtained via a non-parametric local regression (LOESS).

8.2.2.3 Summary

Inter-bin scaling appears to have a very similar effect, in terms of the bias in linear or nonlinear MDOF response it introduces, to that of *intra*-bin scaling. In both cases there is (practically) no bias in θ_{roof}, θ_{max}, or θ_i at a scale factor of unity. For the inter-bin case, recall, this indicates that "pre-scaling" the source bin records such that their median S_a matches that of the target bin does not induce a bias, which is somewhat unexpected given the differences between the (median) response spectra for the source and target bins. For lower and higher scale factors, the bias introduced is as described for intra-bin scaling (in Section **Error! Reference source not found.**). The magnitude of these biases for inter-bin scaling and the MDOF structures, as well as those for the other cases considered, are summarized in the next section.

9 Summary

An overall summary of the detailed results presented above for both the SDOF and MDOF structures is provided here for intra- and inter-bin scaling separately. A comparison of the results for the two types of scaling is made in the inter-bin section (Section 9.2.1.1).

9.2.1.1 Intra-Bin Scaling

The intra-bin scaling results for the SDOF structures covering a range of periods and strengths, and considering the seven different bins of earthquake records, indicate the following:

- For elastic or mildly inelastic SDOF structures (i.e., $R \leq 2$), the bias in drift response (i.e., S_d^I) that is introduced by intra-bin scaling is at most 15% and 60% (i.e., factors of 1.15 and 1.60) for scale factors of 2 and 10 (or 1/1.15 and 1/1.60 for 1/2 and 1/10), respectively, with the exception of a few short-period cases ($T \leq 0.2$sec).
- For relatively long period SDOF structures (i.e., $T \geq 3$sec), the bias introduced is also less than 15% and 60% for scale factors of 2 and 10, respectively, except for Bin VI containing large M_w and long R_{close} records, in which case the bias is large as 27% and 119% (respectively).
- For relatively short periods (i.e., $T \leq 0.5$sec), the bias is *at least* 15% and 60%, and can be as large as 90% and 690%, for scale factors of 2 and 10, respectively. This is true even at the R=2 strength level (with only one exception), but with a few lower-bias exceptions (i) at the R=4 strength level and (ii) for the Near-Source Bin containing "pulse-like" records.
- At moderate periods (i.e., T=1 or 2sec), the magnitude of the bias is dependent on the characteristics (e.g., M_w, R_{close}) of the bin of records that are scaled. For T=1sec, the bias is less than 15% and 60% for scale factors of 2 and 10, respectively, for Bin III and IV, but for the other five bins the bias is larger, up to 50% and 280% (respectively). For T=2sec, the bias is less than 15%/60% for all but Bin II, IV, and VI, for which it is still less than 30%/150% (for scale factors of 2/10).

For the MDOF structure, even the elastic model exhibits a scaling-induced bias, but only for those drift responses that are sensitive to higher modes of vibration (e.g., θ_9, θ_{max}). At most, this bias is about 15% and 60% at scale factors of 2 and 10, respectively (i.e., $b<0.20$). The ductile building model exhibits a comparable bias for the multi-mode-sensitive responses, but also displays a bias for first-mode-dominated responses (e.g., θ_1, θ_{roof}). The latter is as large as 25% and 80% for scale factors of 2 and 10, respectively, but at scale factors less than about unity there is nearly no bias because the response is essentially elastic (and first-mode-dominated).

9.2.1.2 Inter-Bin Scaling

The inter-bin scaling results, recall, are very similar to those for intra-bin scaling in terms of the variation of bias with scale factor (described above), except perhaps at very short periods (e.g., $T \leq 0.5$sec). Inter-bin scaling, however, can also introduce a bias in nonlinear structural response at an "adjusted" scale factor of one, i.e., merely by pre-scaling the earthquake records in the source bin by a common factor such that their median spectral acceleration (S_a) is equal to the median S_a of the target bin. The magnitude of this additional bias for the SDOF structures and 10 different inter-bin scaling cases considered shows the following trends:

- For elastic or mildly inelastic SDOF structures (i.e., $R \leq 2$), the bias in drift response (i.e., S_d^{I}) that is introduced by inter-bin "pre-scaling" is less than 15% (i.e., between a factor of 1/1.15=0.87 and 1.15), except at short periods ($T \leq 0.3$sec) in some cases.
- Roughly speaking, the bias tends to increase with decreasing strength (i.e., increasing R), and can be as large as 80%.
- For Bin I to IV (from smaller to larger M_{w}, for shorter R_{close}), Bin V to VI (from intermediate to shorter R_{close}, for larger M_{w}), and Bin VI to V (from longer to shorter R_{close}, for larger M_{w}), however, the bias is less than 15% for all but a few of the period-strength combinations (always with $T \leq 1$), in which case the bias is still less than 40%.
- For the most part, the largest biases are observed for shorter period ($T \leq 0.2$) structures, except in the Bin III to V case (largest biases at $T \geq 3$sec), the Bin VI to V case (largest biases at T=1sec), and Bin III to I case (largest biases at T=0.5 or 1sec).
- Bin V to IV case (for which the bias is less than 18% across all T-R combination), the

Note that for most (but not all) of the inter-bin cases described above, the S_d^{I} response to the pre-scaled records is biased low because the earthquake records in the source bin are generally more "benign," in terms of the S_d^{I} response that they induce for a given S_a level, than those in the target bin. In practice, it is typically the more "aggressive" target bin (often of larger M_{w} and shorter R_{close}) that is of interest, for which fewer (if any) existing records are available.

Unlike for the SDOF structures, the inter-bin pre-scaling induces practically no bias in the drift response of the MDOF structures. Hence, the inter-bin scaling results for the MDOF structures are very similar to those for intra-bin scaling.

10 Conclusions

For a range of SDOF structures of different periods and strengths, as well as two MDOF structures of different strengths (one elastic), we have quantified the bias in nonlinear structural response induced by scaling input earthquake records to a target spectral acceleration level. The bias is measured with respect to the response to un-scaled records that are naturally at the spectral acceleration of interest. In the case of intra-bin scaling, these un-scaled records have, by definition, the same general characteristics (in terms of M_{w}, R_{close}, etc.) as the records that are scaled. In inter-bin scaling, on the other hand, the un-scaled records lie in a "target bin" with different characteristics than the "source bin" of earthquake records to scale. Of course, in practice this target bin is devoid of records, but we assume that the inter-bin scaling results presented here can be extrapolated to such cases. The nonlinear structural response measures considered are inelastic spectral displacement for the SDOF structures, and inter-story and roof drift for the MDOF structures.

The results of this study demonstrate that scaling earthquake records can introduce a bias in nonlinear structural response that increases with the degree of scaling. As detailed in the preceding section, the magnitude of this bias depends on (i) the fundamental period of vibration of the structure, (ii) the overall strength of the structure, and (iii) the sensitivity of the nonlinear structural response to higher (than the first) modes of vibration. The bias is also observed to depend on the characteristics (e.g., M_w, R_{close}) of the earthquake records that are scaled. In the case of inter-bin scaling, however, the characteristics of these "source records" mainly effects the bias (if any) introduced by first "pre-scaling" them such that their median spectral acceleration matches that of the target bin (e.g., as obtained from an attenuation relation). Any additional bias induced by scaling to a target spectral acceleration level is observed to depend primarily on the characteristics of the target bin.

The biases quantified in this study can be used to place limits on the amount scaling that is acceptable for comparable structures, once one has decided on a tolerable amount of bias. Alternatively, one could, in an approximate fashion, "correct" for a scaling-induced bias by using results like those presented in this paper.

11 Future Work

In this study the bias in nonlinear structural response induced by scaling is quantified as a function of the scale factor only, irrespective of whether it comes from scaling an earthquake record with a relatively small spectral acceleration (S_a) up to a moderate S_a level, for example, or a moderate S_a record to a high S_a level. Whether it is necessary to distinguish between these two cases (as examples) deserves future consideration.

Given that scaling to a spectral acceleration level can, in fact, introduce a bias in nonlinear structural response, other approaches to scaling are worthy of investigation. If, for example, some measure of the shape of the elastic response spectrum at the target spectral acceleration level is considered, can the scaling-induced bias be reduced? Can the effects of scaling be avoided altogether by instead interpolating (or extrapolating) the nonlinear structural responses to un-scaled earthquake records?

12 Acknowledgements

The PEER Lifelines Program funded the work presented in this paper (under an addendum to Task 1G00). The content benefited from discussions with the following individuals: Brian Chiou and Cliff Roblee of Caltrans, Maury Power of Geomatrix, Allin Cornell , Jack backer, Gee-Liek Yeo, and Polsak Tothong of Stanford University.

Appendix

Tables A1-2. Lists of the 73 earthquake records in "Bin I" (M_w=6.4-6.8, R_{close}=0-15km), on the left, and "Bin II" (M_w=6.4-6.8, R_{close}=15-30km), on the right.

	EARTHQUAKE NAME	YEAR	M	R	RECORD NAME
1	Imperial Valley	1979	6.5	8.5	H-AEP045.AT2.txt
2	Imperial Valley	1979	6.5	8.5	H-AEP315.AT2.txt
3	Imperial Valley	1979	6.5	2.5	H-BCR140.AT2.txt
4	Imperial Valley	1979	6.5	2.5	H-BCR230.AT2.txt
5	Imperial Valley	1979	6.5	8.5	H-BRA225.AT2.txt
6	Imperial Valley	1979	6.5	8.5	H-BRA315.AT2.txt
7	Imperial Valley	1979	6.5	10.6	H-CXO315.AT2.txt
8	Imperial Valley	1979	6.5	10.6	H-CXO315.AT2.txt
9	Imperial Valley	1979	6.5	10.4	H-E02140.AT2.txt
10	Imperial Valley	1979	6.5	4.2	H-E04140.AT2.txt
11	Imperial Valley	1979	6.5	4.2	H-E04230.AT2.txt
12	Imperial Valley	1979	6.5	1.0	H-E05140.AT2.txt
13	Imperial Valley	1979	6.5	1.0	H-E05230.AT2.txt
14	Imperial Valley	1979	6.5	1.0	H-E06140.AT2.txt
15	Imperial Valley	1979	6.5	1.0	H-E06230.AT2.txt
16	Imperial Valley	1979	6.5	0.6	H-E07140.AT2.txt
17	Imperial Valley	1979	6.5	0.6	H-E07230.AT2.txt
18	Imperial Valley	1979	6.5	3.8	H-E08140.AT2.txt
19	Imperial Valley	1979	6.5	3.8	H-E08230.AT2.txt
20	Imperial Valley	1979	6.5	8.6	H-E10050.AT2.txt
21	Imperial Valley	1979	6.5	8.6	H-E10320.AT2.txt
22	Imperial Valley	1979	6.5	12.6	H-E11140.AT2.txt
23	Imperial Valley	1979	6.5	12.6	H-E11230.AT2.txt
24	Imperial Valley	1979	6.5	7.6	H-ECC002.AT2.txt
25	Imperial Valley	1979	6.5	7.6	H-ECC092.AT2.txt
26	Imperial Valley	1979	6.5	5.3	H-EDA270.AT2.txt
27	Imperial Valley	1979	6.5	5.3	H-EDA360.AT2.txt
28	Imperial Valley	1979	6.5	0.5	H-EMO000.AT2.txt
29	Imperial Valley	1979	6.5	0.5	H-EMO270.AT2.txt
30	Imperial Valley	1979	6.5	7.5	H-HVP225.AT2.txt
31	Imperial Valley	1979	6.5	7.5	H-HVP315.AT2.txt
32	Imperial Valley	1979	6.5	14.2	H-PTS225.AT2.txt
33	Imperial Valley	1979	6.5	14.2	H-PTS315.AT2.txt
34	Imperial Valley	1979	6.5	11.1	H-SHP000.AT2.txt
35	Imperial Valley	1979	6.5	11.1	H-SHP270.AT2.txt
36	Coalinga	1983	6.4	8.5	H-PVY045.AT2.txt
37	Coalinga	1983	6.4	8.5	H-PVY135.AT2.txt
38	Superstition Hills	1987	6.7	13.9	B-ICC000.AT2.txt
39	Superstition Hills	1987	6.7	13.9	B-ICC090.AT2.txt
40	Superstition Hills	1987	6.7	0.7	B-PTS225.AT2.txt
41	Superstition Hills	1987	6.7	0.7	B-PTS315.AT2.txt
42	Superstition Hills	1987	6.7	13.3	B-WSM090.AT2.txt
43	Superstition Hills	1987	6.7	13.3	B-WSM180.AT2.txt
44	Northridge	1994	6.7	9.2	ARL090.AT2.txt
45	Northridge	1994	6.7	9.2	ARL360.AT2.txt
46	Northridge	1994	6.7	14.6	CWC180.AT2.txt
47	Northridge	1994	6.7	14.6	CWC270.AT2.txt
48	Northridge	1994	6.7	6.2	JEN022.AT2.txt
49	Northridge	1994	6.7	6.2	JEN292.AT2.txt
50	Northridge	1994	6.7	13.0	LOS000.AT2.txt
51	Northridge	1994	6.7	13.0	LOS270.AT2.txt
52	Northridge	1994	6.7	7.1	NWH090.AT2.txt
53	Northridge	1994	6.7	7.1	NWH360.AT2.txt
54	Northridge	1994	6.7	8.2	PKC090.AT2.txt
55	Northridge	1994	6.7	8.2	PKC360.AT2.txt
56	Northridge	1994	6.7	12.3	RO3000.AT2.txt
57	Northridge	1994	6.7	12.3	RO3090.AT2.txt
58	Northridge	1994	6.7	7.1	RRS228.AT2.txt
59	Northridge	1994	6.7	7.1	RRS318.AT2.txt
60	Northridge	1994	6.7	6.1	SCE018.AT2.txt
61	Northridge	1994	6.7	6.1	SCE288.AT2.txt
62	Northridge	1994	6.7	6.2	SCS052.AT2.txt
63	Northridge	1994	6.7	6.2	SCS142.AT2.txt
64	Northridge	1994	6.7	8.9	SPV270.AT2.txt
65	Northridge	1994	6.7	8.9	SPV360.AT2.txt
66	Northridge	1994	6.7	13.3	STC090.AT2.txt
67	Northridge	1994	6.7	13.3	STC180.AT2.txt
68	Northridge	1994	6.7	6.4	SYL090.AT2.txt
69	Northridge	1994	6.7	6.4	SYL360.AT2.txt
70	Northridge	1994	6.7	14.9	UCL090.AT2.txt
71	Northridge	1994	6.7	14.9	UCL360.AT2.txt
72	Northridge	1994	6.7	7.1	WPI046.AT2.txt
73	Northridge	1994	6.7	7.1	WPI316.AT2.txt
	Min		6.4	0.5	
	Max		6.7	14.9	

	EARTHQUAKE NAME	YEAR	M	R	RECORD NAME
1	San Fernando	1971	6.6	21.2	PEL090.AT2.txt
2	San Fernando	1971	6.6	21.2	PEL180.AT2.txt
3	Imperial Valley	1979	6.5	23.8	H-CAL225.AT2.txt
4	Imperial Valley	1979	6.5	23.8	H-CAL315.AT2.txt
5	Imperial Valley	1979	6.5	28.7	H-CHI012.AT2.txt
6	Imperial Valley	1979	6.5	28.7	H-CHI282.AT2.txt
7	Imperial Valley	1979	6.5	26.5	H-CPE147.AT2.txt
8	Imperial Valley	1979	6.5	26.5	H-CPE237.AT2.txt
9	Imperial Valley	1979	6.5	15.5	H-E01140.AT2.txt
10	Imperial Valley	1979	6.5	15.5	H-E01230.AT2.txt
11	Imperial Valley	1979	6.5	18.2	H-E12140.AT2.txt
12	Imperial Valley	1979	6.5	18.2	H-E12230.AT2.txt
13	Imperial Valley	1979	6.5	21.9	H-E13140.AT2.txt
14	Imperial Valley	1979	6.5	21.9	H-E13230.AT2.txt
15	Imperial Valley	1979	6.5	23.6	H-QKP085.AT2.txt
16	Imperial Valley	1979	6.5	26.0	H-SUP045.AT2.txt
17	Imperial Valley	1979	6.5	26.0	H-SUP135.AT2.txt
18	Imperial Valley	1979	6.5	15.1	H-WSM090.AT2.txt
19	Imperial Valley	1979	6.5	15.1	H-WSM180.AT2.txt
20	Coalinga	1983	6.4	25.5	H-CAK270.AT2.txt
21	Coalinga	1983	6.4	25.5	H-CAK360.AT2.txt
22	Coalinga	1983	6.4	29.2	H-GH3000.AT2.txt
23	Coalinga	1983	6.4	29.2	H-GH3090.AT2.txt
24	Coalinga	1983	6.4	29.5	H-PRK090.AT2.txt
25	Coalinga	1983	6.4	29.5	H-PRK180.AT2.txt
26	Coalinga	1983	6.4	26.7	H-PV1000.AT2.txt
27	Coalinga	1983	6.4	26.7	H-PV1090.AT2.txt
28	Coalinga	1983	6.4	29.6	H-Z08000.AT2.txt
29	Coalinga	1983	6.4	29.6	H-Z08090.AT2.txt
30	Coalinga	1983	6.4	28.4	H-Z11000.AT2.txt
31	Coalinga	1983	6.4	28.4	H-Z11090.AT2.txt
32	Coalinga	1983	6.4	29.9	H-Z14000.AT2.txt
33	Coalinga	1983	6.4	29.9	H-Z14090.AT2.txt
34	Coalinga	1983	6.4	29.9	H-Z15000.AT2.txt
35	Coalinga	1983	6.4	29.9	H-Z15090.AT2.txt
36	Coalinga	1983	6.4	28.1	H-Z16000.AT2.txt
37	Coalinga	1983	6.4	28.1	H-Z16090.AT2.txt
38	Superstition Hills	1987	6.7	18.2	B-BRA225.AT2.txt
39	Superstition Hills	1987	6.7	18.2	B-BRA315.AT2.txt
40	Superstition Hills	1987	6.7	28.3	B-CAL225.AT2.txt
41	Superstition Hills	1987	6.7	28.3	B-CAL315.AT2.txt
42	Superstition Hills	1987	6.7	21.0	B-PLS135.AT2.txt
43	Northridge	1994	6.7	25.7	CCN090.AT2.txt
44	Northridge	1994	6.7	25.7	CCN360.AT2.txt
45	Northridge	1994	6.7	15.8	CNP106.AT2.txt
46	Northridge	1994	6.7	15.8	CNP106.AT2.txt
47	Northridge	1994	6.7	23.9	FAR000.AT2.txt
48	Northridge	1994	6.7	23.9	FAR090.AT2.txt
49	Northridge	1994	6.7	17.7	GLE170.AT2.txt
50	Northridge	1994	6.7	17.7	GLE260.AT2.txt
51	Northridge	1994	6.7	20.8	MU2035.AT2.txt
52	Northridge	1994	6.7	20.8	MU2125.AT2.txt
53	Northridge	1994	6.7	19.6	MUL009.AT2.txt
54	Northridge	1994	6.7	19.6	MUL279.AT2.txt
55	Northridge	1994	6.7	22.6	ORR090.AT2.txt
56	Northridge	1994	6.7	22.6	ORR360.AT2.txt
57	Northridge	1994	6.7	25.4	PDL120.AT2.txt
58	Northridge	1994	6.7	25.4	PDL210.AT2.txt
59	Northridge	1994	6.7	19.3	SSU000.AT2.txt
60	Northridge	1994	6.7	19.3	SSU090.AT2.txt
61	Northridge	1994	6.7	27.6	STM090.AT2.txt
62	Northridge	1994	6.7	27.6	STM360.AT2.txt
63	Northridge	1994	6.7	30.0	STN020.AT2.txt
64	Northridge	1994	6.7	30.0	STN110.AT2.txt
65	Northridge	1994	6.7	26.2	SUN190.AT2.txt
66	Northridge	1994	6.7	26.2	SUN280.AT2.txt
67	Northridge	1994	6.7		TPF000.AT2.txt
68	Northridge	1994	6.7	24.2	VAS000.AT2.txt
69	Northridge	1994	6.7	24.2	VAS090.AT2.txt
70	Northridge	1994	6.7	25.7	WIL090.AT2.txt
71	Northridge	1994	6.7	25.7	WIL180.AT2.txt
72	Northridge	1994	6.7	29.0	WST000.AT2.txt
73	Northridge	1994	6.7	29.0	WST270.AT2.txt
	Min		6.4	15.1	
	Max		6.7	30	

Tables A3-4. Lists of the 73 earthquake records in "Bin III" (M_w=6.4-6.8, R_{close}=30-50km), on the left, and "Bin IV" (M_w=6.9-7.6, R_{close}=0-15km), on the right.

	EARTHQUAKE NAME	YEAR	M	R	RECORD NAME
1	Borrego Mountain	1968	6.8	46.0	A-ELC180.AT2.txt
2	Borrego Mountain	1968	6.8	46.0	A-ELC270.AT2.txt
3	San Fernando	1971	6.6	48.1	OPP000.AT2.txt
4	San Fernando	1971	6.6	48.1	OPP270.AT2.txt
5	San Fernando	1971	6.6	31.7	PAS090.AT2.txt
6	San Fernando	1971	6.6	38.9	PPP000.AT2.txt
7	San Fernando	1971	6.6	38.9	PPP270.AT2.txt
8	Friuli	1976	6.5	34.6	A-COD000.AT2.txt
9	Friuli	1976	6.5	34.6	A-COD270.AT2.txt
10	Friuli	1976	6.5	37.7	A-TMZ000.AT2.txt
11	Friuli	1976	6.5	37.7	A-TMZ270.AT2.txt
12	Imperial Valley	1979	6.5	49.3	H-CC4045.AT2.txt
13	Imperial Valley	1979	6.5	49.3	H-CC4135.AT2.txt
14	Imperial Valley	1979	6.5	32.6	H-CMP015.AT2.txt
15	Imperial Valley	1979	6.5	32.6	H-CMP285.AT2.txt
16	Imperial Valley	1979	6.5	35.9	H-NIL090.AT2.txt
17	Imperial Valley	1979	6.5	35.9	H-NIL360.AT2.txt
18	Imperial Valley	1979	6.5	31.7	H-PLS045.AT2.txt
19	Imperial Valley	1979	6.5	31.7	H-PLS135.AT2.txt
20	Coalinga	1983	6.4	41.6	H-C01000.AT2.txt
21	Coalinga	1983	6.4	41.6	H-C01090.AT2.txt
22	Coalinga	1983	6.4	43.9	H-C03000.AT2.txt
23	Coalinga	1983	6.4	43.9	H-C03090.AT2.txt
24	Coalinga	1983	6.4	44.7	H-C04000.AT2.txt
25	Coalinga	1983	6.4	44.7	H-C04090.AT2.txt
26	Coalinga	1983	6.4	49.0	H-C06090.AT2.txt
27	Coalinga	1983	6.4	46.0	H-C4A000.AT2.txt
28	Coalinga	1983	6.4	46.0	H-C4A090.AT2.txt
29	Coalinga	1983	6.4	40.4	H-COW000.AT2.txt
30	Coalinga	1983	6.4	40.4	H-COW090.AT2.txt
31	Coalinga	1983	6.4	40.5	H-TM2090.AT2.txt
32	Coalinga	1983	6.4	37.9	H-Z02000.AT2.txt
33	Coalinga	1983	6.4	37.9	H-Z02090.AT2.txt
34	Coalinga	1983	6.4	34.3	H-Z04000.AT2.txt
35	Coalinga	1983	6.4	34.3	H-Z04090.AT2.txt
36	Coalinga	1983	6.4	32.8	H-Z06000.AT2.txt
37	Coalinga	1983	6.4	32.8	H-Z06090.AT2.txt
38	Coalinga	1983	6.4	31.0	H-Z07000.AT2.txt
39	Coalinga	1983	6.4	31.0	H-Z07090.AT2.txt
40	Coalinga	1983	6.4	30.4	H-Z10000.AT2.txt
41	Coalinga	1983	6.4	30.4	H-Z10090.AT2.txt
42	Northridge	1994	6.7	41.9	116090.AT2.txt
43	Northridge	1994	6.7	41.9	116360.AT2.txt
44	Northridge	1994	6.7	35.7	ALH090.AT2.txt
45	Northridge	1994	6.7	35.7	ALH360.AT2.txt
46	Northridge	1994	6.7	38.4	ANA090.AT2.txt
47	Northridge	1994	6.7	38.4	ANA180.AT2.txt
48	Northridge	1994	6.7	31.3	BLD090.AT2.txt
49	Northridge	1994	6.7	31.3	BLD360.AT2.txt
50	Northridge	1994	6.7	44.2	CAM279.AT2.txt
51	Northridge	1994	6.7	49.6	CAS000.AT2.txt
52	Northridge	1994	6.7	49.6	CAS270.AT2.txt
53	Northridge	1994	6.7	37.2	ELI090.AT2.txt
54	Northridge	1994	6.7	37.2	ELI180.AT2.txt
55	Northridge	1994	6.7	47.4	FAI095.AT2.txt
56	Northridge	1994	6.7	32.3	L4B000.AT2.txt
57	Northridge	1994	6.7	32.3	L4B090.AT2.txt
58	Northridge	1994	6.7	42.4	LOA092.AT2.txt
59	Northridge	1994	6.7	42.4	LOA182.AT2.txt
60	Northridge	1994	6.7	38.5	LV6090.AT2.txt
61	Northridge	1994	6.7	38.5	LV6360.AT2.txt
62	Northridge	1994	6.7	43.6	PHP000.AT2.txt
63	Northridge	1994	6.7	43.6	PHP270.AT2.txt
64	Northridge	1994	6.7	46.6	RHE090.AT2.txt
65	Northridge	1994	6.7	46.6	RHE360.AT2.txt
66	Northridge	1994	6.7	32.3	TEM090.AT2.txt
67	Northridge	1994	6.7	32.3	TEM180.AT2.txt
68	Northridge	1994	6.7	34.6	UNI005.AT2.txt
69	Northridge	1994	6.7	34.6	UNI095.AT2.txt
70	Northridge	1994	6.7	39.3	VER090.AT2.txt
71	Northridge	1994	6.7	39.3	VER180.AT2.txt
72	Northridge	1994	6.7	32.4	W15090.AT2.txt
73	Northridge	1994	6.7	32.4	W15180.AT2.txt
	Min		6.4	30.4	
	Max		6.8	49.6	

	EARTHQUAKE NAME	YEAR	M	R	RECORD NAME
1	Imperial Valley	1940	7	8.3	I-ELC180.AT2.txt
2	Imperial Valley	1940	7	8.3	I-ELC270.AT2.txt
3	Tabas	1978	7.4	14.0	DAY-LN.AT2.txt
4	Tabas	1978	7.4	14.0	DAY-TR.AT2.txt
5	Tabas	1978	7.4	3.0	TAB-LN.AT2.txt
6	Tabas	1978	7.4	3.0	TAB-TR.AT2.txt
7	Irpinia 1	1980	6.9	13.0	A-CTR000.AT2.txt
8	Irpinia 1	1980	6.9	13.0	A-CTR270.AT2.txt
9	Irpinia 2	1980	6.9	13.0	B-CTR000.AT2.txt
10	Irpinia 2	1980	6.9	13.0	B-CTR270.AT2.txt
11	Loma Prieta	1989	6.9	14.5	CAP000.AT2.txt
12	Loma Prieta	1989	6.9	14.5	CAP090.AT2.txt
13	Loma Prieta	1989	6.9	5.1	CLS000.AT2.txt
14	Loma Prieta	1989	6.9	5.1	CLS090.AT2.txt
15	Loma Prieta	1989	6.9	12.7	G02000.AT2.txt
16	Loma Prieta	1989	6.9	12.7	G02090.AT2.txt
17	Loma Prieta	1989	6.9	14.4	G03000.AT2.txt
18	Loma Prieta	1989	6.9	14.4	G03090.AT2.txt
19	Loma Prieta	1989	6.9	11.6	GIL067.AT2.txt
20	Loma Prieta	1989	6.9	11.6	GIL337.AT2.txt
21	Loma Prieta	1989	6.9	13.0	STG000.AT2.txt
22	Loma Prieta	1989	6.9	13.0	STG090.AT2.txt
23	Loma Prieta	1989	6.9	13.7	WVC000.AT2.txt
24	Loma Prieta	1989	6.9	13.7	WVC270.AT2.txt
25	Erzincan	1992	6.9	2.0	ERZ-EW.AT2.txt
26	Erzincan	1992	6.9	2.0	ERZ-NS.AT2.txt
27	Landers	1992	7.3	11.6	JOS000.AT2.txt
28	Landers	1992	7.3	11.6	JOS090.AT2.txt
29	Kobe	1995	6.9	10.2	AMA000.AT2.txt
30	Kobe	1995	6.9	10.2	AMA090.AT2.txt
31	Kobe	1995	6.9	0.6	KJM000.AT2.txt
32	Kobe	1995	6.9	0.6	KJM090.AT2.txt
33	Kobe	1995	6.9	1.2	TAZ000.AT2.txt
34	Kobe	1995	6.9	1.2	TAZ090.AT2.txt
35	Kocaeli	1999	7.4	12.7	DZC180.AT2.txt
36	Kocaeli	1999	7.4	12.7	DZC270.AT2.txt
37	Kocaeli	1999	7.4	3.1	SKR090.AT2.txt
38	Kocaeli	1999	7.4	2.6	YPT060.AT2.txt
39	Kocaeli	1999	7.4	2.6	YPT330.AT2.txt
40	Chi Chi	1999	7.6	7.3	CHY028-N.AT2.txt
41	Chi Chi	1999	7.6	7.3	CHY028-W.AT2.txt
42	Chi Chi	1999	7.6	6.9	CHY080-N.AT2.txt
43	Chi Chi	1999	7.6	6.9	CHY080-W.AT2.txt
44	Chi Chi	1999	7.6	9.7	NSY-E.AT2.txt
45	Chi Chi	1999	7.6	9.7	NSY-N.AT2.txt
46	Chi Chi	1999	7.6	5.7	TCU-E.AT2.txt
47	Chi Chi	1999	7.6	5.7	TCU-N.AT2.txt
48	Chi Chi	1999	7.6	0.3	TCU067-N.AT2.txt
49	Chi Chi	1999	7.6	0.3	TCU067-W.AT2.txt
50	Chi Chi	1999	7.6	4.9	TCU071-N.AT2.txt
51	Chi Chi	1999	7.6	4.9	TCU071-W.AT2.txt
52	Chi Chi	1999	7.6	13.7	TCU074-N.AT2.txt
53	Chi Chi	1999	7.6	13.7	TCU074-W.AT2.txt
54	Chi Chi	1999	7.6	10.0	TCU079-N.AT2.txt
55	Chi Chi	1999	7.6	10.0	TCU079-W.AT2.txt
56	Chi Chi	1999	7.6	8.2	TCU089-N.AT2.txt
57	Chi Chi	1999	7.6	8.2	TCU089-W.AT2.txt
58	Chi Chi	1999	7.6	13.6	TCU104-N.AT2.txt
59	Chi Chi	1999	7.6	13.6	TCU104-W.AT2.txt
60	Chi Chi	1999	7.6	13.1	TCU109-N.AT2.txt
61	Chi Chi	1999	7.6	13.1	TCU109-W.AT2.txt
62	Chi Chi	1999	7.6	9.0	TCU136-E.AT2.txt
63	Chi Chi	1999	7.6	9.0	TCU136-N.AT2.txt
64	Duzce	1999	7.1	0.9	1058-E.AT2.txt
65	Duzce	1999	7.1	0.9	1058-N.AT2.txt
66	Duzce	1999	7.1	8.5	1059-E.AT2.txt
67	Duzce	1999	7.1	8.5	1059-N.AT2.txt
68	Duzce	1999	7.1	13.3	1062-E.AT2.txt
69	Duzce	1999	7.1	13.3	1062-N.AT2.txt
70	Duzce	1999	7.1	8.2	375-E.AT2.txt
71	Duzce	1999	7.1	8.2	375-N.AT2.txt
72	Duzce	1999	7.1	8.2	DZC180.AT2.txt
73	Duzce	1999	7.1	8.2	DZC270.AT2.txt
	Min		6.9	0.3	
	Max		7.6	14.5	

Table A5-6. Lists of the 73 earthquake records in "Bin V" (M_w=6.9-7.6, R_{close}=15-30km), on the left, and "Bin VI" (M_w=6.9-7.6, R_{close}=30-50km), on the right.

	EARTHQUAKE NAME	YEAR	M	R	RECORD NAME
1	Tabas	1978	7.4	26.1	BOS-L1.AT2.txt
2	Tabas	1978	7.4	26.1	BOS-T1.AT2.txt
3	Irpinia 1	1980	6.9	23.0	A-BRZ000.AT2.txt
4	Irpinia 1	1980	6.9	23.0	A-BRZ270.AT2.txt
5	Irpinia 2	1980	6.9	23.0	B-BRZ000.AT2.txt
6	Irpinia 2	1980	6.9	23.0	B-BRZ270.AT2.txt
7	Loma Prieta	1989	6.9	21.4	ADL250.AT2.txt
8	Loma Prieta	1989	6.9	21.4	ADL340.AT2.txt
9	Loma Prieta	1989	6.9	28.2	AGW000.AT2.txt
10	Loma Prieta	1989	6.9	28.2	AGW090.AT2.txt
11	Loma Prieta	1989	6.9	21.4	AND270.AT2.txt
12	Loma Prieta	1989	6.9	21.4	AND360.AT2.txt
13	Loma Prieta	1989	6.9	22.3	CLD195.AT2.txt
14	Loma Prieta	1989	6.9	22.3	CLD285.AT2.txt
15	Loma Prieta	1989	6.9	16.1	G04000.AT2.txt
16	Loma Prieta	1989	6.9	16.1	G04090.AT2.txt
17	Loma Prieta	1989	6.9	19.9	G06000.AT2.txt
18	Loma Prieta	1989	6.9	19.9	G06090.AT2.txt
19	Loma Prieta	1989	6.9	24.2	GMR000.AT2.txt
20	Loma Prieta	1989	6.9	24.2	GMR090.AT2.txt
21	Loma Prieta	1989	6.9	28.2	HCH090.AT2.txt
22	Loma Prieta	1989	6.9	28.2	HCH180.AT2.txt
23	Loma Prieta	1989	6.9	28.8	SVL270.AT2.txt
24	Loma Prieta	1989	6.9	28.8	SVL360.AT2.txt
25	Landers	1992	7.3	21.2	CLW-LN.AT2.txt
26	Landers	1992	7.3	21.2	CLW-TR.AT2.txt
27	Landers	1992	7.3	23.2	DSP000.AT2.txt
28	Landers	1992	7.3	23.2	DSP090.AT2.txt
29	Landers	1992	7.3	19.3	MVH000.AT2.txt
30	Landers	1992	7.3	19.3	MVH090.AT2.txt
31	Landers	1992	7.3	24.2	NPS000.AT2.txt
32	Landers	1992	7.3	24.2	NPS090.AT2.txt
33	Landers	1992	7.3	24.9	YER270.AT2.txt
34	Landers	1992	7.3	24.9	YER360.AT2.txt
35	Kobe	1995	6.9	23.8	ABN000.AT2.txt
36	Kobe	1995	6.9	23.8	ABN090.AT2.txt
37	Kocaeli	1999	7.4	17.0	ARC000.AT2.txt
38	Kocaeli	1999	7.4	17.0	ARC090.AT2.txt
39	Chi Chi	1999	7.6	25.4	CHY010-E.AT2.txt
40	Chi Chi	1999	7.6	25.4	CHY010-N.AT2.txt
41	Chi Chi	1999	7.6	15.3	CHY029-N.AT2.txt
42	Chi Chi	1999	7.6	15.3	CHY029-W.AT2.txt
43	Chi Chi	1999	7.6	18.1	CHY035-N.AT2.txt
44	Chi Chi	1999	7.6	20.4	CHY036-N.AT2.txt
45	Chi Chi	1999	7.6	20.4	CHY036-W.AT2.txt
46	Chi Chi	1999	7.6	29.5	CHY046-N.AT2.txt
47	Chi Chi	1999	7.6	29.5	CHY046-W.AT2.txt
48	Chi Chi	1999	7.6	24.7	TCU029-N.AT2.txt
49	Chi Chi	1999	7.6	24.7	TCU029-W.AT2.txt
50	Chi Chi	1999	7.6	26.8	TCU031-N.AT2.txt
51	Chi Chi	1999	7.6	26.8	TCU031-W.AT2.txt
52	Chi Chi	1999	7.6	16.7	TCU036-N.AT2.txt
53	Chi Chi	1999	7.6	16.7	TCU036-W.AT2.txt
54	Chi Chi	1999	7.6	16.7	TCU039-N.AT2.txt
55	Chi Chi	1999	7.6	16.7	TCU039-W.AT2.txt
56	Chi Chi	1999	7.6	24.1	TCU045-N.AT2.txt
57	Chi Chi	1999	7.6	24.1	TCU045-W.AT2.txt
58	Chi Chi	1999	7.6	17.8	TCU059-N.AT2.txt
59	Chi Chi	1999	7.6	17.8	TCU059-W.AT2.txt
60	Chi Chi	1999	7.6	17.7	TCU061-N.AT2.txt
61	Chi Chi	1999	7.6	17.7	TCU061-W.AT2.txt
62	Chi Chi	1999	7.6	19.1	TCU070-N.AT2.txt
63	Chi Chi	1999	7.6	19.1	TCU070-W.AT2.txt
64	Chi Chi	1999	7.6	20.3	TCU107-N.AT2.txt
65	Chi Chi	1999	7.6	20.3	TCU107-W.AT2.txt
66	Chi Chi	1999	7.6	15.1	TCU123-N.AT2.txt
67	Chi Chi	1999	7.6	15.1	TCU123-W.AT2.txt
68	Duzce	1999	7.1	15.6	1061-E.AT2.txt
69	Duzce	1999	7.1	15.6	1061-N.AT2.txt
70	Duzce	1999	7.1	27.4	362-E.AT2.txt
71	Duzce	1999	7.1	27.4	362-N.AT2.txt
72	Duzce	1999	7.1	17.6	BOL000.AT2.txt
73	Duzce	1999	7.1	17.6	BOL090.AT2.txt
	Min		6.9	15.1	
	Max		7.6	29.5	

	EARTHQUAKE NAME	YEAR	M	R	RECORD NAME
1	Kern County	1952	7.4	41.0	TAF021.AT2.txt
2	Kern County	1952	7.4	41.0	TAF111.AT2.txt
3	Taiwan Smart 1	1986	7.3	39.0	45C00EW.AT2.txt
4	Taiwan Smart 1	1986	7.3	39.0	45C00NS.AT2.txt
5	Loma Prieta	1989	6.9	47.7	A07000.AT2.txt
6	Loma Prieta	1989	6.9	47.7	A07090.AT2.txt
7	Loma Prieta	1989	6.9	46.9	A09137.AT2.txt
8	Loma Prieta	1989	6.9	46.9	A09227.AT2.txt
9	Loma Prieta	1989	6.9	47.8	A10000.AT2.txt
10	Loma Prieta	1989	6.9	47.8	A10090.AT2.txt
11	Loma Prieta	1989	6.9	49.9	BES000.AT2.txt
12	Loma Prieta	1989	6.9	49.9	BES090.AT2.txt
13	Loma Prieta	1989	6.9	43.0	FRE000.AT2.txt
14	Loma Prieta	1989	6.9	43.0	FRE090.AT2.txt
15	Loma Prieta	1989	6.9	31.6	HVR000.AT2.txt
16	Loma Prieta	1989	6.9	31.6	HVR090.AT2.txt
17	Loma Prieta	1989	6.9	34.7	SG3261.AT2.txt
18	Loma Prieta	1989	6.9	34.7	SG3351.AT2.txt
19	Loma Prieta	1989	6.9	32.6	SJW160.AT2.txt
20	Loma Prieta	1989	6.9	32.6	SJW250.AT2.txt
21	Loma Prieta	1989	6.9	36.3	SLC270.AT2.txt
22	Loma Prieta	1989	6.9	36.3	SLC360.AT2.txt
23	Loma Prieta	1989	6.9	39.9	WDS000.AT2.txt
24	Loma Prieta	1989	6.9	39.9	WDS090.AT2.txt
25	Landers	1992	7.3	36.1	BRS000.AT2.txt
26	Landers	1992	7.3	36.1	BRS090.AT2.txt
27	Landers	1992	7.3	37.5	PSA000.AT2.txt
28	Landers	1992	7.3	37.5	PSA090.AT2.txt
29	Kocaeli	1999	7.4	35.5	GYN000.AT2.txt
30	Kocaeli	1999	7.4	35.5	GYN090.AT2.txt
31	Kocaeli	1999	7.4	31.8	IZN090.AT2.txt
32	Kocaeli	1999	7.4	31.8	IZN180.AT2.txt
33	Chi Chi	1999	7.6	47.7	CHY081-N.AT2.txt
34	Chi Chi	1999	7.6	47.7	CHY081-W.AT2.txt
35	Chi Chi	1999	7.6	35.4	CHY086-N.AT2.txt
36	Chi Chi	1999	7.6	35.4	CHY086-W.AT2.txt
37	Chi Chi	1999	7.6	34.5	CHY087-N.AT2.txt
38	Chi Chi	1999	7.6	34.5	CHY087-W.AT2.txt
39	Chi Chi	1999	7.6	46.2	CHY102-N.AT2.txt
40	Chi Chi	1999	7.6	46.2	CHY102-W.AT2.txt
41	Chi Chi	1999	7.6	44.9	ESL-E.AT2.txt
42	Chi Chi	1999	7.6	44.9	ESL-N.AT2.txt
43	Chi Chi	1999	7.6	43.9	HWA005-E.AT2.txt
44	Chi Chi	1999	7.6	43.9	HWA005-N.AT2.txt
45	Chi Chi	1999	7.6	44.9	HWA020-N.AT2.txt
46	Chi Chi	1999	7.6	44.9	HWA020-W.AT2.txt
47	Chi Chi	1999	7.6	44.3	HWA024-N.AT2.txt
48	Chi Chi	1999	7.6	44.3	HWA024-W.AT2.txt
49	Chi Chi	1999	7.6	49.0	HWA033-N.AT2.txt
50	Chi Chi	1999	7.6	49.0	HWA033-W.AT2.txt
51	Chi Chi	1999	7.6	42.0	HWA034-W.AT2.txt
52	Chi Chi	1999	7.6	43.6	HWA036-N.AT2.txt
53	Chi Chi	1999	7.6	43.6	HWA036-W.AT2.txt
54	Chi Chi	1999	7.6	46.6	HWA037-N.AT2.txt
55	Chi Chi	1999	7.6	46.6	HWA037-W.AT2.txt
56	Chi Chi	1999	7.6	46.7	HWA039-N.AT2.txt
57	Chi Chi	1999	7.6	47.7	HWA039-W.AT2.txt
58	Chi Chi	1999	7.6	48.7	HWA055-E.AT2.txt
59	Chi Chi	1999	7.6	48.7	HWA055-N.AT2.txt
60	Chi Chi	1999	7.6	40.5	KAU054-N.AT2.txt
61	Chi Chi	1999	7.6	40.5	KAU054-W.AT2.txt
62	Chi Chi	1999	7.6	47.3	TCU015-N.AT2.txt
63	Chi Chi	1999	7.6	47.3	TCU015-W.AT2.txt
64	Chi Chi	1999	7.6	38.2	TCU033-N.AT2.txt
65	Chi Chi	1999	7.6	38.2	TCU033-W.AT2.txt
66	Chi Chi	1999	7.6	33.0	TCU034-N.AT2.txt
67	Chi Chi	1999	7.6	33.0	TCU034-W.AT2.txt
68	Chi Chi	1999	7.6	33.0	TCU047-N.AT2.txt
69	Chi Chi	1999	7.6	33.0	TCU047-W.AT2.txt
70	Chi Chi	1999	7.6	43.4	TCU095-N.AT2.txt
71	Chi Chi	1999	7.6	43.4	TCU095-W.AT2.txt
72	Duzce	1999	7.1	49.9	SKR090.AT2.txt
73	Duzce	1999	7.1	49.9	SKR180.AT2.txt
	Min		6.9	31.6	
	Max		7.6	49.9	

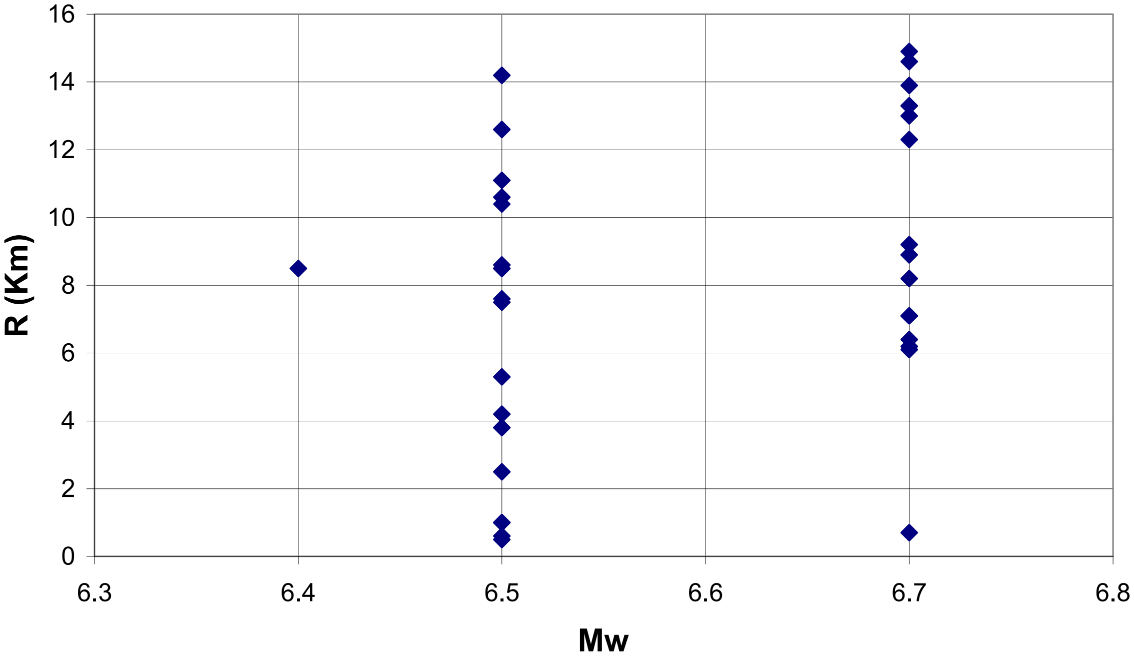

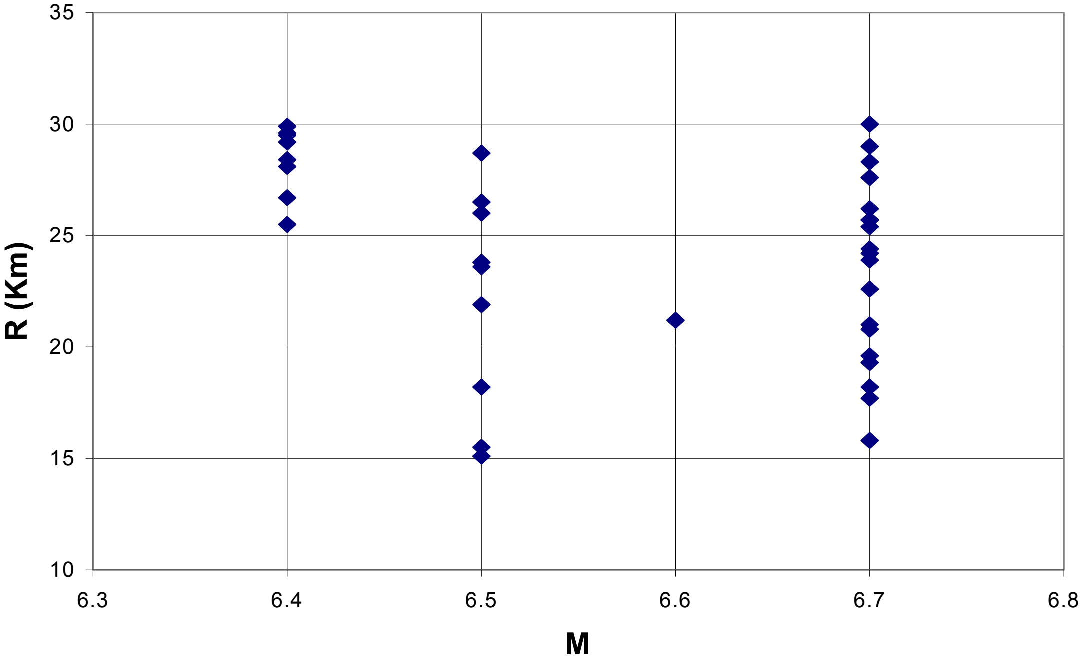

Figures A1-2. Scatter plots of earthquake magnitude (M_w) versus closest source-to-site distance (R_{close}) for the earthquake records in "Bin I" (M_w=6.4-6.8, R_{close}=0-15km), on the top, and "Bin II" (M_w=6.4-6.8, R_{close}=15-30km), on the bottom.

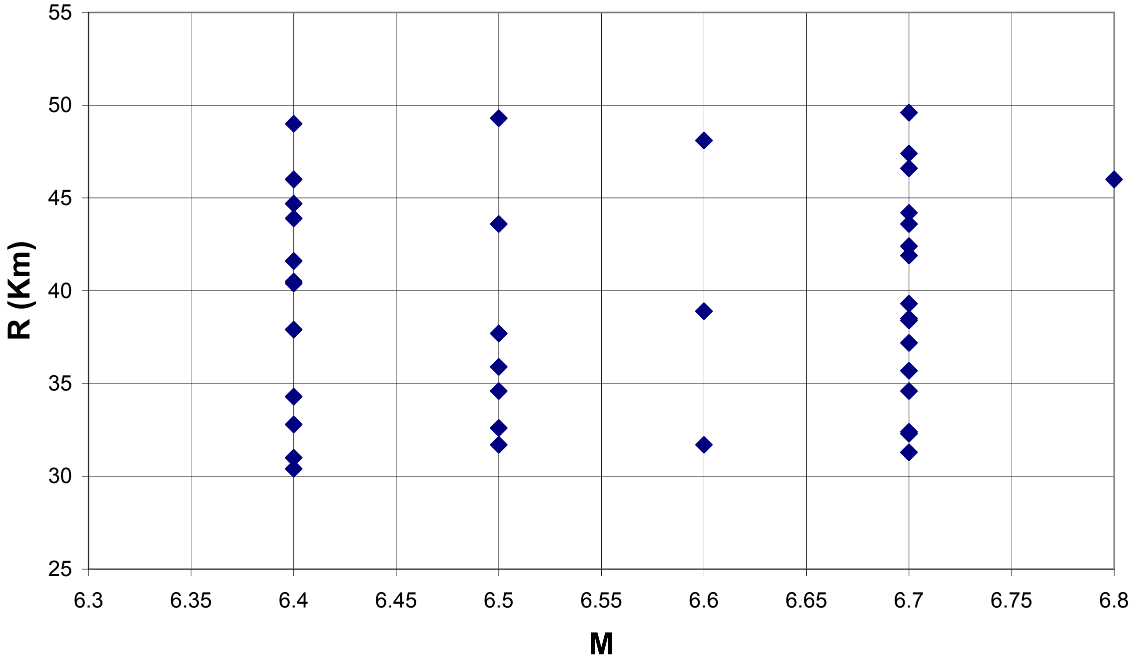

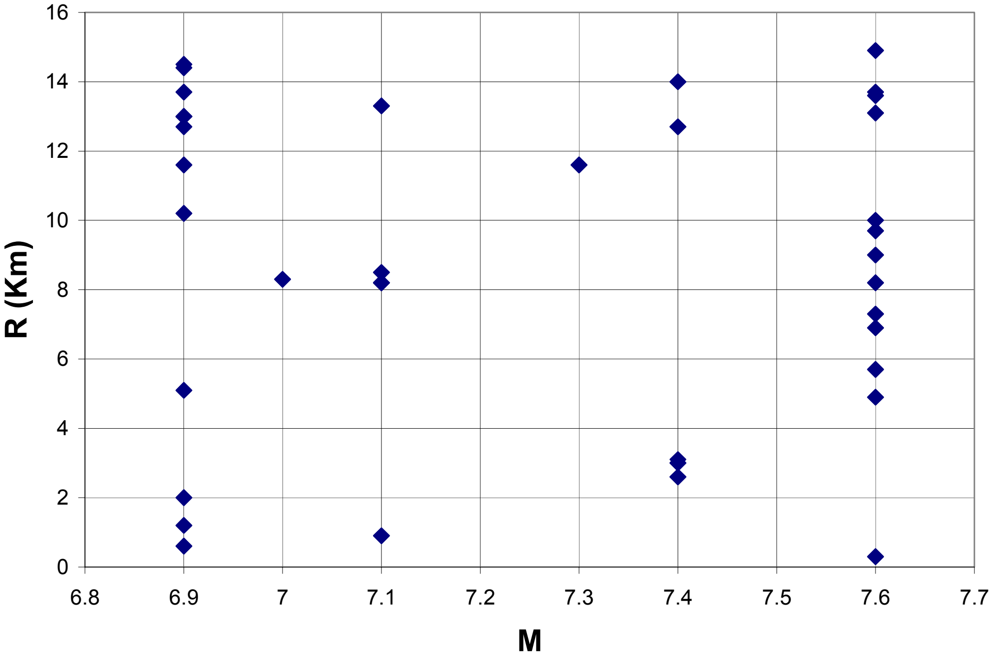

Figures A3-4. Scatter plots of earthquake magnitude (M_w) versus closest source-to-site distance (R_{close}) for the earthquake records in "Bin III" (M_w=6.4-6.8, R_{close}=30-50km), on the top, and "Bin IV" (M_w=6.9-7.6, R_{close}=0-15km), on the bottom.

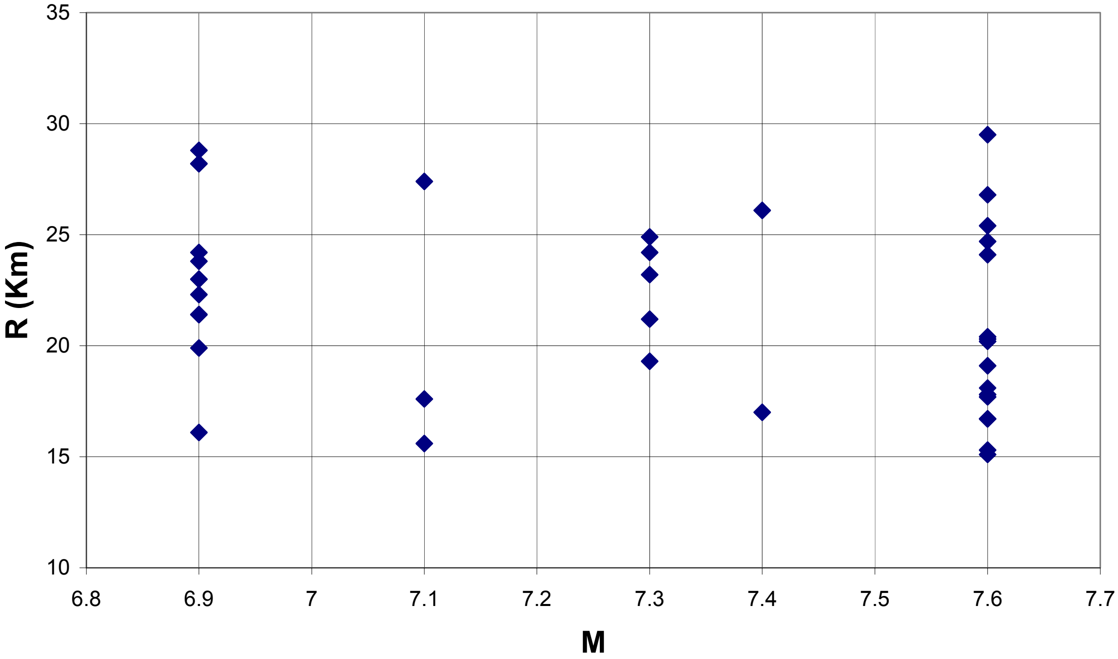

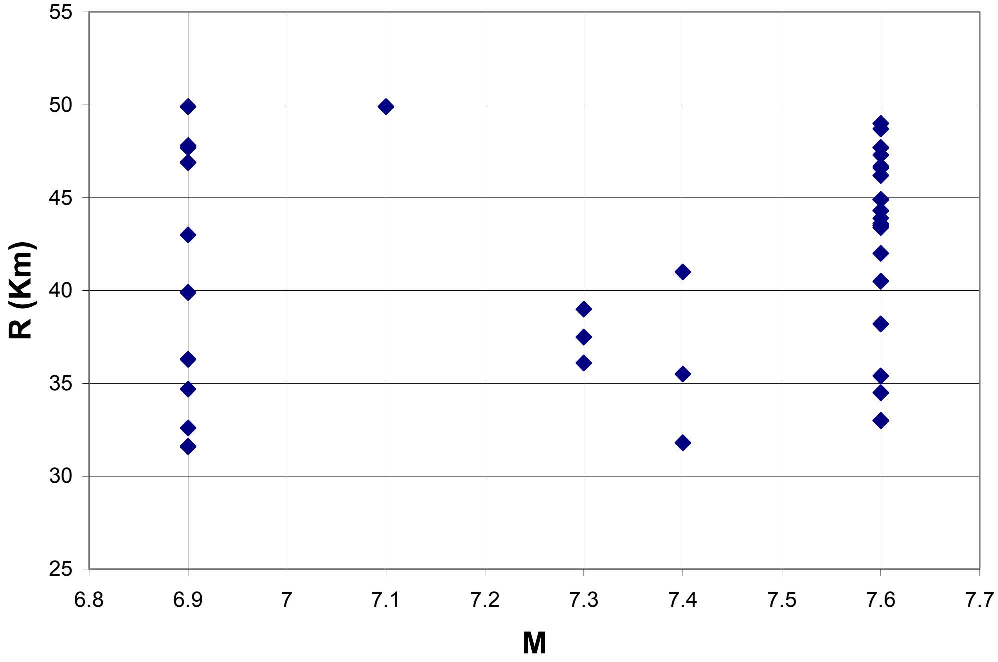

Figures A5-6. Scatter plots of earthquake magnitude (M_w) versus closest source-to-site distance (R_{close}) for the earthquake records in "Bin V" (M_w=6.9-7.6, R_{close}=15-30km), on the top, and "Bin VI" (M_w=6.9-7.6, R_{close}=30-50km), on the bottom.

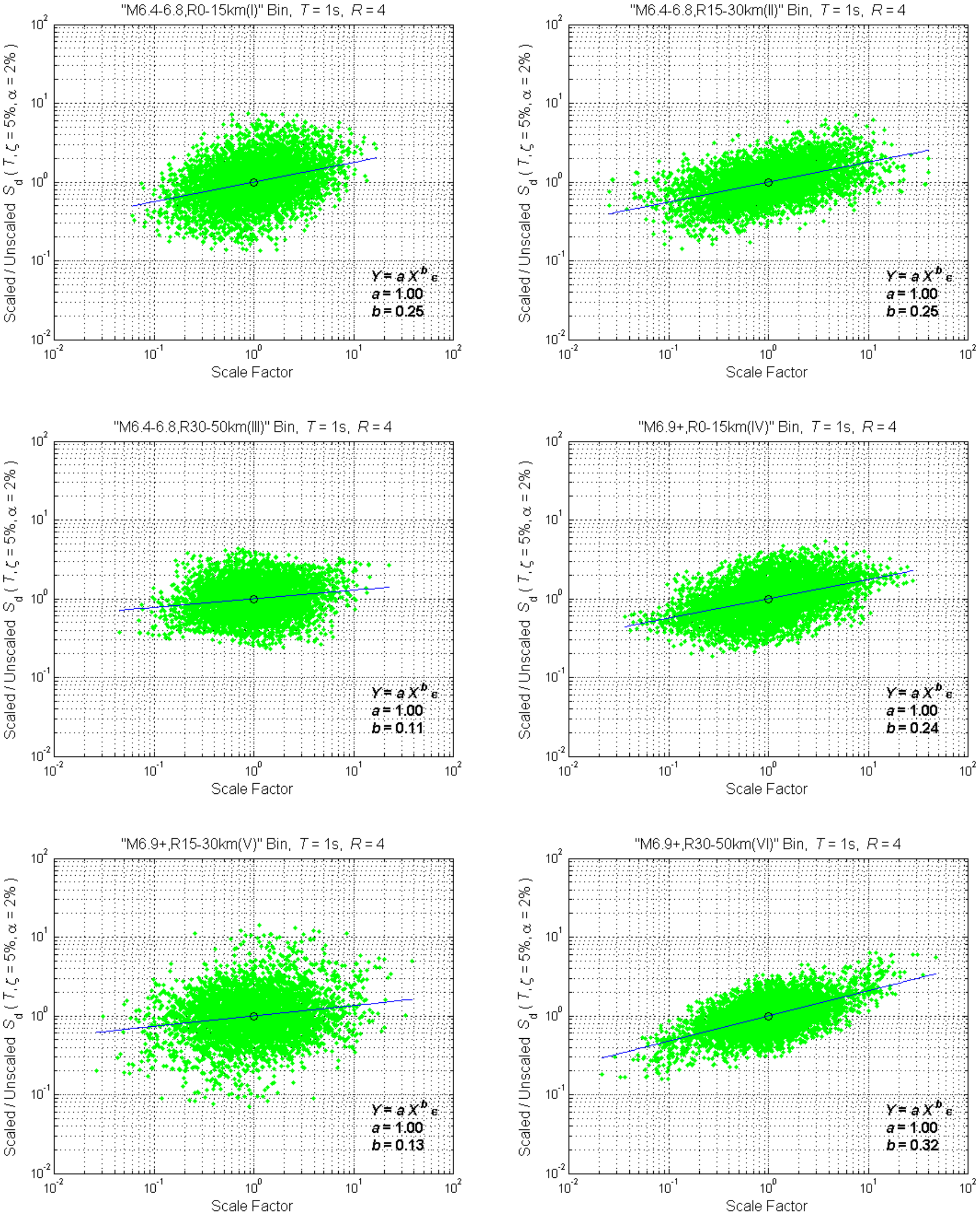

Figure A7. Intra-bin scaling results for a bilinear SDOF structure of period T=1sec and strength reduction factor R=4 for the six M_w-R_{close} bins of earthquake records considered. The analogous results for the Near-Source Bin are shown in Figure 11 of the main text.

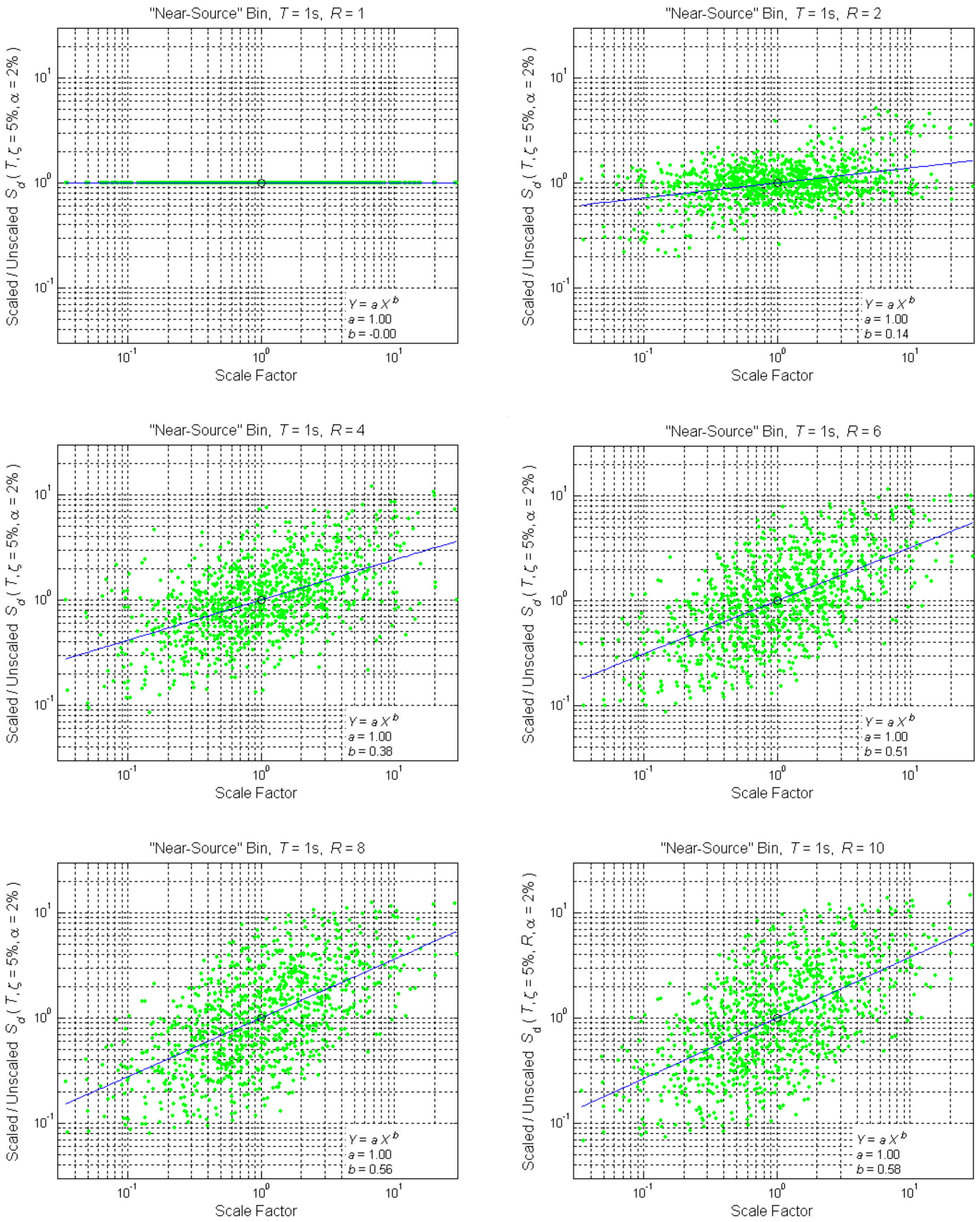

Figure A8. Intra-bin scaling results for the Near-Source Bin and a bilinear SDOF structure of period *T*=1sec but strength reduction factors ranging from *R*=1 to 10. The results for *R*=4 are the same as those shown in Figure 11 of the main text.

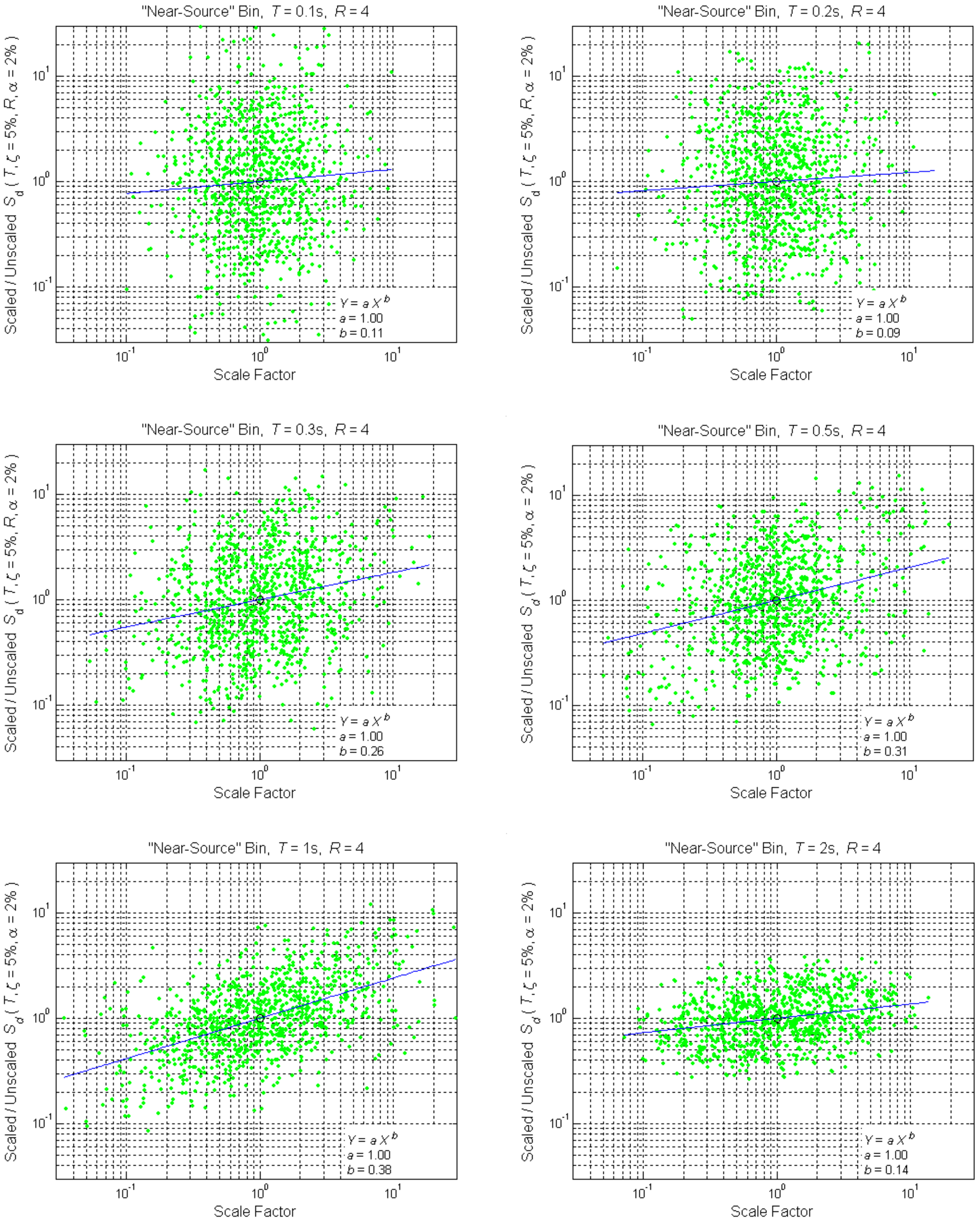

Figure A9(a). Intra-bin scaling results for the Near-Source Bin and a bilinear SDOF structure with periods ranging from T=0.1sec to 2sec and a strength reduction factor of R=4. The results for T=1sec are the same as those shown in Figure 11 of the main text.

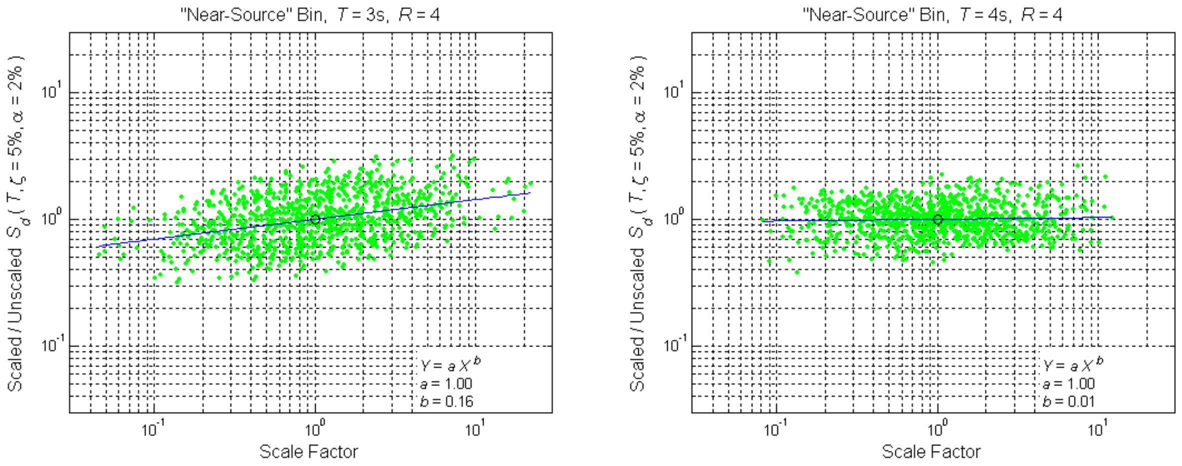

Figure A9(b). Intra-bin scaling results for the Near-Source Bin and a bilinear SDOF structure of period *T*=3sec or 4sec and a strength reduction factor of *R*=4. The results for periods less than 3sec are shown in Figure A9(a).

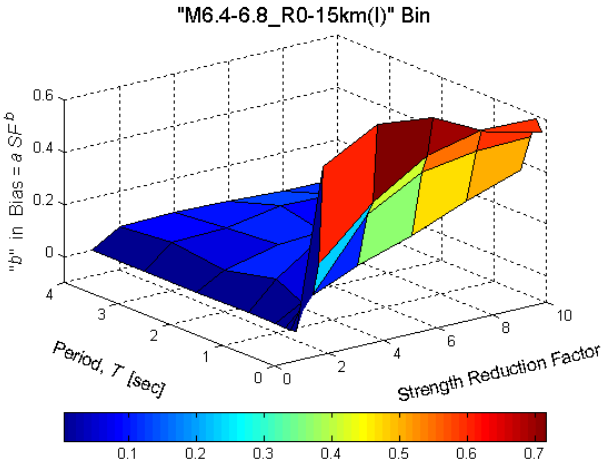

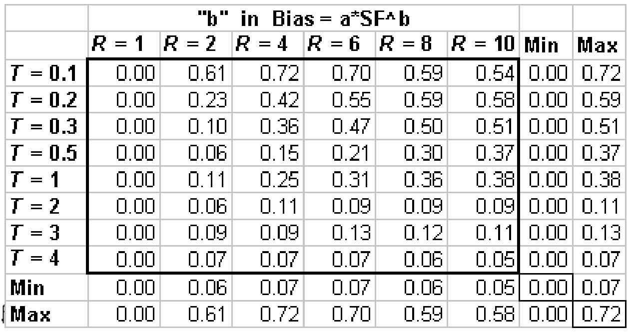

	"b" in Bias = a*SF^b							
	R = 1	*R* = 2	*R* = 4	*R* = 6	*R* = 8	*R* = 10	**Min**	**Max**
***T* = 0.1**	0.00	0.61	0.72	0.70	0.59	0.54	0.00	0.72
***T* = 0.2**	0.00	0.23	0.42	0.55	0.59	0.58	0.00	0.59
***T* = 0.3**	0.00	0.10	0.36	0.47	0.50	0.51	0.00	0.51
***T* = 0.5**	0.00	0.06	0.15	0.21	0.30	0.37	0.00	0.37
***T* = 1**	0.00	0.11	0.25	0.31	0.36	0.38	0.00	0.38
***T* = 2**	0.00	0.06	0.11	0.09	0.09	0.09	0.00	0.11
***T* = 3**	0.00	0.09	0.09	0.13	0.12	0.11	0.00	0.13
***T* = 4**	0.00	0.07	0.07	0.07	0.06	0.05	0.00	0.07
Min	0.00	0.06	0.07	0.07	0.06	0.05	0.00	0.07
Max	0.00	0.61	0.72	0.70	0.59	0.58	0.00	0.72

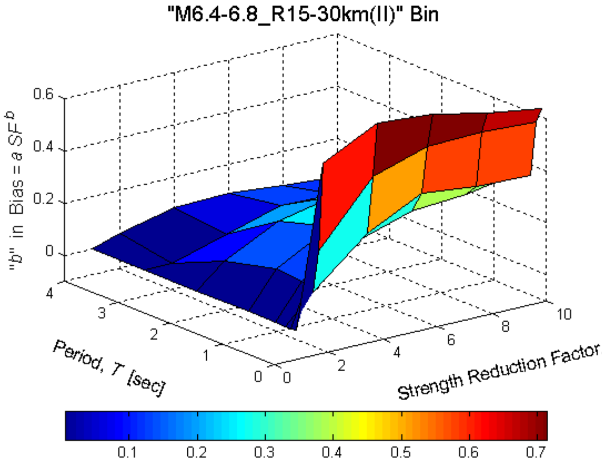

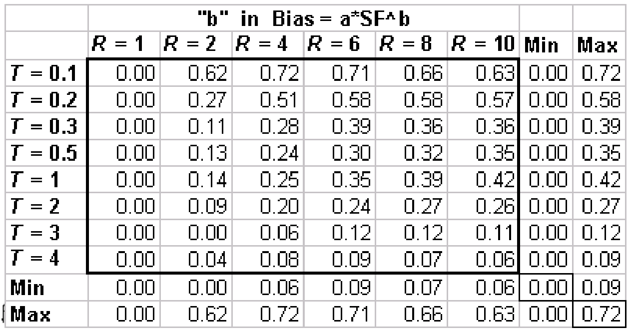

	"b" in Bias = a*SF^b							
	R = 1	*R* = 2	*R* = 4	*R* = 6	*R* = 8	*R* = 10	**Min**	**Max**
***T* = 0.1**	0.00	0.62	0.72	0.71	0.66	0.63	0.00	0.72
***T* = 0.2**	0.00	0.27	0.51	0.58	0.58	0.57	0.00	0.58
***T* = 0.3**	0.00	0.11	0.28	0.39	0.36	0.36	0.00	0.39
***T* = 0.5**	0.00	0.13	0.24	0.30	0.32	0.35	0.00	0.35
***T* = 1**	0.00	0.14	0.25	0.35	0.39	0.42	0.00	0.42
***T* = 2**	0.00	0.09	0.20	0.24	0.27	0.26	0.00	0.27
***T* = 3**	0.00	0.00	0.06	0.12	0.12	0.11	0.00	0.12
***T* = 4**	0.00	0.04	0.08	0.09	0.07	0.06	0.00	0.09
Min	0.00	0.00	0.06	0.09	0.07	0.06	0.00	0.09
Max	0.00	0.62	0.72	0.71	0.66	0.63	0.00	0.72

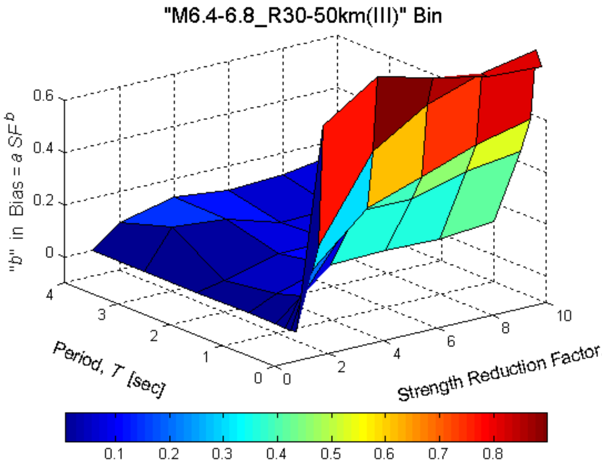

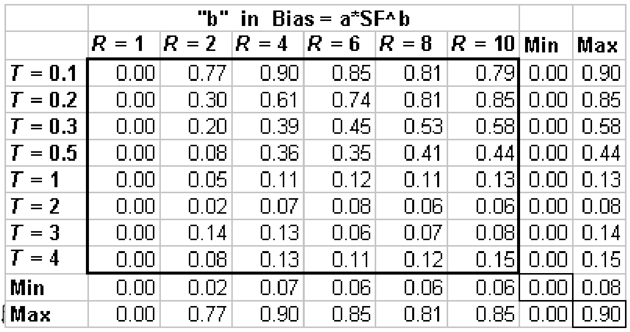

	"b" in Bias = a*SF^b							
	R = 1	*R* = 2	*R* = 4	*R* = 6	*R* = 8	*R* = 10	**Min**	**Max**
***T* = 0.1**	0.00	0.77	0.90	0.85	0.81	0.79	0.00	0.90
***T* = 0.2**	0.00	0.30	0.61	0.74	0.81	0.85	0.00	0.85
***T* = 0.3**	0.00	0.20	0.39	0.45	0.53	0.58	0.00	0.58
***T* = 0.5**	0.00	0.08	0.36	0.35	0.41	0.44	0.00	0.44
***T* = 1**	0.00	0.05	0.11	0.12	0.11	0.13	0.00	0.13
***T* = 2**	0.00	0.02	0.07	0.08	0.06	0.06	0.00	0.08
***T* = 3**	0.00	0.14	0.13	0.06	0.07	0.08	0.00	0.14
***T* = 4**	0.00	0.08	0.13	0.11	0.12	0.15	0.00	0.15
Min	0.00	0.02	0.07	0.06	0.06	0.06	0.00	0.08
Max	0.00	0.77	0.90	0.85	0.81	0.85	0.00	0.90

Figures A10-12. Intra-bin scaling results for Bins I-III and the range of SDOF periods and strength reduction factors considered. Note that the parameter "*a*" is found to equal unity for intra-bin scaling (and the SDOF structures), so a larger value of *b* translates to a larger bias for a given scale factor.

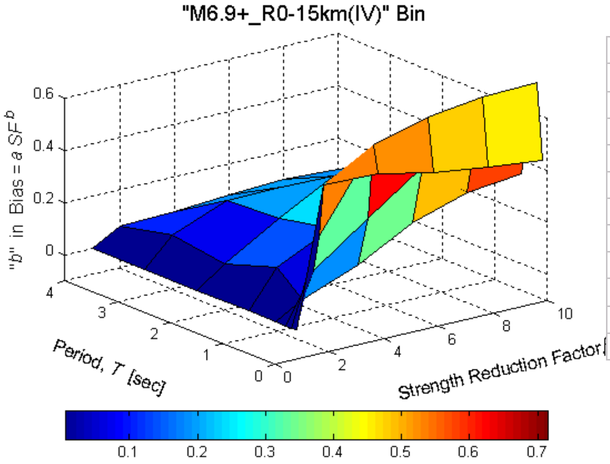

	"b" in Bias = a*SF^b							
	R = 1	*R* = 2	*R* = 4	*R* = 6	*R* = 8	*R* = 10	**Min**	**Max**
***T* = 0.1**	0.00	0.53	0.53	0.48	0.45	0.43	0.00	0.53
***T* = 0.2**	0.00	0.33	0.63	0.69	0.71	0.72	0.00	0.72
***T* = 0.3**	0.00	0.19	0.34	0.48	0.58	0.61	0.00	0.61
***T* = 0.5**	0.00	0.06	0.14	0.25	0.32	0.34	0.00	0.34
***T* = 1**	0.00	0.14	0.24	0.32	0.33	0.35	0.00	0.35
***T* = 2**	0.00	0.08	0.20	0.32	0.37	0.40	0.00	0.40
***T* = 3**	0.00	0.11	0.19	0.19	0.18	0.19	0.00	0.19
***T* = 4**	0.00	0.06	0.07	0.08	0.09	0.08	0.00	0.09
Min	0.00	0.06	0.07	0.08	0.09	0.08	0.00	0.09
Max	0.00	0.53	0.63	0.69	0.71	0.72	0.00	0.72

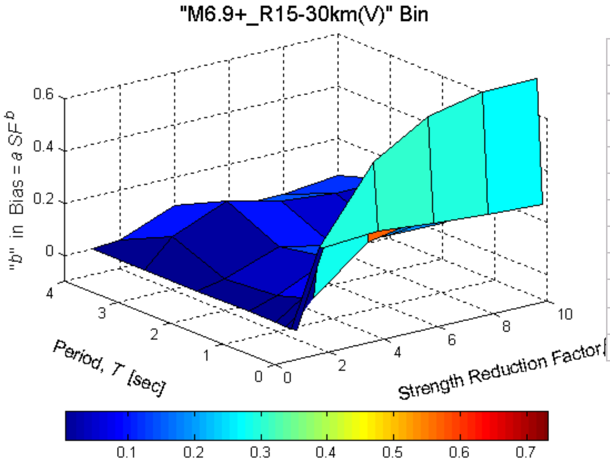

	"b" in Bias = a*SF^b							
	R = 1	*R* = 2	*R* = 4	*R* = 6	*R* = 8	*R* = 10	**Min**	**Max**
***T* = 0.1**	0.00	0.29	0.31	0.29	0.27	0.26	0.00	0.31
***T* = 0.2**	0.00	0.29	0.57	0.69	0.74	0.74	0.00	0.74
***T* = 0.3**	0.00	0.08	0.25	0.29	0.42	0.48	0.00	0.48
***T* = 0.5**	0.00	0.07	0.25	0.29	0.38	0.41	0.00	0.41
***T* = 1**	0.00	0.04	0.13	0.19	0.19	0.20	0.00	0.20
***T* = 2**	0.00	0.02	0.09	0.05	0.04	0.04	0.00	0.09
***T* = 3**	0.00	0.10	0.19	0.14	0.12	0.12	0.00	0.19
***T* = 4**	0.00	0.01	0.09	0.03	0.04	0.06	0.00	0.09
Min	0.00	0.01	0.09	0.03	0.04	0.04	0.00	0.09
Max	0.00	0.29	0.57	0.69	0.74	0.74	0.00	0.74

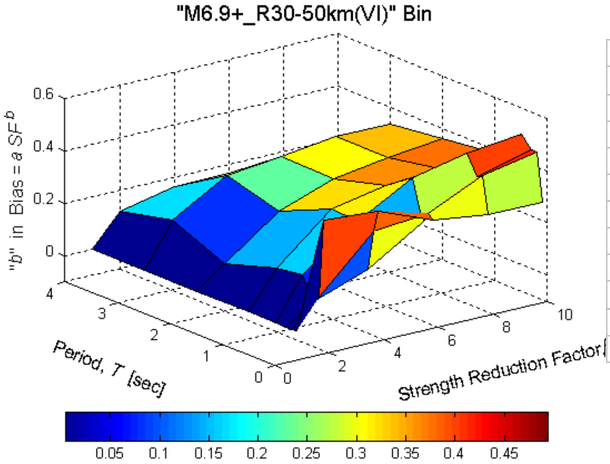

	"b" in Bias = a*SF^b							
	R = 1	*R* = 2	*R* = 4	*R* = 6	*R* = 8	*R* = 10	**Min**	**Max**
***T* = 0.1**	0.00	0.40	0.38	0.30	0.27	0.27	0.00	0.40
***T* = 0.2**	0.00	0.10	0.30	0.32	0.41	0.45	0.00	0.45
***T* = 0.3**	0.00	0.07	0.14	0.28	0.40	0.45	0.00	0.45
***T* = 0.5**	0.00	0.16	0.31	0.43	0.48	0.50	0.00	0.50
***T* = 1**	0.00	0.14	0.32	0.36	0.38	0.39	0.00	0.39
***T* = 2**	0.00	0.08	0.23	0.30	0.34	0.36	0.00	0.36
***T* = 3**	0.00	0.16	0.29	0.31	0.34	0.34	0.00	0.34
***T* = 4**	0.00	0.12	0.17	0.17	0.13	0.13	0.00	0.17
Min	0.00	0.07	0.14	0.17	0.13	0.13	0.00	0.17
Max	0.00	0.40	0.38	0.43	0.48	0.50	0.00	0.50

Figure A13-15. Intra-bin scaling results for Bins IV-VI and the range of SDOF periods and strength reduction factors considered. Note that the parameter "*a*" is found to equal unity for intra-bin scaling (and the SDOF structures), so a larger value of *b* translates to a larger bias for a given scale factor.

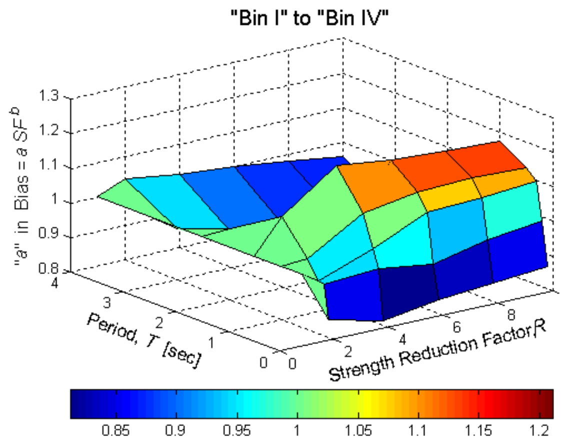

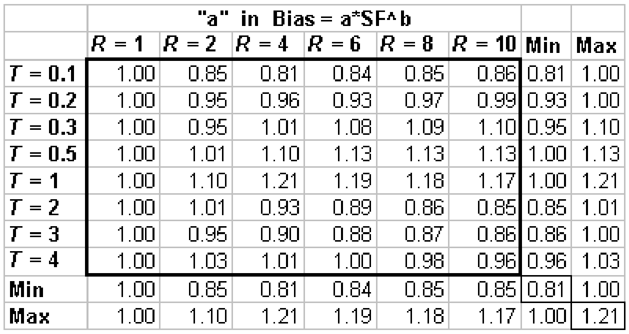

	"a" in Bias = a*SF^b							
	R = 1	*R* = 2	*R* = 4	*R* = 6	*R* = 8	*R* = 10	Min	Max
T = 0.1	1.00	0.85	0.81	0.84	0.85	0.86	0.81	1.00
T = 0.2	1.00	0.95	0.96	0.93	0.97	0.99	0.93	1.00
T = 0.3	1.00	0.95	1.01	1.08	1.09	1.10	0.95	1.10
T = 0.5	1.00	1.01	1.10	1.13	1.13	1.13	1.00	1.13
T = 1	1.00	1.10	1.21	1.19	1.18	1.17	1.00	1.21
T = 2	1.00	1.01	0.93	0.89	0.86	0.85	0.85	1.01
T = 3	1.00	0.95	0.90	0.88	0.87	0.86	0.86	1.00
T = 4	1.00	1.03	1.01	1.00	0.98	0.96	0.96	1.03
Min	1.00	0.85	0.81	0.84	0.85	0.85	0.81	1.00
Max	1.00	1.10	1.21	1.19	1.18	1.17	1.00	1.21

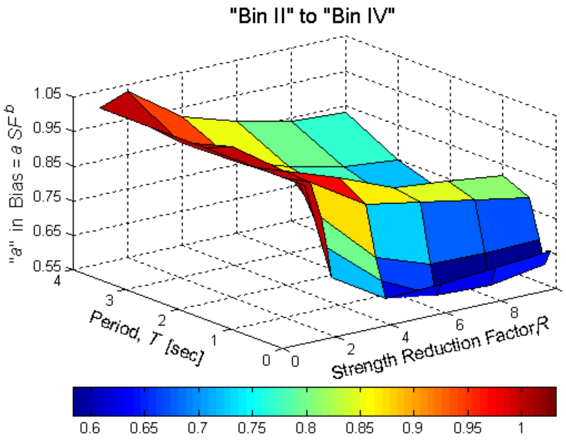

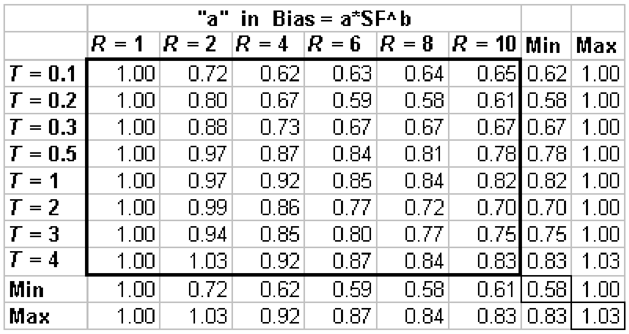

	"a" in Bias = a*SF^b							
	R = 1	*R* = 2	*R* = 4	*R* = 6	*R* = 8	*R* = 10	Min	Max
T = 0.1	1.00	0.72	0.62	0.63	0.64	0.65	0.62	1.00
T = 0.2	1.00	0.80	0.67	0.59	0.58	0.61	0.58	1.00
T = 0.3	1.00	0.88	0.73	0.67	0.67	0.67	0.67	1.00
T = 0.5	1.00	0.97	0.87	0.84	0.81	0.78	0.78	1.00
T = 1	1.00	0.97	0.92	0.85	0.84	0.82	0.82	1.00
T = 2	1.00	0.99	0.86	0.77	0.72	0.70	0.70	1.00
T = 3	1.00	0.94	0.85	0.80	0.77	0.75	0.75	1.00
T = 4	1.00	1.03	0.92	0.87	0.84	0.83	0.83	1.03
Min	1.00	0.72	0.62	0.59	0.58	0.61	0.58	1.00
Max	1.00	1.03	0.92	0.87	0.84	0.83	0.83	1.03

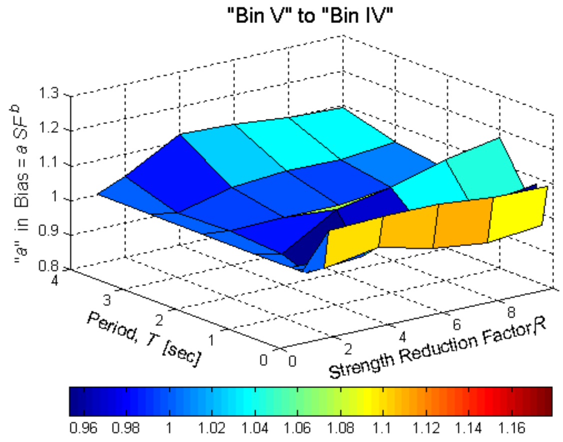

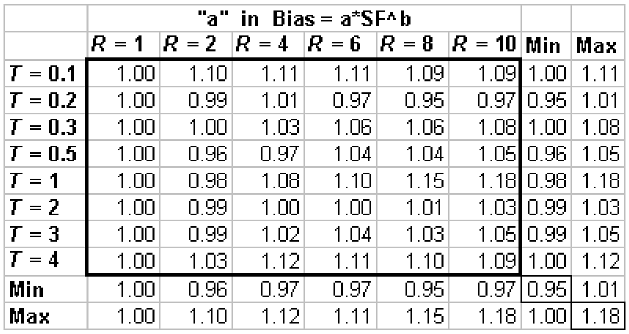

	"a" in Bias = a*SF^b							
	R = 1	*R* = 2	*R* = 4	*R* = 6	*R* = 8	*R* = 10	Min	Max
T = 0.1	1.00	1.10	1.11	1.11	1.09	1.09	1.00	1.11
T = 0.2	1.00	0.99	1.01	0.97	0.95	0.97	0.95	1.01
T = 0.3	1.00	1.00	1.03	1.06	1.06	1.08	1.00	1.08
T = 0.5	1.00	0.96	0.97	1.04	1.04	1.05	0.96	1.05
T = 1	1.00	0.98	1.08	1.10	1.15	1.18	0.98	1.18
T = 2	1.00	0.99	1.00	1.00	1.01	1.03	0.99	1.03
T = 3	1.00	0.99	1.02	1.04	1.03	1.05	0.99	1.05
T = 4	1.00	1.03	1.12	1.11	1.10	1.09	1.00	1.12
Min	1.00	0.96	0.97	0.97	0.95	0.97	0.95	1.01
Max	1.00	1.10	1.12	1.11	1.15	1.18	1.00	1.18

Figures A16-18. Inter-bin scaling results for the Bin I (M_w=6.4-6.8, R_{close}=0-15km) to Bin IV (M_w=6.9-7.6, R_{close}=0-15km), the Bin II (M_w=6.4-6.8, R_{close}=15-30km) to Bin IV, and the Bin V (M_w=6.9-7.6, R_{close}=15-30km) to Bin IV scenarios. The corresponding values of "*b*" are very similar to those observed for intra-bin scaling within the target bin (shown in Figure A13).

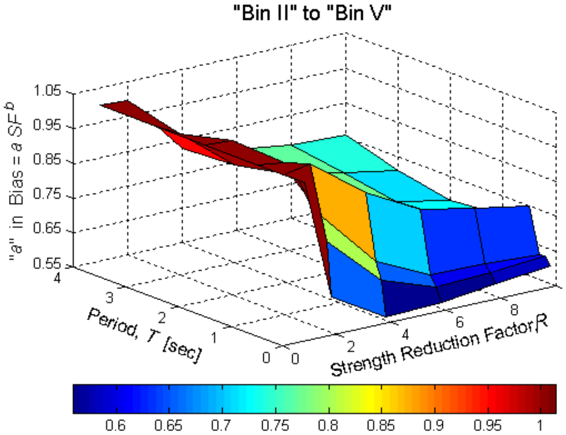
"Bin II" to "Bin V"

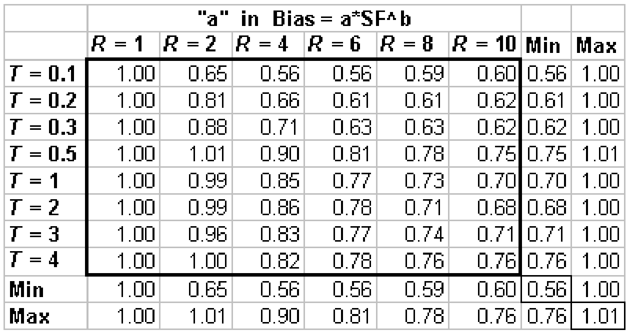

	"a" in Bias = a*SF^b							
	R = 1	*R* = 2	*R* = 4	*R* = 6	*R* = 8	*R* = 10	Min	Max
T = 0.1	1.00	0.65	0.56	0.56	0.59	0.60	0.56	1.00
T = 0.2	1.00	0.81	0.66	0.61	0.61	0.62	0.61	1.00
T = 0.3	1.00	0.88	0.71	0.63	0.63	0.62	0.62	1.00
T = 0.5	1.00	1.01	0.90	0.81	0.78	0.75	0.75	1.01
T = 1	1.00	0.99	0.85	0.77	0.73	0.70	0.70	1.00
T = 2	1.00	0.99	0.86	0.78	0.71	0.68	0.68	1.00
T = 3	1.00	0.96	0.83	0.77	0.74	0.71	0.71	1.00
T = 4	1.00	1.00	0.82	0.78	0.76	0.76	0.76	1.00
Min	1.00	0.65	0.56	0.56	0.59	0.60	0.56	1.00
Max	1.00	1.01	0.90	0.81	0.78	0.76	0.76	1.01

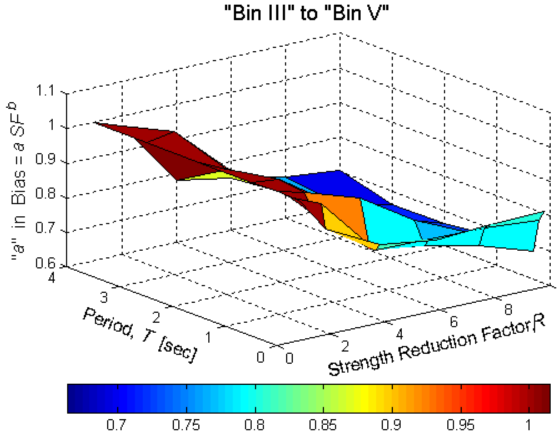
"Bin III" to "Bin V"

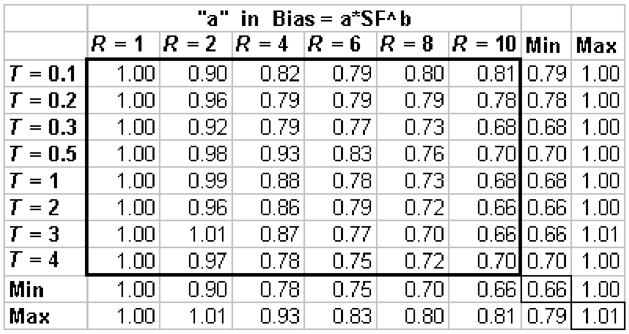

	"a" in Bias = a*SF^b							
	R = 1	*R* = 2	*R* = 4	*R* = 6	*R* = 8	*R* = 10	Min	Max
T = 0.1	1.00	0.90	0.82	0.79	0.80	0.81	0.79	1.00
T = 0.2	1.00	0.96	0.79	0.79	0.79	0.78	0.78	1.00
T = 0.3	1.00	0.92	0.79	0.77	0.73	0.68	0.68	1.00
T = 0.5	1.00	0.98	0.93	0.83	0.76	0.70	0.70	1.00
T = 1	1.00	0.99	0.88	0.78	0.73	0.68	0.68	1.00
T = 2	1.00	0.96	0.86	0.79	0.72	0.66	0.66	1.00
T = 3	1.00	1.01	0.87	0.77	0.70	0.66	0.66	1.01
T = 4	1.00	0.97	0.78	0.75	0.72	0.70	0.70	1.00
Min	1.00	0.90	0.78	0.75	0.70	0.66	0.66	1.00
Max	1.00	1.01	0.93	0.83	0.80	0.81	0.79	1.01

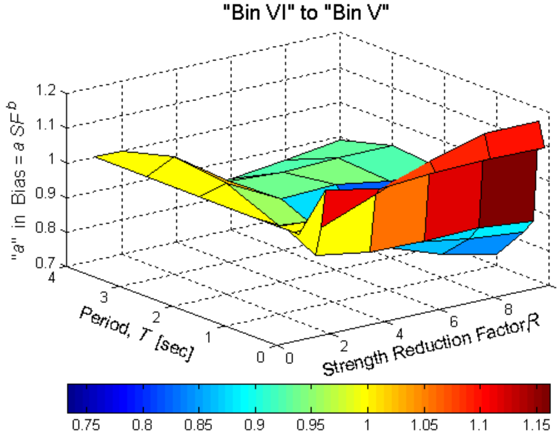
"Bin VI" to "Bin V"

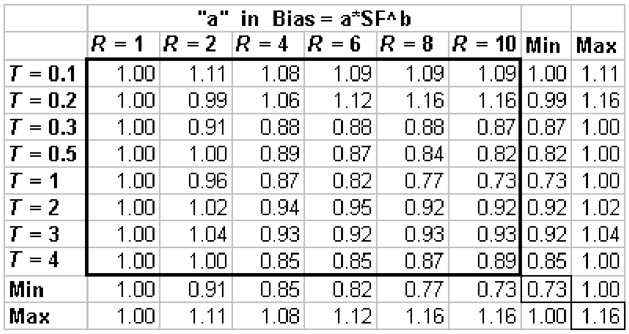

	"a" in Bias = a*SF^b							
	R = 1	*R* = 2	*R* = 4	*R* = 6	*R* = 8	*R* = 10	Min	Max
T = 0.1	1.00	1.11	1.08	1.09	1.09	1.09	1.00	1.11
T = 0.2	1.00	0.99	1.06	1.12	1.16	1.16	0.99	1.16
T = 0.3	1.00	0.91	0.88	0.88	0.88	0.87	0.87	1.00
T = 0.5	1.00	1.00	0.89	0.87	0.84	0.82	0.82	1.00
T = 1	1.00	0.96	0.87	0.82	0.77	0.73	0.73	1.00
T = 2	1.00	1.02	0.94	0.95	0.92	0.92	0.92	1.02
T = 3	1.00	1.04	0.93	0.92	0.93	0.93	0.92	1.04
T = 4	1.00	1.00	0.85	0.85	0.87	0.89	0.85	1.00
Min	1.00	0.91	0.85	0.82	0.77	0.73	0.73	1.00
Max	1.00	1.11	1.08	1.12	1.16	1.16	1.00	1.16

Figures A19-21. Inter-bin scaling results for the Bin II (M_w=6.4-6.8, R_{close}=15-30km) to Bin V (M_w=6.9-7.6, R_{close}=15-30km), the Bin III (M_w=6.4-6.8, R_{close}=30-50km) to Bin V, and the Bin VI (M_w=6.9-7.6, R_{close}=30-50km) to Bin V scenarios. The corresponding values of "*b*" are very similar to those observed for intra-bin scaling within the target bin (shown in Figure A14).

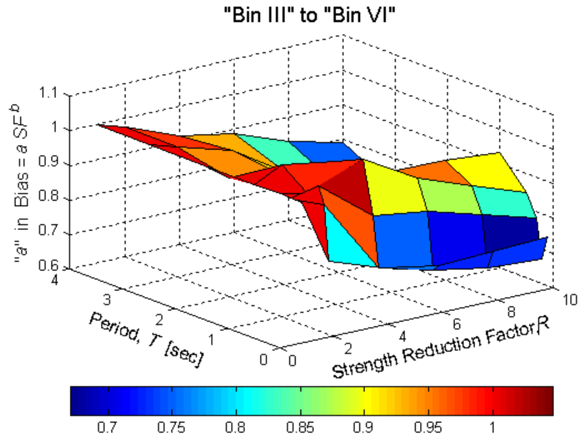

	"a" in Bias = a*SF^b							
	R = 1	*R* = 2	*R* = 4	*R* = 6	*R* = 8	*R* = 10	**Min**	**Max**
***T* = 0.1**	1.00	0.81	0.76	0.73	0.73	0.74	0.73	1.00
***T* = 0.2**	1.00	0.97	0.75	0.71	0.68	0.67	0.67	1.00
***T* = 0.3**	1.00	1.02	0.90	0.87	0.83	0.79	0.79	1.02
***T* = 0.5**	1.00	0.98	1.05	0.96	0.90	0.85	0.85	1.05
***T* = 1**	1.00	1.04	1.01	0.95	0.95	0.93	0.93	1.04
***T* = 2**	1.00	0.94	0.92	0.84	0.78	0.72	0.72	1.00
***T* = 3**	1.00	0.98	0.93	0.83	0.75	0.71	0.71	1.00
***T* = 4**	1.00	0.98	0.91	0.88	0.83	0.79	0.79	1.00
Min	1.00	0.81	0.75	0.71	0.68	0.67	0.67	1.00
Max	1.00	1.04	1.05	0.96	0.95	0.93	0.93	1.05

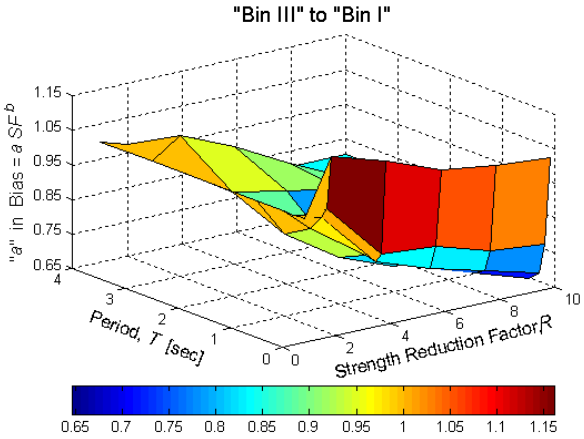

	R = 1	*R* = 2	*R* = 4	*R* = 6	*R* = 8	*R* = 10	**Min**	**Max**
***T* = 0.1**	1.00	1.16	1.11	1.05	1.03	1.02	1.00	1.16
***T* = 0.2**	1.00	1.01	0.84	0.83	0.78	0.76	0.76	1.01
***T* = 0.3**	1.00	0.97	0.81	0.76	0.72	0.67	0.67	1.00
***T* = 0.5**	1.00	0.93	0.82	0.76	0.70	0.65	0.65	1.00
***T* = 1**	1.00	0.89	0.79	0.72	0.71	0.69	0.69	1.00
***T* = 2**	1.00	0.95	0.92	0.89	0.84	0.81	0.81	1.00
***T* = 3**	1.00	1.06	0.99	0.91	0.83	0.81	0.81	1.06
***T* = 4**	1.00	0.97	0.86	0.84	0.81	0.80	0.80	1.00
Min	1.00	0.89	0.79	0.72	0.70	0.65	0.65	1.00
Max	1.00	1.16	1.11	1.05	1.03	1.02	1.00	1.16

Figures A22-23. Inter-bin scaling results for the Bin III (M_w=6.4-6.8, R_{close}=30-50km) to Bin VI (M_w=6.9-7.6, R_{close}=30-50km) and the Bin III to Bin I (M_w=6.4-6.8, R_{close}=0-15km) scenarios. The corresponding values of "*b*" are very similar to those observed for intra-bin scaling within the target bin (shown in Figures A15 and A10, respectively).

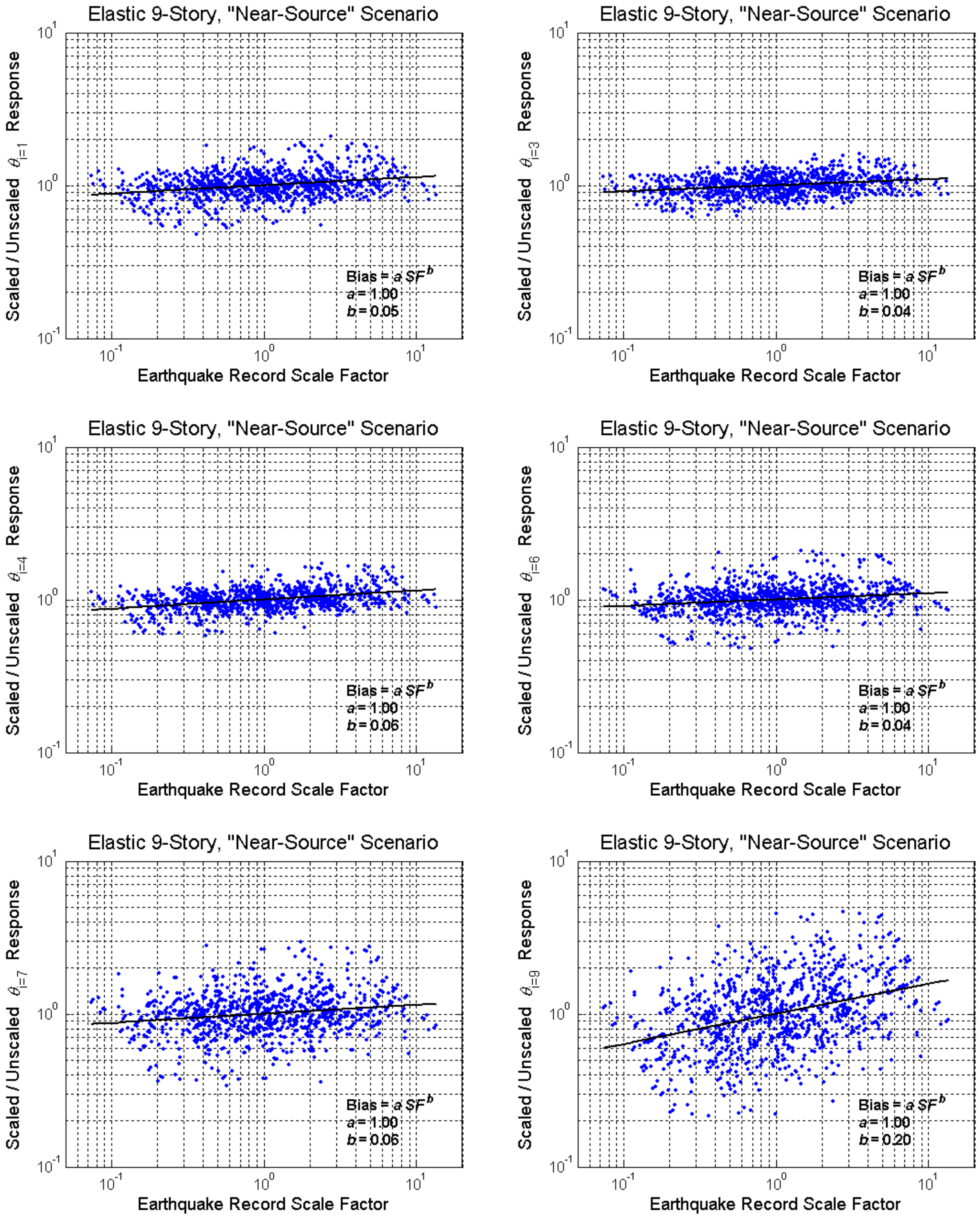

Figure A24. Intra-bin scaling results in terms of the peak inter-story drift ratios (θ_i) at the 1st, 3rd, 4th, 6th, 7th, and 9th stories of the elastic model of the 9-story building considered. The results for the other 3 of the 9 stories are given in the main text (Figure 30).

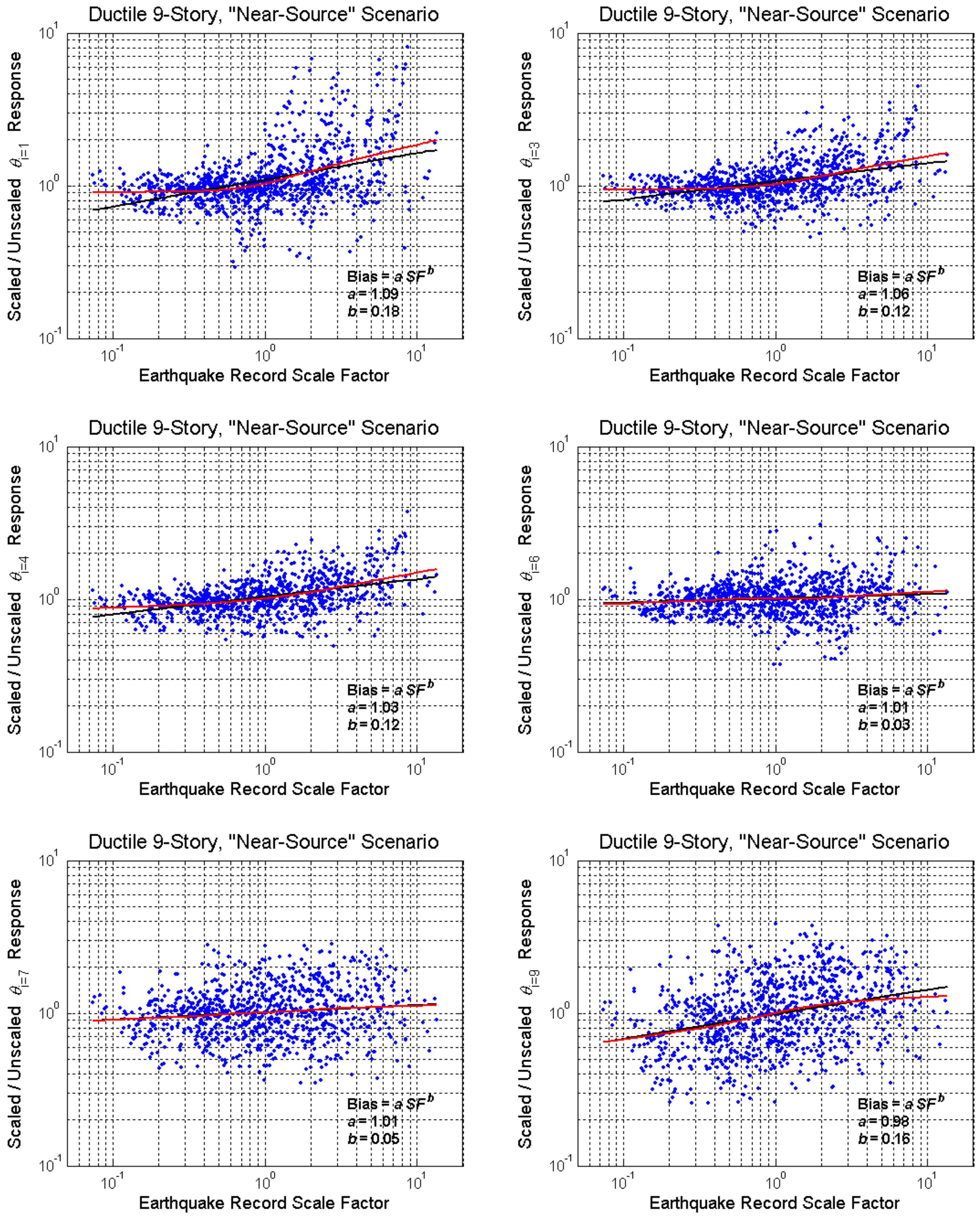

Figure A25. Intra-bin scaling results in terms of the peak inter-story drift ratios (θ_i) at the 1st, 3rd, 4th, 6th, 7th, and 9th stories of the *ductile* model of the 9-story building considered. The results for the other 3 of the 9 stories are given in the main text (Figure 30).

Post-Elastic Response of Structures to Synthetic Ground Motions

By Paolo Bazzurro[1]*, Brian Sjoberg*[1]*, and Nicolas Luco*[1]

Abstract

When real recordings for a specific earthquake scenario are scarce, engineers often use synthetic records generated by seismologists as input to nonlinear dynamic analyses of both existing and new structures. This practice has sometimes generated concerns among practitioners regarding the accuracy of the nonlinear response obtained using simulated ground motions. This article presents a case study where the issue of structural response accuracy is investigated for seven simulation techniques whose derived structural responses are statistically compared against the "correct" answer provided by real accelerograms. The example involves seven suites of synthetic records that emulate real ground motions recorded at 20 stations located within 20km from the Northridge fault rupture. The results show that six out of seven simulation methods appear to be biased, especially in the short period range, both in the linear elastic and in the nonlinear post-elastic regimes. The tendency of these synthetic records is to create linear responses that are more severe than those from the real counterparts in the short period range. This tendency is reversed in the nonlinear regime where responses from synthetic records in the same short period range tend to be less severe than those from real accelerograms. Synthetic records seem to be especially benign in relatively weak and stiff structures. Simulated records also tend to produce nonlinear responses that are less variable than those caused by real records in the short period range and more variable in the long period range. This discrepancy should be taken into consideration when using synthetic records for assessing, for example, the safety of a structure against collapse. The results mentioned above were found to be stable to the sensitivity performed on different parameters and assumptions of the analyses. It should be emphasized, however, that these conclusions were found from one case study only and their validity may not apply to other cases or to different simulation techniques. More research is needed to establish the range of applicability of these findings.

1.0 Introduction

Consideration of the post-elastic dynamic response of structures is of fundamental importance in earthquake engineering as most buildings are expected to deform beyond their linear elastic limit during intense ground shaking. In recent years, the computation of a structure's dynamic inelastic response to an earthquake event has been done more frequently than ever before via time-history analysis. Ideally, the input ground motions to such analyses are past recordings of earthquakes with similar characteristics (e.g. magnitude, distance, and fault mechanism) to the earthquake scenarios that dominate the seismic hazard at the structure's site. Unfortunately, real recordings of ground motions with suitable characteristics are often scarce or non-existent. This shortage of adequate ground motions has led to the engineering practice of modifying real accelerograms to meet a prescribed ground shaking intensity level or target elastic response spectrum. Techniques often used involve scaling the amplitude of real accelerograms or adjusting their frequency content to match a target spectrum. The alternative to modifying real accelerograms is to use completely synthetic (also referred to as simulated) earthquake

---

[1] AIR Worldwide Co., 388 Market Street, Suite 610, San Francisco, CA 94111

time-histories, which are founded upon the basic physical principles controlling fault rupture and seismic wave propagation from source to site. This study is concerned with this latter alternative and the effect that using simulated time-histories may have on seismic performance assessment.

Like the practice of modifying real accelerograms by amplitude scaling or spectrum matching, the use of synthetic time histories has caused concern amongst some engineers. We interpret these concerns here as being twofold:

- Simulated ground motion records may not produce, on average, the same nonlinear structural response as real ground motion recordings with the same nominal intensity. If there were a systematic deviation (sometimes referred to here as bias for conciseness sake), then engineers may either not use simulated records or account for the bias in their seismic performance analyses when using synthetic rather than real recordings.
- The record-to-record variability of nonlinear structural response produced by synthetic and real records with otherwise similar characteristics may not be comparable. This variability has an impact on how likely extreme values of structural responses are and, therefore, on the estimates of probability of occurrence of extreme events such as collapse.

We investigate these issues by comparing the nonlinear response statistics of nonlinear single-degree-of-freedom (SDOF) oscillators of different structural periods and yield strengths to both real and simulated records. In particular, we consider *one real* ground motion dataset, whose response statistics are used as a benchmark, and *seven synthetic* ground motion datasets. A direct comparison of response statistics is legitimate because the seven simulated datasets were developed to match the same earthquake and site conditions of the real recordings.

2.0 Description of the Synthetic and Real Ground Motion Datasets

The simulated ground motion time histories that are used here were originally developed as part of the PEER K201 project entitled "*Ground Motions for the Treasure Island National Geotechnical Experimental Site*". The K201 project compares elastic response spectral values from simulated ground motions with those from real recordings of past earthquakes for the purpose of validating various ground motion simulation methods. The following seismologists developed the synthetic time histories used in the K201 project and in this project:

1. Igor A. Beresnev[2];.
2. Douglas Dreger[3];
3. Alexander A. Gusev[4] *et al.*;

---

[2] Associate Professor of Geophysics, Iowa State University, Ames, Iowa.

[3] Associate Professor of Geophysics, University of California, Berkeley. California.

[4] Head, Laboratory of Seismology, Institute of Volcanic Geology and Geochemistry, Petropavlovsk-Kamchatsky, Russia.

4. Lawrence Hutchings[5] *et al*. (denoted as LLNL hereafter);
5. Walter Silva[6];
6. Paul G. Somerville[7] *et al*. (denoted as URS hereafter);
7. Yuehua Zeng[8].

Note that both Dreger and Zeng, based on the preliminary results from this study, updated their dataset of synthetic motions with respect to those used in the K201 Project.

The seven datasets contain simulated time histories that are intended to reproduce those generated by the M6.7 1994 Northridge earthquake at 20 near-field stations that ranged in distance from 5.2km to 19.1km (Table 1). An eighth dataset contains the real recordings at the same 20 stations. Here we used only the horizontal components, whereas the vertical components are neglected. Table 2 summarizes the details about the time histories provided by each seismologist. In four (i.e., Dreger, Gusev, URS, and Zeng) out of seven cases, the simulated recordings consisted of both horizontal component time histories for each of the 20 stations. Two horizontal components were also available in the LLNL dataset but only for 12 stations. Beresnev and Silva did not provide separate horizontal components but rather a single “average” time history of horizontal ground motion at each one of the 20 stations. Therefore, a total of 224 synthetic horizontal ground motion time histories were considered as input to the nonlinear dynamic analyses carried out in this study.

As discussed above, the available suite of simulated input time histories is partially incomplete and somewhat heterogeneous. Despite this drawback, we intended as much as possible to enable a legitimate comparison of nonlinear responses that encompasses all seven datasets. To achieve this goal, for five datasets (i.e., Dreger, Gusev, LLNL, URS, and Zeng) we computed the spectral responses for the two horizontal components at each station and combined them into an “average” spectral response. For the remaining two datasets (i.e., Beresnev and Silva) we computed the responses to the “average” time history provided by the developers. In the former case the average response was calculated using two different averaging methods, the geometric mean and the root-mean-square (rms) value. For nearly all subsequent comparative analyses, the rms value was used to describe the station-by-station structural response for each synthetic ground motion dataset that contained separate components. This alternative was selected because it is consistent with the methodology used in the generation of the average ground motion time histories. The geometric mean value was used only secondarily to assess whether the trends in the nonlinear responses observed for each modeler would be dependent on the particular component averaging method. The comparison of the results obtained with the two averaging methods is reported in Section 4.2.

---

[5] Lawrence Livermore National Laboratory, Livermore, California.

[6] Pacific Engineering & Analysis, El Cerrito, California.

[7] URS Corporation, Pasadena, California.

[8] Research Associate Professor, Mackay School of Earth and Environmental Sciences, University of Nevada, Reno, Nevada.

With reference to Table 1, the usable bandwidth of the *real records* exceeded 0.1 – 4.0 seconds for all but three recording stations (KAT, LA0, PAR), since the highpass (HP) and lowpass (LP) corner frequencies of the causal Butterworth filter used to process such records were less than 0.2 Hz and greater than 12.5 Hz, respectively[9]. The usable bandwidth of a record processed using a causal Butterworth 4-pole filter, such as that used for these records, is recommended to be between 1/1.25 times the LP frequency and 1.25 times the HP frequency due to the significant reduction imposed by the filter in the neighborhood of the corner frequencies (Abrahamson and Silva, 1997, PEER documentation – http://peer.berkeley.edu/smcat/process.html). Therefore, for records filtered with a high-pass frequency of 0.2 Hz, caution must be exercised when investigating the response of a structure with a period greater than 1/(0.2 Hz * 1.25) = 4.0s. The reader should also keep in mind that the recommendation on the usable bandwidth reported above (and below for the synthetic records) was provided with no specific attention to the use of such records as input to structural *nonlinear* dynamic analyses. The effective structural period of vibration may significantly lengthen outside the suggested usable bandwidth of the record as the damage severity progresses. In this study we have not made any attempt to revisit the adequacy of such recommendations in this light. This topic deserves further research that is beyond the scope of this study.

For the synthetic records, we limited our analyses to the usable bandwidth specified by the developers to ensure that nonlinear response statistics were computed only within the intended range of applicability of the ground motion simulation model. Table 2 lists the usable period range of each model, as well as a summary of the type and number of records provided in each dataset that were discussed earlier. Note that all models are usable up to 4.0s with the exception of the LLNL model, which is limited to 2.0s. For the interested readers, a brief description of the methodology used by each group of seismologists to generate the synthetic time-histories is given in Appendix A. These descriptions were provided directly by the authors of each model.

---

[9] The HP corner frequency was not available in three cases and the LP corner frequency in eight cases.

Station Name	Symbol	Distance (km)	HW/FW	HP (Hz)	LP (Hz)
Arleta	ARL	8.66	NU	0.12	23
Canoga Park, Topanga Canyon	CNP	14.70	HW	0.05	30
Jensen Filter Plant	JEN	5.43	HW	0.08	unknown
Simi Valley - Katherine	KAT	13.42	HW	0.5	30
LA 00	LA0	19.07	NU	0.3	unknown
LA Dam	LDM	5.92	HW	0.1	unknown
Newhall	NWH	5.92	FW	0.12	23
Pacoima Dam	PAC	7.01	FW	0.16	23
Pardee - SCE	PAR	7.46	FW	0.5	20
Pacoima Kagel Canyon	PKC	7.26	NU	0.14	23
Sun Valley - Roscoe	RO3	10.05	NU	0.1	30
Rinaldi Receiving Station	RRS	6.50	HW	unknown	unknown
Sylmar Converter Stn. East	SCE	5.19	HW	unknown	unknown
Sylmar Converter Stn.	SCS	5.35	HW	unknown	unknown
Sepulveda VA	SPV	8.44	HW	0.1	unknown
Santa Susana	SSU	16.74	HW	0.2	unknown
Northridge - Saticoy	STC	12.09	HW	0.1	30
Sylmar Hospital	SYL	5.30	FW	0.12	23
Tarzana - Cedar Hill	TAR	15.60	NU	0.1	23
Newhall - W. Pico Canyon	WPI	5.48	NU	0.05	30

Table 1: List of the twenty recording stations for the 1994 Northridge earthquake accelerograms, including the Butterworth filter corner frequencies for the recorded accelerograms. Legend: HW = hanging wall, FW = foot wall, NU = neutral, HP = high-pass corner frequency, LP = low-pass corner frequency.

Modeler	Components	# Records	Usable Bandwidth
Beresnev	Average	20	0.1s – 4.0s
Dreger	Separate	40	0.1s – 4.0s
Gusev	Separate	40	0.1s – 4.0s
LLNL	Separate	24	0.1s – 2.0s
Silva	Average	20	0.1s – 4.0s
URS	Separate	40	0.1s – 4.0s
Zeng	Separate	40	0.1s – 4.0s
Real	Separate	40	0.1s – 4.0s

Table 2: Summary of synthetic ground motion datasets.

3.0 Description of the SDOF Structures

The eight datasets of records described in the previous section were applied to 46 5%-damped nonlinear Single-Degree-of-Freedom (SDOF) oscillators with natural periods ranging from 0.1 to 4.0s. The backbone force-deformation curve was bilinear with 2% post-yield hardening and a hysteretic rule that had no degradation of either strength or stiffness. The selected period range, which encompasses the fundamental periods of typical engineering structures, is, with the exception of the LLNL dataset, within the usable bandwidth of each ground motion model (see Table 2).

To ensure a response that ranged from mildly inelastic to severely inelastic, we selected five "strength" levels for the SDOF system at each oscillator period. In addition, we also included in this study the elastic response case both for completeness and for checking purposes. The nominal strength levels of the SDOF oscillators were set as a fraction of peak elastic base shear, which follows the common seismic design practice of reducing the structural strength for a ductile structure by a force reduction factor, R. The five selected strength levels are characterized by R values equal to two (mildly inelastic), four, six, eight, and ten (severely inelastic). Note that the level of nonlinear responses imply, for some SDOF systems, very large ductility values that, of course, may not be physically attainable by all real structures.

The peak value of the elastic base shear, or equivalently the peak elastic deformation, experienced by an elastic structure is, however, a ground-motion-specific quantity. Therefore, one can achieve the same value of R either a) for *each record* in a dataset or b) on an *average sense for all the records* in the same dataset.

In the former case the same target R value can be achieved by varying the yield displacement of the structure, d_y, from record to record. More precisely, for each record d_y needs to be set equal to the peak elastic displacement for that record divided by the desired value of R (see Figure 1). This case is hereinafter referred to as "constant-R" case. In this set of analyses each record is effectively applied to SDOF systems with slightly different strength characteristics.

In the latter case, the same R value can be obtained in multiple ways. In this study we kept constant the yield strength, d_y, of the oscillator for all the records and we set its value equal to the *median* peak elastic response displacement across all the records in the real dataset divided by R. This is, of course, equivalent to keeping the yield strength, F_y, constant. In this way the same structure, with an "average" strength, that varies with any given period and R-value, is used to evaluate the nonlinear response to all the records. This case is hereinafter referred to as "constant-strength" (or constant-F_y) case.

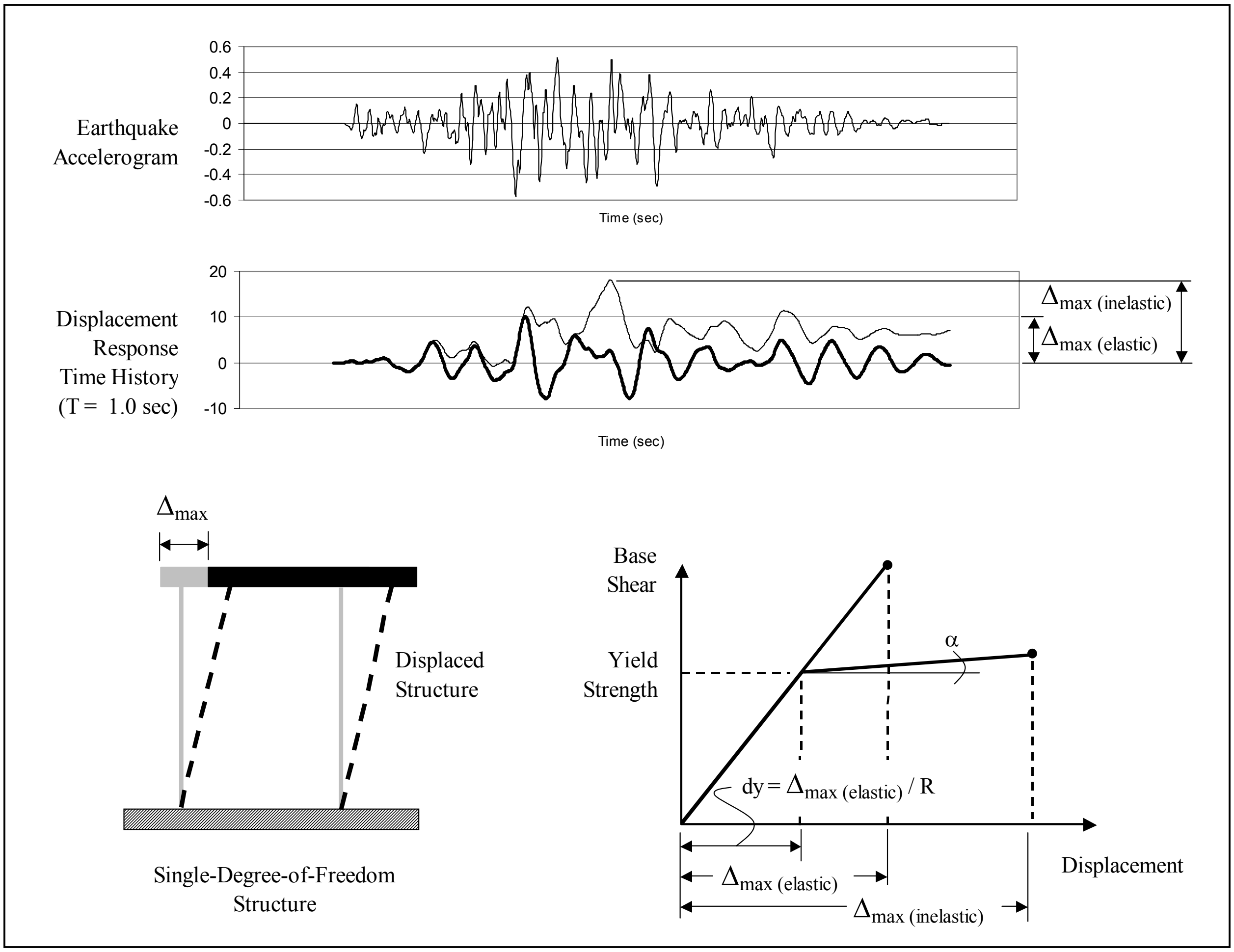

Figure 1: Schematic of SDOF structure and yield strength definition. The quantity α is the post-yield hardening here set equal to 2%. The yield strength in the figure is called F_y in this study.

In this study, we considered both constant-R and constant-strength analyses. The constant-strength case was selected as the primary focus of our investigations because of its simpler physical interpretation. For conciseness, we often neglected to remind the reader that the results were obtained using the constant-strength alternative. The results found using the alternative constant-R approach are, however, clearly marked. Nonlinear response spectra from both sets of analyses are briefly compared and contrasted in Section 4.4.

4.0 Results

The comparison of SDOF responses generated using different datasets is conveniently accomplished using the median (calculated as the geometric mean) and a standard deviation (of the natural logarithms of the data) of the 5%-damped elastic and inelastic spectra computed for the 20 stations (12 for the LLNL case). The spectra for each station are calculated for the "average" horizontal component in the sense explained in Section 2. It is legitimate to use statistics across all the stations in this context because they are all within 20 kilometers from the fault rupture (Table 1), which is a fairly tight distance range.

Figure 2 shows the median *elastic* pseudo-acceleration spectrum (panel *a*) and corresponding standard deviations (panel *b*) across stations in log-log scale for each synthetic dataset as well as for the real record one. Figure 3 displays the same results plotted as the ratio of the same quantities, that is the median in the top panel and the standard deviation in the bottom panel, for each synthetic model to the corresponding ones for the real dataset. A ratio above unity, if statistically significant, means overestimation of the response by a model and below unity means underestimation[10].

From inspecting the graphs in the top panels of Figures 2 and 3, it is clear that the median spectral amplitudes and shapes of the response spectra for some of the seven simulated cases is quite different than the median response spectrum from the real recordings. This amplitude difference can be large, especially in the short period range (up to about 80% at 0.1s). It is also interesting to note that only the model developed by Gusev provides a median elastic spectrum that is within ±20% of the median spectrum from the real Northridge records across the entire frequency range. The LLNL model also is within ±20% of the target for almost all its range of applicability, which has an upper bound of 2s. All the other models tend to overestimate by different amounts the elastic response of SDOF systems with periods below 0.3s and, with the exception of the models by URS and Zeng, to underestimate it above 0.3s. The URS and Zeng models seem to provide elastic responses even at periods larger than 0.3s that are, always in an average sense, either equally or more severe than those of the real records. Finally, any trend across period in the median ratios shown in Figure 3 that departs from a horizontal line suggests that the elastic spectra generated by the synthetic model have, on average, a different shape than those produce by nature, at least in this Northridge earthquake test case.

---

[10] In Figure 1 we have used pseudo-acceleration to produce the elastic spectra because most of the engineers are accustomed to seeing spectra in acceleration terms rather than in displacement terms. All the figures that follow, however, use displacement response spectra because displacement is the quantity most widely use when dealing with post-elastic response of structures.

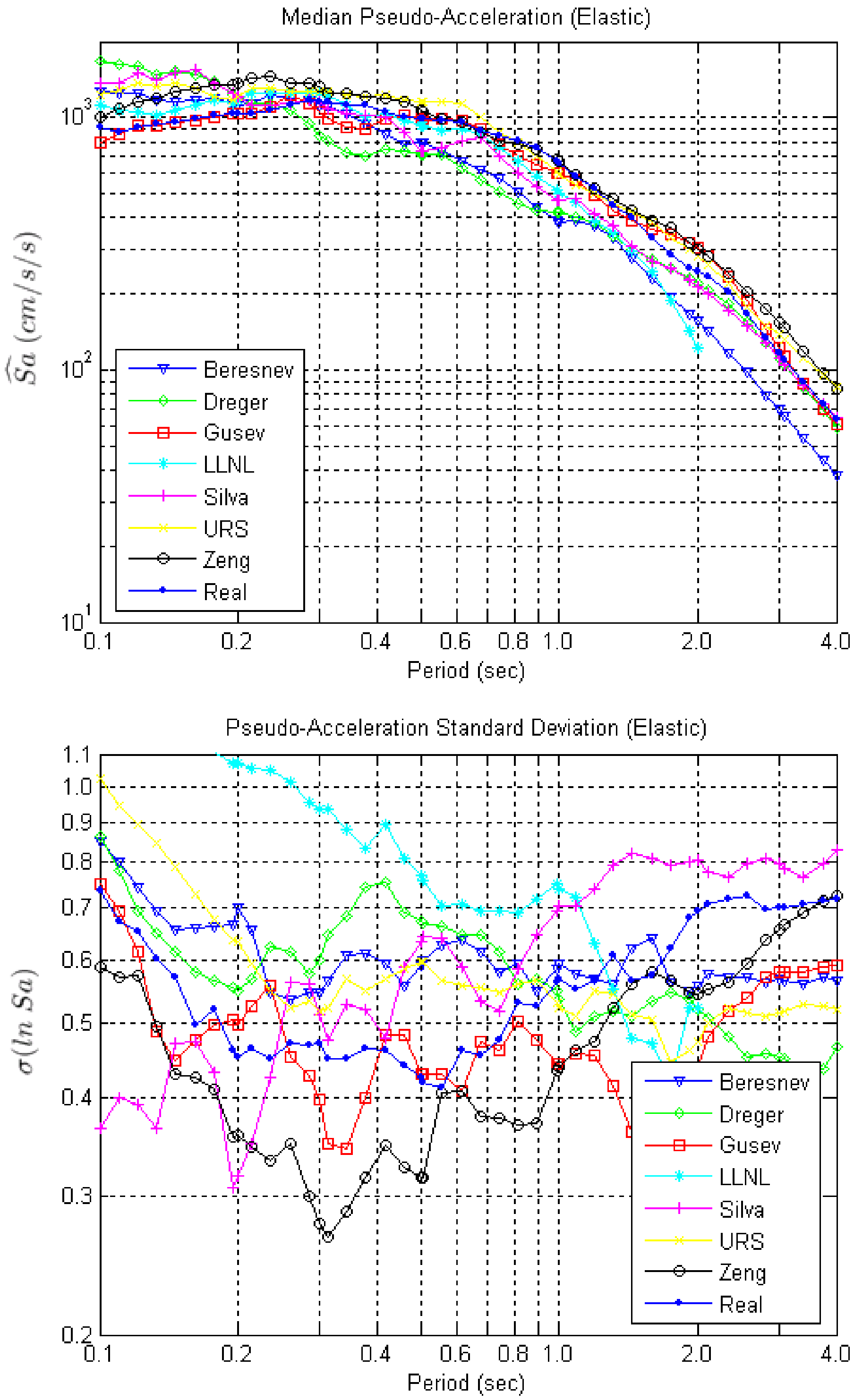

Figure 2: Median (top panel) and standard deviation (bottom panel) of the 5%-damped *elastic* pseudo-acceleration response spectra for the "average" horizontal component computed for all the available stations (12 for the LLNL model and 20 in the other seven cases). Note: 981 cm/s/s is equal to one *g*.

Note that the dispersion in the record-to-record ratio of inelastic spectra (not shown here) decreases with increasing period. The values of the COV vary with the model and they range between 0.3 at 4s to more than 1.0 at 0.1s. Hence, given these COV values and a sample size of 20 records per model (12 for the LLNL one), we can state that the elastic spectral ratios in Figure 3a are different than one with 90% confidence either in the long period range, or in the short period range, or in both for all seven models but Gusev's. More precisely, the period ranges where the ratios significantly differ from one are approximately above 0.6s for Beresnev, above 0.3s and below 0.15s for Dreger, above 1.5s for LLNL, between 0.8s and 1.1s and below 0.15s for Silva, above 3s and below 0.15s for URS, and above 1.5s for Zeng.

The inspection of the bottom panel of Figures 2 and 3 shows that none of the synthetic models provide a dispersion measure of the linear responses that is within ±20% of those from the real ones across the entire frequency range. The standard deviation across frequency from all the models, with the exception of the LLNL one for periods below 0.8s, is within ±40% with only minor departures from it. The LLNL model, on the other hand, seems in this case to provide records that produce significantly more variable elastic responses in the short period range than those from nature. Recall, however, that the statistics for the LLNL model are based on 12 records only and not 20 like in the other cases.

We presented here a short summary of the elastic results, which were more thoroughly investigated in the PEER K201 Treasure Island project, only to set the stage for the post-elastic nonlinear results that are the core of this study. The differences in the elastic response between the simulated and real records have an influence on the nonlinear response statistics at all strength levels. This is apparent from Figure 4, which presents the ratio of the medians and standard deviations of the inelastic *displacement* response spectra for the R=2 case. Note that for all the figures that relate to nonlinear post-elastic responses we measure the response in terms of spectral displacement rather than pseudo-spectral acceleration as we did in the linear elastic case. The spectral ratios displayed in Figure 3, of course, are not affected by which one of these two variables is used for the spectra. The signature of the elastic results in Figure 3 is obvious in the post-elastic ratios displayed in Figure 4. The trend of the ratios for R=1 and R=2 for each modeler are very similar. A similar statement, although less strong due to the increase in the record-to-record response variability for larger values of R, can be made for the more severely nonlinear cases.

A convenient way of investigating the effects of each modeling technique *above and beyond the elastic regime* is to normalize the nonlinear displacement response spectra generated for a given value of R (greater than one) by the corresponding elastic spectra obtained using the same dataset of synthetic records. We will refer to this ratio of inelastic-to-elastic spectra as *C,* that is:

$$C = \frac{\left(S_d\right)_{nonlinear}}{\left(S_d\right)_{elastic}} \tag{1}$$

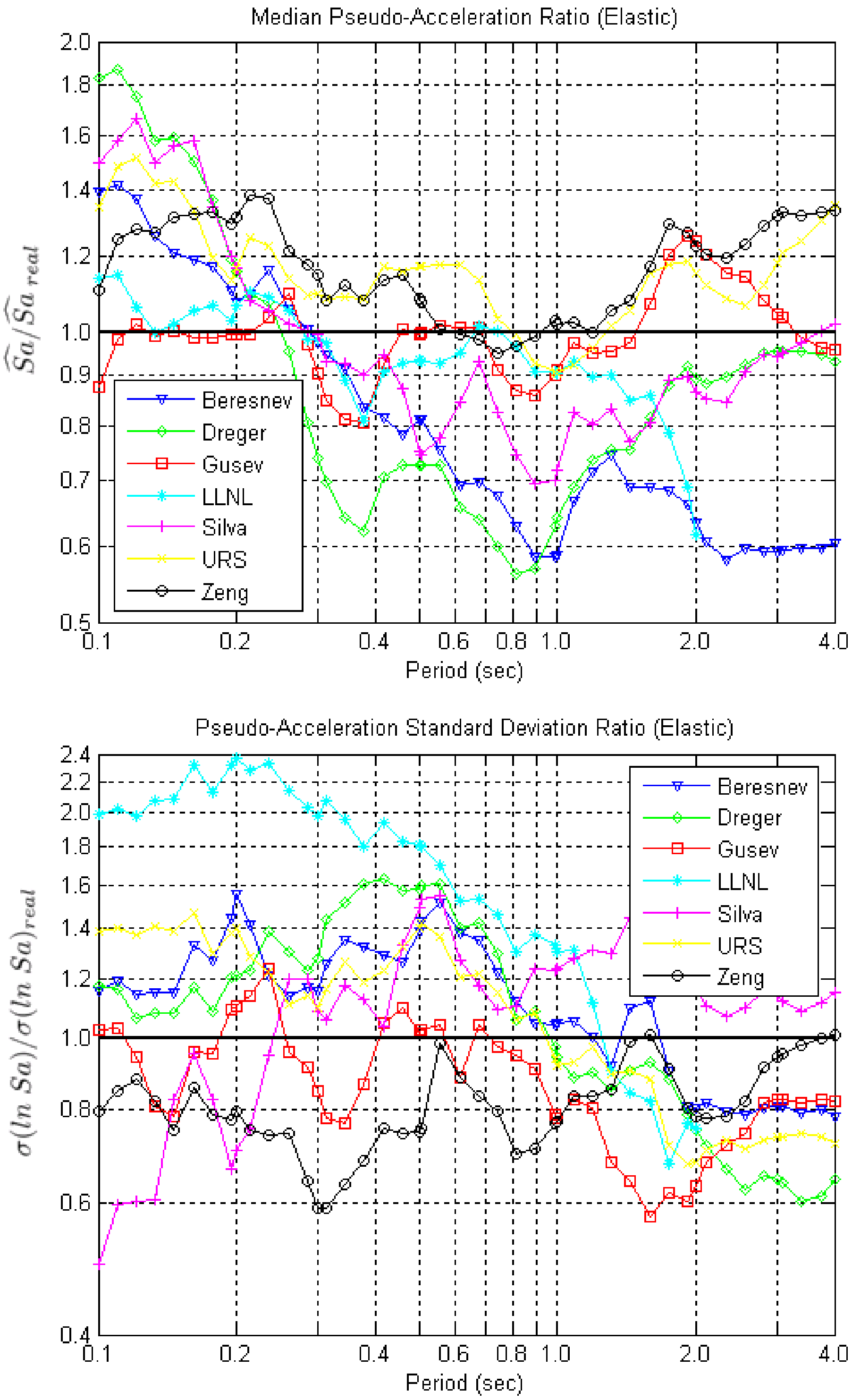

Figure 3: Ratio of the medians (top panel) and standard deviations (bottom panel) of the 5%-damped linear *elastic* displacement response spectra of each synthetic model to the corresponding quantity computed for the real record dataset.

Of course, *C* is a function of the oscillator period, *T*. In addition, given that we are comparing the results from synthetic datasets with the target ones from the real recordings, it is useful to divide the quantity *C* by the inelastic-to-elastic spectra ratio obtained for the real records, C_{real}. The quantity *C* (or C_{real} in the case of real records) is the response measure for which median values and standard deviations across the twenty recording stations (or twelve in the LLNL case) are computed. Also, for conciseness of notation, the ratio of C/ C_{real} is sometime called q_c in the sections that follow. Namely:

$$q_C = \frac{C}{C_{real}}, \tag{2}$$

The value of *C* is, on average, greater than one only for short periods (the shorter the period, the larger the average value of *C*), whereas it tends to one for moderate to longer periods (e.g., greater or equal to 1.0s). This is essentially the well-known equal displacement rule that was introduced by Veletsos and Newmark (1960) some forty years ago. The quantity *C* can be interpreted as a correction to the linear maximum elastic displacement to obtain the maximum nonlinear displacement of an SDOF oscillator.

In the following sections we will present the differences (as ratios) in *C* between synthetic and real ground motions. We will also briefly discuss the influence of the component averaging method and the impact of the yield strength definition on the observed results. Finally, we will report some results that were obtained by replacing the spectral displacement as the nonlinear structural response measure with energy-based quantities, such as the input energy and the absorbed energy.

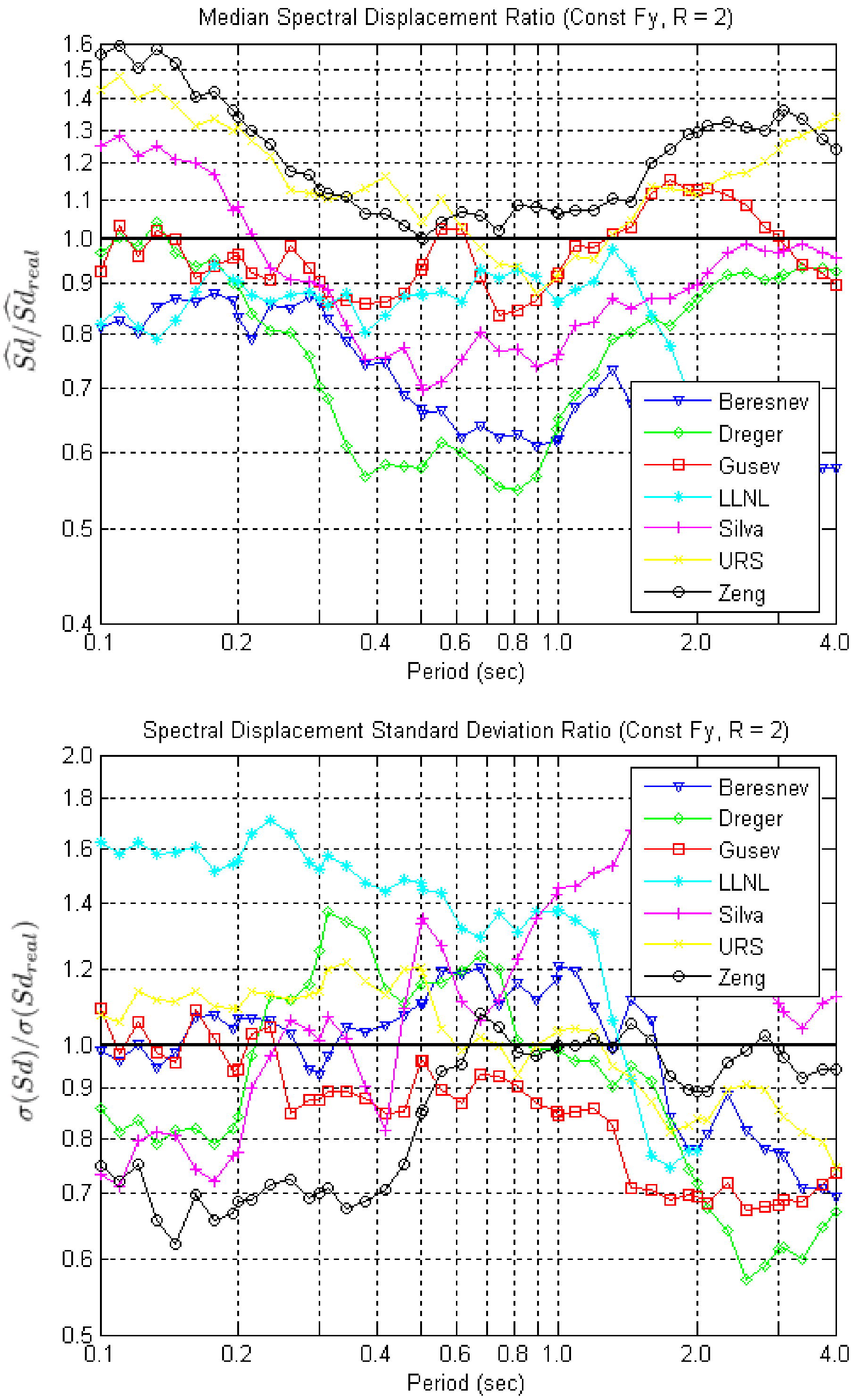

Figure 4: Ratio of the medians (top panel) and standard deviations (bottom panel) of the 5%-damped *nonlinear* response spectra (R=2) of each synthetic model to the corresponding quantity computed for the real record dataset.

4.1 **Nonlinear Structural Response to Simulated and Real Ground Motions**

The median value[11], $\hat{C}$, of the inelastic-to-elastic spectral ratio C for each of the seven synthetic datasets divided by the median value, $\hat{C}_{real}$, of C for the real records is plotted across the period range of 0.1s to 4.0s in panel (*a*) of Figures 5 to 7. The bottom panel shows the ratio of the standard deviation of C divided by the standard deviation of C_{real}. Attention is focused on the C/C_{real} results for strength levels R = 2, 4 and 10. The results for strength levels R = 6 and 8 are similar to those for R=10 and, therefore, they are not shown here.

4.1.2 *Median responses*

A deviation above unity of any of the $\hat{C}/\hat{C}_{real}$ curves in the top panel of Figures 5 to 7 indicates that, median *elastic response* for a simulated and the real record datasets *being equal*, the synthetic records in that dataset tend to produce, on average, systematically larger nonlinear spectral displacements than those by real records. Conversely, deviations below unity indicate that the simulated records tend to be, on average, more benign in producing nonlinear responses than those in nature. It is emphasized here that the equality of the linear responses generated by simulated and real records is postulated here only as a tool to compare the effectiveness of synthetic and real records in creating *nonlinear* responses. From Figure 3a, however, it is clear that this equality is often not statistically achieved for some of the seven simulated datasets at some period ranges. In the rest of this section we will assume that this equality of linear responses holds.

From the top panel of Figures 5 to 7 it is apparent that the difference in the ratio of median nonlinear to elastic response between the synthetic datasets and the real records is more period-dependent for some ground motion models than for others. For example, the $\hat{C}/\hat{C}_{real}$ results for R=2 in Figure 5a show that all the models provide nonlinear responses that are within ±20% from those of the real ones for all periods larger than about 0.3s. For periods shorter than 0.3s the records generated by the models by Beresnev, Dreger, LLNL, and, at some periods, Silva tend to be significantly less aggressive than real records. Conversely, the model by Zeng seems to create records that are, on average, more damaging. As before, the model by Gusev, being always within ±10% of the target, appears to be the more accurate one overall. For R=4 and R=10 in Figures 6 and 7, the models by Gusev, URS, and Zeng produce nonlinear responses that are statistically closest to those created by real records. The other four models provide similarly accurate results only for long periods, while in the region of shorter periods they seem to generate significantly less severe responses than their real counterparts. These systematically benign responses are more prominent at shorter periods for a given R, and in general at all periods for larger R values. A summary of the peak and average values of $\hat{C}/\hat{C}_{real}$ across the period range is given in Table 3, along with the structural periods at which the peak values occur.

---

[11] The median value was computed as the geometric mean, i.e., the exponential of the mean of the natural log of the ratios across all the available stations (i.e., 12 for the LLNL case and 20 for all other cases).

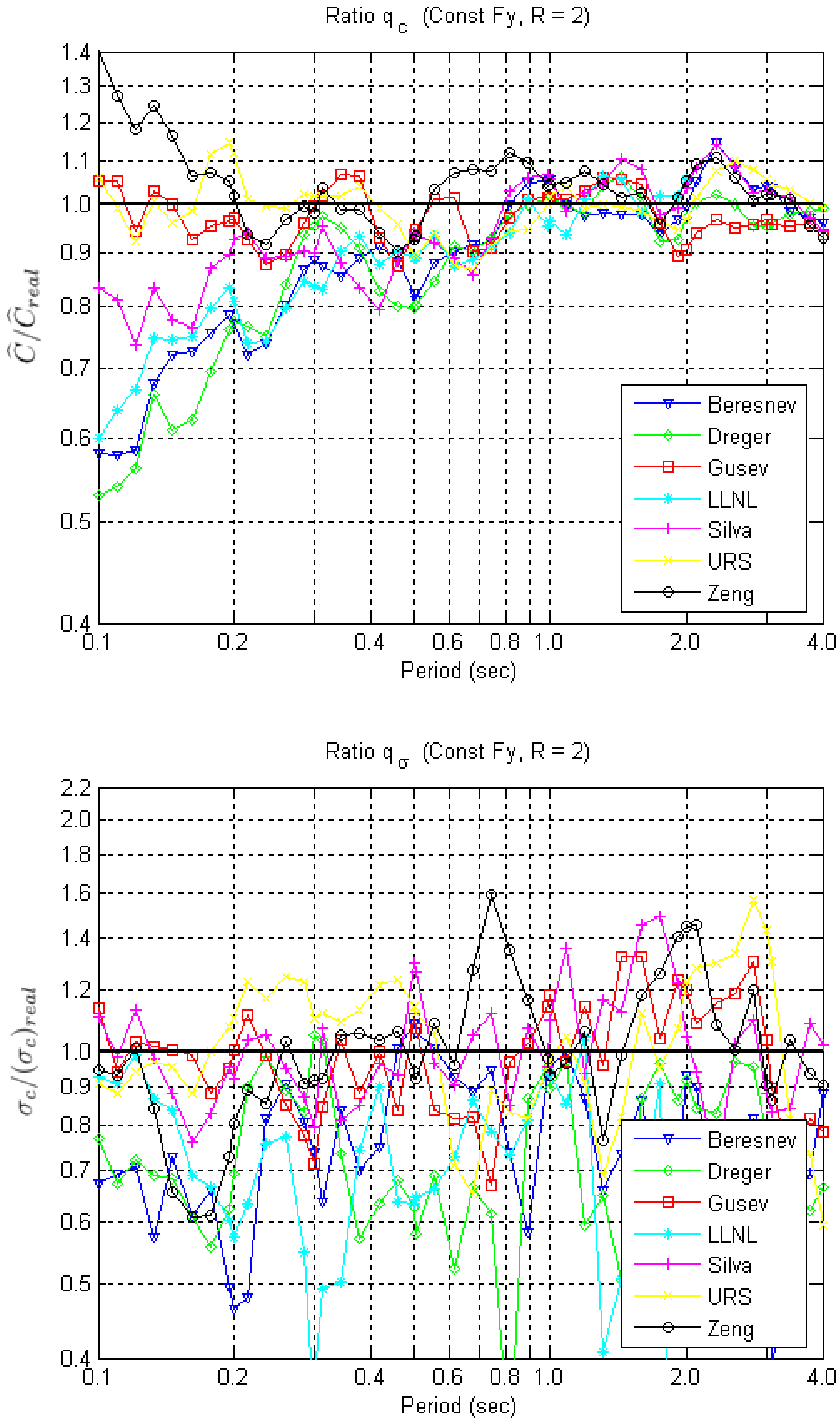

Figure 5: Statistics of the inelastic-to-elastic spectral ratio, *C*, for the seven synthetic datasets, normalized by the corresponding quantity, C_{real}, obtained from the suite of real records, for a level of inelasticity defined by **R=2**. The top panel presents the ratio of the medians while the bottom panel displays the ratio of the standard deviations.

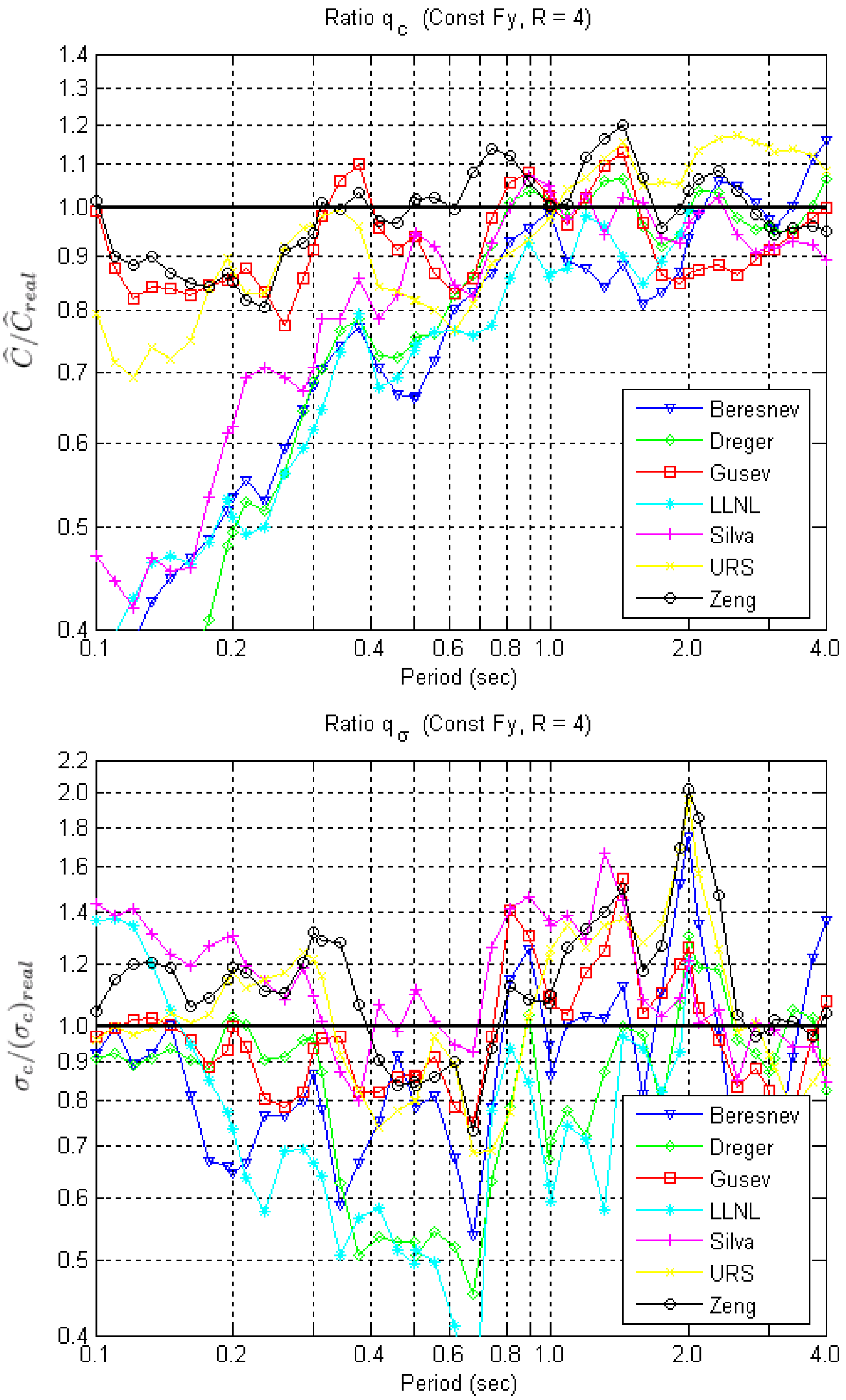

Figure 6: Statistics of the inelastic-to-elastic spectral ratio, *C*, for the seven synthetic datasets, normalized by the corresponding quantity, C_{real}, obtained from the suite of real records, for a level of inelasticity defined by **R=4**. The top panel presents the ratio of the medians while the bottom panel displays the ratio of the standard deviations.

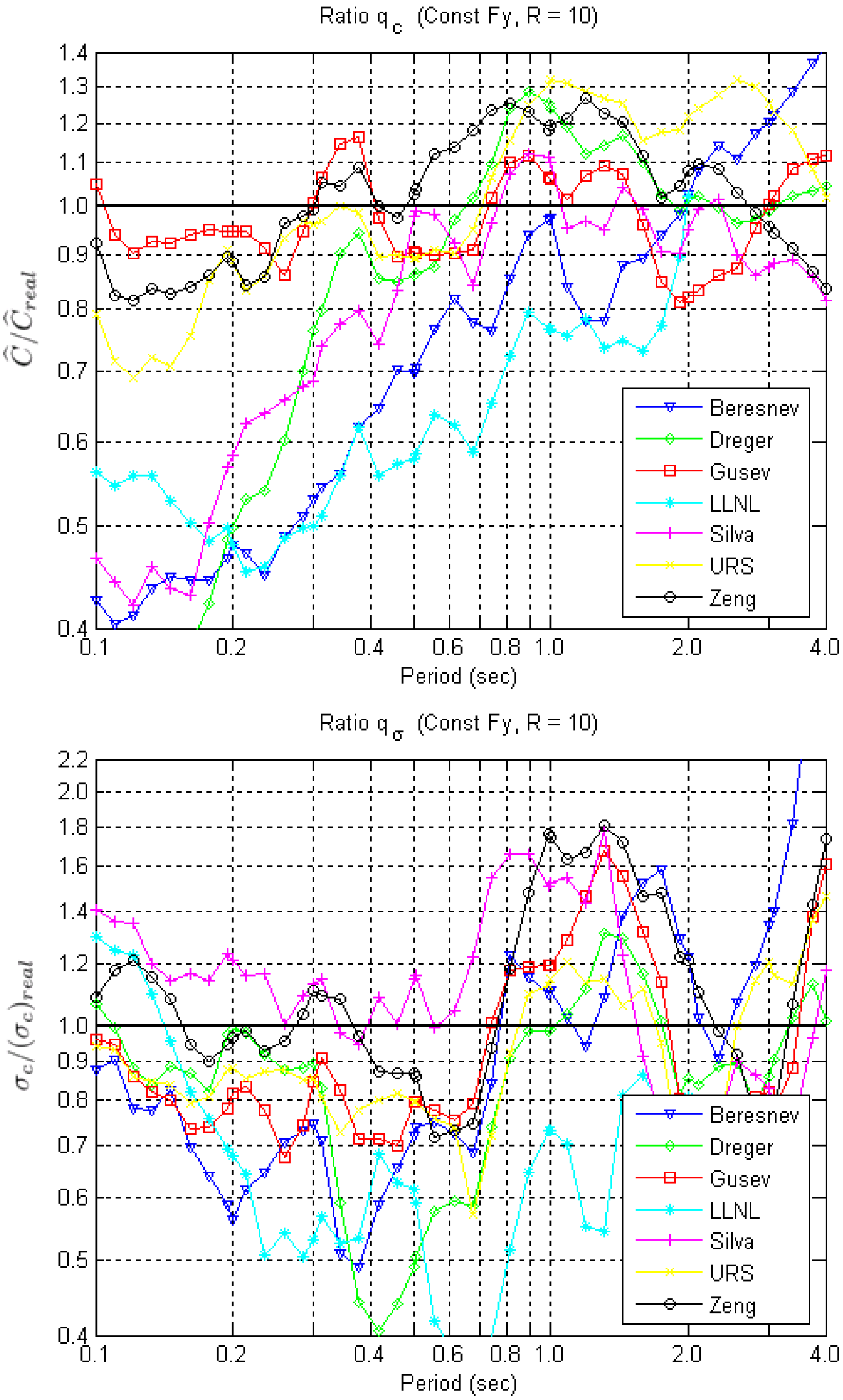

Figure 7: Statistics of the inelastic-to-elastic spectral ratio, *C*, for the seven synthetic datasets, normalized by the corresponding quantity, C_{real}, obtained from the suite of real records, for a level of inelasticity defined by **R=10**. The top panel presents the ratio of the medians while the bottom panel displays the ratio of the standard deviations.

	R = 2					R = 4					R = 10				
Model	**Min**	**T_{min}**	**Max**	**T_{max}**	**Avg**	**Min**	**T_{min}**	**Max**	**T_{max}**	**Avg**	**Min**	**T_{min}**	**Max**	**T_{max}**	**Avg**
Beresnev	0.58	0.11	1.15	2.32	0.90	0.38	0.11	1.16	4.00	0.77	0.40	0.11	1.41	4.00	0.78
Dreger	0.53	0.10	1.06	1.44	0.88	0.30	0.11	1.07	1.44	0.78	0.32	0.11	1.28	0.90	0.86
Gusev	0.88	0.46	1.07	0.35	0.97	0.78	0.26	1.13	1.44	0.93	0.81	1.92	1.17	0.38	0.98
LLNL	0.60	0.10	1.07	1.31	0.88	0.39	0.11	1.00	2.00	0.70	0.45	0.21	1.02	2.00	0.62
Silva	0.74	0.12	1.14	2.32	0.95	0.42	0.12	1.07	0.90	0.82	0.42	0.12	1.12	0.90	0.81
URS	0.87	0.67	1.15	0.19	1.00	0.69	0.12	1.17	2.55	0.95	0.69	0.12	1.32	2.55	1.04
Zeng	0.90	0.46	1.41	0.10	1.04	0.81	0.24	1.20	1.44	0.99	0.81	0.12	1.26	1.19	1.02

Table 3: Peak and average values of $\hat{C}/\hat{C}_{real}$ for strength levels R = 2, 4 and 10. The table shows also the structural periods at which each peak value of $\hat{C}/\hat{C}_{real}$ occurred.

To determine the statistical significance of the observed $q_c=\hat{C}/\hat{C}_{real}$, the 2-sided 90% t-student confidence limits for q_c were calculated across the period range at each strength level for each ground motion model. At oscillator periods where the upper and lower confidence limits do not bracket the line $\hat{C}/\hat{C}_{real}$ = 1, the median nonlinear spectral displacement for the synthetic dataset is statistically biased at a 10% level of significance. Figures 8 to 14 show the confidence limits for each ground motion model at the three key structural strength levels. As anticipated, only the model by Gusev seems to be unbiased across the whole spectrum of periods regardless of the level of nonlinearity. In general, with the exception of the two by Beresnev and Dreger, all the models are unbiased for R=2 across the entire period range. All the models but Gusev's are biased at some periods for R=4 and R=10. The amount of bias is larger for larger R values and for shorter periods. In these cases most of the synthetic models create records that are more benign than real ones. The model by URS, on the other hand, is the only one that creates records that produce statistically more severe inelastic responses at the R=10 level than those in nature for SDOF oscillators of 0.8s and longer natural period.

The average deficiency of the *nonlinear* responses generated by some of these synthetic ground motions at short periods (e.g., below 0.3s) is likely due to a systematic difference in that period range in the average shape of the *linear* response spectra generated by synthetic and by real records. Figure 2a shows, in fact, that some of the models, such as Beresnev and Dreger, on average, produce linear pseudo-acceleration spectra that are either flat or falling instead of climbing with increasing periods below 0.3s like the spectrum from real records does. The difference in spectral shape is more evident in Figure 3a, which shows the ratio of the elastic spectra for the synthetic models and the real ones. Given this discrepancy, it is not surprising that when the effective period of the oscillator lengthens because of the nonlinear behavior of the oscillator these records become less aggressive than real ones.

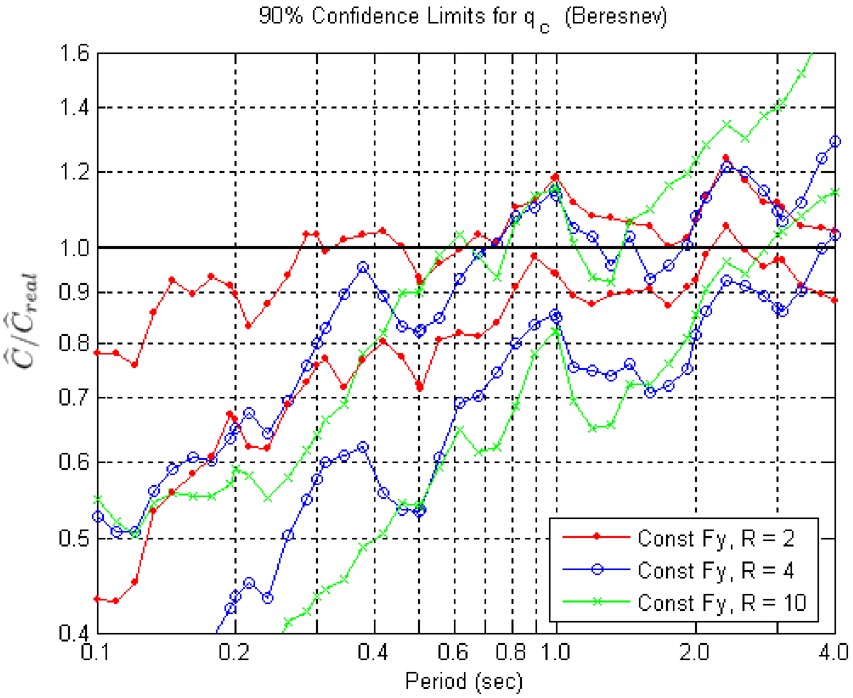

Figure 8: Upper and lower 90% confidence limits for q_c for constant-strength levels R = 2, 4 and 10 for the Beresnev model. The ratio is significantly different than one at those periods where the unity line is not bracketed by the lower and upper bounds of the confidence band.

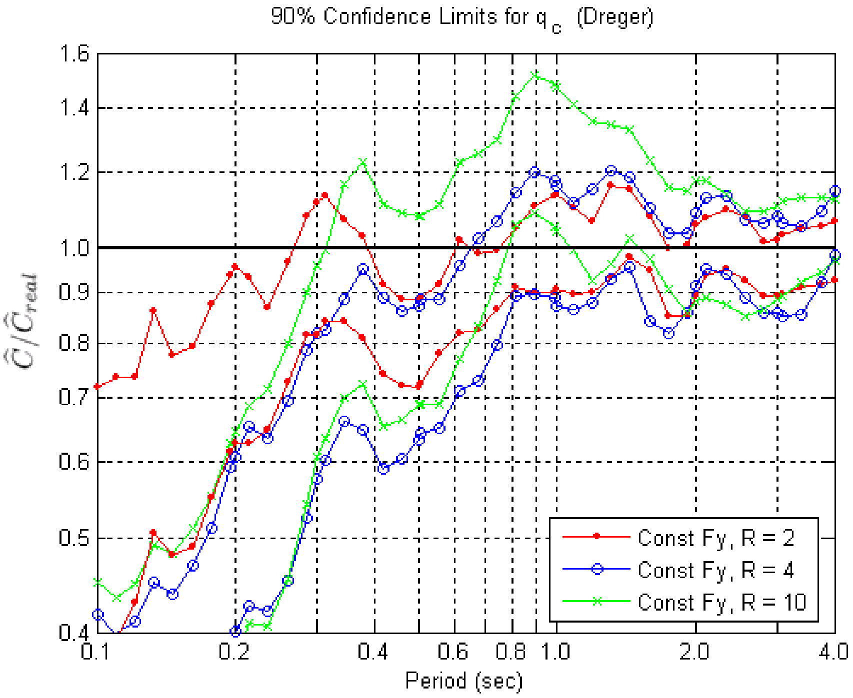

Figure 9: Upper and lower 90% confidence limits for q_c for constant-strength levels R = 2, 4 and 10 for the Dreger model. The ratio is significantly different than one at those periods where the unity line is not bracketed by the lower and upper bounds of the confidence band.

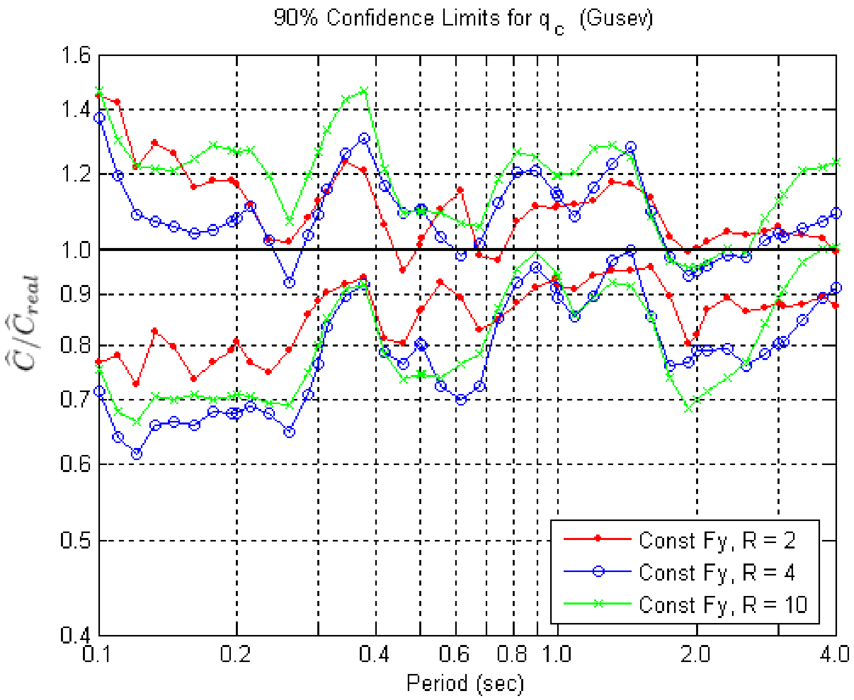

Figure 10: Upper and lower 90% confidence limits for q_c for constant-strength levels R = 2, 4 and 10 for the Gusev model. The ratio is significantly different than one at those periods where the unity line is not bracketed by the lower and upper bounds of the confidence band.

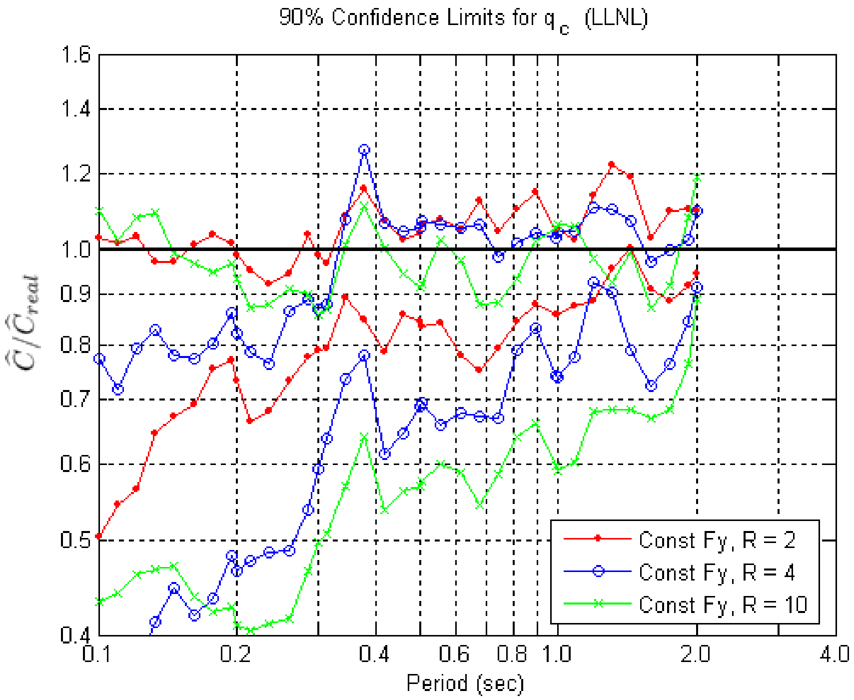

Figure 11: Upper and lower 90% confidence limits for q_c for constant-strength levels R = 2, 4 and 10 for the LLNL model. The ratio is significantly different than one at those periods where the unity line is not bracketed by the lower and upper bounds of the confidence band.

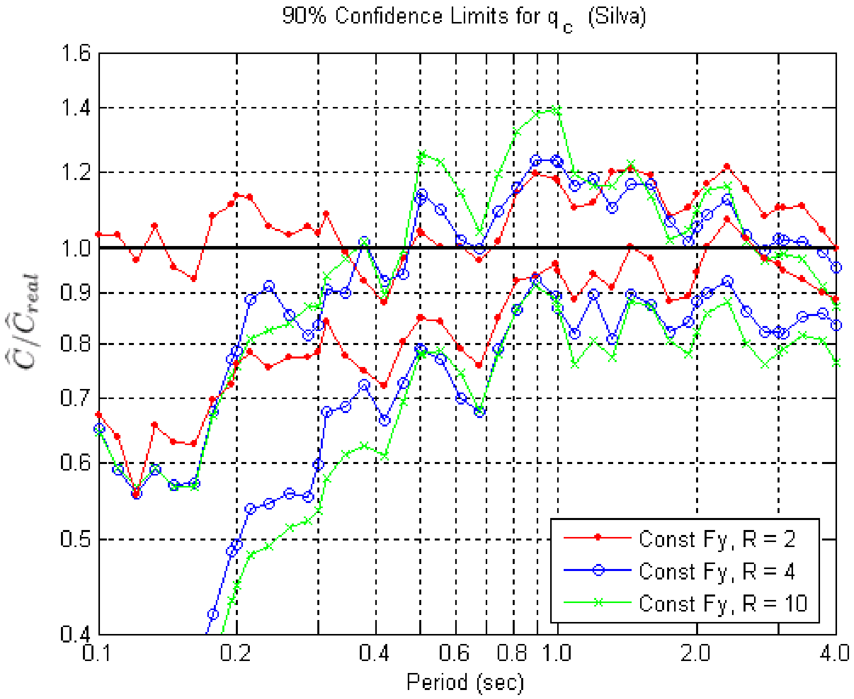

Figure 12: Upper and lower 90% confidence limits for q_c for constant-strength levels R = 2, 4 and 10 for the Silva model. The ratio is significantly different than one at those periods where the unity line is not bracketed by the lower and upper bounds of the confidence band.

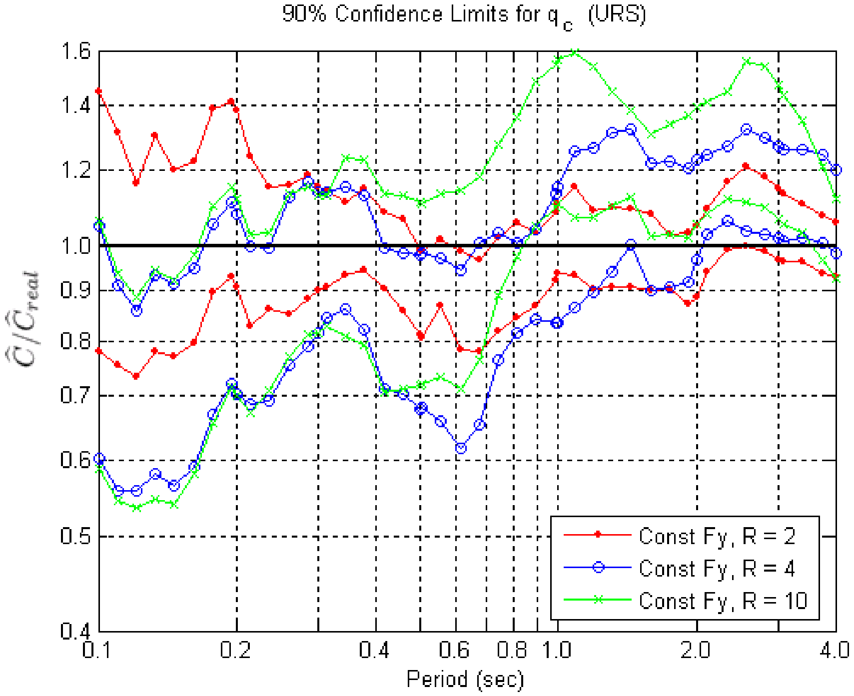

Figure 13: Upper and lower 90% confidence limits for q_c for constant-strength levels R = 2, 4 and 10 for the URS model. The ratio is significantly different than one at those periods where the unity line is not bracketed by the lower and upper bounds of the confidence band.

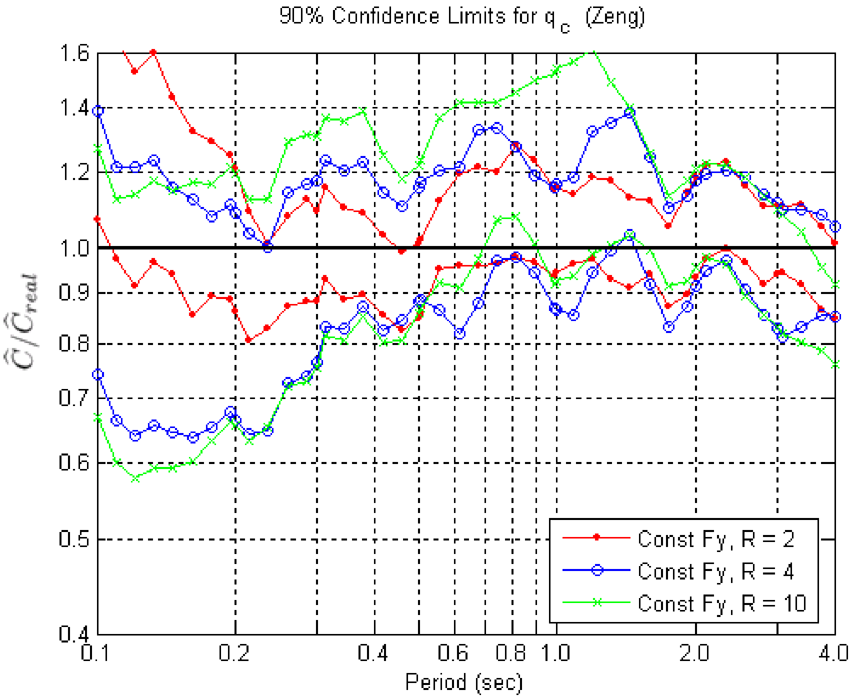

Figure 14: Upper and lower 90% confidence limits for q_c for constant-strength levels R = 2, 4 and 10 for the Zeng model. The ratio is significantly different than one at those periods where the unity line is not bracketed by the lower and upper bounds of the confidence band.

4.1.2 *Record-to-record nonlinear response variability*

The bottom panel of Figures 5 to 7 shows the relative dispersion of *nonlinear (still normalized by elastic) responses* to synthetic records and to real records. As before, a line above unity means relatively more record-to-record variability produced by synthetic records whereas the opposite is true for a line below unity. The relative variability of nonlinear responses to synthetic and real records is, again, model-dependent and varies with the level of response severity. For R=2 most of the models, especially those from Beresnev, Dreger, and LLNL, seem to underestimate the record-to-record variability of the response from real records, in particular at shorter periods. For the more severe responses (R=4 and R=10) the general tendency of most of the models is to underestimate the response variability for periods ranging between 0.3s and 0.8s and to overestimate it between 0.8s and about 3s. A summary of statistics of $\sigma_c/(\sigma_c)_{real}$ across the period range is given in Table 4.

	R = 2					R = 4					R = 10				
Model	Min	T_{min}	Max	T_{max}	Avg	Min	T_{min}	Max	T_{max}	Avg	Min	T_{min}	Max	T_{max}	Avg
Beresnev	0.38	3.09	1.09	0.50	0.76	0.54	0.67	1.76	2.00	0.90	0.49	0.38	3.71	4.00	1.04
Dreger	0.31	0.81	1.05	0.30	0.75	0.45	0.67	1.31	2.00	0.85	0.40	0.42	1.32	1.31	0.87
Gusev	0.67	0.74	1.33	1.44	1.00	0.75	0.67	1.55	1.44	0.98	0.64	2.11	1.68	1.31	0.94
LLNL	0.07	1.92	1.04	1.19	0.69	0.28	0.67	1.37	0.11	0.77	0.31	0.67	1.30	0.10	0.69
Silva	0.69	2.32	1.50	1.74	1.02	0.80	0.38	1.67	1.31	1.15	0.69	2.11	1.78	1.31	1.14
URS	0.59	4.00	1.58	2.81	1.04	0.69	0.67	1.95	2.00	1.08	0.57	0.67	1.46	4.00	0.93
Zeng	0.61	0.16	1.59	0.74	1.01	0.73	0.67	2.01	2.00	1.15	0.72	0.56	1.81	1.31	1.13

Table 4: Peak and average values of $\sigma_c/(\sigma_c)_{real}$, which is the ratio of the standard deviation of *C* for simulated records to the standard deviation of C_{real}. The values are reported for strength levels R = 2, 4 and 10. Included are also the SDOF periods at which each peak value of $\sigma_c/(\sigma_c)_{real}$ occurred.

If synthetic records tend to generate less variable nonlinear responses than real ones, then simple statistical considerations show that an analyst would be better off using them rather than real ones to estimate the *median* nonlinear response of a structure[12] for a given earthquake scenario. From a practical standpoint, the same accuracy would be achieved with fewer runs with simulated rather than real records as input. However, if an engineer seeks to design a new structure or assess the safety of an existing one against collapse, for example, the use of simulated records that tend to generate less variable responses would underestimate the likelihood of extreme response values and, therefore, the chances of collapse. This shortcoming should be taken into consideration.

---

[12] This statement assumes that the synthetic ground motions generate statistically unbiased responses. If that is untrue, like in a few cases among those considered here, the bias needs to be corrected when using such records.

4.2 Influence of Response Component Averaging Method

To determine if using the geometric mean of the response to both horizontal components at each station rather than the root-mean-square, as done so far, would result in different trends in the results, we investigated the following ratio:

$$q_{avg} = \frac{\hat{C}_{RMS}}{\hat{C}_{geometric}} \tag{3}$$

where $\hat{C}_{RMS}$ and $\hat{C}_{geometric}$ are the median values of the inelastic-to-elastic spectral ratio C across the available stations computed using the two different averaging schemes. The averaging method is pertinent to only five of the seven simulation models: Dreger, Gusev, LLNL, URS, and Zeng. Beresnev and Silva provided only one "average" ground motion component per station and, therefore, the results for their models will not be affected by the averaging technique.

Using simple mathematics, it can be shown that the ratio of rms to geometric average of nonlinear responses divided by their elastic counterparts is almost always greater than one and that it tends to one for long periods. This trend is confirmed in Figure 15, which shows q_{avg} computed for a constant-strength level R = 4 for the real records and for each of the five synthetic datasets mentioned above. Therefore, the effect of using the geometric mean rather than the rms mean is expected to have a noticeable effect only in the short period range.

Replacing the rms mean with the geometric mean when computing the inelastic-to-elastic median spectral ratios makes these ratios slightly closer to unity in the short period range than the ratios shown in top panels of Figures 5 to 7. The effect of using the geometric instead of the rms mean decreases with increasing R value such that this difference almost disappears for R=10. Figure 16, which is analogous to top panel of Figure 5, shows the case where the effect of the averaging technique is largest[13]. Note that at periods above approximately 0.5s the component averaging technique has no effect on the assessment of the median response at all the structural strengths considered here.

---

[13] Beresnev and Silva provided only one component per station. The curves for the Beresnev and Silva models in Figures 4 and 15 are different because the different averaging technique affects the computation of the normalizing factor that uses two components of the real records.

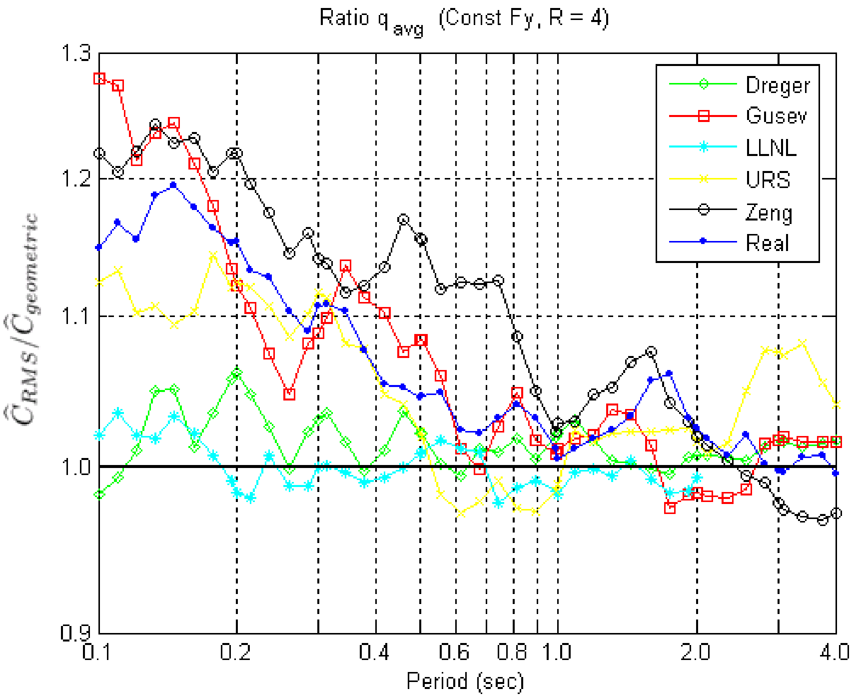

Figure 15: Ratio q_{avg} based on constant-strength analysis (R = 4). See Eq. (3) for the definition of $q_{avg.}$ Note that only those datasets that contained component pairs of records at each recording station are shown.

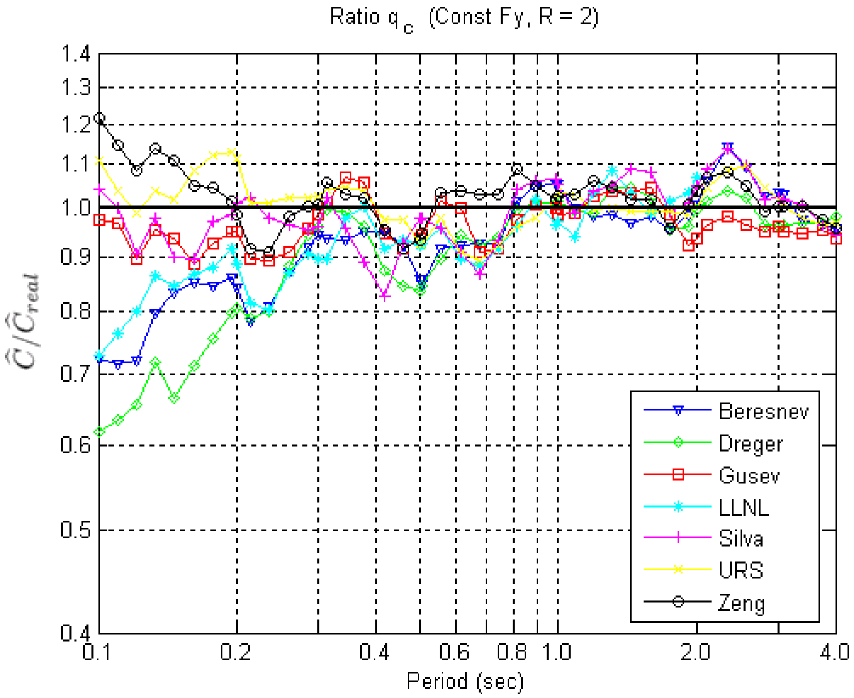

Figure 16: Ratio of the medians of the inelastic-to-elastic spectral ratio, C, for the seven synthetic datasets normalized by the corresponding quantity, C_{real}, obtained from the suite of real records. Both C and C_{real} were computed for a level of inelasticity defined by R=2 using the geometric mean of the responses to the two horizontal components, when available. The difference between averaging techniques decreases with increasing period and increasing R. This figure should be inspected in conjunction with the top panel of Figure 5.

4.3 Influence of Yield Strength Definition

All the results shown so far were computed for SDOF systems with constant strength (or constant yield force, F_y) for all the records. Therefore, as mentioned earlier, the value of R referred to above applies only in an average sense for all the records and not necessarily for each single record. Alternatively, we could keep a constant-R for all the records by appropriately modifying F_y for each one. The choice of preferring a constant-strength to a constant-R approach is, of course, entirely subjective. Other analysts could prefer the use of the constant-R approach instead. To assess whether the results that were shown so far still hold for the constant-R case, we investigated the statistical differences in the two following quantities, q_c and q'_c:

$$q_C = \left(\frac{C}{C_{real}},\right)_{Const-Fy} \quad ; \quad q'_C = \left(\frac{C}{C_{real}},\right)_{Const-R} \tag{4}$$

The graphs of q_c for R=2, 4, and 10 were shown in the top panels of Figures 5 to 7. The computed values of the ratio q'_c/q_c are shown in Figure 17a, 17b, and 17c for R = 2, 4 and 10, respectively. This ratio, which is clearly both model-dependent and R-dependent, can be significantly different than unity. This translates into potentially different systematic differences between nonlinear responses generated by the real dataset and the synthetic ones if the constant-R definition rather than the constant-strength definition is adopted.

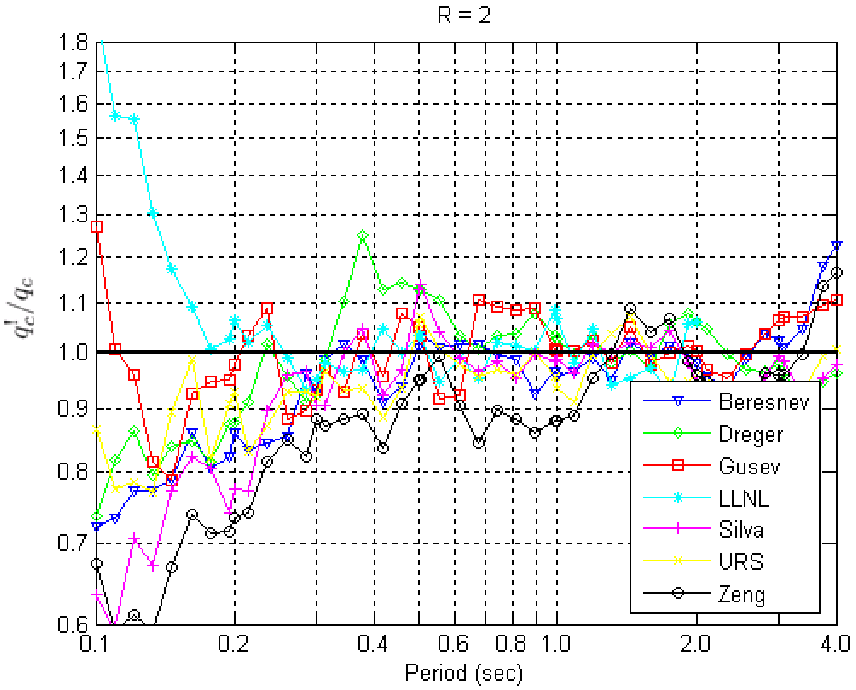

Figure 17a: Trend of the q'_c/q_c curves computed for R=2 for the seven simulation models. Note that q'_c refers to the constant-R results while q_c refers to the constant-strength results that have been discussed throughout the report. See Eq. (4) for the definitions of q_c and q'_c.

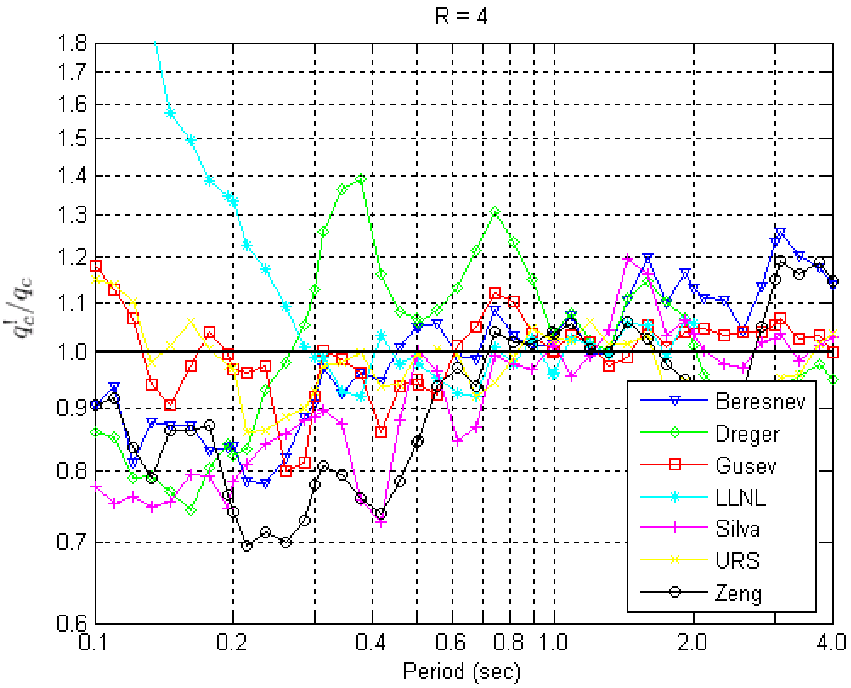

Figure 17b: Trend of the q'_c/q_c curves computed for R=4 for the seven simulation models. Note that q'_c refers to the constant-R results while q_c refers to the constant-strength results that have been discussed throughout the report. See Eq. (4) for the definitions of q_c and q'_c.

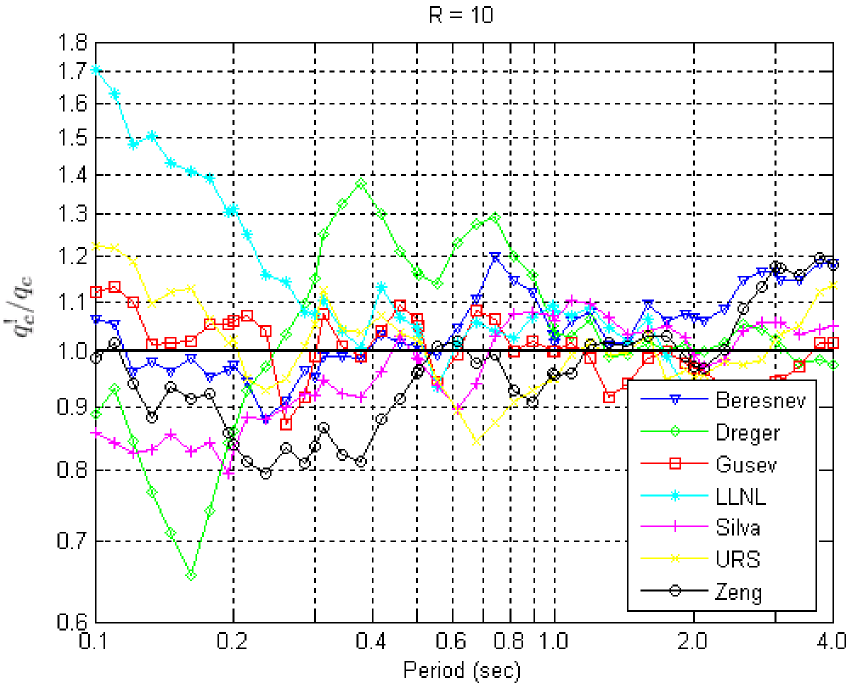

Figure 17c: Trend of the q'_c/q_c curves computed for R=10 for the seven simulation models. Note that q'_c refers to the constant-R results while q_c refers to the constant-strength results that have been discussed throughout the report. See Eq. (4) for the definitions of q_c and q'_c.

To quantify the extent of such differences, if any, we repeated all the nonlinear response analyses using the constant-R definition for all the datasets, both real and synthetics. The effect on the confidence limits for *q'*$_c$ of using this alternative R definition is shown in Figures 18 to 24. These graphs should be compared with those in Figures 8 to 14. From inspecting this second batch of plots one can conclude that none of the conclusions that applied to the constant-strength approach are significantly affected by the adoption of the constant-R approach to the yield strength definition. The major differences affect the model by LLNL, that becomes unbiased for R=2 and 4 across the entire period range, and both the models by Silva and Zeng, whose amounts of bias are slightly worsened.

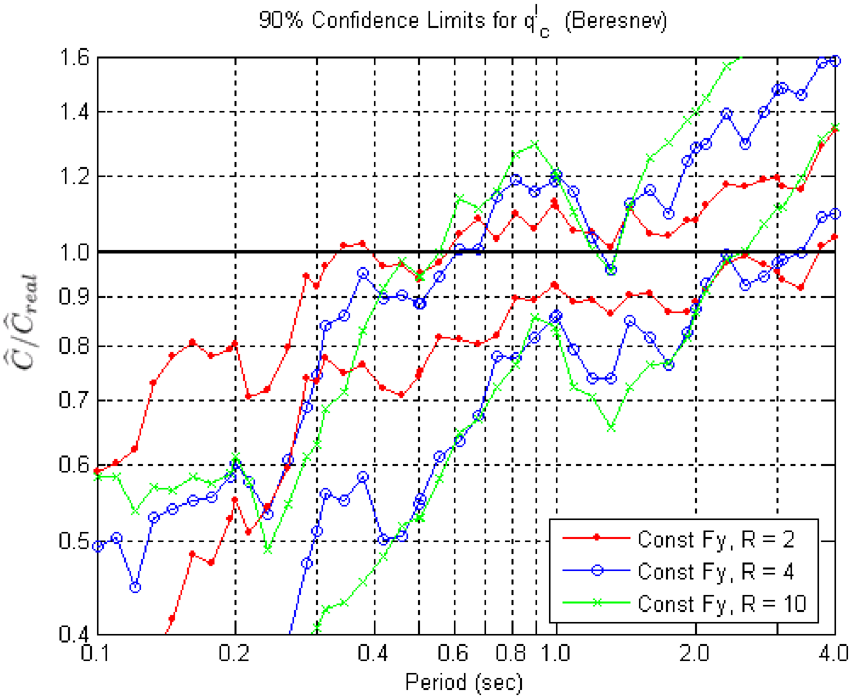

Figure 18: Upper and lower 90% confidence limits for *q'*$_c$ for constant-strength levels R = 2, 4 and 10 for the Beresnev model. The ratio is significantly different than one at those periods where the unity line is not bracketed by the lower and upper bounds of the confidence band. Compare these confidence limits with those computed using the constant-strength approach (Figure 8).

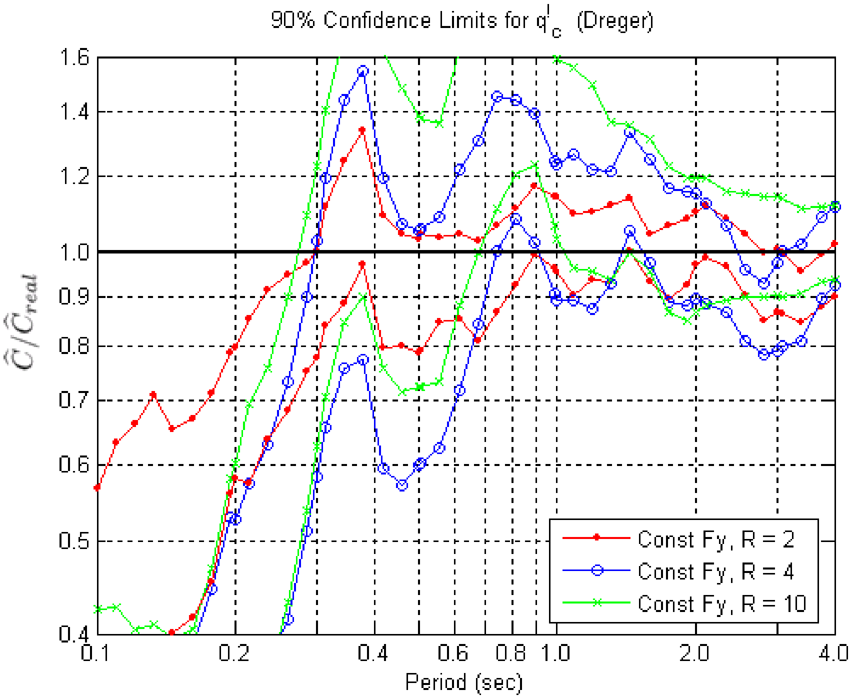

Figure 19: Upper and lower 90% confidence limits for q'_c for constant-strength levels R = 2, 4 and 10 for the Dreger model. The ratio is significantly different than one at those periods where the unity line is not bracketed by the lower and upper bounds of the confidence band. Compare these confidence limits with those computed using the constant-strength approach (Figure 9).

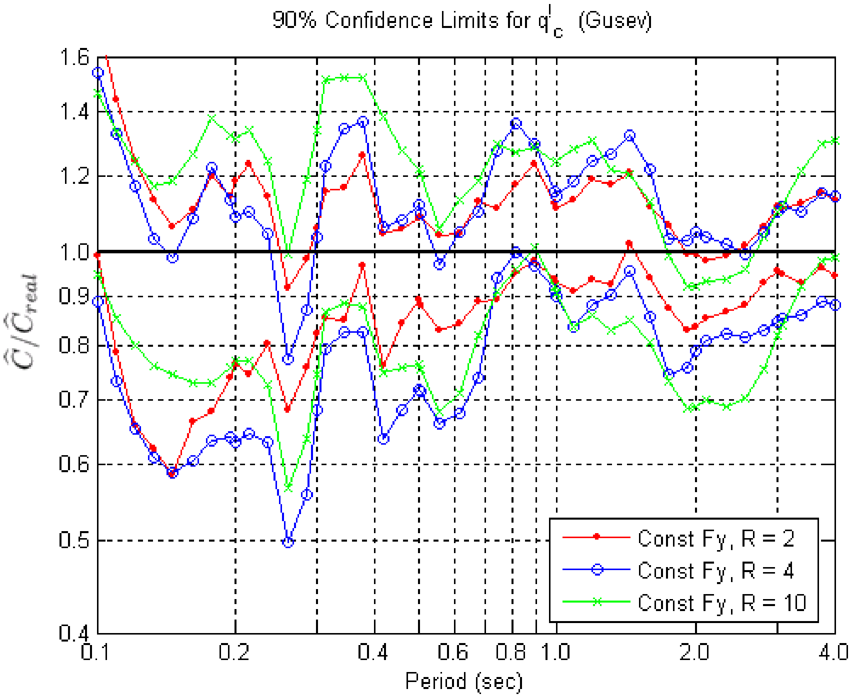

Figure 20: Upper and lower 90% confidence limits for q'_c for constant-strength levels R = 2, 4 and 10 for the Gusev model. The ratio is significantly different than one at those periods where the unity line is not bracketed by the lower and upper bounds of the confidence band. Compare these confidence limits with those computed using the constant-strength approach (Figure 10).

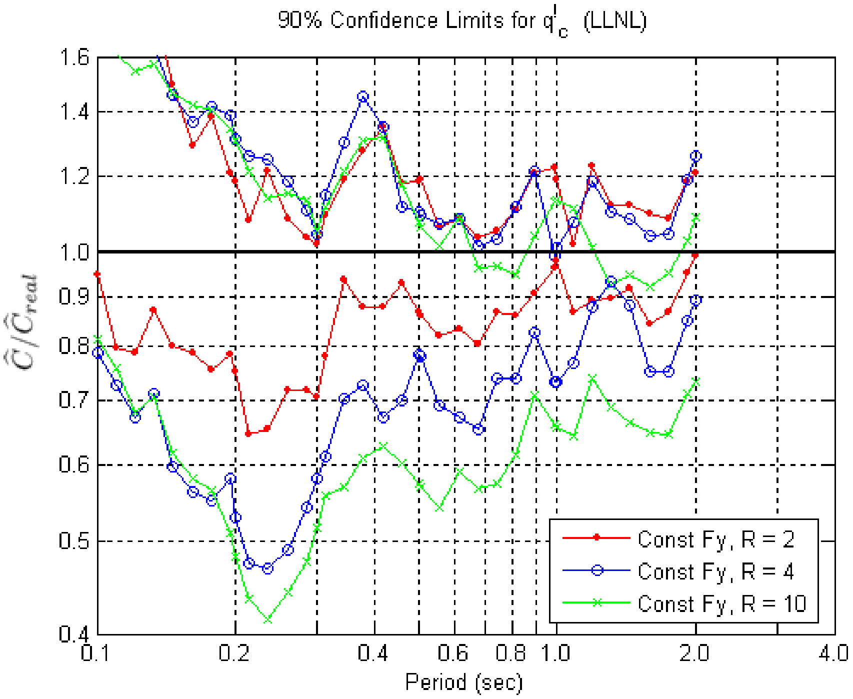

Figure 21: Upper and lower 90% confidence limits for q'_c for constant-strength levels R = 2, 4 and 10 for the LLNL model. The ratio is significantly different than one at those periods where the unity line is not bracketed by the lower and upper bounds of the confidence band. Compare these confidence limits with those computed using the constant-strength approach (Figure 11).

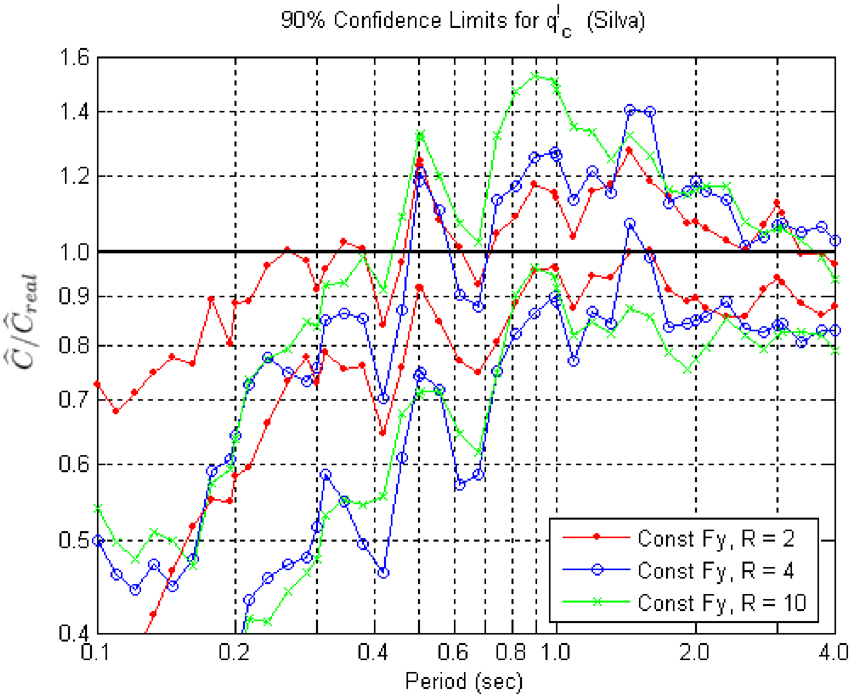

Figure 22: Upper and lower 90% confidence limits for q'_c for constant-strength levels R = 2, 4 and 10 for the Silva model. The ratio is significantly different than one at those periods where the unity line is not bracketed by the lower and upper bounds of the confidence band. Compare these confidence limits with those computed using the constant-strength approach (Figure 12).

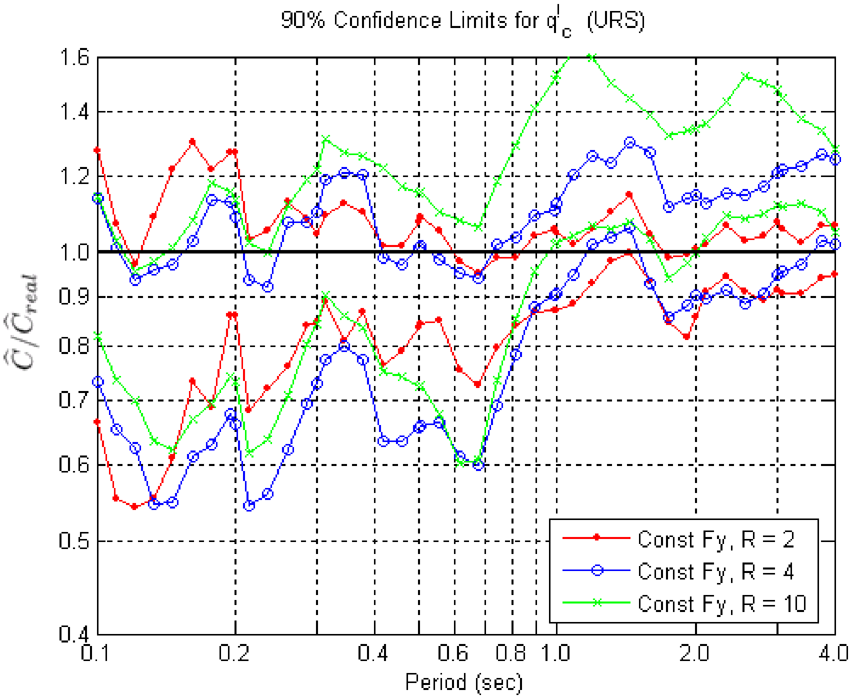

Figure 23: Upper and lower 90% confidence limits for q'_c for constant-strength levels R = 2, 4 and 10 for the URS model. The ratio is significantly different than one at those periods where the unity line is not bracketed by the lower and upper bounds of the confidence band. Compare these confidence limits with those computed using the constant-strength approach (Figure 13).

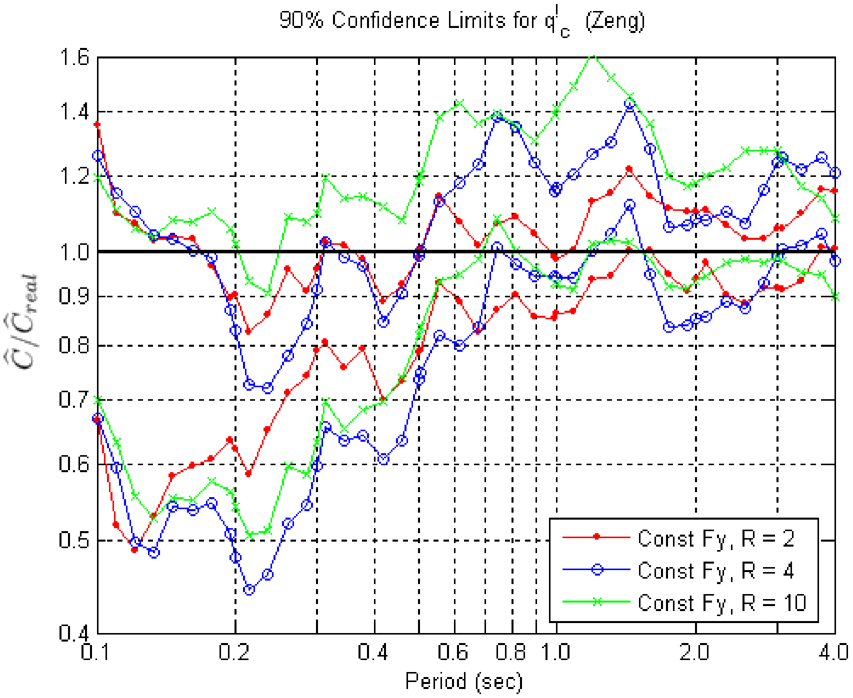

Figure 24: Upper and lower 90% confidence limits for q'_c for constant-strength levels R = 2, 4 and 10 for the Zeng model. The ratio is significantly different than one at those periods where the unity line is not bracketed by the lower and upper bounds of the confidence band. Compare these confidence limits with those computed using the constant-strength approach (Figure 14).

4.4 Effects on Nonlinear Responses Measured by Energy-Based Parameters

An alternative to quantifying the nonlinear dynamic response of a structure by a peak measure such as spectral displacement involves the use of a cumulative energy-based measure, such as input energy (E_i) or absorbed energy (E_a). Some researchers prefer the use of cumulative rather than peak response measures because they are supposed to capture the effects of both strength and stiffness degradation and the ground motion duration. These energy parameters are determined by integrating the equation of motion with respect to the relative structural displacement (u). The energy balance form of the equation of motion is given by:

$$\frac{m(\dot{u}_t)^2}{2} + \int_0^t c\dot{u}du + \int_0^t f_s du = \int_0^t m\ddot{u}_t du_g \qquad (5)$$

where u_t is the total structural displacement, f_s is the structural restoring force, u_g is the ground displacement, m is the system mass and c is the system damping. The first term in (5) is the *absolute* kinetic energy (E_k) at time t, the second term is the damping energy (E_d), the third term is the absorbed energy (E_a), and the right-hand side of (5) is the *absolute* input energy (E_i). An alternative form of (5) may also derived in terms of the *relative* kinetic and input energy, which can differ significantly from their *absolute* counterparts for extremely long and short period structures (Uang and Bertero, 1988). In the period range considered here the difference between absolute and relative quantities is negligible.

Before plunging into performing additional nonlinear dynamic analyses, we investigated the correlation between the response quantity used so far, namely the spectral displacement, S_d, and E_i or E_a to determine if an energy-based parameter is likely to provide additional insight into nonlinear response bias associated with the ground motion simulation techniques. In this correlation study, we considered the equivalent velocity form of the two energy parameters. The input energy-equivalent velocity (V_i) and absorbed energy-equivalent velocity (V_a) were chosen because they are commonly used energy measures for which attenuation models have been developed (Lawson, 1996; Chou and Uang, 2000). The equations for the energy-equivalent velocities are given by:

$$V_i = \sqrt{\frac{2(E_i)_{\max}}{m}} \quad ; \quad V_a = \sqrt{\frac{2(E_a)_{\max}}{m}} \qquad (6)$$

where m is the mass of the SDOF structure. Note that in the case of elastic analysis, the absorbed energy-equivalent velocity (V_a) converges to the pseudo-velocity of the SDOF system.

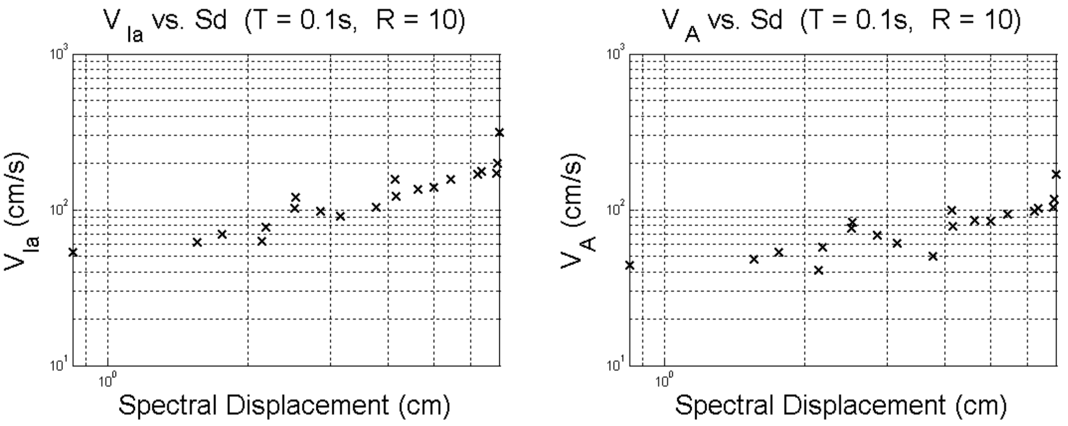

(a) T = 0.1s

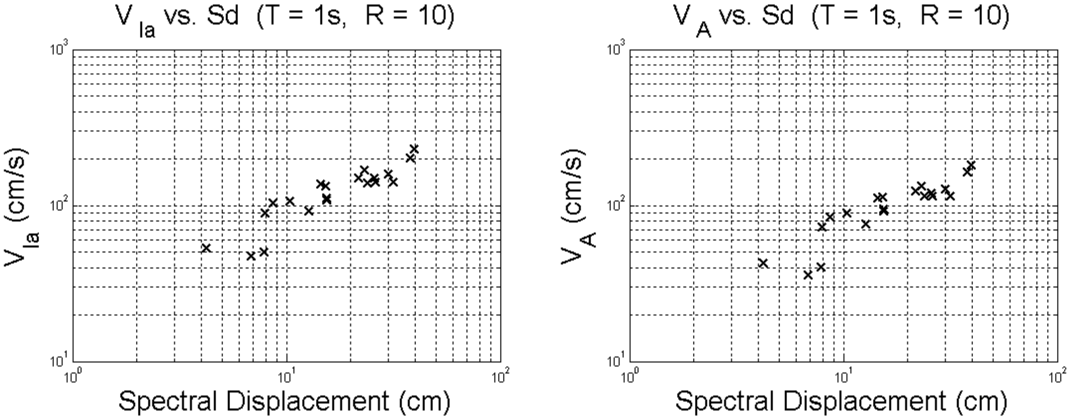

(b) T = 1s

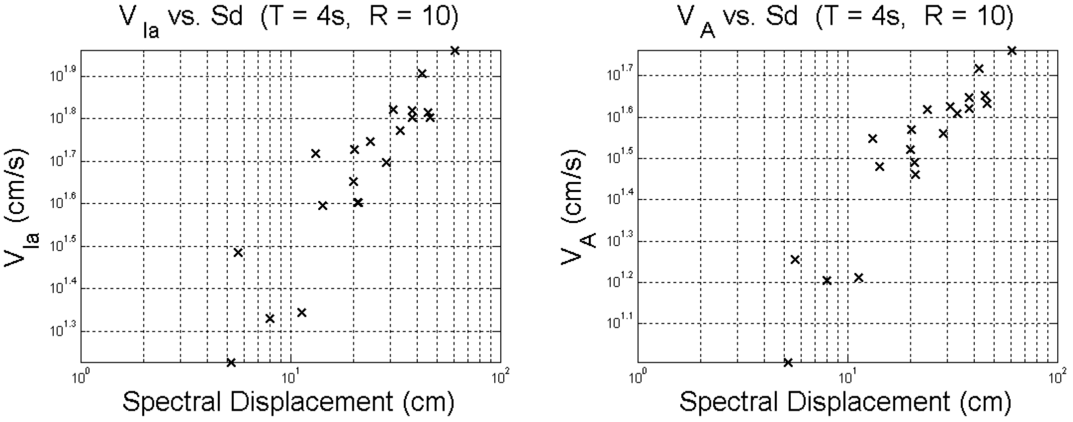

(c) T = 4s

Figure 25: Correlation between spectral displacement and both *absolute* input energy-equivalent velocity (V_i) (figures on the left) and absorbed energy-equivalent velocity (V_a) (figures on the right) for the twenty real records and constant-strength R = 10 at T = 0.1s, 1s, and 4s.

The three figures on the left-hand side of Figure 25 show the relationship between spectral displacement and *absolute* V_i for the twenty real records and constant-strength R equal to 10 at a structural periods of 0.1s (Panel a), 1s (Panel b), and 4s (Panel c).

Similar relationships between S_d and the absorbed energy-equivalent velocity, V_a, are displayed on the right-hand side of the same figure. The lowest constant-strength corresponding to R=10 was chosen to ensure that each of the twenty records produced significant nonlinear response to avoid mixing elastic and inelastic behavior in the computed absorbed energy results. It is apparent from Figure 25 that a strong linear relationship (i.e., correlation coefficients range from 0.84 to 0.92) exists between spectral displacement and each energy-equivalent velocity parameter. Hence, an investigation of nonlinear response bias associated with synthetic ground motion time histories using an energy-based parameter would most likely not bring any additional insights. One can conclude that the systematic differences between energy-based nonlinear responses computed by synthetic and real records are similar to those shown in the Figures 5 to 14.

5.0 Inelastic Response Spectra for NGA[14] Database and Related Software

Developers of synthetic ground motions may have the need to test on their own whether the nonlinear responses of SDOF oscillators subject to simulated ground motions are in agreement with those produced by real records for the same earthquake scenario. To help this effort we are going to compute the *nonlinear displacement response spectra* for R=2,4,6,8, and 10 for all the records in the soon-to-be-developed NGA database. The horizontal components of this database are rotated into the two directions normal and parallel to the fault strike. The spectra will be computed for 5%-damped nonlinear Single-Degree-of-Freedom (SDOF) oscillators with natural periods ranging from 0.1 to 4.0s, a bilinear backbone force-deformation curve with 5% post-yield hardening[15], and a hysteretic rule that has no degradation of either strength or stiffness. The nonlinear displacement response spectra will be provided in the same format as that used in the NGA project to store the elastic pseudo-acceleration response spectra for the same records. Also, we will provide a MATLAB subroutine to assist in the computation of nonlinear response spectra for additional records not included in this database.

Both the nonlinear spectra and the MATLAB subroutine with instructions for its use will be provided to PEER immediately after the NGA database is made available to us.

6.0 Conclusions

This study has investigated whether ground motion simulation techniques produce *nonlinear* displacement response spectra that are statistically distinguishable from those created by real records. The spectra were computed for nonlinear SDOF systems with bilinear backbone curves and no degrading stiffness or strength, a hardening ratio of 2%, and periods ranging from 0.1s to 4.0s. The level of response nonlinearity was defined by different levels of the force reduction factor, R, ranging from two (mild nonlinearity) to

---

[14] Next Generation Attenuation (NGA) Relationships Project funded by the PEER Lifelines Program.

[15] Note that in this study we have used SDOF systems with only 2% of post-yield hardening. The nonlinear displacement response spectra, however, will be provided for 5% hardening ratio rather than 2%. This choice is made to be consistent with a currently ongoing research project at Stanford University that is set to develop an attenuation relationship for S_d for SDOF systems with 5% hardening.

ten (severe nonlinearity). The investigation was done by means of a case study that used real accelerograms of the Northridge earthquake recorded at 20 stations located within 20km of the fault rupture. The nonlinear responses of the real records were considered as the target for the responses produced by the synthetic records that were provided by seven groups of seismologists. The comparisons were performed using the "average" of the responses generated by the two horizontal components at each station.

The agreement between elastic responses from records generated by these seven models and those from the real recordings for this case study has been thoroughly considered in another PEER-funded Project K201. We limit ourselves to saying here that six out of seven models were found to produce <u>*elastic*</u> spectra that have systematic deviations of different severity from the elastic spectra of real records, mostly (but not only) at short periods. The synthetic records seem to be more aggressive than those in nature in this period range. The deviations are statistically significant at the 10% level.

The core of this study, however, deals with the issue of whether any systematic deviations can be detected in the *post-elastic nonlinear* regime under the assumption that the elastic responses of real and synthetic records are in statistical agreement. To separate the elastic from the post-elastic nonlinear results, we considered the ratio of nonlinear to linear responses as the quantity to investigate for possible statistical discrepancies in the results generated by the synthetic models compared to those from real records. We found, again, that six out of seven models produced statistically biased nonlinear response spectra at least at some periods. Again, the systematic deviation, which is significant with 90% confidence, is more prominent at lower periods and at larger R values. Unlike the elastic case, however, the synthetic records tend to be more benign than real ones in producing nonlinear responses in stiff structures especially in the severe nonlinear range. One model, however, produces records that at long periods generate nonlinear responses for R=10 that are more severe than those from real records. The reason for the deficiency in the *nonlinear* responses to synthetic records at short periods lies in the difference that, on average, exists between the *linear* response spectra of these synthetic records and those of real ones in that period range. When the response of an SDOF system becomes severely nonlinear, its effective vibration period lengthens significantly and, therefore, it becomes dependent on the frequency content of the record in a fairly large bandwidth and not only in the neighborhood of the initial elastic natural period of vibration.

Besides the possible bias in the assessment of nonlinear structural responses introduced by the use of simulated records, we also compared the variability of nonlinear responses generated by simulated and real records. Most of these models appear to underestimate the record-to-record response variability from real records at shorter periods and, for high level of nonlinearity (e.g., R≥4) only, to overestimate it at longer periods. A more limited variability may become useful in practice when one wants to assess the median response of structures because, once any bias is corrected, the same accuracy can be achieved with fewer runs involving synthetic rather than real records. However, nonlinear response variability for simulated records lower or higher than that for real records can affect the safety assessment of structures against collapse, for example. Collapse probability estimates are controlled by extreme response values, and if they are less likely to occur for synthetic than for real records, such as it seems for some of the models in the short period range, then the "true" collapse probability would be underestimated and the safety assessment possibly misguided.

These conclusions about systematic differences in nonlinear responses from synthetic and real records were tested by evaluating their sensitivity to a) a two different schemes of averaging the ground motion horizontal components, b) to an alternative definition of R, and c) to the use of a cumulative energy-based ground motion parameter rather than peak displacement. We detected some differences but the conclusions were found to be sufficiently robust to all three of these tests.

We must emphasize, however, that all the conclusions drawn here were based on one case study involving only 20 stations and one earthquake. They may not apply to other cases and/or other simulation techniques. More research should be done to test the validity of these conclusions with additional test cases.

Acknowledgements

The authors are deeply indebted to the developers of the synthetic ground motion records for allowing their use in this comparative study. The help provided by Prof. Pedro de Alba in coordinating the release of the records and of the support information is also gratefully acknowledged. Finally, we are very thankful to Dr. Norman Abrahamson, Dr. Brian Chiou, and Cliff Roblee for their constant support that made this study possible. The PEER Lifelines Program provided the funding for this study.

References

Abrahamson, N.A., and Silva, W.J. (1997), "Empirical Response Spectral Attenuation Relations for Shallow Crustal Earthquakes", *Seismological Research Letters*, 68(1), 94-127.

Chou, C.C., and Uang, C.M. (2000), "An Evaluation of Seismic Energy Demand: An Attenuation Approach", PEER Report 2000/04, Univ. of California, Berkeley, California.

Lawson, R.S. (1996), "Site-Dependent Inelastic Seismic Demands", Ph.D. Thesis, Stanford Univ., Stanford, California.

Uang, C.M., and Bertero, V.V. (1988) "Use of Energy as a Design Criterion in Earthquake-Resistant Design", Rep. No. UCB/EERC-88/18, Earthquake Engineering Research Center, Univ. of California, Berkeley, California.

Veletsos AS, Newmark NM. (1960). "Effect of inelastic behavior on the response of simple systems to earthquake motions", *Proceedings of the 2nd World Conference on Earthquake Engineering*, Japan, vol. 2, 1960; 895–912.

Appendix A: Simulation Methodologies

Modeler 1: Dr. Igor Beresnev

Simulation of records for the Northridge earthquake was performed using the stochastic finite-fault ground-motion modeling technique. In the method, the fault plane is discretized into rectangular elements (subfaults), each of which is treated as a point source and assigned an average ω^{-2} spectrum with a stochastic component superimposed on it, in the same manner as for the stochastic point sources introduced by Boore (1983). The total number of subfaults is prescribed by the seismic moment of the target event. The rupture starts at the hypocenter and propagates radially outward with a prescribed constant velocity, triggering subsources as it reaches them. Subsource trigger times are randomized. The generated subfault acceleration time history is propagated to the observation point using empirical (distance-dependent) duration, geometric-attenuation, and anelastic-attenuation (Q) models, which are user-defined and thus can be adjusted to any specific region. The contributions from all subsources are summed up in the time domain at the observation point, with proper delays accounting for the propagation-distance differences. Site effects can be introduced by specifying a site amplification function and an Anderson-Hough low-pass filtering parameter "kappa".

The subfault size in the method is chosen from the empirical model established from the method calibration on 26 large earthquakes,

$$\log \Delta l = -2 + 0.4\,\mathbf{M},\ 4 \leq M \leq 8,$$

where log is base 10, Δl is the subfault linear dimension in km, and **M** is the moment magnitude of the target event (Beresnev and Atkinson, 2002, equation 1). The only free parameter of the simulations is the maximum-slip velocity on the fault, which reflects parametric variability in ground-motion predictions for future events.

The method is implemented in the FORTRAN code FINSIM (Beresnev and Atkinson, 1998a). The details of the technique and the results of its multiple calibrations are fully described in a series of publications by the authors (Beresnev and Atkinson, 1997, 1998a,b, 1999, 2002).

References

Beresnev, I. A. and G. M. Atkinson (1997). Modeling finite-fault radiation from the ω^n spectrum, *Bull. Seism. Soc. Am*. **87**, 67-84.

Beresnev, I. A. and G. M. Atkinson (1998a). FINSIM - a FORTRAN program for simulating stochastic acceleration time histories from finite faults, *Seism. Res. Lett*. **69**, 27-32.

Beresnev, I. A. and G. M. Atkinson (1998b). Stochastic finite-fault modeling of ground motions from the 1994 Northridge, California, earthquake. I. Validation on rock sites, *Bull. Seism. Soc. Am.* **88**, 1392-1401.

Beresnev, I. A. and G. M. Atkinson (1999). Generic finite-fault model for ground-motion prediction in eastern North America, *Bull. Seism. Soc. Am*. **89**, 608-625.

Beresnev, I. A. and G. M. Atkinson (2002). Source parameters of earthquakes in eastern and western North America based on finite-fault modeling, *Bull. Seism. Soc. Am*. **92**, 695-710.

Boore, D. M. (1983). Stochastic simulation of high-frequency ground motions based on seismological models of the radiated spectra, *Bull. Seism. Soc. Am.* **73**, 1865-1894.

Modeler 2: Dr. Douglas Dreger

The spatial and temporal description of fault slip from Wald *et al*. (1996) was used for Northridge record simulation. The Wald model is a multiple time window parameterization following the method of Hartzell and Heaton (1983), and the code for this model (Dreger and Kaverina, 2000; Kaverina et al., 2002) is the same. In the Wald model there are six time windows. Three describe how slip is released with time following the passage of a constant velocity rupture front, and for each time window there are two possible slip directions (55-degree and 145-degree (90 degrees apart)). The actual slip direction is the linear sum of these two components. The rise time and rupture velocity used by Wald to best fit the data were used in this model. The original set of ground motions assumed a triangular rise time function, and in the second set an omega-squared model was used. The second set is considered to be better since the records do not suffer from spectral nulls that the triangular function suffers from. I also assumed The 1D rock velocity model Wald specified was assumed in this model. Given the source parametric information and Green's functions from the 1D model the time histories were simulated by direct point-source summation where contributions from each of the subfaults for each time window and slip direction were delayed according to the rupture trigger time and summed. Non-rock sites were adjusted by multiplying by a factor representing the site amplification. Factors of 1.4 and 1.78 were used for NEHRP C and D sites, respectively. The factors were determined based on vertical SH wave amplifiction from the 1 km/s rock velocity to the corresponding NEHRP site velocities. The Wald *et al*. (1996) model is band limited due to their bandpass filtering of the data between 0.1 to 1 Hz.

References

Dreger, D. S. and A. Kaverina (2000). Seismic remote sensing for the earthquake source process and near-source strong shaking: a case study of the October 16, 1999 Hector Mine earthquake, Geophys. Res. Lett., 27, 1941-1944.

Hartzell, S. H., and T. H. Heaton (1983). Inversion of strong ground motion and teleseismic waveform data for the fault rupture history of the 1979 Imperial Valley, California, earthquake, Bull. Seism. Soc. Am., 73, 1553-1583.

Kaverina, A., D. Dreger, and E. Price (2002) The combined inversion of seismic and geodetic data for the source process of the 16 October 1999 M (sub w) 7.1 Hector Mine, California, Earthquake, Bull. Seism. Soc. Am., vol.92, no.4, pp.1266-1280.

Wald, D. J., T. H. Heaton, and K. W. Hudnut (1996). The slip history of the 1994 Northridge, California, earthquake determined from strong-motion, teleseismic, GPS and leveling data, Bull. Seism. Soc. Am., 86, s49-s70.

Modeler 3: Dr. Alexander Gusev *et al.*, **Institute of Volcanic Geology and Geochemistry**

The earthquake ground motion simulation technique in the model was developed by A.Gusev and V.Pavlov. It permits the simulation of realistic earthquake ground motions at a site and the ability to study the variability of such a motion. Eventually, a suite of design ground motions for scenario earthquake(s) may be generated. The technique combines a multiple-point-source version of a stochastic earthquake fault model and a suite of Green's functions calculated for layered weakly anelastic medium. The source model consists of a grid of point subsources with appropriate random time histories. A large number of properties/parameters of the simulated earthquake fault can be adjusted in order to: (1) tune the model to a particular seismological situation; and/or (2) to analyze the variability and uncertainties of strong motion prediction; or also (3) to generate a suite of motions that represents these uncertainties. These parameters consist of two large groups: (1) physical parameters that are fixed in a particular run of the simulator (their variation produces "parametric variability") and (2) "random" parameters that are essentially random seeds; they produce "model variability".

The source simulation module is based on the generalization of the classic Haskell (1966) stochastic fault model. Its important modifications are: (1) variable final slip governed by the power spectrum that is a power-law with respect to wave number; (2) circular rupture front with an arbitrary nucleation point and variable rupture velocity, random with a prescribed mean; (3) local slip velocity, or the moment rate of a subsource, is random, with a common duration or rise time. The grid of subsources covers the rupture. Individual subsources have no geophysical meaning, its number is arbitrary, and can be large if the site in question is located at a small distance from a large-magnitude fault. Instead of Haskell's omega-cube far field spectrum, the far-field spectrum of a simulated source is adjusted, in its high-frequency part, to a particular, preset, average (regional) spectral scaling law.

To calculate the pulse response of the layered elastic medium from double-couple source for distances less than 50 km, a version of the method of Alekseev and Mikhailenko (1976) is used, developed by Pavlov (2002) who advanced the "auxiliary functions" approach first introduced by Fatyanov and Mikhailenko (1988). The main advantage of this method is the lack of numerical instability inherent within propagator methods, because in the auxiliary function method all relevant exponential factors are below unity by absolute value. To ensure preset uniform numerical accuracy, the number of terms in the series expansion is selected adaptively. The developed numerical method provides accurate broad-band representation of ground motions in a layered medium, from static terms to high frequencies.

References

Alekseev A.S., Mikhilenko B.G. (1976). "Solution of Lamb problem for a vertically inhomogeneous elastic half-space", Izv. Akad. Nauk USSR, Fizika Zemli, 12, 11-25 (in Russian).

Fatyanov A.G., Mikhilenko B.G. (1988). A technique for calculation of non-stationary seismic wave fields in inelastic layered media. Dokl. Akad. Nauk USSR, 301, 834-839 (in Russian).

Pavlov V., (2002). "A convenient technique for calculating synthetic seismograms in a layered half-space". *Proceedings of the 4th International Conference* "Problems of Geocosmos", St. Petersburg, pp. 320-323.

Modeler 4: Dr. Lawrence Hutchings et al., **LLNL**

We numerically compute the discretized representation relation in a form that utilizes analytical slip functions and empirical or synthetic Green's functions. We derive rupture models that are consistent with physical understanding of how earthquakes rupture. An important claim in this approach is that we use physical and measurable parameters, so that they can be identified and bounded in a prediction. Discretization is small enough (for elemental areas) and short enough (for time steps) to model continuous rupture to the highest frequency of interest. Empirical Green's functions are obtained from recordings of small earthquakes with effectively a step-source time functions, and are adjusted for source location and focal mechanism solution to model the Green's function from each elemental area. We often use synthetic Green's functions for low frequencies, but we did not do that for this exercise. Rupture parameters include rupture geometry, hypocenter, rupture roughness, rupture velocity, healing velocity, Kostrov slip function, asperity size and location, and slip vector. Slip follows the Kostrov slip function for the time required for the rupture front to reach the fault edge from the hypocenter and for a healing phase to reach an element from the fault edge. We used a rupture velocity of 2.9 km/sec and a healing velocity of 2.3 km/s. Asperities are modeled as areas with high slip amplitudes and high stress drop. Fault displacement for asperities grade from the value of background rupture at the edge to greatest at the center. Stress drop is a dependent variable derived from the Kostrov slip function; for this exercise it has a value of 180 bars for the non-asperity portion of rupture, and between 300 and 600 bars for asperities. Stress drop also diminishes near the surface at the rate of the lithostatic load. Rupture roughness is modeled by a percentage of elemental areas having rise time randomly shortened to between 0.1 and 0.9 times the original value. Roughness is implemented by delaying an element's rupture time so that it finishes slip at the same time as neighboring elements. Elements with rough rupture have higher stress drop. In our model of the Northridge earthquake 20% of the elements had rough rupture. Our model of the Northridge earthquake was previously published (Hutchings, 1994) and utilized previously published reports of fault geometry, hypocenter, slip vector, and slip distribution. We did not iterate around rupture parameters to find the best fit to observed seismograms for this exercise.

References

Hutchings, L. (1994). "Kinematic earthquake models and synthesized ground motion using empirical Green's functions, *B.S.S.A.*, Vol 84, No. 4, pp. 1028-1050.

Modeler 5: Dr. Walter Silva

STOCHASTIC FINITE-SOURCE MODEL GROUND MOTION MODEL

In the near-source region of large earthquakes, aspects of a finite-source including rupture propagation, directivity source-receiver geometry, and saturation of high-frequency ($\geq$ 1 Hz) motions with increasing magnitude can be significant and may be incorporated into strong ground motion predictions. To accommodate these effects, a methodology that combines the aspects of finite-earthquake-source modeling techniques (Hartzell, 1978; Irikura 1983) with the stochastic point-source ground motion model has been developed to produce response spectra as well as time histories appropriate for engineering design (Silva et al., 1990; Silva and Stark, 1993; Schneider et al., 1993). The approach is very similar to the empirical Green function methodology introduced by Hartzell (1978) and Irikura (1983). In this case however, the stochastic point-source is substituted for the empirical Green function and peak amplitudes; PGA, PGV, and response spectra (when time histories are not produced) are estimated using random process theory.

Use of the stochastic point-source as a Green function is motivated by its demonstrated success in modeling ground motions in general and strong ground motions in particular (Boore, 1983, 1986; Silva and Stark, 1993; Schneider et al., 1993; Silva and Darragh, 1995) and the desire to have a model that is truly site- and region-specific. The model can accommodate a region specific Q(f), Green function sources of arbitrary moment or stress drop, and site specific kappa values and soil profiles. The necessity for having available regional and site specific recordings distributed over the rupture surface of a future earthquake or modifying possibly inappropriate empirical Green functions is eliminated.

For the finite-source characterization, a rectangular fault is discretized into NS subfaults of moment M_0^S. The empirical relationship

$$\log (A) = \mathbf{M} - 4.0, \quad A \text{ in km}^2 \qquad \text{(A1)}$$

is used to assign areas to both the target earthquake (if its rupture surface is not fixed) as well as to the subfaults. This relation results from regressing log area on **M** using the data of Wells and Coppersmith (1994). In the regression, the coefficient on **M** is set to unity which implies a constant static stress drop of about 30 bars. This is consistent with the general observation of a constant static stress drop for earthquakes based on aftershock locations (Wells and Coppersmith 1994). The static stress drop, defined by Equation A4, is related to the average slip over the rupture surface as well as rupture area. It is theoretically identical to the stress drop which defines the omega-square source corner frequency assuming the rupture surface is a circular crack model (Brune, 1970; 1971). The stress drop determined by the source corner frequency (or source duration) is usually estimated through the Fourier amplitude spectral density while the static stress drop uses the moment magnitude and an estimate of the rupture area. The two estimates for the same earthquake seldom yield the same values with the static generally being the smaller. In a recent study (Silva et al., 1997), the average stress drop based on Fourier amplitude spectra determined from an empirical attenuation relation (Abrahamson and Silva, 1997) is about 70 bars while the average static stress drop for the crustal earthquakes studied by Wells and Coppersmith (1994) is about 30 bars. These results reflect a general factor of about 2 on average between the two values. These large differences may simply be the result of using an inappropriate estimate of rupture area as the zone of actual slip is difficult to determine unambiguously. In general however, even for individual earthquakes, the two stress drops scale similarly with high static stress drops (> 30 bars) resulting in large high frequency (> 1 Hz for **M**. 5) ground motions which translates to high corner frequencies.

The subevent magnitude M_S is generally taken in the range of 5.0-6.5 depending upon the size of the target event. M_S 5.0 is used for crustal earthquakes with **M** in the range of 5.5 to 8.0 and M_S 6.4 is used for large subduction earthquakes with **M** > 7.5. The value of NS is determined as the ratio of the target event area to the subfault area. To constrain the proper moment, the total number of events summed (N) is given by the ratio of the target event moment to the subevent moment. The subevent and target event rise times (duration of slip at a point) are determined by the equation

$$\log \tau = 0.33 \log M_0 - 8.54 \tag{A2}$$

which results from a fit to the rise times used in the finite-fault modeling exercises, (Silva et al., 1997). Slip on each subfault is assumed to continue for a time τ. The ratio of target-to-subevent rise times is given by

$$\frac{\tau}{\tau} = 10^{0.5(\mathrm{M} - \mathrm{M_S})} \tag{A3}$$

and determines the number of subevents to sum in each subfault. This approach is generally referred to as the constant-rise-time model and results in variable slip velocity for nonuniform slip distributions. Alternatively, one can assume a constant slip velocity (as do Beresnev and Atkinson, 2002) resulting in a variable-rise-time model for heterogenous slip distributions. This approach was implemented and validations resulted in an overall "best" average slip velocity of about 70 cm/sec, with no significant improvement over a magnitude dependent rise time (Equation A3). The feature is retained as an option in the simulation code.

Recent modeling of the Landers (Wald and Heaton, 1994), Kobe (Wald, 1996) and Northridge (Hartzell et al. 1996) earthquakes suggests that a mixture of both constant rise time and constant slip velocity may be present. Longer rise times seem to be associated with areas of larger slip with the ratio of slip-to-rise time (slip velocity) being depth dependent. Lower slip velocities (longer rise times) are associated with shallow slip resulting in relatively less short period seismic radiation. This result may explain the general observation that shallow slip is largely aseismic. The significant contributions to strong ground motions appear to originate at depths exceeding about 4 km (Campbell, 1993; Boore et al., 1994) as the fictitious depth term in empirical attenuation relation (Abrahamson and Silva, 1997; Boore et al., 1997). Finite-fault models generally predict unrealistically large strong ground motions for large shallow (near surface) slip using rise times or slip velocities associated with deeper (> 4 km) zones of slip. This is an important and unresolved issue in finite-fault modeling and the general approach is constrain the slip to relatively small values or rise time to large values in the top 2 to 4 km. For the composite source model, the approach is to taper the subevent stress drop to zero from a depth of 5 km to the ground surface (Yehua Zeng, personal communication 1999). This approach is also followed in the stochastic finite source model. For earthquakes with significant shallow slip, greater than 20% moment released in the top 5 km, expected short period (< 1 - 2 second) motions are significantly lower (20 – 50%) than those of deep slip events, of the same magnitude (Silva et al., 1997). To capture this effect, shallow slip earthquakes are modeled with a 5 bar, rather than 30 bar subevent stress drop, over the entire rupture surface, based on the validation exercises (Silva et al., 1997). These results imply significantly different source processes affecting short periods between earthquakes which do not interact with low stresses associated with shallow rupture and those earthquakes which have deep rupture only. The implications to seismic hazard are obvious.

To introduce heterogeneity of the earthquake source process into the stochastic finite-fault model, the location of the sub-events within each subfault (Hartzell, 1978) are randomized as well as the subevent rise time ($\sigma_{\ln} = 0.8$). The stress drop of the stochastic point-source Green function is taken as 30 bars, consistent with the static value based on the **M** 5.0 subevent area using the equation

$$\Delta\sigma = \frac{7}{16}\left(\frac{M_e}{R_e^3}\right) \qquad \text{(Brune, 1970, 1971)} \qquad \text{(A4)}$$

where R_e is the equivalent circular radius of the rectangular sub-event.

Different values of slip are assigned to each subfault as relative weights so that asperities or non-uniform slip can be incorporated into the methodology. For validation exercises, slip models are taken from the literature and are based on inversions of strong motion as well as regional or teleseismic recordings. To produce slip distributions for future earthquakes, random slip models are generated based on a statistical asperity model with parameters calibrated to the published slip distributions. This approach has been validated by comparing the modeling uncertainty and bias estimates for the Loma Prieta and Whittier Narrows earthquakes using motion at each site averaged over several (30) random slip models to the bias and uncertainty estimates using the published slip model. The results show nearly identical bias and uncertainty estimates suggesting that averaging the motions over random slip models produces as accurate a prediction at a site as a single motion computed using the "true" slip model which is determined from inverting actual recordings.

The rupture velocity is taken as depth independent at a value of 0.8 times the shear-wave velocity, generally at the depth of the dominant slip. This value is based on a number of studies of source rupture processes which also suggest that rupture velocity is non-uniform. To capture the effects of non-uniform rupture velocity, a random component is added through the randomized location of the subevents within each subfault. The radiation pattern is computed for each subfault, a random component added, and the RMS applied to the motions computed at the site when modeling an average horizontal component. To model individual horizontal components, the radiation pattern for each subfault is used to scale each subfault’s contribution to the final summed motion.

The ground-motion time history at the receiver is computed by summing the contributions from each subfault associated with the closest Green function, transforming to the frequency domain, and convolving with the appropriate Green function spectrum. The locations of the Green functions are generally taken at center of each subfault for small subfaults or at a maximum separation of about 5 to 10 km for large subfaults. As a final step, the individual contributions associated with each Green function are summed in the frequency domain, multiplied by the RMS radiation pattern, and the resultant power spectrum at the site is computed. The appropriate duration used in the RVT computations for PGA, PGV, and oscillator response is computed by transforming the summed Fourier spectrum into the time domain and computing the 5 to 75% Arias intensity (Ou and Herrmann, 1990).

As with the point-source model, crustal response effects are accommodated through the amplification factor (A(f)) or by using vertically propagating shear waves through a vertically heterogenous crustal structure. Soil nonlinearity is accommodated through the equivalent-linear approximation. Propagation path damping, through the Q(f) model, is incorporated from each fault element to the site. Near-surface crustal damping is incorporated through the kappa operator (Equation A1). To model crustal propagation path effects, the raytracing method of Ou and Herrmann (1990) is applied from each subfault to the site.

Time histories may be computed in the process as well by simply adding a phase spectrum appropriate to the subevent earthquake. The phase spectrum can be extracted from a recording made at close distance to an earthquake of a size comparable to that of the subevent (generally **M** 5.0 to 6.5). Interestingly, the phase spectrum need not be from a recording in the region of interest (Silva et al., 1989). A recording in WNA (Western North America) can effectively be used to simulate motions appropriate to ENA (Eastern North America). Transforming the Fourier spectrum computed at the site into the time domain results in a computed time history which then includes all of the aspects of rupture propagation and source finiteness, as well as region specific propagation path and site effects.

References

Abrahamson, N.A. and W.J. Silva (1997). "Empirical response spectral attenuation relations for shallow crustal earthquakes." *Seismological Research Let.,* 68(1), 94-127.

Beresnev, I.A. and G. M. Atkinson (2002). “Source parameters of earthquakes in Eastern and Western North America.” *Bull. Seism. Soc. Am.,* 92(2), 695-710.

Boore, D.M., W.B. Joyner, and T.E. Fumal (1997). "Equations for estimating horizontal response spectra and peak acceleration from Western North American earthquakes: A summary of recent work." *Seism. Res. Lett.* 68(1), 128-153.

Boore, D.M., W.B. Joyner, and T.E. Fumal (1994). "Estimation of response spectra and peak accelerations from western North American earthquakes: and interim report. Part 2. *U.S. Geological Survey Open-File Rept.* 94-127.

Boore, D.M. (1986). "Short-period P- and S-wave radiation from large earthquakes: implications for spectral scaling relations." *Bull. Seism. Soc. Am.*, 76(1) 43-64.

Boore, D.M. (1983). "Stochastic simulation of high-frequency ground motions based on seismological models of the radiated spectra." *Bull. Seism. Soc. Am.*, 73(6), 1865-1894.

Brune, J.N. (1971). "Correction." *J. Geophys. Res.* 76, 5002.

Brune, J.N. (1970). "Tectonic stress and the spectra of seismic shear waves from earthquakes." *J. Geophys. Res.* 75, 4997-5009.

Campbell, K.W. (1993) "Empirical prediction of near-source ground motion from large earthquakes." in V.K. Gaur, ed., *Proceedings, Intern'l Workshop on Earthquake Hazard and Large Dams in the Himalya.* INTACH, New Delhi, p. 93-103.

Hartzell, S., A. Leeds, A. Frankel, and J. Michael (1996). "Site response for urban Los Angeles using aftershocks of the Northridge earthquake." *Bull. Seism. Soc. Am.*, 86(1B), S168-S192.

Hartzell, S.H. (1978). "Earthquake aftershocks as Green's functions." *Geophys. Res. Letters*, 5, 1-4.

Irikura, K. (1983). "Semi-empirical estimation of strong ground motions during large earthquakes." *Bull. Disaster Prevention Res. Inst.*, Kyoto Univ., 33, 63-104.

Ou, G.B. and R.B. Herrmann (1990). "Estimation theory for strong ground motion." *Seism. Res. Letters.* 61.

Schneider, J.F., W.J. Silva, and C.L. Stark (1993). "Ground motion model for the 1989 **M** 6.9 Loma Prieta earthquake including effects of source, path and site." *Earthquake Spectra*, 9(2), 251-287.

Silva, W.J., N. Abrahamson, G. Toro, and C. Costantino (1997). "Description and validation of the stochastic ground motion model." Submitted to Brookhaven National Laboratory, Associated Universities, Inc. Upton, New York.

Silva, W.J. and R. Darragh (1995). "Engineering characterization of earthquake strong ground motion recorded at rock sites." Palo Alto, Calif:Electric Power Research Institute, TR-102261.

Silva, W.J. and C.L. Stark (1993) "Source, path, and site ground motion model for the 1989 **M** 6.9 Loma Prieta earthquake." CDMG draft final report.

Silva, W. J., R. Darragh, C. Stark, I. Wong, J. C. Stepp, J. Schneider, and S-J. Chiou (1990). "A Methodology to Estimate Design Response Spectra in the Near-Source Region of Large Earthquakes Using the Band-Limited-White-Noise Ground Motion Model". *Procee. of the Fourth U.S. Conf. on Earthquake Engineering,* Palm Springs, California. 1, 487-494.

Silva, W.J., R.B. Darragh, R.K. Green and F.T. Turcotte (1989). *Estimated Ground Motions for a new madrid Event.* U.S. Army Engineer Waterways Experiment Station, Wash., DC, Misc. Paper GL-89-17.

Wald, D.J. (1996). "Slip history of the 1995 Kobe, Japan, earthquake determined from strong motion, teleseismic, and geodetic data." *J. of Physics of the Earth,* in press.

Wald, D.J. and T.H. Heaton (1994). "Spatial and temporal distribution of slip for the 1992 Landers, California, earthquake." *Bull. Seism. Soc. Amer.*, 84(3), 668-691.

Wells, D.L. and K.J. Coppersmith (1994). "New empirical relationships among magnitude, rupture length, rupture width, rupture area, and surface displacement." *Bull. Seism. Soc. Am.* 84(4), 974-1002.

Modeler 6: Dr. Paul Somerville et al., **URS Corporation**

The primary reference for the simulation procedure and its application to the 1994 Northridge earthquake is Somerville et al. (1996), pages S-116 through S-118. The application of the simulation procedure to the generation of ground motion time histories and response spectra at the sites of steel buildings in the FEMA/SAC Steel Project is described in Somerville et al. (1995).

The simulation procedure is based on rigorous seismological representations of the earthquake source and wave propagation. To simulate broadband time histories, a hybrid method is used which computes the ground motions separately in the short period and long period ranges and then combines them into a single time history (e.g. Somerville et al., 1996). The earthquake source is represented as a shear dislocation. The ground motion time history is calculated in the time domain using the elastodynamic representation theorem. In order to represent near-fault effects, ground motion simulations need to be based on the summation of complete Green's functions that contain near-, intermediate-, and far-field terms. This is done using the elastodynamic representation theorem, which states that the ground motion U(t) can be calculated from the convolution of the slip time function D(t) on the fault with the Green's function G(t) for the appropriate distance and depth, integrated over the fault rupture surface (Aki and Richards, 1980):

$$U(t) = \sum D(t) * G(t)$$

At long periods, theoretical source models including the theoretical radiation pattern are used, while at short periods, empirical source functions derived from the recordings of small earthquakes are used that incorporate the radiation pattern empirically. For both procedures, the fault rupture plane is discretized into a number of equal size sub-fault regions. Fault asperities are represented by spatial variations in the amount of slip or slip velocity. The Green's functions are generated using frequency-wavenumber integration for long-periods and generalized rays for short periods.

References

Aki, K. and P.G. Richards (1980). *Quantitative Seismology: Theory and Methods*. W.H. Freeman & Co.

Somerville, P., C.K. Saikia, D. Wald, and R. Graves (1996). Implications of the Northridge earthquake for strong ground motions from thrust faults, *Bull. Seism. Soc. Am.,* 86, S115- S125.

Somerville, P.G., R.W. Graves, and C.K. Saikia (1995a). Characterization of Ground Motions during the Northridge Earthquake of January 17, 1994. *Program to Reduce the Earthquake Hazards of Steel Moment Frame Buildings,* SAC Report 95-03.

Modeler 7: Dr. Yuehua Zeng

Based on fundamental earthquake source physics and seismic wave propagation, we have developed and improved a numerical simulation procedure to compute synthetic strong motion seismogram using a composite source model (Zeng et al., 1994). The method has been successful in generating realistic strong motion seismograms. The realism is demonstrated by comparing synthetic strong motions with observations from the recent California earthquakes at Landers, Loma Prieta (Su et al., 1994a,b) and Northridge (Zeng and Anderson, 1996; Anderson and Yu, 1996; Su et al., 1998), earthquakes in the eastern US (Ni et al., 1999) and earthquakes in Guerrero, Mexico (Zeng et al., 1994; Johnson, 1999), Turkey (Anderson et al., 2001) and India (Khattri et al, 1994; Zeng et al, 1995). We have also successfully applied the method for earthquake engineering applications to compute the ground motion of scenario earthquakes. During the process of continuing development, we have included scattering waves from small scale heterogeneity structure of the earth, site specific ground motion prediction using weak motion site amplification, and nonlinear soil response using the geotechnical engineering model. We have evaluated the numerical procedure for simulating near-fault long-period ground motions and rupture directivity, revisiting some of the above earthquake events, including Loma Prieta, Landers and Northridge. We also tested its ability to predict the near-fault ground motion observation from the 1979 Imperial Valley, California earthquake and the 1995 Kobe event (Zeng and Anderson, 2000).

The composite source model assumes a large earthquake is a superposition of smaller subevents that all break during the earthquake rupture processes. The number and radius of the subevents follow the Guttenberg and Richter frequency-magnitude relation given in form of a power law distribution of radii, $N(r) \sim r^{-p}$, where p is the fractal dimension. The source is kinematic, but this source description has the capability to generate realistic accelerograms with the proper frequency content (Zeng et al., 1994), and has a capability to predict ground motions (e.g. Anderson and Yu, 1996; Anderson et al., 2002). Also, it is possible, using a genetic algorithm, to find specific composite sources that are consistent with both the statistics and the phase of observed records (e.g. Zeng and Anderson, 1996). Several physical parameters of earthquake source (radiated energy, stress drops) can be expressed in terms of the composite source model parameters (Anderson, 1997). The high frequency radiation of the model is controlled by the subevent stress drops, maximum subevent radius and rupture velocity.

References

Anderson, J., Graves, R, Zeng, Y., Somerville, P. (2002). Blind prediction of near-fault strong ground motions, AGU fall annual meeting, Abstract S72F-1349.

Anderson, J. G., Y. Zeng and H. Sucuoglu (2001). Analysis of accelerations from the Dinar, Turkey earthquake, *Bull. Seis. Soc. Am.* **91**, 1433-1445.

Anderson, J. G. (2000). Expected shape of regressions for ground-motion parameters on rock, *Bull. Seism. Soc. Am.* **90,** no. 6B, S43–S52.

Anderson, J. G. (1997). Seismic energy and stress drop parameters for a composite source model. *Bull. Seism. Soc. Am.* **87**, 85-96.

Anderson , J. G. and G. Yu (1996). Predictability of strong motions from the Northridge, California, earthquake, Bull. Seism. Soc. Am. No. 86, 1B, S100-S114.

Johnson, M. (1999). Composite source model parameters for large earthquakes (M>5.0) in the Mexican subduction zone, M. S. thesis, University of Nevada, Reno.

Keaton, J. R. (2000). Synthetic seismograms for normal-faulting earthquakes using the composite source model, Report of the EERI-FEMA National Earthquake Hazards Reduction Program 1999 Professional Fellowship in Earthquake Engineering.

Khattri, K. N., Y. Guang, J. G. Anderson, J. N. Brune and Y. Zeng (1994). Seismic hazard estimation using modelling of earthquake strong ground motions: A brief analysis of 1991 Uttarkashi earthquake, Himalaya and prognostication for a great earthquake in the region, *Current Science*, 67, 343-353

Lee, M. K. W. and W. D. L. Finn (1982). Dynamic effective stress response analysis of soil deposites with energy transmitting boundary including assessment of liquefaction potential, Rev., Dept. of Civil Eng., Soil Mechanics Serirs No. 38, the Univ. of British Columbia, Vancouver, Canada.

Lee, Y., J. G. Anderson, and Y. Zeng (2000). Evaluation of empirical ground-motion relations in southern California, *Bull. Seism. Soc. Am.***90,** no. 6B, S136–S148.

Luco, J. E. and R. J. Apsel (1983). On the Green's function for a layered half-space, part I, *Bull. Seism. Soc. Am*. 73, 909-929.

Ni., S.-D., J. G. Anderson, Y. Zeng (1999). Comparison of strong ground motions from the 1988 Seguenay earthquake with the synthetic simulations using the composite source model, manuscript in progress.

Su, Feng, Y. Zeng and J. G. Anderson (1994a). Simulation of the Loma Prieta earthquake strong ground motion using a composite source model, EOS, Trans. A.G.U., **75**, 44, p448.

Su, F., Y. Zeng and J. G. Anderson (1994b). Simulation of Landers earthquake strong ground motion using a composite source model, Seism. Res. Lett., **65**, p52.

Su, F., J. G. Anderson and Y. Zeng (1998). Study of weak and strong motion including nonlinearity in the Northridge, California, earthquake sequence, *Bull. Seis. Soc. Am*. **88**, 1411-1425.

Zeng, Y., J. G. Anderson and G. Yu (1994). A composite source model for computing realistic synthetic strong ground motions, *J. Res. Lett.*, **21**, 725-728.

Zeng, Y., J. G. Anderson and Feng Su (1995). Subevent rake and scattering effects in realistic strong ground motion simulation, *Geophy. Res. Lett*, **22**, 17-20.

Zeng, Y. and J. G. Anderson (1996). A composite source modeling of the 1994 Northridge earthquake using Genetic Algorithm,Bull. Seism. Soc. Am. 86, No. 1B, 71-83.

Zeng, Y. and J. G. Anderson (2000). Earthquake source and near-field directivity modeling of several large earthquakes, EERI Proceedings for the Sixth International Conference on Seismic Zonation.

Zeng, Y. (2002). Final Technical Report on Validation of 1-D Numerical Simulation Procedures, Final Technical Report, PEER Project 1C02, Task 1: Earthquake ground motion, Seismological Lab, University of Nevada – Reno.

13th World Conference on Earthquake Engineering
Vancouver, B.C., Canada
August 1-6, 2004
Paper No. 2405

DYNAMIC VERSUS STATIC COMPUTATION OF THE RESIDUAL CAPACITY OF A MAINSHOCK-DAMAGED BUILDING TO WITHSTAND AN AFTERSHOCK

Nicolas LUCO[1], Paolo BAZZURRO[2], and C. Allin CORNELL[3]

SUMMARY

The residual capacity against collapse of a mainshock-damaged building can be coupled with the aftershock ground motion hazard (demand) at its site to make an objective decision regarding the occupancy of the building based on its probability of collapse in an aftershock. For a case-study building, a relatively simple nonlinear static-pushover approach to computing residual capacities is found to underestimate the median results of more accurate nonlinear dynamic analyses. By reflecting the dependence observed from the dynamic analyses of residual capacity on residual roof drift, a "calibrated" static approach is proposed that computes more consistent residual capacities.

INTRODUCTION

In the aftermath of a major earthquake, structural engineers must assess whether damaged buildings can continue to be occupied, with due consideration to the threat of aftershocks. An objective and quantifiable criterion that can be used to green/yellow/red-tag a damaged building is the probability (within a specified time period) of its localized or complete collapse in an aftershock. Computing this collapse probability can be accomplished by convolving the aftershock ground motion hazard (demand) at the site, e.g., [1], with the probabilistic residual capacity of the damaged building to withstand aftershock shaking (i.e., its "aftershock fragility"). The residual capacity can be computed via nonlinear structural analyses, e.g., [2,3,4,5], but if a tagging decision needs to be made soon after the mainshock, such analyses should be conducted *a priori* for a range of potential post-mainshock damage states.

As part of Phase I of a project for the Pacific Earthquake Engineering Research Lifelines (PEER-LL) Program and Pacific Gas & Electric, Bazzurro *et al.* [6] have developed guidelines for tagging that involve nonlinear structural analyses performed prior to a mainshock to determine the residual capacity of a given building in several different states of potential damage. To be more practical, the guidelines call for a static-pushover (SPO) analysis and the use of a tool called SPOIDA [7,8] to infer dynamic response rather than carrying out more accurate nonlinear dynamic analyses (NDA's). Phase II of the PEER-LL project has been to verify whether the results of the "static" computations called for in the guidelines are

---

[1] Senior Analysis Engineer, AIR Worldwide Corporation, USA (nluco@air-worldwide.com)
[2] Manager – Engineering Analysis, AIR Worldwide Corporation, USA (pbazzurro@air-worldwide.com)
[3] Professor, Stanford University, USA (cornell@stanford.edu)

consistent with those of a dynamic approach involving back-to-back NDA's of the building model for numerous mainshock and aftershock pairs of earthquake records. Part of this verification phase is summarized in this paper. For a summary of the guidelines by Bazzurro *et al.* [6], refer to the 13WCEE paper 1708 [9].

OBJECTIVES

The general objectives of this paper are three-fold: (i) to demonstrate for a case-study building the dynamic and the static approaches to computing the residual capacity of a mainshock-damaged building, (ii) to compare the results of the dynamic and the static computations, and (iii) to use the results of the dynamic approach to calibrate the static approach. In all of the approaches, residual capacities are computed for a range of potential post-mainshock damage states obtained via static or dynamic analyses.

CASE-STUDY BUILDING

The building considered in this paper is borrowed from one of the case studies presented in the guidelines by Bazzurro *et al.* [6]. The building is a 3-story steel moment-resisting frame (SMRF) constructed in San Francisco in 1989. It is roughly symmetric, so only one of its 3-bay MRF's is modeled. The beam-column connections are modeled as brittle, with fracture occurring at a plastic hinge rotation of 0.03 radians, at which point the moment strength drops to 30% of the plastic value. A static pushover (SPO) curve for the building model computed using the RAM-Perform V1.04 [10] structural analysis program is shown in Figure 1. The SPO analysis is ceased when the first shear-tab fails, which is assumed to occur at a plastic hinge rotation of 0.07 radians. At this point of local collapse, the SPO curve is assumed to drop to zero base shear.

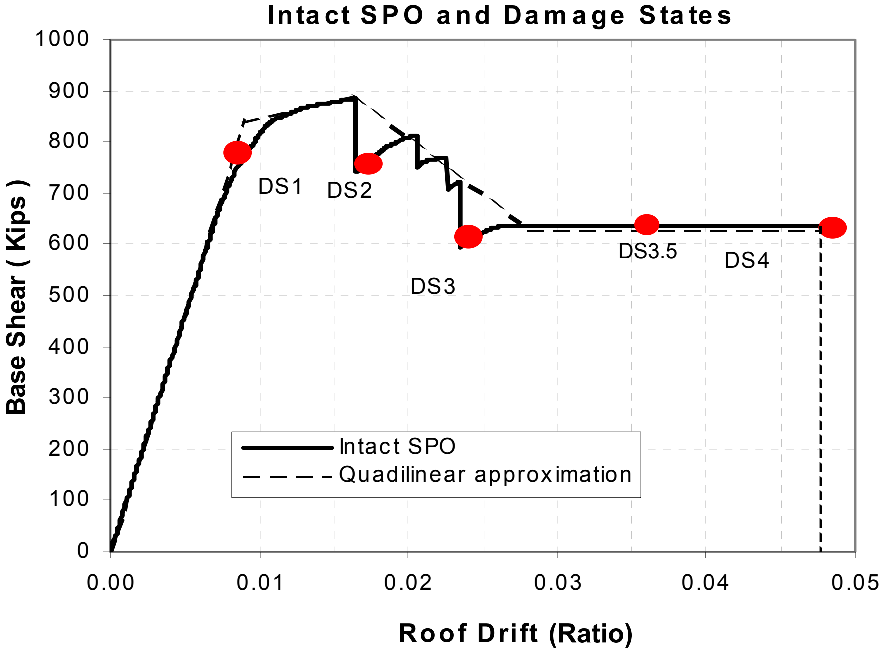

Figure 1. Nonlinear static-pushover (SPO) curve for the intact, or undamaged, three-story SMRF case-study building. The quadrilinear approximation is the SPO curve for the SDOF idealizations of this first-mode dominated building that are analyzed in this paper. The five post-mainshock damage states considered are also identified. This figure was excerpted, with few modifications, from [6].

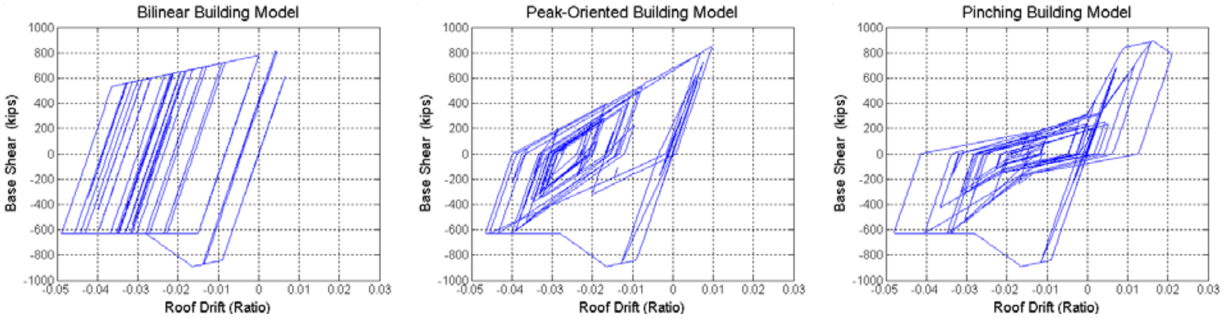

Figure 2. Examples of the hysteretic behavior of the bilinear, peak-oriented, and pinching SDOF building models analyzed in this paper. The backbone for all three models is the same as the quadrilinear approximation of the SPO curve for the first-mode dominated case-study building (shown in Figure 1).

Mainly because the dynamic computation of residual capacity involves a large number of NDA's, three single-degree-of-freedom (SDOF) idealizations of the first-mode-dominated 3-story building model described above are analyzed in this paper. All three SDOF building models have the same fundamental period (T_1=0.73s) and approximately the same force-deformation backbone curve (see Figure 1) as the full multi-degree-of-freedom (MDOF) building model. The three SDOF models differ only in their hysteretic behaviors. As illustrated in Figure 2, the hysteresis rules considered are bilinear, peak-oriented (or "Clough" [11]), and pinching, which are the three options available in the SDOF time-history analysis program used [12].

POST-MAINSHOCK DAMAGE STATES

The five post-mainshock damage states considered for the case-study building are identified on its SPO curve in Figure 1 above. Note that DS1 corresponds to the onset of damage, so in this state the building is still in its intact, or pre-mainshock, condition. At the opposite end of the range of potential damage states, DS4 corresponds to collapse, or in this case local failure of a shear-tab. As defined in the guidelines case-study by Bazzurro *et al.* [6,9], DS2 and DS3 correspond to fracture of the exterior and interior beam-column connections at the first floor, respectively. The intermediate DS3.5 is added in this paper without regard to the corresponding physical damage, but it could be determined from the SPO results. These descriptions of physical damage could be used by an inspector to determine which damage state the case-study building is in after an earthquake.

Also based on the SPO results, each post-mainshock damage state is linked to a peak (during the mainshock) roof drift, as illustrated in Figure 1 above and summarized in Table 1 below. For the SDOF models of the case-study building, these peak roof drifts are synonymous with the associated post-mainshock damage states. In fact, in this paper the results for each damage state are usually plotted versus the corresponding peak roof drift. To estimate results for damage states not considered in this paper, one could interpolate between the corresponding peak roof drifts.

Table 1. Peak roof drift (normalized by roof height) associated with each of the five post-mainshock damage states identified in Figure 1 on the SPO curve for the case-study building.

Peak Roof Drift (Ratio)				
DS1 (Intact)	DS2	DS3	DS3.5	DS4 (Collapsed)
0.009	0.016	0.024	0.036	0.048

DEFINITION OF RESIDUAL CAPACITY

In the guidelines by Bazzurro *et al.* [6,9], the residual capacity of a building in a given post-mainshock damage state is defined as the smallest ground motion spectral acceleration (at T_1 and a damping ratio of 5%) that would induce localized or complete collapse in an aftershock. This residual capacity is a random quantity in the sense that it varies across potential aftershock ground motions (among other things). In this paper, only the medians (calculated as the geometric means) of the residual capacity as computed via the dynamic and static approaches are compared. Although not reported here, the dispersion of the residual capacity, which can be coupled with the median to arrive at the "aftershock fragility" of a mainshock-damaged building, has also been computed.

DYNAMIC COMPUTATION OF RESIDUAL CAPACITY

The dynamic approach to computing the median residual capacity of a building in each post-mainshock damage state involves the following steps:

1. Obtain multiple realizations of the building in each post-mainshock damage state by performing NDA of the intact building model subjected to multiple mainshock ground motions, each one scaled (in amplitude only) to induce the roof drift associated with each damage state.
2. Compute residual capacities for each of these realizations of the building by subjecting them, via NDA, to aftershock ground motions scaled to induce the roof drift associated with collapse.
3. Calculate the median residual capacity for each damage state over all the pairs of mainshock-damaged building realization (Step 1) and potential aftershock ground motion (Step 2).

The details of these steps and their results for the three SDOF models of the case-study building are discussed in the subsections below. To simplify the comparison of results from this dynamic approach with those from the static approach presented in the next section, the same 30 earthquake recordings used by Vamvatsikos [7,8] in developing the SPO2IDA tool are also used here. Furthermore, this single set of earthquake recordings is used to represent both potential mainshock and aftershock ground motions. If, instead, different sets of earthquake recordings are used to represent mainshocks and aftershocks, the median residual capacity for each damage state may change, but its value relative to that for DS1 (e.g., see Figure 9 below) is expected to remain the same.

Step 1: NDA of intact building subjected to mainshocks

In addition to multiple realizations of the building in each post-mainshock damage state, three by-products of the NDA's of the intact building model subjected to multiple mainshock ground motions are (i) incremental dynamic analysis (IDA) curves, (ii) residual roof drifts in each damage state, and (iii) capacities against collapse of the intact building. These results are noteworthy because (i) the IDA curves depict the mainshock spectral accelerations that lead to each damage state, which can be used before an earthquake has occurred to compute the annual probability of experiencing each damage state [6,9], (ii) the residual roof drifts have an effect on the residual capacities, as demonstrated later in this paper, and (iii) the intact capacities serve as a basis of comparison for the residual capacities. The three by-products are also results of the static approach demonstrated in the next section. In the section after the next, those static results are compared with the dynamic results summarized in the subsections below.

IDA Curves

Scaling an earthquake record to obtain a realization of the building in each post-mainshock damage state is an iterative process not unlike computing a constant ductility response spectrum. The first by-product of this iterative scaling is an IDA curve that relates the spectral acceleration of the ground motion (proportional to the scale factor) to the peak roof drift of the building. Figure 3(a) shows, for the

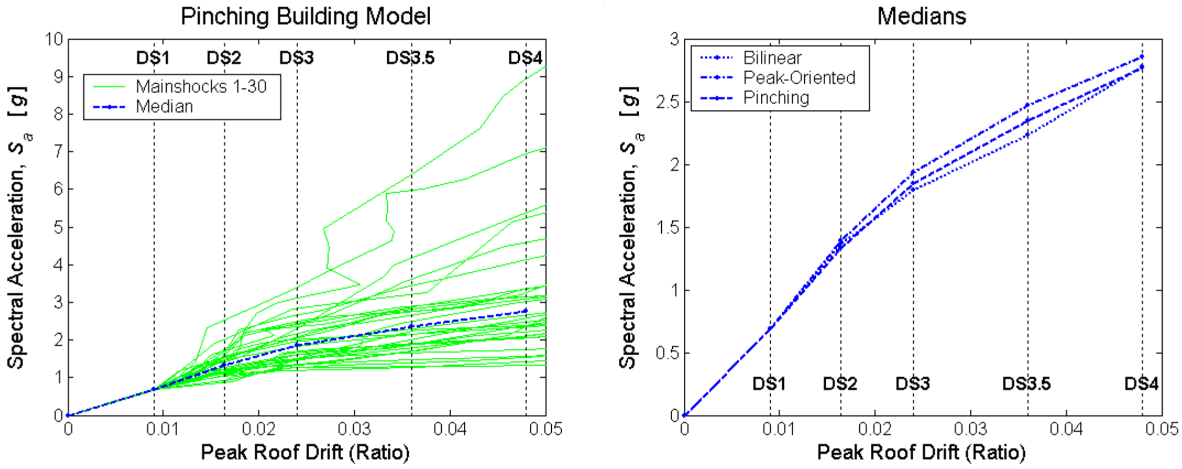

Figure 3. Incremental Dynamic Analysis (IDA) curves computed while obtaining multiple realizations of each post-mainshock damage state. Panel (a) shows, for the pinching building model, the individual IDA curves for the 30 mainshock ground motions considered. Panel (b) shows the median IDA curves across the 30 mainshocks for all three of the case-study building models.

pinching model of the case-study building, the 30 IDA curves obtained for the 30 "mainshock" earthquake records. Also shown in Figure 3(a) is a median IDA curve established by connecting the median spectral accelerations that induce the peak roof drifts associated with the five damage states. The median IDA curves for the bilinear, peak-oriented, and pinching building models are shown in Figure 3(b). Note their similarity despite the differences in hysteretic behavior.

Residual Roof Drifts

Each earthquake record that is scaled to induce the peak roof drift associated with a post-mainshock damage state will also induce a residual roof drift. For the 30 mainshock earthquake records and the pinching building model, the residual roof drifts (absolute values) in each damage state are plotted in Figure 4(a); also plotted is a curve connecting the median residual roof drift values for the five damage states. The median residual roof drifts for all three building models are plotted in Figure 4(b).

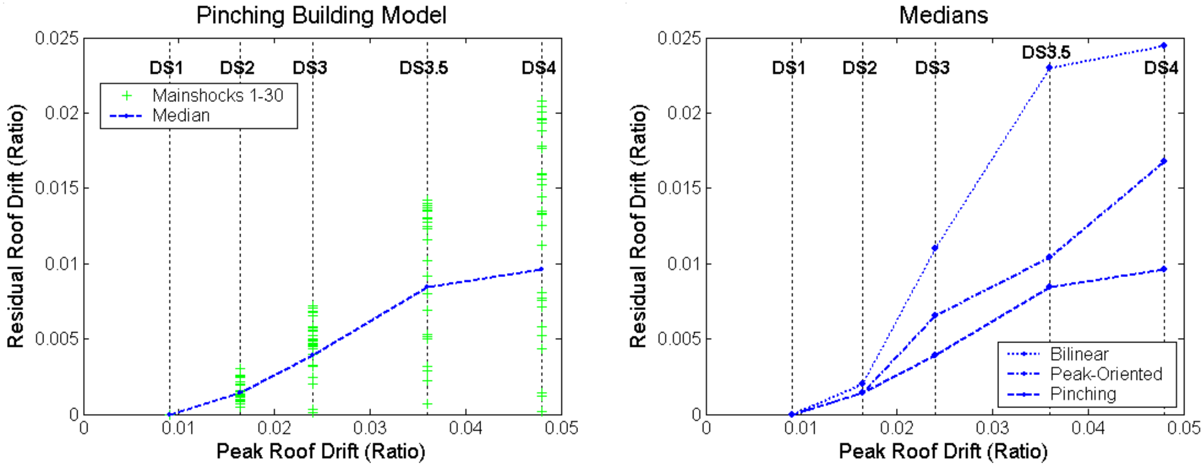

Figure 4. Residual roof drifts for each post-mainshock damage state (or associated value of peak roof drift). Panel (a) shows, for the pinching building model, the residual roof drifts caused by the 30 mainshock ground motions considered. Panel (b) shows the median residual roof drift across the 30 mainshocks for all three of the case-study building models.

Recall that in DS1 the building is still elastic, so there is no residual roof drift. As the damage (or peak roof drift) increases, so does the median residual roof drift, particularly for the bilinear building model. The stiffness reductions in the peak-oriented and pinching hysteresis loops have a "self-centering" effect that leads to relatively small residual drifts, as observed by other researchers as well, e.g., [13,14,15].

Intact Capacities

From each of the median IDA curves in Figure 3(b) above, the spectral acceleration that induces the peak roof drift associated with collapse (i.e., DS4) is the median capacity of the intact building. For the bilinear, peak-oriented, and pinching models of the case-study building, these median intact capacities are 2.78*g*, 2.86*g*, and 2.77*g*, respectively. Like the median IDA curves themselves, the median intact capacities for the three building models are very similar (within 4% of each other). Note that these intact capacities are also the residual capacities in DS1, which provides a convenient basis of comparison for the median residual capacities computed in the next step for the other damage states.

Step 2: NDA of mainshock-damaged building subjected to aftershocks

For each realization of a mainshock-damaged building created in Step 1, residual capacities are computed by performing NDA with aftershock earthquake records, each one scaled to induce the peak roof drift associated with collapse. As for the mainshocks in Step 1, scaling the aftershocks is an iterative process. Unlike the mainshocks, however, scaling the aftershocks by positive and negative factors typically results in two different spectral accelerations (both absolute values) that trigger collapse. The smaller value is kept, since the residual capacity is defined (above) as the smallest aftershock spectral acceleration that induces collapse. Over all of the realizations and mainshocks considered in this paper, the larger of the two spectral accelerations is on average 1.23 times and at most 3.19 times the smaller value.

In effect, back-to-back mainshock-aftershock NDA's are performed in Steps 1-2, as illustrated in Figure 5 for the pinching building model. In this example, the mainshock NDA produces a realization of the building in DS3 (i.e., peak roof drift ratio of 0.024), whereas the aftershock NDA results in collapse (at a peak roof drift of 0.048). The spectral acceleration of the aftershock ground motion is the residual capacity for this particular realization of the pinching building model in DS3. The residual capacities for all 30x30 of the mainshock-aftershock pairs considered are listed in Table 2.

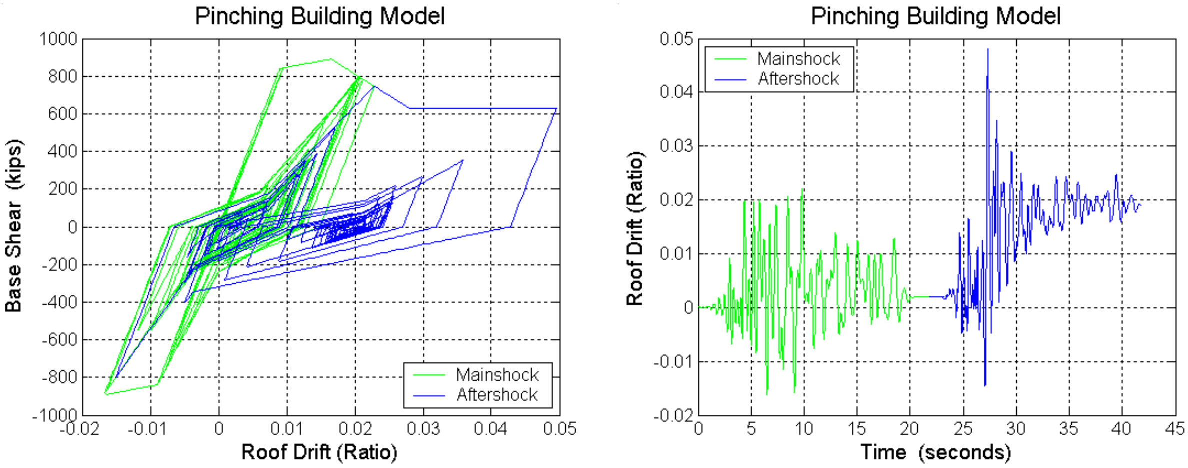

Figure 5. Example hysteresis loops and roof drift time histories from the back-to-back mainshock-aftershock dynamic analyses performed to compute the residual capacity of a mainshock-damaged building. The mainshock ground motion is scaled to induce the peak roof drift associated with DS3, and the aftershock ground motion is scaled to induce the peak roof drift associated with collapse (DS4).

Table 2. Residual capacities (i.e., minimum spectral accelerations to cause collapse) of the pinching building model in damage state DS3 for the 30x30 potential mainshock-aftershock pairs considered.

Mainshock	Residual S_a Capacity (g) for Aftershock																													
	1	2	3	4	5	6	7	8	9	10	11	12	13	14	15	16	17	18	19	20	21	22	23	24	25	26	27	28	29	30
1	1.68	2.83	3.19	2.10	3.30	2.48	2.95	2.24	2.19	2.09	3.74	2.13	5.41	4.72	1.90	1.04	2.48	1.41	1.34	3.88	2.03	2.37	2.72	7.75	2.18	4.19	2.70	4.03	1.39	2.11
2	1.67	2.73	3.16	1.97	3.25	2.46	2.87	2.24	2.16	2.03	3.37	2.06	5.30	4.12	1.86	1.05	2.48	1.33	1.34	3.71	1.95	2.27	2.68	7.20	2.09	3.99	2.62	4.13	1.34	2.11
3	1.67	2.67	3.14	1.96	3.32	2.46	2.83	2.12	2.19	2.02	3.37	2.06	5.29	4.20	1.84	1.06	2.34	1.32	1.34	3.71	1.96	2.25	2.70	6.80	2.07	4.04	2.65	4.17	1.32	2.11
4	1.72	3.38	3.38	2.10	3.30	2.49	3.97	2.31	2.06	2.47	5.10	2.13	6.34	5.13	2.07	0.95	2.82	1.41	1.42	5.10	2.00	2.37	2.88	8.91	2.55	5.00	2.87	4.05	1.57	2.78
5	1.66	2.63	3.09	1.68	3.25	2.43	2.78	2.00	2.18	1.98	3.37	2.06	5.22	4.14	1.79	1.06	2.25	1.30	1.34	3.64	1.95	2.22	2.66	6.54	2.04	3.95	2.69	3.89	1.27	2.11
6	1.66	2.62	3.09	1.68	3.24	2.43	2.78	2.00	2.18	1.97	3.37	2.06	5.22	4.14	1.79	1.06	2.24	1.30	1.34	3.62	1.95	2.22	2.66	6.94	2.04	3.96	2.69	3.89	1.27	2.11
7	1.68	2.69	3.16	2.00	3.26	2.47	2.86	2.16	2.18	2.04	3.37	2.06	5.32	4.18	1.87	1.06	2.48	1.34	1.34	3.74	1.97	2.28	2.71	7.10	2.09	3.99	2.67	4.16	1.34	2.25
8	1.68	2.74	3.17	2.00	3.26	2.47	2.89	2.24	2.17	2.08	3.59	2.06	5.32	4.15	1.87	1.05	2.48	1.35	1.34	3.82	2.00	2.28	2.69	7.40	2.11	4.00	2.64	4.15	1.36	2.11
9	1.68	2.78	3.19	2.10	3.28	2.48	3.08	2.38	2.17	2.25	3.85	2.13	5.53	5.13	1.90	1.04	2.65	1.41	1.34	4.14	2.05	2.37	2.64	8.28	2.33	4.20	2.74	4.03	1.43	2.27
10	1.70	2.59	3.09	1.94	2.99	2.45	2.78	2.03	2.26	1.97	3.15	2.06	5.25	4.38	1.80	1.09	2.19	1.28	1.34	3.60	2.00	2.27	2.78	6.89	2.06	4.00	2.80	4.10	1.27	2.11
11	1.67	2.75	3.20	2.00	3.25	2.48	3.20	2.45	2.13	2.23	3.95	2.12	5.58	5.13	1.89	1.02	2.69	1.41	1.34	4.14	2.04	2.37	2.65	8.37	2.38	4.71	2.75	3.99	1.43	2.38
12	1.67	2.68	3.15	1.99	3.35	2.46	2.84	2.14	2.19	2.04	3.37	2.06	5.30	4.19	1.86	1.05	2.36	1.33	1.34	3.74	1.97	2.25	2.71	6.92	2.08	3.96	2.66	4.18	1.33	2.11
13	1.67	2.64	3.09	1.73	3.27	2.44	2.80	2.01	2.19	2.00	3.37	2.06	5.25	4.14	1.81	1.06	2.28	1.31	1.34	3.68	1.96	2.23	2.68	6.59	2.05	3.99	2.71	4.11	1.27	2.11
14	1.68	2.74	3.17	2.00	3.26	2.47	2.88	2.24	2.17	2.07	3.56	2.06	5.32	4.17	1.87	1.06	2.48	1.34	1.34	3.79	1.96	2.27	2.70	7.29	2.10	3.99	2.64	4.16	1.35	2.11
15	1.66	2.69	3.09	1.71	3.32	2.43	2.84	2.13	2.15	2.03	3.37	2.06	5.26	4.08	1.84	1.03	2.48	1.32	1.34	3.72	1.93	2.24	2.65	7.00	2.06	4.00	2.63	3.92	1.32	2.11
16	1.67	2.73	3.18	1.98	3.25	2.46	2.98	2.24	2.15	2.14	3.80	2.11	5.38	4.43	1.87	1.03	2.64	1.36	1.34	3.93	2.02	2.29	2.54	7.83	2.17	4.07	2.67	4.11	1.39	2.11
17	1.67	2.65	3.09	1.71	3.28	2.45	2.81	2.02	2.19	2.01	3.37	2.06	5.26	4.15	1.82	1.06	2.27	1.31	1.34	3.69	1.97	2.24	2.69	6.61	2.05	4.00	2.72	4.13	1.27	2.11
18	1.68	2.69	3.15	1.98	3.26	2.46	2.86	2.15	2.18	2.00	3.37	2.06	5.31	4.20	1.86	1.06	2.38	1.33	1.34	3.66	1.96	2.28	2.69	7.05	2.08	4.01	2.66	4.14	1.33	2.11
19	1.68	2.73	3.18	1.99	3.25	2.47	2.93	2.24	2.16	2.12	3.69	2.11	5.33	4.03	1.87	1.04	2.48	1.35	1.34	3.88	2.01	2.28	2.64	7.62	2.12	4.02	2.66	4.13	1.37	2.11
20	1.69	2.70	3.17	2.10	3.27	2.48	2.87	2.24	2.19	2.05	3.37	2.06	5.33	4.21	1.88	1.05	2.48	1.35	1.34	3.76	1.98	2.29	2.72	7.16	2.10	4.01	2.65	4.18	1.35	2.27
21	1.66	2.60	3.09	1.70	3.22	2.42	2.77	2.05	2.17	1.93	3.19	2.06	5.20	4.14	1.78	1.06	2.20	1.29	1.34	3.52	1.95	2.22	2.65	6.91	2.03	3.97	2.68	3.63	1.27	2.11
22	1.67	2.75	3.18	2.10	3.27	2.48	2.94	2.24	2.17	2.12	3.73	2.12	5.37	4.75	1.88	1.05	2.48	1.36	1.34	3.90	2.02	2.30	2.67	7.71	2.15	4.08	2.68	4.14	1.38	2.11
23	1.72	3.44	3.31	2.10	3.28	2.50	3.86	2.37	2.06	2.47	4.80	2.14	6.12	5.13	1.98	0.96	2.81	1.41	1.41	4.91	2.03	2.37	2.80	8.91	2.54	4.89	2.89	4.06	1.51	2.76
24	1.66	2.73	3.19	1.98	3.25	2.45	3.08	2.36	2.14	2.19	3.84	2.12	5.49	5.13	1.93	1.02	2.64	1.41	1.34	4.14	2.03	2.37	2.63	8.17	2.30	4.17	2.71	3.98	1.42	2.30
25	1.75	3.57	3.33	2.10	3.34	2.54	3.84	2.42	2.12	2.47	5.10	2.16	6.17	5.13	2.07	1.00	2.84	1.41	1.42	5.10	2.11	2.43	2.76	8.91	2.67	5.01	2.93	4.13	1.53	2.91
26	1.68	2.66	3.09	1.98	3.30	2.46	2.82	2.04	2.23	2.01	3.37	2.06	5.29	4.22	1.84	1.06	2.28	1.33	1.34	3.67	1.98	2.26	2.72	6.82	2.07	3.97	2.66	4.19	1.31	2.11
27	1.70	3.13	3.23	1.99	3.23	2.49	3.77	2.36	2.06	2.47	4.51	2.12	5.90	5.13	1.94	0.97	2.76	1.41	1.39	4.59	2.01	2.37	2.70	8.91	2.48	4.72	2.83	4.00	1.48	2.70
28	1.67	2.77	3.17	1.88	3.24	2.46	2.89	2.24	2.15	2.06	3.61	2.06	5.30	4.09	1.86	1.04	2.48	1.34	1.34	3.78	1.99	2.27	2.65	7.42	2.09	3.99	2.63	4.12	1.35	2.11
29	1.65	2.64	3.21	1.72	3.21	2.49	3.20	2.40	2.06	2.27	4.08	2.06	5.62	5.13	1.88	0.98	2.72	1.41	1.34	4.14	2.01	2.37	2.65	8.91	2.36	4.69	2.72	3.96	1.44	2.56
30	1.69	2.77	3.18	2.10	3.28	2.48	2.90	2.24	2.20	2.08	3.59	2.13	5.35	4.70	1.89	1.05	2.48	1.36	1.34	3.83	1.98	2.30	2.73	7.43	2.13	4.06	2.68	4.18	1.36	2.11

Note from Table 2 that the residual capacities vary much less across the realizations of mainshock damage (rows of the matrix) than they do across potential aftershocks (columns of the matrix), suggesting that the nature of the mainshock that induces the given damage state (in this case DS3) has relatively little effect on the residual capacity. As discussed later in this paper, what little variation there is across the mainshocks is related to the residual roof drifts. In the next step, the median residual capacity over all 30x30 mainshock-aftershock pairs is computed for each of the three building models and each damage state.

Step 3: Calculate median of residual capacities for each post-mainshock damage state

The median residual capacity over all 30x30 pairs of mainshock-damage realizations and potential aftershocks is reported in Table 3 for the three case-study building models in each damage state. Note that the values for DS1 are equal to those computed for the intact building in Step 1. In DS4, there is no (zero) residual capacity because collapse has already occurred. As expected, the median residual capacity decreases with increasing severity of the damage state, particularly for the bilinear building model. Overall, though, the reductions in capacity may seem to some to be surprisingly small considering the degradation in strength and stiffness. The differences among the three hysteretic models are discussed in the section after the next, which compares the results of the dynamic approach presented in this section with those of the static approach presented next.

Table 3. Median residual capacities (over the 30x30 potential mainshock-aftershock pairs) for the three case-study building models in each damage state. In DS1, the residual capacities are equal to those of the intact building. Once in DS4, the building has no residual capacity against collapse.

Building	Median Residual S_a Capacity (g)				
Model	DS1 (Intact)	DS2	DS3	DS3.5	DS4 (Collapsed)
Bilinear	2.78	2.64	2.09	1.64	0
Peak-Oriented	2.86	2.75	2.52	2.35	0
Pinching	2.77	2.70	2.53	2.35	0

STATIC COMPUTATION OF RESIDUAL CAPACITY

The static approach to computing the median residual capacity for each post-mainshock damage state of a building, as proposed in the guidelines by Bazzurro *et al.* [6,9], involves the following steps:

1a. Obtain a realization of the building in each post-mainshock damage state by performing a SPO analysis of the intact building model up to the peak roof drift associated with the damage state, followed by unloading to zero base shear.
1b. Obtain a SPO curve for the building in each damage state by re-loading the realization obtained in Step 1a up to collapse.
2. Compute the median residual capacity by inputting the SPO curve for each damage state from Step 1b into the SPO2IDA tool for inferring dynamic response.

The details of these steps and their results for the SDOF models of the case-study building are discussed in the subsections below. Note that the results for the bilinear, peak-oriented, and pinching models are identical, because the backbone and un/re-loading rule to/from zero base shear, and hence the SPO curve for each damage state, is the same for all three building models.

Step 1a: SPO of intact building (simulates mainshock response)

The SPO analyses (including unloading) of the intact building model called for in Step 1a, which each produce a realization of the building in one of the post-mainshock damage states, are illustrated in Figure 6 for the SDOF building models. Note that the unloading stiffness is parallel to the elastic stiffness, which is true for all three of the hysteretic models (e.g., see Figure 2). The residual roof drifts for the five post-mainshock damage states that are implied by these SPO analyses are circled in the figure (at zero base shear); their values will be compared with the results of NDA in the next section.

Step 1b: SPO of mainshock-damaged building (simulates aftershock response)

Since the re-loading stiffness for each of the damaged-building realizations obtained in Step 1a is parallel to the elastic stiffness (for all three hysteretic models), Figure 6 also shows the SPO curves for the five post-mainshock damage states. Note that the triangular SPO curve for DS4 is not used in Step 2 to compute a median residual capacity, because collapse has already occurred in DS4.

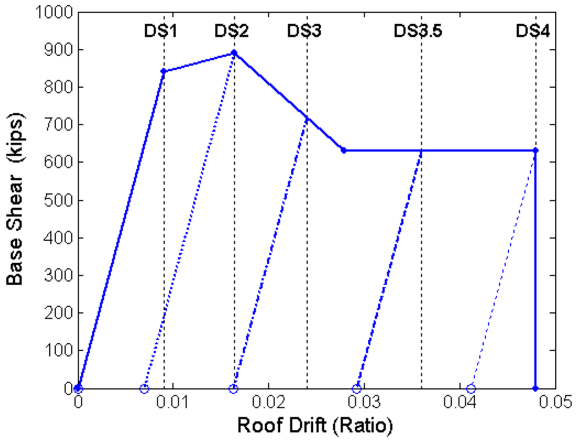

Figure 6. Static pushover (SPO) curve in each post-mainshock damage state for all three of the SDOF building models considered. Circled at zero base shear are the implied residual roof drifts. The SPO curves are input into the SPO2IDA tool [7,8] to compute the median residual capacities.

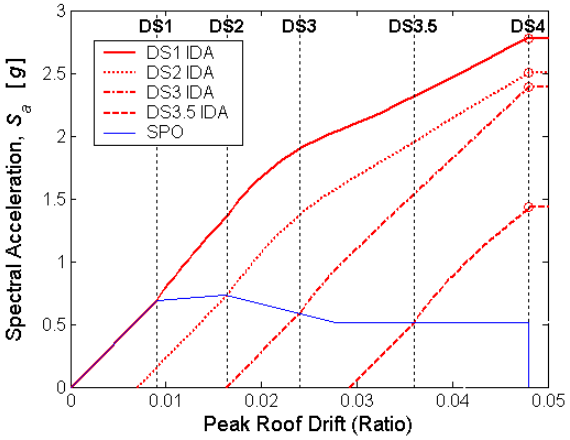

Figure 7. **Median IDA curves computed using SPO2IDA [7,8] for each post-mainshock damage state. The curves are the same for all three models of the case-study building. The median residual capacity for each damage state is circled, as given by the spectral acceleration at which each IDA reaches a peak roof drift of 0.048 (corresponding to collapse, or DS4).**

Step 2: SPO2IDA for mainshock-damaged building (simulates aftershock response)

SPO2IDA [7,8] is a spreadsheet tool that, as its name suggests, converts a static pushover curve into incremental dynamic analysis curves (median and 16th- and 84th-percentiles). The tool is based on NDA's of numerous SDOF oscillators with various quadrilinear backbone curves and pinching hysteretic behavior, all subjected to the 30 ground motion recordings that are also used in this paper.

Using SPO2IDA, the SPO curve obtained in Step 1 for each post-mainshock damage state (DS1-DS3.5) is translated into a median IDA curve, as shown in Figure 7. The spectral acceleration at the plateau of this median IDA curve, which is also the spectral acceleration that induces the peak roof drift associated with collapse, is the median residual capacity for the damage state. These median residual capacities are circled in Figure 7 and enumerated in Table 4. Note that there is no (zero) residual capacity in DS4, which corresponds to collapse. These results apply to all three of the models of the case-study building, and will be compared with the results of the dynamic approach in the next section.

It should be kept in mind that, although it is used here and in the guidelines by Bazzurro *et al.* [6,9] for such, SPO2IDA was not designed to provide IDA curves for mainshock-damaged buildings with residual roof drifts. Hence, the median residual capacities computed here via the static approach cannot necessarily be expected to agree with the results of the more accurate dynamic approach. In concept, an "aftershock" version of SPO2IDA could be developed using back-to-back mainshock-aftershock NDA's like those performed in the dynamic approach.

Table 4. **Median residual capacities for each post-mainshock damage state computed via the static approach. The values are the same for all three models of the case-study building. In damage state DS4, local collapse has already occurred, implying zero residual capacity.**

Median Residual S_a Capacity (g)				
DS1 (Intact)	DS2	DS3	DS3.5	DS4 (Collapsed)
2.77	2.50	2.39	1.43	0

COMPARISON OF DYNAMIC VERSUS STATIC RESULTS

Despite their differences, the dynamic and static approaches to computing the median residual capacity of a mainshock-damaged building both generate, as by-products, a median IDA curve and a median capacity for the intact building (i.e., for DS1), and an estimate of the residual roof drift in each post-mainshock damage state. These results from the two approaches, in addition to the median residual capacities for each damage state, are compared in this section.

Median IDA curves and median capacities for the intact building

For brevity, the median IDA curves for the intact building computed via the static (i.e., SPO2IDA) and dynamic (NDA) approaches are not re-plotted here, but a visual review of the intact IDA curve in Figure 7 and those in Figure 3(b) reveals that the two approaches provide nearly the same results. From these IDA curves it is also apparent that the median capacity of the intact building (or the building in DS1) computed via the static approach is close to those computed via nonlinear dynamic analyses. In fact, the median "intact" capacity from the static approach (2.77*g* – see Table 4) is within 4% of those computed via the dynamic approach (2.78*g*, 2.86*g*, and 2.77*g* for the bilinear, peak-oriented, and pinching models, respectively – see Table 3). The results are especially close in part because the same 30 earthquake recordings used by Vamvatsikos [7,8] to develop the SPO2IDA tool are also used here.

Residual roof drifts for each post-mainshock damage state

For each of the post-mainshock damage states (or corresponding peak roof drifts) considered, the residual roof drift implied by the static approach is compared in Figure 8 with the median values computed NDA of the bilinear, peak-oriented, and pinching building models. Note that what is plotted in the figure is the residual roof drift normalized by the peak roof drift associated with each damage state, and hence the ordinate is at most equal to one. Except in DS1, when there is no residual roof drift because the building is elastic, the residual roof drift implied by the SPO curve for each damage state clearly over-estimates the median results of NDA. This is to be expected, since the SPO curves do not allow for the possibility that the building may oscillate in the opposite direction after reaching its peak roof drift. As noted above in the dynamic computation section, the median residual roof drifts from NDA of the bilinear building model are larger than those for the peak-oriented and pinching models, and hence are closer to those implied in the static approach.

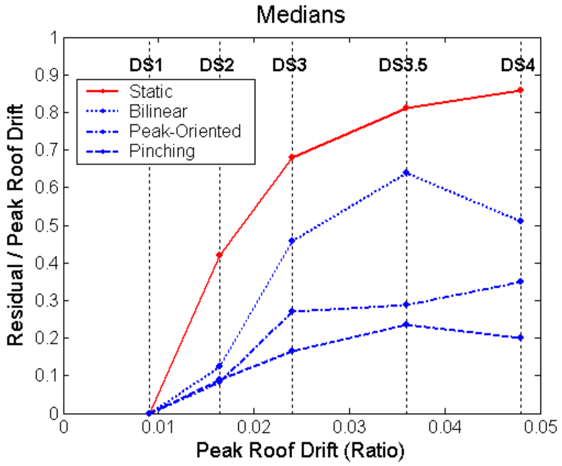

Figure 8. Comparison of (i) the median residual roof drifts (normalized by the peak roof drift) computed via nonlinear dynamic analyses of the three case-study building models with (ii) the residual roof drift implied by the static pushover curve for each post-mainshock damage state.

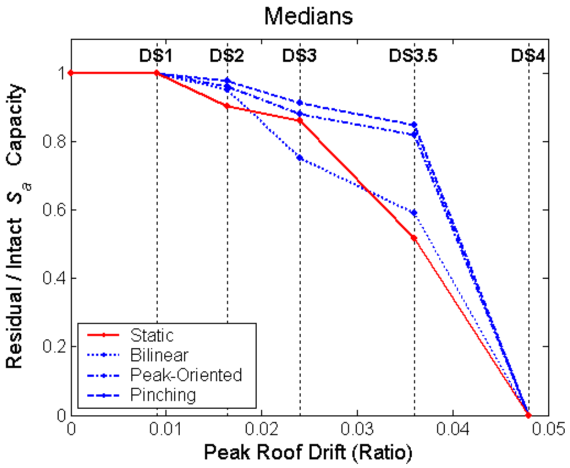

Figure 9. **Comparison of the median residual capacities (normalized by the corresponding median *intact* capacities) computed via the static versus dynamic approaches. Recall from Tables 3 and 4 that the median intact capacities (i.e., median residual capacities in post-mainshock damage state DS1) are approximately the same for the three case-study building models whether computed via the static or dynamic approaches.**

Median residual capacities for each post-mainshock damage state

The principal results of the dynamic and static computations, namely the median residual capacity for each post-mainshock damage state, are compared in Figure 9. What is actually plotted in the figure is the median residual capacity normalized by the median *intact* capacity (i.e., the median residual capacity for DS1). This residual/intact ratio, which measures the drop in median capacity resulting from mainshock damage, is used in the guidelines by Bazzurro *et al.* [6,9] as a basis for tagging decisions. Note that Figure 9 would look nearly the same if the median residual capacities were plotted instead of the residual/intact ratios, because the median intact capacities computed via the static and dynamic approaches (for all three building models), recall, are approximately the same.

From Figure 9 it is apparent that the static approach generally underestimates the median residual (normalized by intact) capacities computed via the dynamic approach, at least for the peak-oriented and pinching building models. For the bilinear building model, the static results underestimate by a lesser amount, or even overestimate (in DS3), those computed via the dynamic approach. The error in the static computation of median residual/intact capacity, expressed as a percentage of the dynamic result, is provided in Table 5. Note the relatively large error for the peak-oriented and pinching building models in DS3.5. All of the (non-zero) errors are reduced by the calibrated static approach proposed in the next section.

Table 5. **Error in the median residual (normalized by intact) capacities computed via the static approach, expressed as a percentage of the more accurate dynamic results also shown in Figure 9. The errors for DS1 are zero because, by definition, the residual/intact ratio is always one. In DS4, local collapse has already occurred, so there are no residual capacities to compute.**

Building Model	Error in Median Residual/Intact Capacity from Static Computation				
	DS1 (Intact)	DS2	DS3	DS3.5	DS4 (Collapsed)
Bilinear	0	-5.1%	14.9%	-12.5%	--
Peak-Oriented	0	-6.1%	-2.1%	-37.0%	--
Pinching	0	-8.0%	-5.3%	-39.1%	--

CALIBRATED STATIC COMPUTATION OF RESIDUAL CAPACITY

As shown in the preceding section, overall the results of the static approach are most similar to the dynamic results for the bilinear building model, both in terms of the median residual capacities and the residual roof drifts. This observation, coupled with intuition, suggests that the median residual capacities computed via the static and dynamic approaches might be more similar, particularly for the peak-oriented and pinching building models, if the residual roof drifts were more consistent as well. The median residual roof drifts from the dynamic analyses can be reflected in the static approach by appropriately "shifting" the SPO curve for each damage state obtained in Step 1. As demonstrated below, this shifting is the second step of the "calibrated" static approach.

Step 2: Shift SPO curve for each post-mainshock damage state to "expected" residual roof drift
As an example, in Figure 10(a) the SPO curve for DS2 is shifted back horizontally until its origin is at the median residual roof drift (also in DS2) from NDA of the pinching building model. Note that the roof drift associated with collapse (i.e., 0.048), which is considered an intrinsic property of the building, is not shifted. The resulting median residual capacity computed via SPO2IDA of the shifted SPO curve is larger and, in this example, closer to the value computed via the dynamic approach. For other potential residual roof drifts between zero and the peak roof drift associated with collapse (i.e., 0.048), the resulting median residual (normalized by intact) capacities are plotted in Figure 10(b) for DS2 through DS3.5. Note that each of these plots is simply a mirror image of the median IDA curve that is inferred from the damaged SPO curve shifted to have zero residual roof drift.

Also shown in Figure 10(b) are the median residual/intact capacities versus median residual roof drifts computed via the dynamic approach. Recall that the largest median residual roof drift (and smallest capacity) in each damage state is observed for the bilinear building model. From the dynamic results, it appears that the median residual capacity approaches the median *intact* capacity as the median residual roof drift approaches zero. Although not presented in this paper, this is also observed if the residual roof drift caused by each of the 30 mainshocks considered is plotted against the median residual capacity across the 30 potential aftershocks. Unlike these dynamic results, the static results in Figure 10(b) for DS3 suggest that the median residual capacity is greater than the median intact capacity if the residual roof drift is small. Correcting for this discrepancy is the next step of the calibrated static approach.

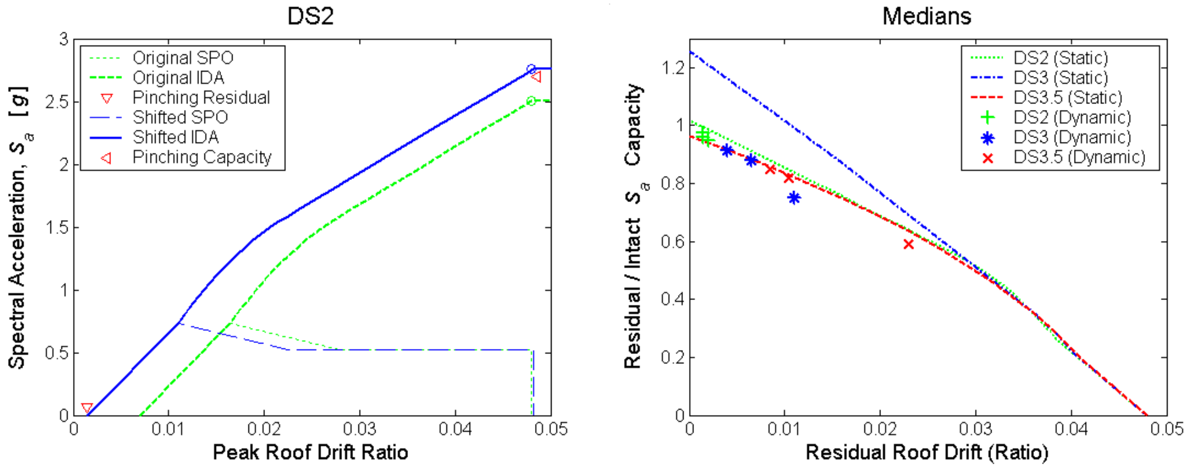

Figure 10. **Median residual capacities after Step 2 of the calibrated static approach, i.e., shifting the SPO curve for each post-mainshock damage state to the expected (or measured) residual roof drift. Panel (a) shows an example for the pinching building model in DS2. Panel (b) shows the results for the range of potential residual roof drifts, and compares them with the dynamic results.**

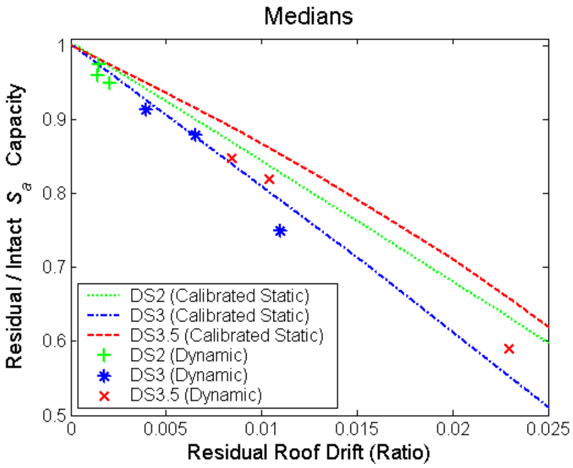

Figure 11. **Median residual (normalized by intact) capacities computed via the calibrated static approach for a given residual roof drift. For DS3.5, the curve matches the results of the dynamic approach more closely if the updated "all periods" version of SPO2IDA [16] is used.**

Step 3: Scale median residual capacity for each post-mainshock damage state

In order to be consistent with the dynamic results when there is no residual roof drift, the median residual/intact capacities computed in Step 2 over the range of potential residual roof drifts [see Figure 10(b)] are divided by their value at zero residual roof drift. A close-up of the resulting median residual/intact capacities plotted against the residual roof drifts is shown in Figure 11. As a result of this scaling, the median residual capacity is equal to the median intact capacity when the residual roof drift is zero, consistent with the trend of the dynamic results also shown in the figure.

The errors in the median residual/intact capacities computed via the calibrated static approach, expressed as percentages of the dynamic results, are enumerated in Table 6. Here the residual roof drifts assumed for the calibrated static approach are the median values computed via NDA of the three building models (see Figure 8 above). Compared to the errors from the "un-calibrated" static approach (see Table 5 above), the errors from the calibrated approach are smaller for all of the building models in DS2 through DS3.5. In fact, the errors are less than about 5%, except for the bilinear building model in DS3.5. For all three of the building models in DS3.5, the errors can be reduced further (to less than 2.3%), without affecting much the errors for DS2 and DS3, if one uses the version of SPO2IDA that covers "all periods" [16] instead of just "moderate periods." The latter is used in this paper merely to be consistent with the case studies presented in the guidelines by Bazzurro *et al.* [6], which are being updated to incorporate the calibrated static approach. Using the updated "all periods" version of SPO2IDA, the median residual capacities computed via the calibrated static approach have been found to be within about 5% of those computed via the dynamic approach for three other SDOF building models and an MDOF model of the case-study building.

Table 6. **Error in the median residual (normalized by intact) capacities computed via the calibrated static approach, expressed as a percentage of the more accurate dynamic results also shown in Figure 11.**

Building	Error in Median Residual/Intact Capacity from Calibrated Static Computation				
Model	DS1 (Intact)	DS2	DS3	DS3.5	DS4 (Collapsed)
Bilinear	0	2.4%	5.6%	11.5%	--
Peak-Oriented	0	2.4%	-0.3%	5.1%	--
Pinching	0	0.7%	1.5%	4.8%	--

Summary of steps for calibrated static computation

Subsequent to obtaining an SPO curve for the building in each post-mainshock damage state (i.e., Step 1 of the "un-calibrated" static approach), the additional steps involved in the "calibrated" static computation of median residual capacity can be summarized as follows:

2a. Shift the SPO curve for each post-mainshock damage state to be consistent with the expected (or measured, as discussed below) residual roof drift, and compute the resulting median residual capacity using SPO2IDA.

2b. Repeat Step 2a supposing no (i.e., zero) residual roof drift.

3. Divide the median residual capacities computed in Step 2a by the corresponding median residual capacities compute in Step 2b, and multiply by the median intact capacity (i.e., the median residual capacity for DS1, which has no residual roof drift). If, in fact, the residual roof drift is zero, the resulting median residual capacity for each damage state will equal the median intact capacity, consistent with the results of dynamic analyses.

Left open is the matter of determining the "expected" residual roof drift used in Step 2a. In the demonstration of the calibrated static approach above, recall that the expected residual roof drifts were set equal to the median residual roof drifts computed via NDA's of the three building models. Needless to say, NDA's are not carried out in the calibrated static approach, but expected residual roof drifts can be estimated from generic NDA results. For example, results like those in Figure 8 above, or from other researchers, e.g. [15,17], can be used to estimate the expected residual roof drift as a fraction of the peak roof drift associated with each damage state. Alternatively, but also based on NDA results, the expected residual roof drift could be estimated as a fraction of the residual roof drift implied by the SPO curve for each damage state (before shifting). As mentioned in Step 2a, even the residual roof drift measured in the field could be used. In this case, the median residual capacity for each post-mainshock damage state should be computed prior to the mainshock for a range of potential residual roof drifts, like in Figure 11 above.

CONCLUSIONS

Based on the results of back-to-back mainshock-aftershock nonlinear dynamic analyses (NDA's) of case-study building models, a "calibrated" static approach is developed for computing the median residual capacity of a mainshock-damaged building in terms of the aftershock ground motion it can withstand without collapsing. As originally proposed by Bazzurro *et. al.* [6], the static computation involves static pushover (SPO) analysis and use of the SPO2IDA spreadsheet tool [7,8] to infer the corresponding dynamic capacity. The "calibrated" computation takes into account the residual roof drift of the mainshock-damaged building, as either (i) measured in the field or (ii) expected for the observed state of damage based on, for example, generic research results of NDA's of buildings. The calibration also reflects the observation from the mainshock-aftershock dynamic computations that, as the residual roof drift approaches zero, the median residual capacity approaches the median capacity of the building in its undamaged state. Without the calibration, the static computation of median residual capacity is observed to underestimate the more accurate results of the dynamic computation. In fact, the median residual capacities computed via the dynamic approach in this paper (for the case-study building models over a range of potential post-mainshock damage states) may seem to some to be surprisingly large considering the degradation in strength and stiffness. This resilience of mainshock-damaged buildings has also been observed by other researchers, e.g., [3,4], and is somewhat corroborated by the historical rarity of aftershock-induced collapses. Given the economic and other costs associated with restricted or denied occupancy (i.e., yellow or red tags), it is important that the residual capacities of mainshock-damaged buildings be computed accurately. To this end, both the calibrated static and dynamic approaches to computing residual capacities should be investigated further.

ACKNOWLEDGEMENTS

The authors gratefully acknowledge (i) the Pacific Earthquake Engineering Research Lifelines (PEER-LL) Program for funding the study described in this paper, and (ii) several individuals for contributing to the study through discussions, including Joseph Maffei of Rutherford & Chekene, Kent Ferre of Pacific Gas & Electric, and Charles Menun of Stanford University.

REFERENCES

1. Yeo GL, Cornell CA. "Building tagging criteria based on aftershock PSHA." Proceeding of the 13WCEE, Vancouver, Canada. Paper No. 3283. August, 2004.
2. SAC Joint Venture. "FEMA 352: Recommended post-earthquake evaluation and repair criteria for welded steel moment-frame buildings." Sacramento, California. 2000.
3. Lee K, Foutch DA. "Performance evaluation of damaged steel frame buildings subjected to seismic loads." ASCE Journal of Structural Engineering 2004; 130(4): 588-599.
4. Amadio C, Fragiacomo M, Rajgelj S. "The effects of repeated earthquake ground motions on the non-linear response of SDOF systems." Earthquake Engineering and Structural Dynamics 2003; 32: 291-308.
5. Luco N, Cornell CA, Yeo GL. "Annual limit-state frequencies for partially-inspected earthquake-damaged buildings." Structural Safety 2002; 24: 281-296.
6. Bazzurro P, Cornell CA, Menun C, Motahari M. "Advanced seismic assessment guidelines." PEER Report Draft. February, 2003.
7. Vamvatsikos D, Cornell CA. "Practical estimation of the seismic demand and capacity of oscillators with multi-linear static pushovers through incremental dynamic analysis." Proceeding of the 7th U.S. National Conference on Earthquake Engineering, Boston, MA. July, 2002.
8. Vamvatsikos D, Cornell CA. "Direct estimation of the seismic demand and capacity of MDOF systems through Incremental Dynamic Analysis of an SDOF approximation." ASCE Journal of Structural Engineering (to be published).
9. Bazzurro P, Cornell CA, Menun C, Motahari M. "Guidelines for seismic assessment of damaged buildings." Proceeding of the 13WCEE, Vancouver, Canada. Paper No. 1708. August, 2004.
10. RAM International. "RAM Perform 2D Software, V1.04." Carlsbad, CA. October, 2000.
11. Clough RW. "Effect of stiffness degradation of earthquake ductility requirements." Report No. 66-16, Department of Civil Engineering, University of California, Berkeley. 1996.
12. Krawinkler H, Rahnama M, Gupta A, Miranda M, Ayoub A, Ibarra L. "SNAP: SDOF nonlinear analysis program." Stanford University, Stanford, CA. October, 2002.
13. Mahin SA, Bertero VV. "An evaluation of inelastic seismic design spectra." ASCE Journal of Structural Engineering 1981; 107(ST9): 1777-1795.
14. Christopoulos C, Pampanin S, Priestley MJN. "Performance-based seismic response of frame structures including residual deformations. Part I: Single-degree of freedom systems." Journal of Earthquake Engineering 2003; 7(1): 97-118.
15. Ruiz-Garcia J (under the direction of Miranda E). "Performance-based evaluation of existing structures accounting for residual displacements" (Personal communication). PhD dissertation, Department of Civil and Environmental Engineering, Stanford University, Stanford, CA. Expected date of completion: December, 2004.
16. Vamvatsikos D. "SPO2IDA: All periods" (Excel spreadsheet). Available from http://tremble.stanford.edu/nausika/software/spo2ida-allt.xls as of March, 2004.
17. Pampanin S, Christopoulos C, Priestley MJN. "Performance-based seismic response of frame structures including residual deformations. Part II: Multi-degree of freedom systems." Journal of Earthquake Engineering 2003; 7(1):119-147.